Crowd-induced lateral bridge vibration

Seán P. Carroll, B.Eng (Hons), M.Sc

Thesis submitted to The University of Nottingham
for the degree of Doctor of Philosophy

July 2013

The University of Nottingham

Ethos – Thesis for digitisation

Redactions

Thesis details:

Title: Crowd-induced lateral bridge vibration

Author: Carroll, Sean P.

Please exclude the following sections/pages:

Page 64 Figure 3.2 (a)

Subject standing on a narrow ridge.

To Jen

Abstract

Vibration induced by walking pedestrians has motivated research in the civil engineering community for many years. An area within this broad field that has received particular attention is the dynamic interaction that can occur between pedestrians and laterally flexible bridge structures. Perhaps the most notable example occurring on the opening day of London's Millennium Bridge. The enduring interest in this research problem is fuelled by two of its key features; (i) the sensitivity and adaptability of human balance to lateral motion and (ii) the spatial and temporal variation in flow characteristics exhibited by a pedestrian crowd. Both of these features are addressed herein.

In this project an experimental campaign was executed with the aim of identifying the interaction mechanism by which pedestrians produce force harmonics, that resonate with the oscillating structure on which they walk. These so-called self-excited forces have been experimentally identified by others but the underlying reason for their existence has remained an open question. In an effort to address this, human balance behaviour while walking on a laterally oscillating treadmill was recorded using 3-dimensional motion capture equipment. Subsequent analysis revealed that human response to sinusoidal base motion is dominated by periodic alteration of foot placement position. This produces amplitude modulation of the lateral component of the ground reaction force and is ultimately responsible for the self-excited force harmonics. It was further revealed that human centre of mass motion while walking on an oscillating structure is predominantly passive. The passive inverted pendulum model is thus an excellent model of pedestrian frontal plane balance.

The second facet of this work is concerned with developing a crowd-structure interac-

tion model that builds upon the current state of the art. The model presented utilises the understanding of human-structure interaction identified above and employs an agent-based modelling approach. Thus, the resulting 'virtual crowd' is capable of simulating key crowd features, such as inter-subject variability and emergent velocity-density flow behaviour. Using this model, it is shown that the experimentally identified human-structure interaction mechanism can lead to large amplitude lateral deck oscillations, consistent with field observations reported in the literature. The model successfully predicts the multi-mode instability of Bristol's Clifton Suspension Bridge in the absence of step frequency tuning among the crowd. This provides supporting evidence for the model's validity.

The work described above has resulted in a clearer understanding of the feedback between pedestrian balance behaviour and bridge response. Furthermore, the modelling techniques developed have potential for application in the wider study of crowd-induced vibration of dynamically susceptible structures.

Publications

- S.P. Carroll, J.S. Owen, M.F.M. Hussein. Modelling crowd-bridge dynamic interaction with a discretely defined crowd. *The Journal of Sound and Vibration*, 331: 2685-2709, 2012.
  [See chapter 5]

- S.P. Carroll, J.S. Owen, M.F.M. Hussein. Reproduction of lateral ground reaction forces from visual marker data and analysis of balance response while walking on a laterally oscillating deck. *Engineering Structures*, 49: 1034-1047, 2013.
  [See chapter 6]

- S.P. Carroll, J.S. Owen, M.F.M. Hussein. A coupled biomechanical/discrete element crowd model of crowd-bridge dynamic interaction & application to the Clifton Suspension Bridge. *Engineering Structures*, 49: 58-75, 2013.
  [See chapters 8 & 9]

- S.P. Carroll. Crowd-bridge interaction modelling utilising a discretely defined crowd - Research Update. *The Structural Engineer* 89 (23/24) 25-26, December 2011.

- S.P. Carroll, J.S. Owen, M.F.M. Hussein. Modelling crowd-bridge interaction with a discretely defined crowd. In: *Proceedings of Society for Earthquake and Civil Engineering Dynamics, Young Engineer's Conference.* London, United Kingdom. November 2010.

- S.P. Carroll, J.S. Owen, M.F.M. Hussein. Crowd-bridge interaction by combining biomechanical and discrete element models. In: *Proceedings of Eurodyn 2011, The* 8^{th} *International Conference on Structural Dynamics.* Leuven, Belgium. July 2011.

Acknowledgements

This Ph.D has been without doubt the most challenging and rewarding activity I have undertaken as an engineer...so far. However, it has not been a solo effort; its successful completion was only possible with the support and help of many others. I must first acknowledge the excellent and committed guidance provided by my two supervisors, Dr. John S. Owen and Dr. Mohammed F.M. Hussein. Their willingness to provide freedom, time and stimulating discussion has allowed this body of work to develop to its current state. Their approach to my Ph.D supervision has been exemplary.

My thanks and appreciation are also extended to my fellow Ph.D students, many of whom gave up their time without question to take part in my experimental campaign. Their friendship has been a sustaining force over the last 4 years. Any experimental campaign would be impossible without the contribution of the lab technicians who have gone above and beyond what could be expected of them. In particular, Craig for his technical wizardry (and being a test subject), Jim in the workshop who it seems could and would fabricate anything without difficulty and Mike for never saying no...and being a willing van driver.

A special thanks is given to Dr. Vicky Hood. Without her help in providing access to the Human Performance Lab, and her patience throughout the course of testing, the experimental campaign would never have got off the ground. I must also thank The University of Nottingham for providing the opportunity and funding to allow me to undertake this Ph.D.

However, if there is one person who deserves this Ph.D every bit as much as me, it's my partner Jen. Her support, patience and encouragement have been limitless. From making sure I don't go hungry, to rolling up her sleeves and helping me through experi-

mental testing, to being a sounding board for my ramblings (both related and unrelated to the Ph.D), without her it simply would not have been possible.

Finally, I give a wry thanks to the designers of the Millennium Bridge, for not getting it 100 % right the first time around. Without them I may never have found myself immersed in the fascinating world of structural dynamics.

Contents

Nomenclature

a_{env}	Peak bridge acceleration envelope
a_l	Local bridge acceleration
a_{lock}	Acceleration lock-in threshold
a_{max}	Maximum bridge acceleration
a_{ret}	Acceleration retardation threshold
a_{stop}	Acceleration stop threshold
$A_{E,95}$	Extreme peak acceleration with 5 % chance of exceedance
$A_{E,\text{peak}}$	Expected extreme peak acceleration
$\mathbf{A}_p$	Pedestrian acceleration vector
A_{peak}	Peak bridge acceleration observed
b	Rear distance to neighbouring pedestrian
b_{dyn}	Stability margin obtained from tuning on an oscillating deck
b_{fac}	Ratio of b_{dyn} to b_{min}
b_{min}	Minimum stability margin
B	Bridge deck width
c	Damping coefficient
c_n	Modal damping coefficient
d	Distance between pedestrians
d_{eq}	Equivalent uniform pedestrian density
d_w	Distance between pedestrian and obstacle
$d_{z,\text{eq}}$	Zonal equivalent pedestrian density
DLF_{eq}	Equivalent lateral dynamic load factor
$\bar{D}$	Energy dissipated by structural damping
f_{base}	Treadmill oscillation frequency
$f_{l,\mu}$	Mean lateral forcing frequency

$f_{l,\sigma}$ Standard deviation of lateral forcing frequencies

f_m Maximum frequency of oscillation

fn Probability distribution function

f_{n} Modal frequency

f_{p} Pedestrian lateral forcing frequency

f_{per} Pedestrian perception factor

f_{subject} Subject's lateral forcing frequency

f_{vert} Pedestrian pacing frequency

$\mathbf{F}_b$ Pedestrian boundary force vector

$F_{c,i}$ Load imposed on the i^{th} load cell

$F_{L,rep}$ Reproduced lateral ground reaction force

$F_{L,meas}$ Measured lateral ground reaction force

F_n Crowd-induced modal excitation

$\mathbf{F}_m$ Pedestrian motive force vector

F_{p} Pedestrian-induced footfall force

$\mathbf{F}_p$ Inter-pedestrian force vector

$\mathbf{F}_{\mathrm{res}}$ Pedestrian resultant force vector

g Acceleration due to gravity

G_f Magnitude of the lateral component of the ground reaction force

G_p Pedestrian weight

H Inverted pendulum lateral ground reaction force

k_1 Force constant

k_2 Distance constant

k_m Rotational spring constant

k_n Modal stiffness

k_p Perception factor constant

K Kinetic energy

l_p Pedestrian step length

L Bridge length

L_p Inverted pendulum leg length

m_d Treadmill deck mass

$m_{s,i}$ Mass of the i^{th} body segment

m_n Modal mass

m_p	Pedestrian mass
m_{reg}	Linear regression line slope
M	Bridge mass per unit length
M_m	Pedestrian motive moment
n	Vibration mode number
n_{eq}	Equivalent uniform pedestrian density
N	Number of pedestrian on the bridge
N_l	Limiting number of pedestrians
p	pedestrian index
P	Instantaneous power input
$\bar{P}$	Averaged power input
r	Pedestrian retardation function
r_{psy}	Pedestrian psychological radius
s	Step index
$\hat{S}_F$	Force power spectral density
$\hat{S}_U$	Displacement power spectral density
$\hat{S}_{\ddot{U}_n}$	Acceleration power spectral density
t	Time
t_f	Footfall force duration
t_r	Crowd model reaction time
t_{start}	Pedestrian start time
t_{stop}	Pedestrian stop duration
T	Single stance duration
T_d	Desired single stance duration
T_r	Return period
u	Lateral support position
u_0	Initial lateral support position
$\bar{u}$	Lateral distance between pendulum root and mass
v_{l}	Local bridge velocity
v_{lower}	Lower limit on walking velocity
$v_{z,\text{avg}}$	Average zonal pedestrian velocity
V	Potential energy
$\mathbf{V}_d$	Pedestrian desired velocity vector

$\mathbf{V}_p$	Realised pedestrian velocity vector
W	Bridge width
U	Lateral bridge displacement
$\dot{U}$	Lateral bridge velocity
$\ddot{U}$	Lateral bridge acceleration
$\ddot{U}_d$	Treadmill deck acceleration
x_b	Longitudinal bridge coordinate
x_m	Vertical position of inverted pendulum mass
x_p	Pedestrian x position coordinate
$\ddot{x}_{s,i}$	Frontal plane acceleration of the i^{th} body segment
$\mathbf{X}_p$	Pedestrian position vector
y / y_m	Lateral position of inverted pendulum
y_0	Initial inverted pendulum position
$\dot{y}$	Inverted pendulum velocity
$\dot{y}_0$	Initial inverted pendulum velocity
$\bar{\dot{y}}_0$	Modified initial inverted pendulum velocity
$\ddot{y}$	Inverted pendulum acceleration
α	Pendulum angle of inclination
$\dot{\alpha}$	Pendulum angular velocity
$\ddot{\alpha}$	Pendulum angular acceleration
β	Frequency modulation ratio
δ_f	Frequency resolution
Δt	Time-step
Δt_{crowd}	Crowd model time-step
Δt_{dyn}	Dynamical system time-step
ζ	Bridge damping ratio
η	Number of positive acceleration peaks observed
θ_d	Angle denoting pedestrian desired orientation
θ_p	Angle denoting realised pedestrian orientation
μ	Mean
σ	Standard deviation
ϕ	Mode shape ordinate
ψ	Load reduction factor

ω	Angular frequency
$\mathcal{L}$	The Lagrangian function
AM	Amplitude modulation
CC	Correlation coefficient
CDF	Cumulative distribution function
CoM	Centre of mass
CoP	Centre of pressure
CoV	Coefficient of variation
DET	Discrete element theory
FFT	Fast Fourier transform
GRF	Ground reaction force
HSI	Human-structure interaction
IP	Inverted pendulum
ISV	Inter-subject variability
MD	Modulation depth
pdf	Probability density function
PSD	Power spectral density
SD	Standard deviation
SDoF	Single degree of freedom
SLE	Synchronous lateral excitation
XCoM	Extrapolated centre of mass

List of Figures

List of Tables

CHAPTER 1

Introduction

The problem of excessive lateral bridge vibration induced by pedestrian traffic has received much attention from the engineering community for more than a decade. Interest was sparked in 1999 by the closure of the Solférino Bridge in Paris [26]. However it was the closure of London's Millennium Bridge the following year [2] that brought the issue to the attention of the wider public. Much of the guidance available to engineers regarding human-induced bridge vibration and the lateral instability phenomenon that can occur has resulted from the investigation of these two loading events. This has resulted in restrictive design criteria for pedestrian numbers and acceleration limits. The financial cost of this potentially conservative design philosophy is difficult to asses, but a better understanding of the problem is almost certain to result in economies in design.

1.1 The research challenge

From a civil engineering perspective, a walking pedestrian constitutes one of the most complex sources of dynamic excitation a structure is likely to experience. If the structure on which a pedestrian walks is excited laterally to a level perceived by the pedestrian, a complex interaction may develop between the walking pedestrian and flexible structure. The perceived motion may induce alterations in the pedestrian's gait with a knock-on influence on the footfall forces imposed on the structure. This can in turn generate larger amplitude structural oscillations. A feedback loop is thereby established

between structural response and pedestrian balance behaviour. This can be considered a coupling between two dynamic systems, one of which is controlled by the human brain. This interaction mechanism is referred to as human-structure interaction (HSI) and its exact nature remains one of the biggest unanswered questions in the study of human-induced vibration.

The problem becomes considerably more challenging when expanded to consider the dynamic influence of a pedestrian crowd. Not only must the interaction between each pedestrian and the structure be considered, but also the interactions between individual pedestrians. Pedestrians moving within a crowd are subject to many physical and psychological influences. Social norms tend to force pedestrians to maintain certain distances between each other, respecting so-called 'personal space'. Individual pedestrians will also have varying levels of motivation to reach their destination. Each pedestrian must navigate through the environment, avoiding obstacles and other pedestrians as efficiently as possible. These factors all influence the behaviour of each individual within the crowd. When the influence of these factors is considered for each pedestrian in parallel, the overall behaviour of the crowd emerges. Emerging crowd behaviour is characterised by a spatially and temporally varying distribution of crowd density and walking velocities.

Information on the time varying location of pedestrians is critical for a realistic dynamic analysis of the structure. Pedestrians at different locations are subject to different levels of vibration response. Therefore the analysis of HSI between each pedestrian and the structure will differ depending on the pedestrian's location at a given instant in time.

One of the most influential parameters when modelling a pedestrian-induced dynamic load is frequency. This is directly related to walking velocity which is itself a function of the local crowd density. Thus the distribution of pedestrians influences the walking speeds and therefore forcing frequencies experienced by the structure.

The evolution of crowd flow behaviour is therefore a fundamental requirement for any dynamic analysis wishing to quantify the dynamic influence of a pedestrian crowd. The influence of emergent crowd behaviour on the structure, exhibited through the spatial and temporal variation of crowd velocity and density, is herein referred to as 'crowd-structure interaction'. This is distinct from HSI which refers to the interaction

between individual pedestrian balance behaviour and structural response.

The approach taken in the execution of this project will be to split the investigation into;

1. a study of HSI in an effort to better understand the interaction between a walking pedestrian and laterally oscillating structure. This will be achieved through experimental investigation and numerical modelling.
2. development of a modelling framework that utilises the improved understanding of HSI and also captures the dynamic influence of an evolving pedestrian crowd. This will primarily be a modelling exercise with validation against data and observations in the literature.

It is intended that the final model should predict the development of lateral instability based on a more complete understanding of HSI. However, it should also serve as a tool for the prediction of lateral bridge response under typical 'every day' or subcritical traffic conditions. It is arguably more important at the design stage to determine the peak bridge response under these conditions. A design focus on the 'worst case' loading event is conservative but also potentially expensive. Such conditions normally occur on the opening day of a new bridge when traffic densities are well above daily norms. This raises the question of whether or not it is necessary to design mitigation measures for such rare events.

1.2 Thesis outline

This thesis consists of 10 chapters. Chapter 2, contains a review of what may be considered the traditional literature relating to crowd-induced bridge vibration. This is followed by a discussion of fundamental concepts relating to the biomechanics and control of locomotion, in chapter 3. This chapter serves as a 'primer', establishing concepts and terminology used in later discussion.

Having reviewed the relevant material in chapters 2 and 3, the project aims and associated objectives are formally stated in chapter 4. A hypothesis regarding the HSI mechanism, formulated on the strength of the reviewed literature is also set out.

In chapter 5 a novel modelling approach is investigated. A model of crowd-bridge dynamic interaction is presented that utilises an agent-based crowd model. This allows the evolving nature of the crowd as well as the influence of inter-subject variability (ISV) to be simulated. The dynamic forcing effect of the crowd is generated through the use of empirical load models from the literature. This can be considered an exploratory model, the development and validation of which is presented in later chapters.

The experimental campaign is presented in chapter 6. The reproduction of ground reaction forces (GRFs) from marker data is discussed followed by an investigation of subject balance response while walking on a laterally oscillating treadmill. The discussion presented in this chapter identifies the HSI mechanism.

The suitability of the inverted pendulum biomechanical model is examined in chapter 7, by direct comparison with experimental observations. The justification necessary for the biomechanical modelling employed in the following chapter is established and a conclusion regarding the previously outlined hypothesis on HSI is also reached.

Chapter 8 brings together the novel modelling technique proposed in chapter 5 with the improved understanding of HSI established in chapter 6. The crowd are again characterised by an agent-based model, however each pedestrian within the crowd is modelled as an inverted pendulum biomechanical model, dynamically coupled to the oscillating structure. In this model, lateral bridge response is generated through the direct simulation of HSI. Thus the dual effects of HSI and crowd flow behaviour are simulated.

In chapter 9, the case for model validation is presented. A well documented crowd loading event on the Clifton Suspension Bridge is presented as a benchmark case study [24]. Validation is achieved through the successful simulation of key features of the loading event.

In chapter 10, final conclusions are drawn regarding both HSI, and the effectiveness of the modelling technique developed. The limitations of this work are highlighted as well as areas that require further investigation.

CHAPTER 2

Literature review

Chapter Summary

The body of literature concerning lateral excitation of footbridges is extensive. What is reviewed in this chapter is a selection of work that is considered particularly relevant to this project.

In section 2.1 a review of documented loading events on full scale bridges is presented. This serves to highlight that although development of large amplitude lateral bridge response is relatively rare, it is not limited to the well known London Millennium Bridge.

In 2.2, test campaigns involving subjects walking on laboratory based oscillating platforms are discussed. The experimental campaign in this project is a development of some of the work discussed in 2.2.

Biomechanically based load models and their application in civil engineering are discussed in section 2.3. This section also includes a discussion of the seminal work of Hof et al. on frontal plane stability. This is followed by a discussion of load models based on crowd-structure interaction modelling in section 2.4, a concept that is further developed in this project. A summary of the reviewed material and where progress remains to be made is given in 2.5.

2.1 Field observations and full scale testing

What follows in this section is a presentation of field observations and experimental investigations carried out on full scale bridges. The list is not exhaustive, however it encompasses the key landmarks in the literature. To aid the reader, where appropriate the key finding or outcome (in this author's opinion) from an investigation is presented in *italic* headline form at the start of the relevant subsection.

2.1.1 Paris pont de Solférino

An acceleration threshold of 0.1 m/s^2 - 0.2 m/s^2 is identified, at which a transition from random to synchronised pedestrian excitation occurs - step synchronisation is assumed to describe the interaction mechanism.

The pont de Solférino footbridge (SF) is a steel arch footbridge that spans 140 m across the river Seine, Fig. 2.1. When it opened to the public in December 1999, large amplitude lateral vibrations developed in the first lateral mode at 0.81 Hz. The bridge was temporarily closed shortly after to allow a campaign of testing and investigation to begin.

Figure 2.1: Pont de Solférino, Paris (image after [1]).

Several crowd loading tests were carried out on the bridge during the initial closure in 2000 and later in 2002. In the latter test campaign, pedestrians were directed to circulate around a predefined route while the number circulating was progressively increased to a maximum of between 207 and 229 [3]. Figure 2.2 shows the lateral acceleration response recorded during one crowd loading test.

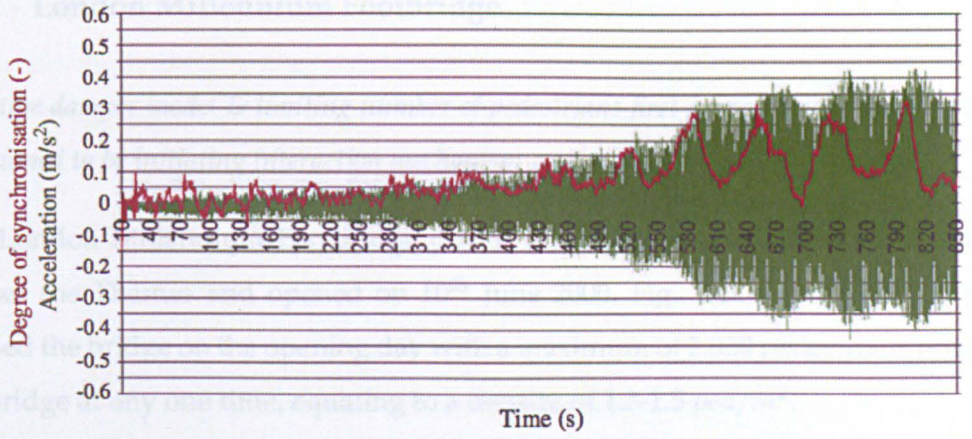

Figure 2.2: Lateral acceleration recorded on the SF during crowd loading tests in which pedestrian numbers were progressively increased to a maximum of 202 , after [27], reproduced from [3]

Also indicated in Fig. 2.2 is the *'synchronisation rate'*, defined as the ratio between the equivalent number of pedestrians and the total number of pedestrians present on the footbridge. The equivalent number of pedestrians is determined as the number of synchronised pedestrians who, uniformly distributed on the structure, input the same amount of energy per oscillation cycle as the entire group of uncorrelated pedestrians. The synchronisation rate is used to identify a transition from random to synchronised excitation.

Based on Fig. 2.2 and similar analyses, the transition from random to synchronised excitation is identified as occurring at between 0.1 m/s^2 and 0.2 m/s^2. The guidance in the French Sétra Technical Guide, [27] is therefore to limit lateral acceleration to below 0.1 m/s^2 to avoid 'lock-in' by the pedestrian crowd.

The Sétra Technical Guide, which emerged as a result of investigations carried out on the SF contains very little discussion regarding the frequency dependence of the lock-in phenomenon. It is demonstrated that when the pedestrian crowd were directed to 'walk fast', the previously observed large responses were not developed. It is also stated that *'Lock-in appears to initiate and develop more easily from an initial pedestrian walking frequency for which half the value is lower than the horizontal swinging risk natural frequency of the structure'*. Beyond this, there is very little to indicate the likelihood of lock-in as a function of modal frequency

2.1.2 London Millennium Footbridge

Negative damper model & limiting number of pedestrians first proposed, step synchronisation is assumed to be initiating interaction mechanism

The London Millennium Footbridge (LMB) is a shallow suspension footbridge that crosses the Thames and opened on 10^{th} June 2000, Fig. 2.3. Up to 100,000 people crossed the bridge on the opening day with a maximum of 2,000 pedestrians occupying the bridge at any one time, equating to a density of 1.3-1.5 ped/m^2.

Figure 2.3: Millennium Footbridge (image after [1]).

On the opening day, lateral vibration occurred on the south span at approximately 0.8 Hz (first lateral mode) and the central span at 0.5 Hz and 1.0 Hz (first and second lateral modes). Vibration also occurred less often on the north span at 1.0 Hz. The acceleration amplitude was estimated from video footage to be between 2.0 and 2.5 m/s^2 with maximum lateral displacement of around 70 mm. This response was sufficient to cause pedestrians to stop walking and use handrails for support where possible. As the crowd density increased so too did the magnitude of lateral oscillations, [2]. Although crowd loading tests carried out during the ensuing investigation revealed that the relationship between crowd density and magnitude of response was not linear, Fig. 2.4. It

can be seen in Fig. 2.4 that the lateral acceleration grows rapidly at approximately t = 1375 s, corresponding to only a marginal increase in the number of pedestrians on the bridge. The bridge was temporarily closed two days later.

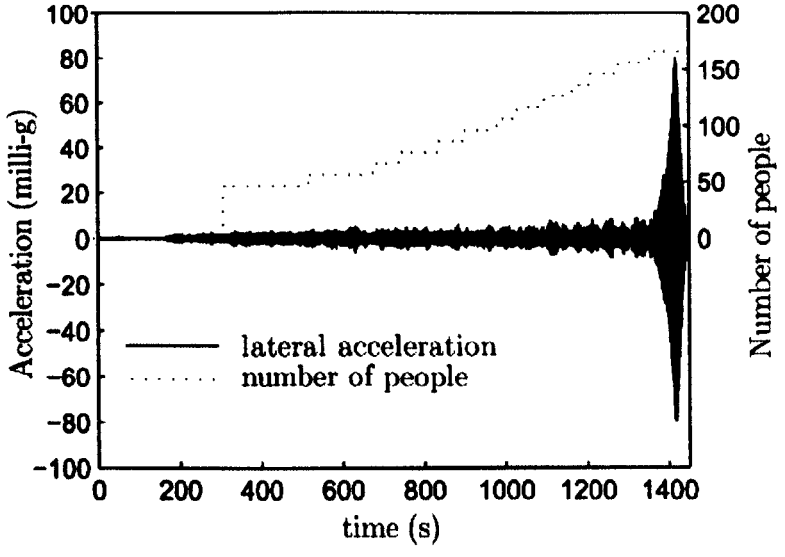

Figure 2.4: Lateral vibration of the north span at 1.0 Hz during crowd loading tests on the LMB. The number of pedestrians present on the structure is also shown, after [28], reproduced from [3]

Dallard et al. [2] referred to the observed phenomenon as 'synchronous lateral excitation' (SLE). Until the publication of observations by Brownjohn [6] and Macdonald [24], Dallard et al's description of the HSI mechanism formed the foundation of the understanding of crowd-induced lateral excitation.

Dallard et al. proposed that when a pedestrian walks on a structure undergoing lateral oscillations, they synchronise their pacing frequency, such that the frequency of their lateral GRF synchronises with the oscillating structure. As the pedestrian's lateral CoM motion increases, so too does the GRF amplitude. Although within their explanation of the phenomenon, Dallard et al. do not actually mention 'step synchronisation', instead talking of 'force synchronisation', step synchronisation is implicit in their explanation of the phenomenon, and was fairly assumed to be at the heart of their explanation. Video footage recorded on the opening day also shows pedestrians appearing to step in time with the bridge during large amplitude oscillations.

The lateral GRF is applied at half the pacing frequency, meaning a bandwidth of approximately 0.8 - 1.1 Hz is common among the population. This correlates well with

the 0.8 Hz and 1.0 Hz vibration on LMB. However, the 0.5 Hz vibration was attributed to pedestrians possibly adopting a 'snaking walk' to maintain balance [28]. No further discussion or evidence for this was presented.

Crowd loading tests on LMB showed that the lateral GRF generated by pedestrians was proportional to the local bridge velocity, Fig. 2.5.

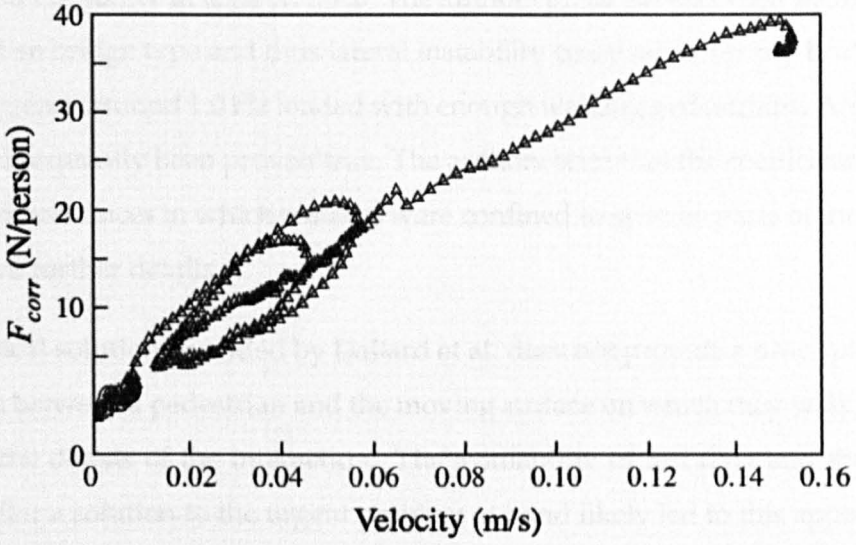

Figure 2.5: Typical lateral force versus velocity for LMB testing, after [2], reproduced from [3].

Dallard et al. therefore proposed that the correlated force per pedestrian, αF, could be related to the local deck velocity, $\dot{U}_{local}$, by a lateral walking force coefficient, c:

$$\alpha F = c\,\dot{U}_{local} \tag{2.1.1}$$

where c was determined to be 300 Ns/m in the frequency range 0.5 to 1.0 Hz, from tests carried out on LMB (Fig. 2.5). The p^{th} pedestrian's contribution to the modal force is,

$$\phi_p\,\alpha F = \phi_p\,c\,\dot{U}_{local} = \phi_p^2\,c\,\dot{U} \tag{2.1.2}$$

where ϕ_p is the mode shape ordinate corresponding to the location of the p^{th} pedestrian. Therefore the modal excitation force, F_n generated by N people across the bridge span is,

$$F_n = \sum_{p=1}^{N} \phi_p^2\,c\,\dot{U} = c\,\dot{U} \sum_{p=1}^{N} \phi_p^2 \tag{2.1.3}$$

By equating the excitation force F_n to the modal damping force, $D = 2m_n\omega_n\zeta\dot{U}$, assuming a uniform distribution of pedestrians across the span and a sinusoidal mode

shape, the limiting number of pedestrians N_l to avoid lateral instability can be derived,

$$N_l = \frac{8\pi c_n f_n m_n}{k_n} \tag{2.1.4}$$

where c_n is the damping ratio, f_n is the modal frequency and m_n is the modal mass.

Dallard et al. report that Eq. (2.1.4) predicted the number of pedestrians required to cause lateral instability in tests on LMB. The authors point out that their solution is not dependent on bridge type and thus lateral instability could occur on any bridge with a lateral frequency around 1.0 Hz loaded with enough walking pedestrians. An assertion that has subsequently been proven true. The authors state that the coefficient k, varied in other circumstances in which walkers were confined to specific parts of the span but did not give further details.

The analytical solution provided by Dallard et al. does not provide a description of the interaction between a pedestrian and the moving surface on which they walk, nor does it require the details of the interaction. The availability of test data and the requirement to tailor a solution to the urgent problem at hand likely led to this approach. The solution proposed is based on global observations of the phenomenon (such as video footage of the phenomenon at a well developed stage) and from these global observations, logical assumptions are made regarding the nature of HSI, namely footfall force synchronisation with the bridge.

2.1.3 Maple Valley Suspension Footbridge

Step synchronisation & de-tuning demonstrated on a Japanese footbridge suggesting the self-limiting nature of SLE.

The Maple Valley Great Suspension Bridge (MVB), Fig. 2.6, is located in Japan. It has a central span of 320 m and back-spans of 60 m. The bridge vibrates laterally in the third mode at 0.88 Hz and the fourth mode at 1.02 Hz, depending on pedestrian distribution.

Nakamura carried out an investigation, [4], in which a pedestrian, equipped with a waist mounted accelerometer traversed the bridge. Bridge response data was compared against that obtained from the waist mounted accelerometer, approximating the

Figure 2.6: The Maple Valley Great Suspension Bridge (MVB), Japan, after [4].

pedestrian's frontal plane centre of mass motion.

In one case, bridge displacement amplitude reached 24 mm while the pedestrian's CoM displacement amplitude was 43 mm (displacements were derived from double integration of acceleration data). This data relates to a period when the pedestrian was in the immediate vicinity of the bridge mounted accelerometer. Comparison of the displacement-time histories revealed the pedestrian CoM motion to be synchronised with the bridge and between 120° and 160° ahead of the bridge, thus adding energy to the bridge system.

In a second case, the bridge amplitude reached 45 mm, Fig. 2.7. The pedestrian was initially synchronised with the bridge until they apparently 'de-tuned', possibly due to a loss of balance. Nakamura suggested that this is proof of pedestrian step synchronisation. He further proposed that pedestrian-induced lateral excitation is not a divergent phenomenon but converges to a level beyond which pedestrians cannot maintain a steady pace due to loss of balance.

A drawback of Nakamura's analysis is that he did not present data showing a transition from an unsynchronised to a synchronised state. By merely showing a comparison between pedestrian and bridge motion for large amplitudes of bridge response, he has confirmed what was already visible from video footage of the LMB, i.e. for large vibration amplitudes pedestrians do synchronise their lateral forcing frequency to that of the oscillating structure and at some point they must stop walking to regain balance.

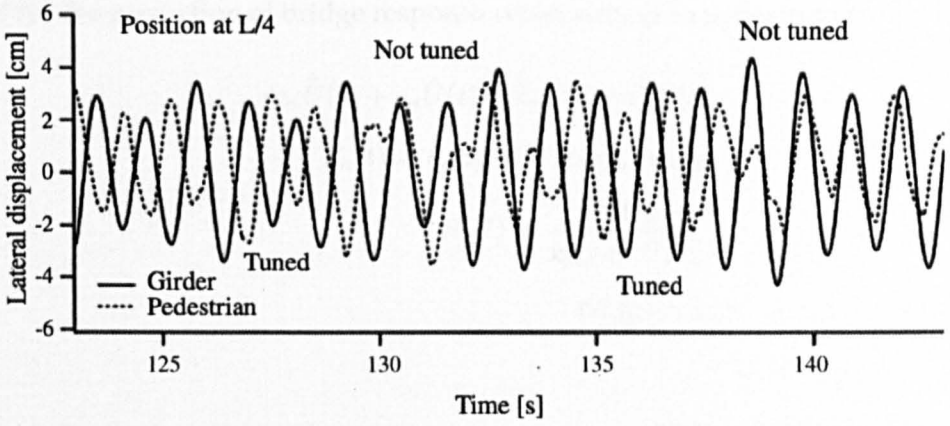

Figure 2.7: Lateral displacement of MVB and pedestrian, after [4], reproduced from [3].

A comparison of pedestrian and bridge motion covering a wider range of bridge vibration amplitudes would in theory capture a transition from unsynchronised walking to fully synchronised walking. It is this onset of synchronisation that is of more interest.

2.1.4 Toda Park Footbridge

SLE investigated on the Toda Park Footbridge, 'predictive' model proposed to describe bridge behaviour

Nakamura et al. subsequently reported a case study of a crowd loading event on the Toda Park Bridge (TPB) [5]. This is a cable-stayed steel box-girder footbridge also located in Japan, Fig. 2.8. It is one of the first bridges on which human-induced lateral excitation was observed and studied by Fujino et al. [29], approximately 7 years prior to the LMB. TPB has a main span of 134 m and back-span of 45 m. It vibrated in its first lateral mode at 0.93 Hz when congested with approximately 0.8-1.3 ped/m^2.

Based on their observations of both the MVB and TPB, Nakamura et al. proposed a

model for the prediction of bridge response when subject to pedestrian crowd loading:

$$m_n\ddot{U}(t) + c_n\dot{U}(t) + k_nU(t) = F_n(t) \tag{2.1.5}$$

$$F_n(t) = k_\alpha k_\beta \, S(\dot{U}) \, G(f_n) \, m_p \, g \tag{2.1.6}$$

$$S(\dot{U}) = \frac{\dot{U}(t)}{k_{sat} + |\dot{U}(t)|} \tag{2.1.7}$$

$$G(f_n) = 1 \tag{2.1.8}$$

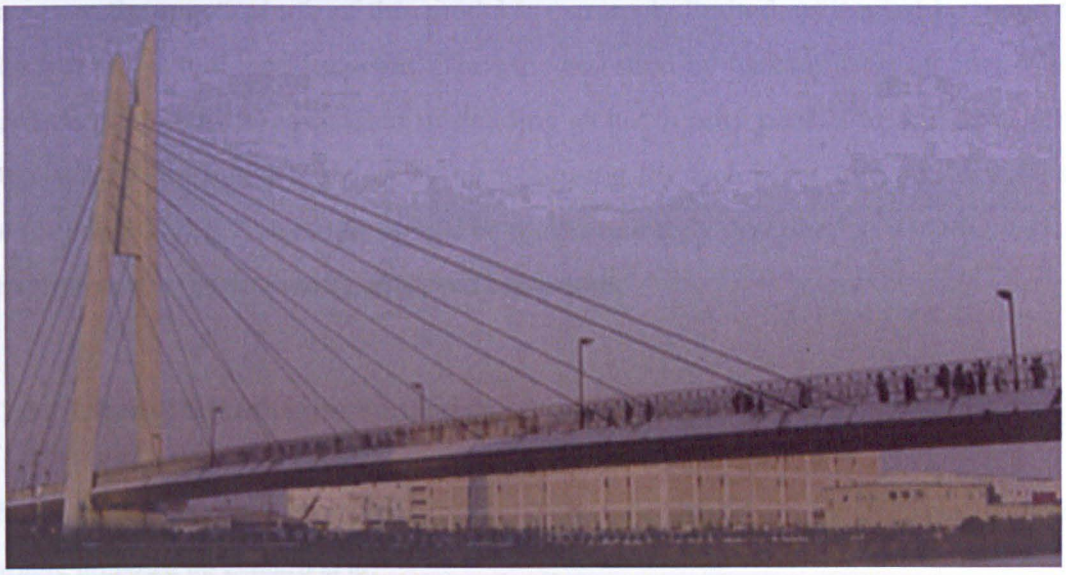

Figure 2.8: Toda Park Bridge (TPB), Japan [5].

Equation (2.1.5) is the standard equation for a single degree of freedom (SDoF) oscillator used to represent the response of a single vibration mode, all parameters have their usual meaning. Equation (2.1.6) is the lateral pedestrian-induced modal force. k_α is the ratio of lateral GRF to pedestrian weight, assumed to be 0.04. k_β is the proportion of pedestrians that synchronise with the bridge vibration. $S(\dot{U})$ is a function describing the nature of the pedestrian synchronisation. Nakamura et al. assume pedestrians synchronise proportionally to bridge response for low vibration levels, but as velocity magnitude increases pedestrians become increasingly uncomfortable and slow down. Equation (2.1.7) expresses this saturation phenomenon, with k_{sat} determining the saturation rate.

$G(f_n)$ is a function to take into account the tendency for pedestrians to synchronise with the bridge frequency. Nakamura et al. assume this to be 1.0 in the case of the

TPB, because the bridge frequency (0.93 Hz) is close to the usual lateral force frequency ($\approx$ 1.0 Hz). Presumably a different value would be applicable for modal frequencies further away from 1.0 Hz, however no recommendation is provided.

While Eq. (2.1.1) proposed by Dallard et al. predicts an infinitely increasing response, Eq. (2.1.7) accounts for an upper limit to the pedestrian induced excitation, observed in practice [4]. Also the fact that not all pedestrians necessarily synchronise with bridge oscillations is recognised via the factor k_β.

However, the practical use of this model is extremely limited, as it must be tuned to data from an actual loading event. Thus the assertion by Nakamura et al. that it is a 'prediction method' is somewhat misleading as it can only predict bridge behaviour after is has been tuned to do so by incorporating the factors k_β, and k_{sat} as well as the function $G(f_n)$. This model would be more accurately described as a mathematical description of experimentally observed behaviour.

2.1.5 Changi Mezzanine Footbridge

Observations of Changi Airport Bridge cast doubt over the popular step synchronisation theory initially proposed by Dallard et al.

Brownjohn et al [6, 30] carried out dynamic testing on a pedestrian bridge in Singapore Changi Airport known as the Changi Mezzanine Bridge (CMB), Fig. 2.9. The bridge is a 140 m span, flat arch constructed from tubular steel sections and connects two passenger terminals. Testing during construction confirmed that the bridge had dynamic characteristics that may make it susceptible SLE. The first lateral mode (LS1) had a frequency of 0.9 Hz while the first torsional mode (TS1) had a frequency of 1.64 Hz.

Application of Eq. (2.1.4) indicated that 145 people would be sufficient to cause lateral dynamic instability. It was therefore decided to carry out crowd load tests on the bridge prior to opening. 150 people took part in the first test. They walked in a circuit from one end of the bridge to the other, entering the bridge in groups of 10, separated by 15 second intervals. After circulating for 3 minutes they were told to stop and the free vibration was observed. Walking resumed and was stopped briefly before resuming to

Figure 2.9: Changi Mezzanine Bridge (CMB), Singapore [6].

allow pedestrians to vacate the bridge.

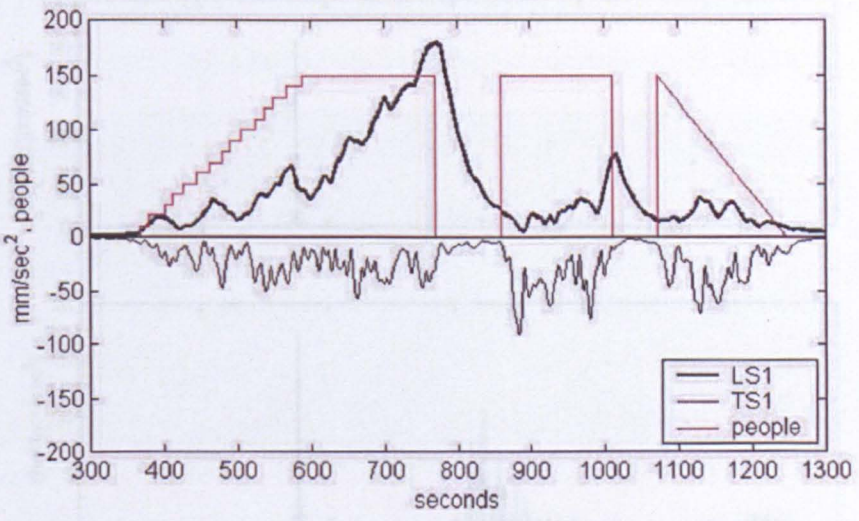

Figure 2.10: Envelopes of filtered lateral & vertical mid-span response with number of circulating pedestrians, after [6].

Examination of the lateral response at mid-span, Fig.2.10, shows that the response grew as pedestrians occupied the bridge, however after all pedestrians were present, at approximately 600 s, the response continued to grow until all pedestrians were directed to stop walking, at approximately 780 s. The maximum lateral acceleration achieved was 0.17 m/s^2. The growth in response appears to start at 600 s at which time the lat-

eral acceleration is approximately 0.04 m/s^2, well below the threshold identified in [31] for the onset of SLE. Pedestrians reported feeling uncomfortable during the test, with the feeling more pronounced while standing still. The feeling of discomfort was such that some pedestrians refused to take part in further testing despite the apparently low acceleration amplitude experienced. Although it was not established what was the minimum number of pedestrians required to cause this uncharacteristic growth in lateral response, 150 pedestrians was sufficient.

With reference to Fig. 2.10, it is significant that while the lateral response was increasing, the vertical response appears to be the result of random excitation. If pedestrians were synchronised with the bridge, as per the step synchronisation mechanism, one would expect to see a corresponding increase in the vertical response at twice the lateral forcing frequency. This is not observed here. A comparison of the Fourier amplitudes for mid-span lateral and vertical response highlights this lack of synchronization, Fig. 2.11.

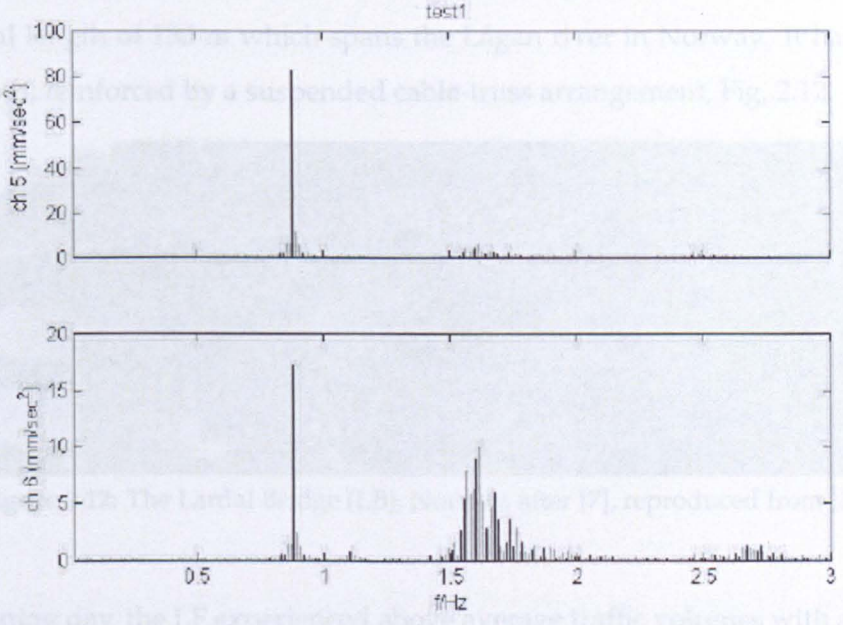

Figure 2.11: Fourier amplitudes of mid-span lateral (upper) and vertical (lower) response from 655-735 s, after [6].

The upper plot shows a prominent spectral line for the lateral response at a frequency around 0.9 Hz. If step synchronisation had occurred, the lower plot should show an equally dominant spectral line at 1.8 Hz. However this is not the case, instead a relatively broadband spectrum from around 1.6 Hz to 1.8 Hz is evident. Brownjohn et al.

also report that video recordings of the test did not show pedestrians to be synchronised while walking.

This is a key paper as it is the first documented loading event in which the theory of step synchronisation being a necessary prerequisite for lateral instability is questioned. Although the acceleration levels achieved were not of the same magnitude as those experienced on the LMB [2] or TPB [5], lateral dynamic instability was observed in the apparent absence of step synchronisation.

2.1.6 Lardal Footbridge

The importance of considering the spatial distribution of the pedestrian crowd highlighted as a key factor for consideration when simulating realistic crowd-induced excitation.

As part of his doctoral thesis [7], Rönnquist investigated the response of the Lardal footbridge (LF) to pedestrian excitation. The LF is a glue-laminated timber structure with a total length of 130 m which spans the Lågan river in Norway. It has a central span of 91 m, reinforced by a suspended cable-truss arrangement, Fig, 2.12.

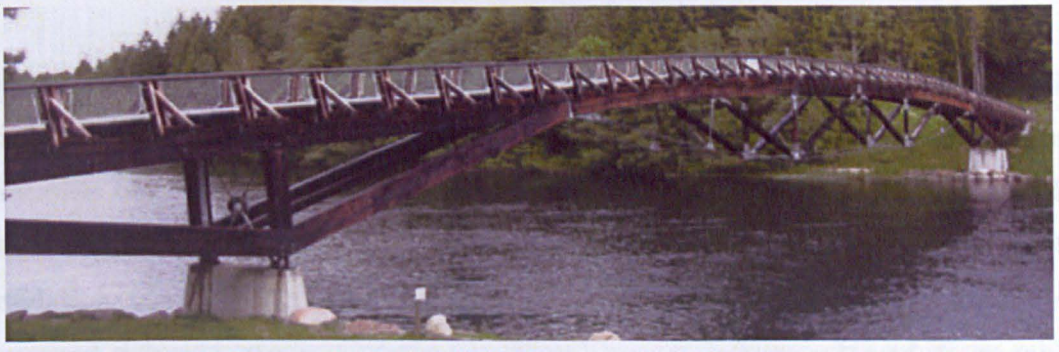

Figure 2.12: The Lardal Bridge (LB), Norway, after [7], reproduced from [3].

On its opening day, the LF experienced above average traffic volumes with a relatively dense and continuous flow of pedestrians crossing the bridge. Large amplitude lateral oscillations developed in the first lateral mode at 0.83 Hz, to the extent that pedestrians are reported to have been concerned by the motion [7]. However, typical daily traffic volumes are such that this level of response is rare and thus the dynamic behaviour does not pose a significant problem.

The motion of the first mode is similar to an inverted pendulum, therefore lateral os-

cillations at 0.83 Hz are accompanied by vertical oscillations at 1.66 Hz, a forcing frequency not uncommon in a slow moving or dense pedestrian crowd . Thus vertical excitation can lead to the development of large lateral responses, which may in turn trigger lateral HSI within an occupying crowd.

During crowd loading tests, Rönnquist observed exceptionally large lateral accelerations resulting from relatively modest pedestrian occupancy, Fig. 2.13. Furthermore, the relationship between peak lateral acceleration and crowd size was approximately linear.

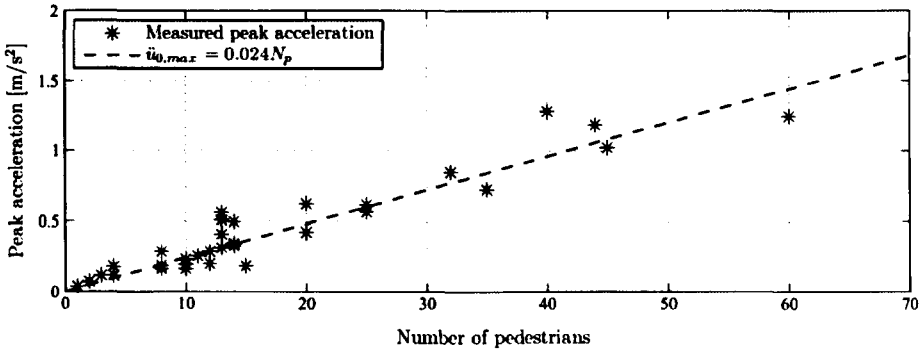

Figure 2.13: Recorded maximum mid-span acceleration as a function of the number of pedestrians present on the structure, after [7], reproduced from [3].

When comparing simulation results with experimental data, Rönnquist noted that the spatial distribution of pedestrians was an important factor to consider. A typical simplification often employed in the simulation of crowd-induced vibration is that the crowd are uniformly distributed across the bridge deck, and remain so throughout the simulation. However Rönnquist observed that as pedestrians at different locations experienced different levels of bridge vibration, some pedestrians slowed down while some stopped walking completely. Therefore what may start as one homogeneous group can fragment, leading to difficulty when comparing simulated and observed bridge response.

2.1.7 Clifton Suspension Bridge

Experimental observations lead to the theory of step synchronisation as the initiating mechanism for excessive lateral excitation being challenged.

Macdonald [24] published findings from his observation of a crowd loading event on Bristol's Clifton Suspension Bridge (CSB). The bridge has a clear span of 193.85 m and a deck width of 9.46 m, Fig. 2.14.

Figure 2.14: Clifton Suspension Bridge, Bristol (image after [1]).

The second (L2) and third (L3) lateral modes have frequencies of 0.524 Hz and 0.746 Hz and damping ratios of 0.58% and 0.68% respectively. The bridge was monitored for two weeks in the summer of 2003. This period included two crowd loading events during which the bridge was closed to vehicular traffic.

Examination of the lateral displacement at mid-span, recorded during one such crowd loading event, Fig. 2.15, reveals the sudden onset of large amplitude lateral oscillations in both modes L2 and L3. The response in L3 is initiated while there is already a large response in mode L2. Therefore it cannot be said that pedestrians simply responded to stimulus and locked-in to a single mode. Furthermore the first mode to exhibit a large amplitude response was mode L2 at a frequency of 0.524Hz. It is unlikely, although not impossible, that pedestrian's fundamental lateral forcing frequency was synchronised at 0.52 Hz. This would result in a pacing frequency of 1.04 Hz, well below than of an unobstructed pedestrian.

Macdonald reported that the mean lateral vibration frequencies of the responses during crowd loading, increased compared with the frequencies obtained during ambient vibration testing. This is in contrast to a drop in natural frequency that would be expected if pedestrians simply acted as passive added mass. Macdonald suggests these observations are evidence that HSI is more complex phenomenon than can be described by

step synchronisation alone.

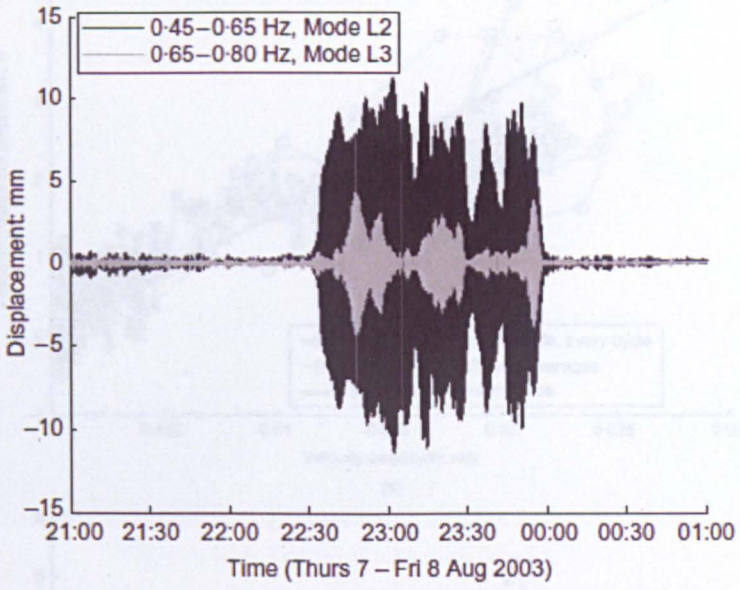

Figure 2.15: Observations from full-scale testing on the Clifton Suspension Bridge, Bristol. Filtered lateral displacement at mid-span for modes L2 & L3, after [24]

Similarly to Brownjohn et al. [6], Macdonald examined the power spectral density of the vertical response for peaks at double the lateral vibration frequencies (i.e. at 1.07 Hz & 1.53 Hz), no peaks were present at these frequencies. The peak lateral response was 0.2 m/s^2 which is relatively low in comparison to the LMB and TPB, however the vibrations were perceived by at least some of those on the bridge who reported feeling alarmed by the motion.

Macdonald carried out a similar analysis to that in [2]. He plotted the effective force amplitude per pedestrian against local velocity amplitude and observed similar proportionality between force magnitude and bridge velocity, Fig. 2.16. Thus pedestrians on the CSB acted as negative dampers as proposed by Dallard et al. however step synchronisation was not observed.

The proportionality between velocity and force extends to low levels of bridge velocity, this is not consistent with the assumption that a lower threshold exists for the initiation of the behaviour. However, Macdonald rightly points out that such a threshold may exist for step synchronisation, as observed in [31].

Although step synchronisation is clearly visible from footage of the LMB, based on ob-

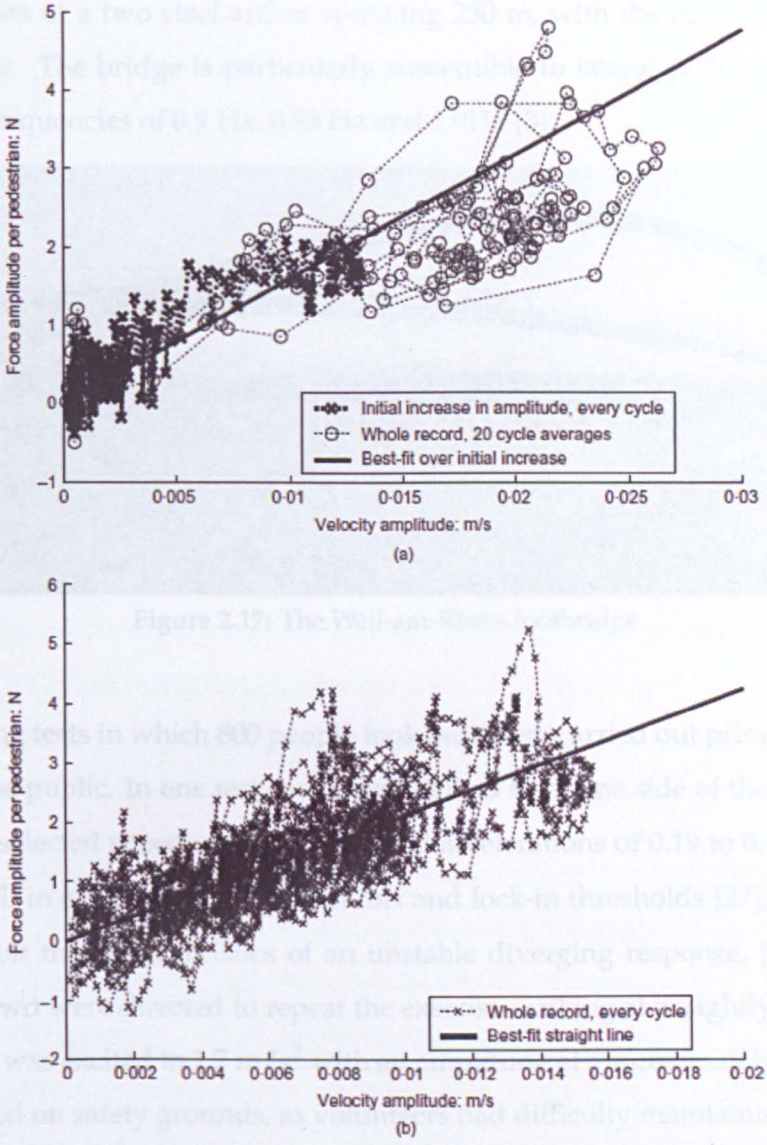

Figure 2.16: Observations from full-scale testing on the Clifton Suspension Bridge, Bristol. Relationship between bridge velocity & force (in phase with velocity) per pedestrian: (a) mode L2; (b) mode L3, after [24]

servation from the CSB, Macdonald proposes that step-synchronisation is not the initiating mechanism for large amplitude lateral oscillations. This is supported by earlier observations by Brownjohn et al.

2.1.8 Weil-am-Rhein Footbridge

The Weil-am-Rhein footbridge (WRF) spans the river Rhine between the German town of Weil-am-Rhein and the French town of Huningue and was opened in March 2007

[32]. It consists of a two steel arches spanning 230 m, with the pedestrian deck suspended below. The bridge is particularly susceptible to lateral pedestrian excitation with modal frequencies of 0.9 Hz, 0.95 Hz and 1.0Hz [3].

Figure 2.17: The Weil-am-Rhein footbridge

Crowd loading tests in which 800 people took part were carried out prior to the bridge opening to the public. In one test the crowd walked from one side of the bridge to the other, at self selected speeds. Although lateral accelerations of 0.19 to 0.45 m/s^2 were recorded, well in excess of the both comfort and lock-in thresholds [27], the response did not exhibit the characteristics of an unstable diverging response, [3]. However when the crowd were directed to repeat the exercise walking at a slightly faster speed, the 5^{th} mode was excited to 1.7 m/s^2 with an amplitude of approximately 40 mm. This test was halted on safety grounds, as volunteers had difficulty maintaining stability.

Despite this alarming response level, no additional damping measures have been installed on the bridge. It was concluded by the bride designers that the traffic conditions required to produce this response were unlikely to be seen on a regular basis, therefore retrofitting of additional damping measures was unwarranted, [32]

2.1.9 Simone-de-Beauvoir Footbridge

The Simone-de-Beauvoir Footbridge (SBF) spans the river Seine in Paris and was inaugurated in July 2006 [33]. It consists of shallow arch and stressed ribbon structures that combine at the quarter-span points, Fig. 2.18.

The SBF was designed from the outset with pedestrian excitation in mind. Design stage

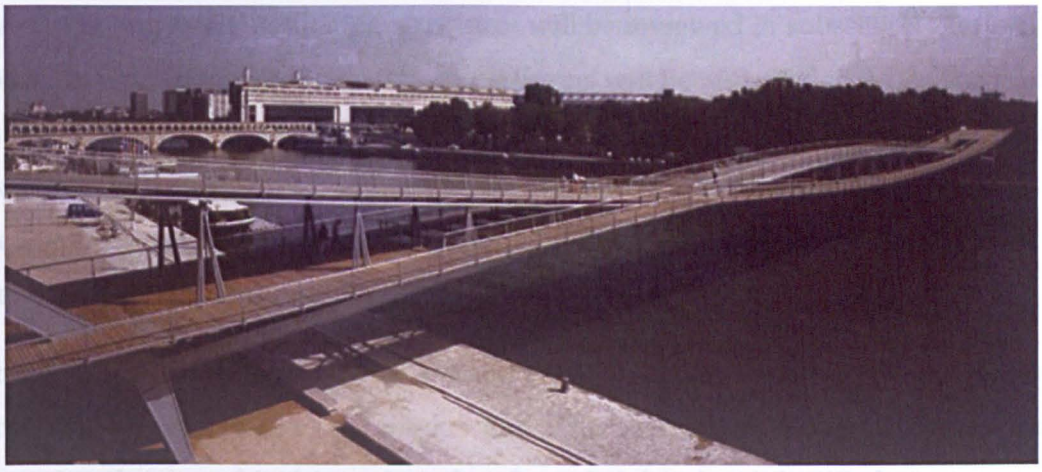

Figure 2.18: The Simone-de-Beauvoir Footbridge, reproduced from [3]

analyses revealed that the bridge may posses up to 9 modes with frequencies below 2 Hz. Among these, the first, third and fifth lateral modes with frequencies of 0.456 Hz, 0.959 Hz and 1.122 Hz were of particular concern. Modal testing on the actual structure confirmed the existence of the 1^{st} and 5^{th} modes with frequencies of 0.555 Hz and 1.154 Hz.

In order to validate the vibration mitigation measures employed (viscous and tuned-mass dampers), a series of crowd loading tests were undertaken immediately prior to the bridge opening to the public. Between 20 and 120 volunteers took part in tests in which the 'walking rhythm' was regulated and varied from slow walking to running [33]. The maximum displacement amplitude observed was approximately 30 mm in mode 1. This was achieved by a group of 80 to 100 pedestrians walking randomly and by a group of 20 walking in a synchronised fashion. Hoorpah et al. [33] note that during the bridge inauguration, approximately 400 people traversed the bridge, however similar response levels were not observed.

2.2 Laboratory based investigations

In this section the literature relating to laboratory based investigations is reviewed. These investigations typically involve an examination of HSI on specifically constructed platforms. Such platforms can be divided into two groups, those that are mechanically driven and those that are free to oscillate under the action of test subjects. Experimental

work involving freely oscillating structures will be reviewed in subsection 2.2.1. After which, investigations involving driven platforms will be reviewed in 2.2.2. The proliferation of research in this field since 1999/2000 has lead to a large number of platform-based tests being reported, [7–11, 27, 29, 34, 35]. What is contained in this review is not intended to be a catalogue of this work. Only those investigations of particular note or relevance are discussed here.

Subsection 2.2.3 reviews the work of Racic et al. [12] in reproducing vertical jumping and bobbing forces from visual marker data. The methods discussed are particularly relevant to those used in this project, therefore a brief review is justified.

2.2.1 Freely oscillation platform tests

McRobie et al. 2003:

McRobie et al [8] carried out tests on a full size section model of the centre span of the LMB, Fig. (2.19). The test structure was a three bar linkage with all stiffness provided by gravity. Three treadmills were placed on the platform deck allowing subjects to walk continuously on the oscillating structure. Human-induced forces were inferred from the structural response.

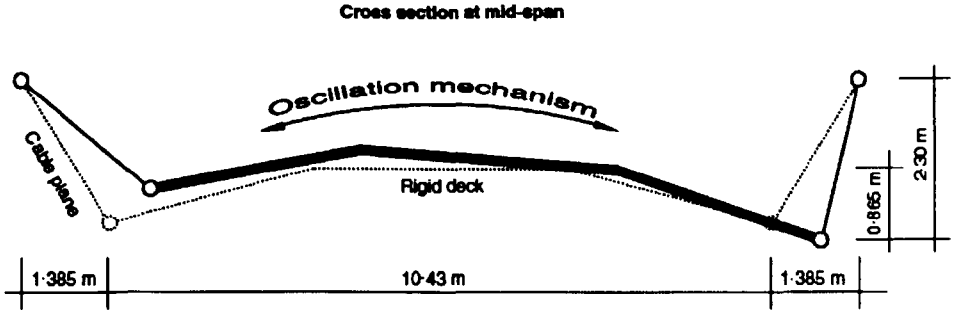

Figure 2.19: Test rig mechanism, after [8].

McRobie et al. reported that a common subject response to base motion was to increase gait width and walk at the same frequency as the structural motion. However it was also reported that the human-structure system quickly self-excited to amplitudes approaching 100 mm, even at natural frequencies as low as 0.35 Hz. It is not stated whether or not these tests involved synchronisation between the subject(s) and struc-

ture. Synchronisation at 0.35 Hz is unlikely, suggesting synchronisation may not have been a necessary ingredient for large amplitude oscillations. Subject step frequency alterations and transitions to a state of synchronisation with the structure should be cautiously considered. It is not stated that the treadmills utilised had variable belt-speeds. If belt speeds were fixed, then it is reasonable to hypothesis that a subject's choice of step frequency was biased by the need to keep pace with the treadmill belt.

It was noted that some subjects adopted a gait that effectively caused them to dissipate energy and bring the oscillations to a halt. McRobie et al. concluded that the lateral force from a single pedestrian does not grow linearly with velocity but grows suddenly with the transition to a feet apart gait. This is contrary to the model proposed by Dallard et al [2] for pedestrian crowds. This highlights the potential problem with inferring or assuming the nature of HSI based on observations at a macroscopic level. McRobie et al. suggest that the proportionality observed by Dallard et al (Fig. 2.5) is due to 'increasing transition probabilities (from a state of normal to synchronous walking) of individuals as oscillation amplitudes grow'.

A number of observations were also made regarding inter-subject synchronisation. A larger treadmill allowing two subjects to walk side-by-side was placed on the oscillating deck, with a third single person treadmill behind. It was found that step synchronisation between subjects was encouraged by a need to avoid stepping on a neighbour's feet or bumping shoulders. Subjects also reported that visual signals from subjects swaying in front of them altered their sense of stability. The significance of visual stimulus and sensory feedback generally, in maintaining stability is further discussed in section 3.3. These observations raise interested questions regarding inter-subject synchronisation in dense crowds with obvious implications for footbridge excitation.

Rönnquist 2005:

Investigations by Dallard et al. [2], Nakamura et al. [35] and McRobie et al. [8] all concluded that the magnitude of a pedestrian's lateral GRF increases as a function of deck motion. As part of his doctoral thesis, Rönnquist proposed a function identifying lateral GRF magnitude as a function of deck response.

A platform measuring 6 m $\times$ 1 m was suspended vertically from four corners and restrained laterally by springs. Horizontal force and displacement was recorded at

each end of the platform. Four subjects completed multiple walking tests across the platform resulting in 1087 'foot-pair' force samples being recorded.

Rönnquist analysed the time domain signal for each foot-pair force sample. By employing the common simplifying assumption; that the deviation from perfect periodicity is negligibly small, the GRF was represented by the sum of its first four Fourier components. The magnitude of the Fourier component can be considered a dynamic load factor (DLF) and was presented as a function of deck acceleration (at the position of the footfall), $\ddot{U}$, and the difference between lateral forcing frequency f_p and natural frequency f_n:

$$DLF_L^{1st} = 0.14 - 0.095\, exp\left[- \left(0.45 + 1.5\, exp\left[- \frac{1}{2}\left(\frac{f_p - f_n}{0.07} \right)^2 \right] \right) \ddot{U}^{1.35} \right] \quad (2.2.1)$$

$$DLF_L^{2nd} = 0.010 + 0.008\, \ddot{U} \quad (2.2.2)$$

$$DLF_L^{3rd} = 0.015 \quad (2.2.3)$$

$$DLF_L^{4th} = 0.005 \quad (2.2.4)$$

Eq. (2.2.1) predicts an increase in the magnitude of the first harmonic with increasing structural response, as observed by other researchers [2, 8, 35]. Eq. (2.2.2) also predicts an increase in the second harmonic although the trend is less significant. The third and fourth harmonics show no clear trend and are defined as constants (2.2.3) & (2.2.4).

Rönnquist also defined an equivalent sinusoidal load having the same load impulse energy as an actual step, Eq. (2.2.5). It was shown that the equivalent sine load was a good match to the actual footfall force-time history.

$$DLF_{eq} = 0.145 - 0.100\, exp\left[- \left(0.45 + 1.5\, exp\left[- \frac{1}{2}\left(\frac{f_p - f_n}{0.07} \right)^2 \right] \right) \ddot{U}^{1.35} \right] \quad (2.2.5)$$

This expression is very similar to that for the first harmonic, Eq. (2.2.1), indicating that higher harmonics can be ignored with negligible loss of accuracy. In support of this assumption Rönnquist cites Bachmann & Weber [36] who point out that a pedestrian is unlikely to maintain an exact frequency that gives higher Fourier components long enough time to create a steady-state excitation.

With regard to synchronisation effects, Rönnquist proposed that the lateral forcing fre-

quency tends to synchronise with the bridge oscillation frequency if it is initially within $\pm 10\%$ of the bridge oscillation frequency. He also proposed that the frequency ratio, f_p/f_n tended towards 1 for increasing acceleration. Unfortunately due to the length of the platform (6 m) it was difficult to study the synchronisation effect and the data presented in support of these claims is inconclusive.

The mass of the oscillating deck was 500 kg, while the mass of the pedestrian (who carried out the majority of the tests) was 55 kg. Thus a mass ratio of approximately 10:1 was achieved. Rönnquist himself notes that this is 'far from fulfilling the similarity requirements of the mass ratio between pedestrian[*s*] and [*the*] structural system'. The influence of this low mass ratio is difficult to quantify; on one hand if the magnitude of acceleration developed is representative of a real bridge, then the GRF generated on the deck should match than generated on the full size structure. However, if the objective is to understand how HSI develops, and then map that understanding to HSI on full scale structures, poor scaling may allow erroneous conclusions to be drawn.

Rönnquist attempted to validate the DLF expressions by carrying out numerical simulations of multiple pedestrians crossing a lively footbridge and then comparing results with recorded loading events. By representing individual pedestrian-induced loads as a series of load impulses progressing across the bridge, a Duhamel integral was used to determine the combined modal response. However, the nonuniform and varying pedestrian distribution observed during field testing led to difficulty comparing simulated and recorded responses. The main contribution from this work is the identification of DLFs as an empirical function of lateral deck response amplitude and frequency.

The (French) Technical Department for Transport, Roads, Bridge Engineering and Road Safety, Sétra 2006

As part of their investigation into the dynamic behaviour of the Solférino footbridge, the Technical Department for Transport, Roads, Bridge Engineering and Road Safety, Sétra, carried out walking tests on a 7 m $\times$ 2 m platform, Fig. 2.20, free to oscillate laterally. Their findings are contained in the French technical guidance document on footbridge design, [27].

Two 'crowd' tests involving 6 and 10 subjects are reported. In a similar manner to McRobie et al. the force imposed on the structure is derived from the structural re-

Figure 2.20: Laboratory based platform tests carried out by Sétra as part of the investigation into the dynamic behaviour of the Solférino footbridge, after [27].

sponse. By multiplying the instantaneous crown-induced force by the sign of the platform's velocity, the component of the force in phase with the velocity and therefore adding energy over each oscillation cycle is identified, Fig. 2.21.

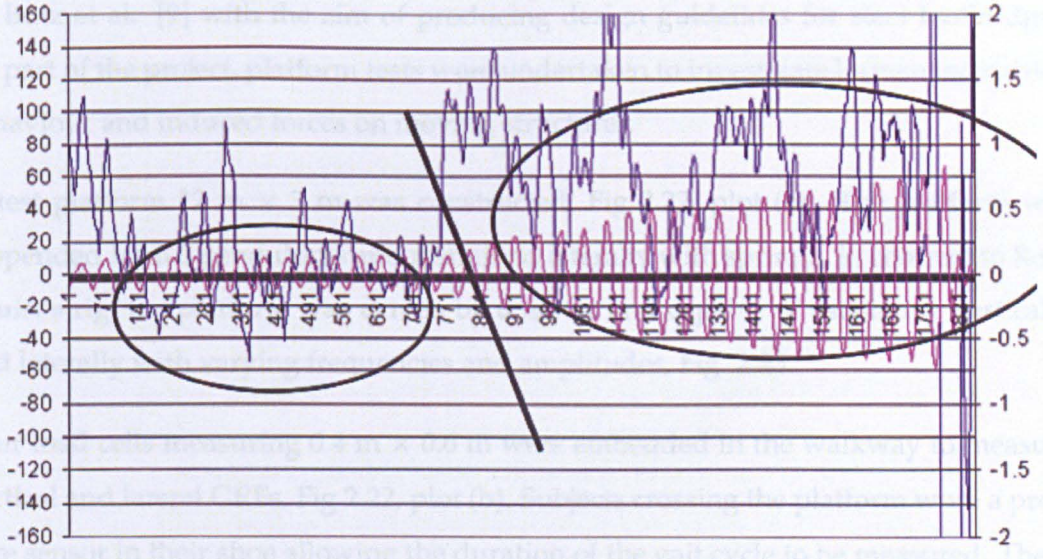

Figure 2.21: Data from a test in which 6 subjects walked across the deck. The left side scale indicates the value of the crowd-induced force (N) in phase with platform velocity, shown by the dark coloured trace. The right side scale indicates the value of platform acceleration (m/s^2) shown by the pink trace, after [27].

This data is used to identify a threshold of acceleration at which the crowd-induced

loading changes from random to synchronised. Random loading is defined as that which is equally likely to reduce as to increase the platform's instantaneous response. This is clearly seen in the left-most region in Fig. 2.21, in which negative force values indicate energy dissipation by the crowd. However, synchronised crowd-induced loading is identified in the right side circle in which the crowd-induced loading (in phase with deck velocity) is predominantly positive, indicating consistent energy supply by the crowd. This threshold value is identified as approximately 0.15 m/s^2.

There is no discussion of the potential frequency dependence of this threshold. Furthermore there is no attempt to identify the interaction mechanism responsible for the crowd's transition to an apparent synchronous state. Nevertheless the threshold value identified was adopted as the trigger acceleration for the initiation of lateral instability.

2.2.2 Driven oscillation platform tests

Butz et al.

A substantial project funded by the Research Fund for Coal and Steel was undertaken by Butz et al. [9] with the aim of producing design guidelines for steel footbridges. As part of the project, platform tests were undertaken to investigate human interaction behaviour and induced forces on moving structures.

A test platform 12 m × 3 m was constructed, Fig 2.22, plot (a). The platform was suspended from 8 pendulums and restrained laterally with springs. In contrast to Rönnquist's rig, the platform was driven by a motor and capable of oscillating vertically and laterally with varying frequencies and amplitudes, Fig. 2.23.

Four load cells measuring 0.4 m × 0.6 m were embedded in the walkway to measure vertical and lateral GRFs, Fig 2.22, plot (b). Subjects crossing the platform wore a pressure sensor in their shoe allowing the duration of the gait cycle to be measured. These pressure sensors facilitated the investigation of synchronisation and were not used to measure GRFs. Subjects were asked not to specifically target load cells while walking, thus acquisition of GRF data relied on chance contact with one of the 4 load cells. 98 subjects took part in testing during horizontal vibration tests and 60 took part during vertical vibration tests.

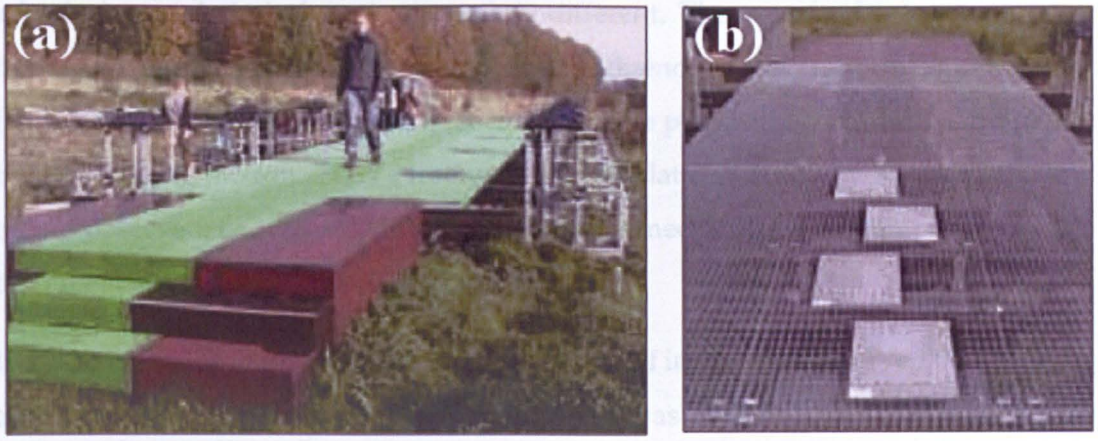

Figure 2.22: Plot (a), 12 m × 3 m platform employed by Butz et al. Plot (b), 4 load cells measuring 0.4 m × 0.6 m embedded in the walkway, after [9].

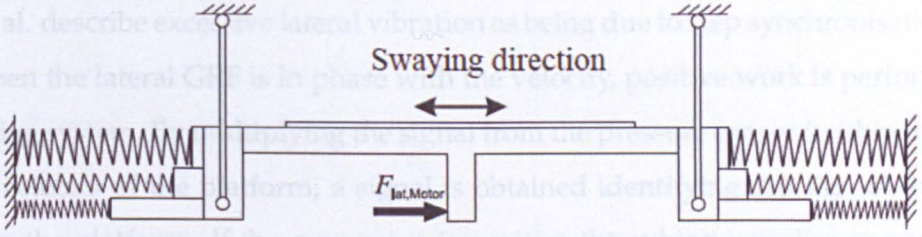

Figure 2.23: Schematic section view of test platform employed by Butz et al. after [9].

Vertical GRF data was normalised by body weight and characterised with the use of a number of parameters. However the time-history of the lateral GRF does not exhibit such well defined characteristics. Therefore the authors defined an equivalent rectangular force having the same load impulse as the measured GRF. This is similar to Rönnquist's approach in which an equivalent harmonic load is defined as a half sine wave with amplitude according to Eq. (2.2.5). Surprisingly Butz et al. report that it was not possible to confirm that lateral GRF magnitude increases considerably with acceleration amplitude. This is in complete disagreement with Rönnquist's findings.

It is worth considering the fundamental differences between both experimental investigations. The platform used by Rönnquist was driven solely by the actions of the test subject, the lateral GRF data was determined via load cells restraining the platform. This allowed Rönnquist to capture GRF data from the entire crossing. Despite the platform used by Butz et al. being twice as long at 12 m, force data could only be captured by chance contact with four force plates.

The interaction that can be observed when using a mechanically driven platform and

a freely suspended platform is also subtly different. The use of a driving motor stops the subject-induced GRF having a significant influence on the platform's motion. On a freely oscillating platform the subject can drive the platform and in turn is influenced by the resulting motion. Thus a freely oscillating platform (used by Rönnquist) allows one to observe true two-way interaction while a mechanically driven platform (used by Butz et al.) is limited to one way interaction.

Irrespective of the subtle differences in the nature of interaction observed by Rönnquist and Butz et al. the means by which GRF data was obtained by Rönnquist is likely to have provided a more complete and therefore robust data set. Furthermore, Rönnquist's conclusions are in broad agreement with previous observations [2, 8, 35].

Butz et al. describe excessive lateral vibration as being due to step synchronisation such that when the lateral GRF is in phase with the velocity, positive work is performed on the bridge system. By multiplying the signal from the pressure sensor (within the shoe) by the velocity of the platform, a signal is obtained identifying the sign of the work done on the platform. If the expression is positive the subject supplies energy to the oscillating structure, if it is negative the subject serves to dissipate energy, attenuating the vibration response (in a freely oscillating structure). Through this energy analysis, Butz et al. experimentally identify four interaction states, Fig. 2.24:

1. random, non synchronous walking
2. positive synchronous walking
3. transition to positive synchronous walking
4. negative synchronous walking

The authors acknowledge it is not possible to determine whether a pedestrian synchronises by chance or as a direct result of the lateral motion experienced. Nevertheless the following results are reported:

- fast single minded walking is rarely influenced by the motion of the platform
- no synchronous walking is detected for vibration frequencies of 0.6Hz and 1.5Hz

- no synchronous walking is detected for fast walking and a vibration frequency of 0.8Hz
- the most critical vibration frequency is 0.8Hz because slowly and normally walking pedestrians show synchronisation behaviour

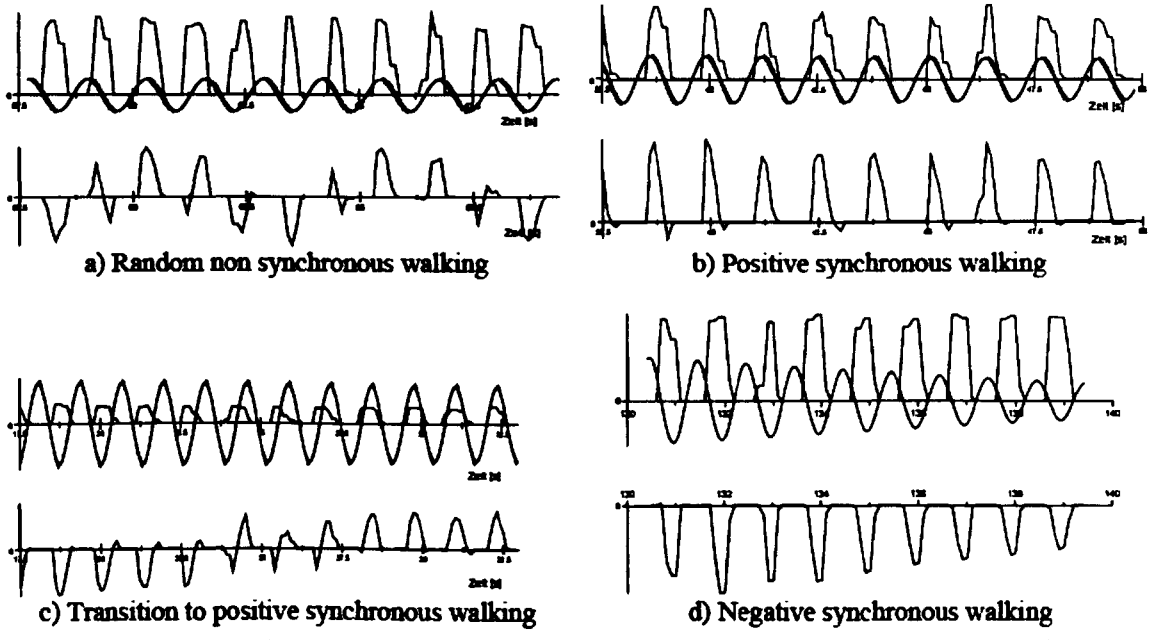

Figure 2.24: Four interaction states identified for subjects walking on a laterally oscillating platform. Upper plots show platform velocity and pressure sensor signal, lower plots show the product of pressure sensor and platform velocity, after [9].

Based on these observations the authors conclude that single pedestrians who walk within ± 0.2 Hz of the modal frequency of interest tend to synchronise with the structure. This is similar to the frequency ratio criteria proposed by Rönnquist. Notably a lock-in trigger amplitude of 0.1 - 1.5 m/s^2 reported in [31] and [27] could not be verified.

Ingólfsson et al. 2010/2011

A considerable contribution to the understanding of HSI was made by Ingólfsson et al. [10, 11]. Against a background of increasing uncertainty regarding the role of step synchronisation in the development of lateral instability [6, 24, 37], Ingólfsson examined the GRFs generated by subjects walking on a laterally oscillating treadmill, Fig. 2.25. This investigation involved 71 test subjects. Each subject was required to walk for 30 s

at a range of oscillation frequencies and amplitudes during which the lateral GRF, lateral acceleration at waist level and deck displacement and acceleration were recorded (Note that x is used in this case to represent base motion, consistent with the original author's figures).

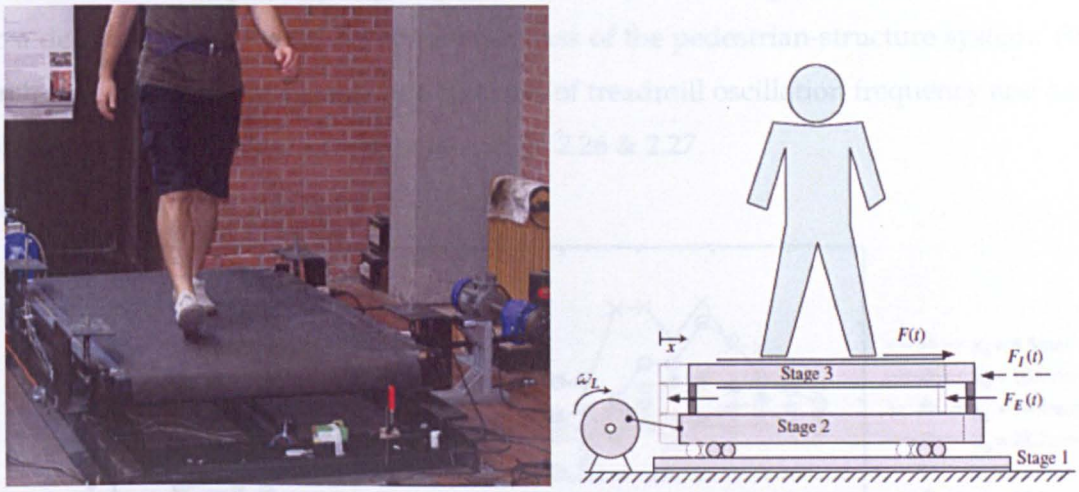

Figure 2.25: Test subject on the laterally oscillating treadmill (left), after [10] and schematic overview of the treadmill setup (right), after [11].

The lateral forces were characterised as an equivalent damping force $F_{D,eq}(t)$ proportional to the lateral velocity of the treadmill and an equivalent inertia force $F_{I,eq}(t)$ proportional to the lateral acceleration.

$$\begin{aligned} F_{D,eq}(t) &= c_p\,\dot{x}(t) = c_p\,\dot{x}_0\,sin(2\pi f_l\,t) \\ F_{I,eq}(t) &= \rho_p\,m_p\,\ddot{x}(t) = \rho_p\,m_p\,\ddot{x}_0\,sin(2\pi f_l\,t + \pi/2) \end{aligned} \tag{2.2.6}$$

in which c_p and ρ_p are the velocity and acceleration proportional constants, f_l is the deck oscillation frequency, $\dot{x}_0$ and $\ddot{x}_0$ are the deck velocity and acceleration amplitude while m_p is the subject mass. The velocity coefficient is obtained by equating the average work done by a velocity proportional force per unit time, with the average work done by the subject's GRF over the duration of a single test,

$$\frac{1}{2}\,c_p\,\dot{x}_0^2 = \tilde{\sigma}_{F\dot{x}}(\Delta f) \tag{2.2.7}$$

in which $\tilde{\sigma}_{F\dot{x}}(\Delta f)$ is the area of the cross-spectral density between F, the GRF and $\dot{x}$, the deck velocity over a bandwidth, $\Delta f = 0.05$ Hz, centred on the oscillation frequency. Therefore the equivalent damping coefficient is obtained as,

$$c_p = \frac{2}{\dot{x}_0^2}\,\tilde{\sigma}_{F\dot{x}}(\Delta f) \tag{2.2.8}$$

The acceleration proportional coefficient is obtained in a similar manner as,

$$\rho_p = \frac{2}{m_p \, \ddot{x}_0^2} \, \tilde{\sigma}_{F\ddot{x}}(\Delta f) \tag{2.2.9}$$

Positive values of c_p and ρ_p, if generated on a freely oscillating structure, would equate to a decrease in the modal damping and mass of the pedestrian-structure system. Examination of these coefficients as a function of treadmill oscillation frequency and amplitude reveal some interesting trends, Figs. 2.26 & 2.27.

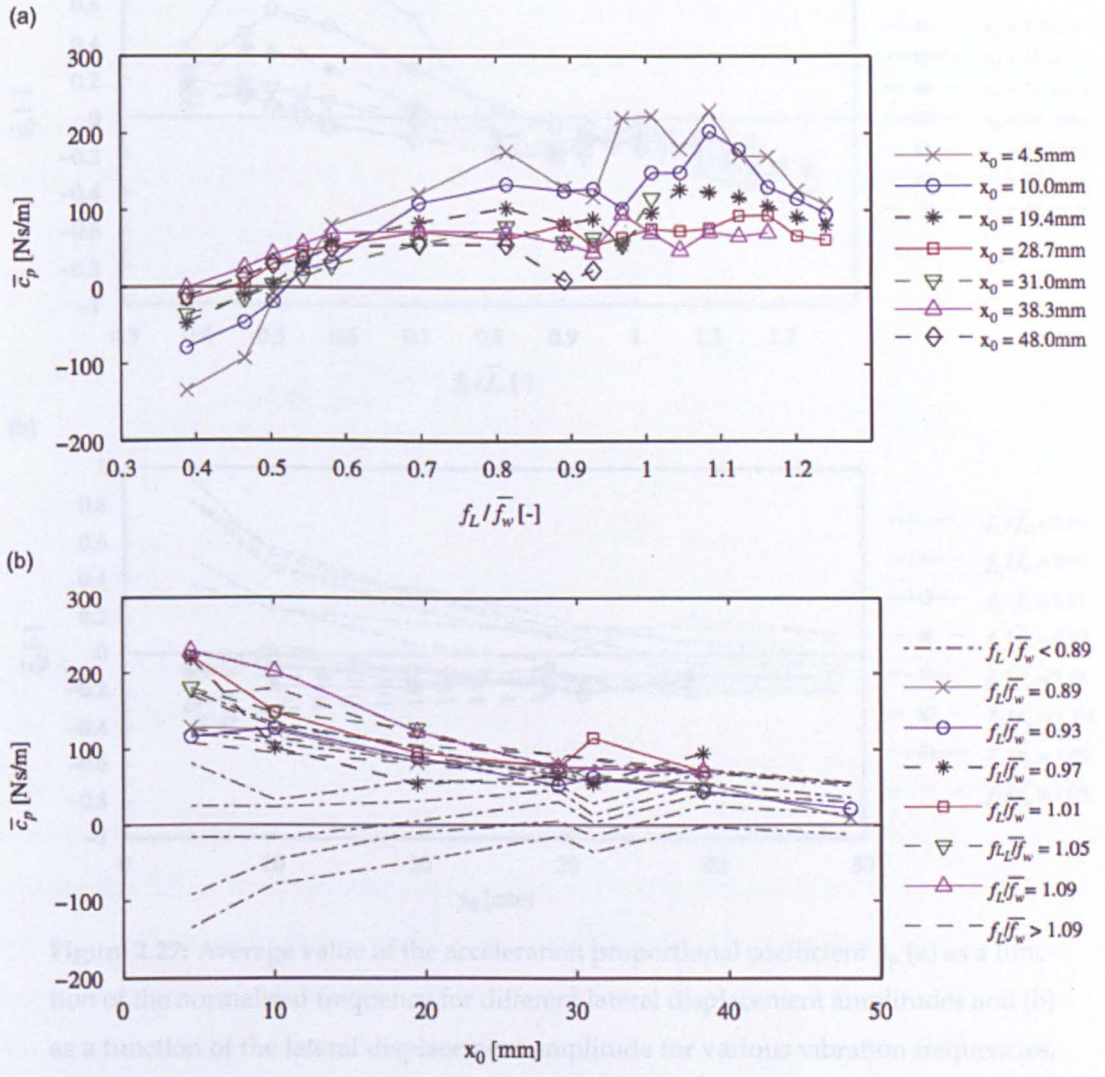

Figure 2.26: Average value of pedestrian load coefficient $\bar{c}_p$ (a) as a function of the normalised frequency for different lateral displacement amplitudes and (b) as a function of the lateral displacement amplitude for various vibration frequencies, after [11].

Note that the deck oscillation frequency f_L has been normalised by the mean walking frequency for the population $\bar{f}_w$. It can be seen at low frequencies ($\frac{f_L}{\bar{f}_w} \leq \approx 0.5$), the

subject-induced force corresponds to an increase in modal damping. However in the range typically of interest ($0.8 \leq \frac{f_L}{f_w} \leq 1.2$), the GRF corresponds to a reduction in modal damping. Also of interest is the amplitude dependance of the coefficients. As the displacement amplitude increases the negative damping effect is reduced. This may be indicative of the self-limiting nature of HSI.

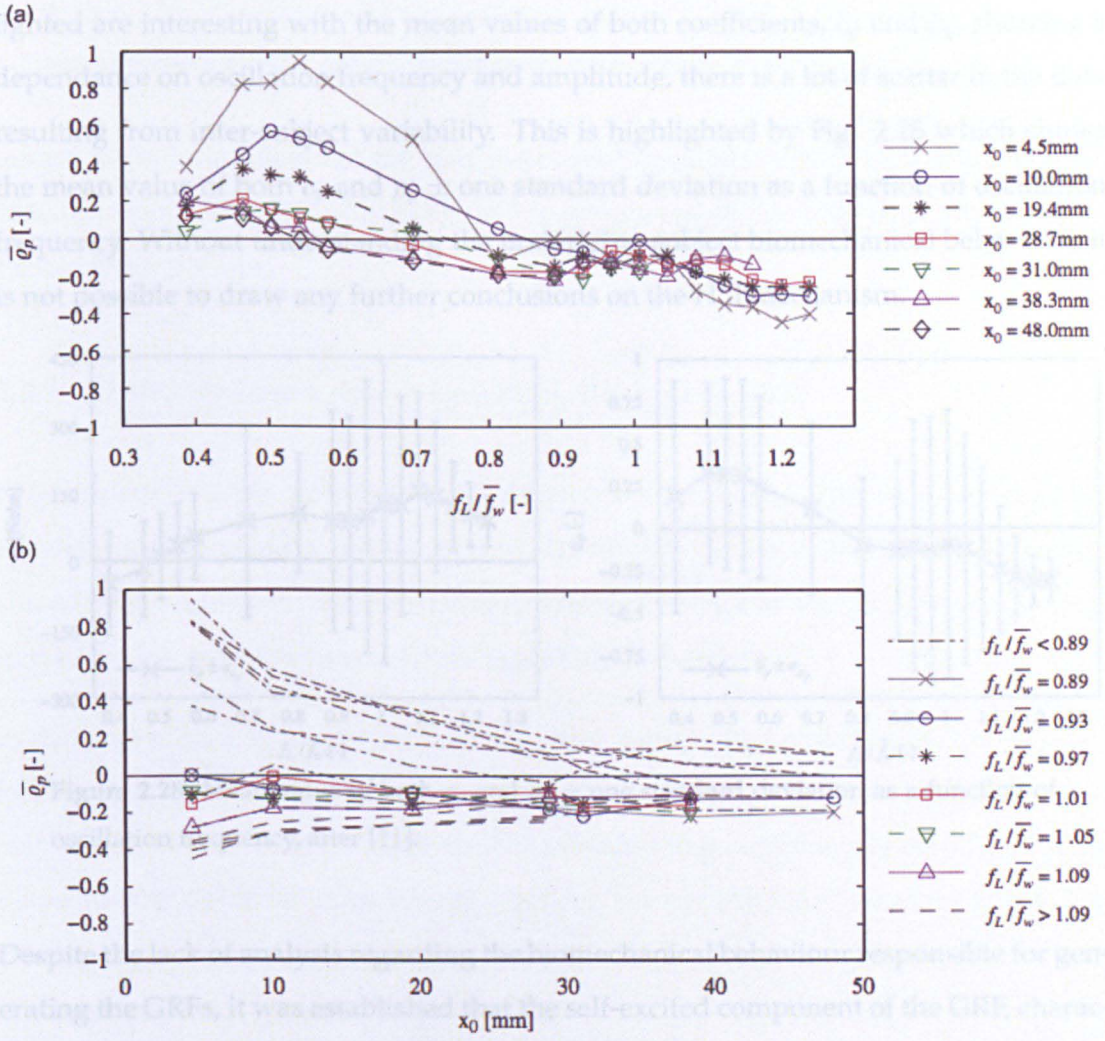

Figure 2.27: Average value of the acceleration proportional coefficient $\bar{\rho}_p$ (a) as a function of the normalised frequency for different lateral displacement amplitudes and (b) as a function of the lateral displacement amplitude for various vibration frequencies, after [11].

The average value of the acceleration proportional coefficient $\bar{\rho}_p$ is positive for low oscillation frequencies indicating a reduction in modal mass, however for the range of interest in which the oscillation frequency is close to the walking frequency there

appears to be a near constant addition to the modal mass of the system for all oscillation amplitudes. The transition from mass subtraction to addition is amplitude and frequency dependent.

This analysis represents the most comprehensive study of the lateral footfall force as a function of base oscillation frequency and amplitude. Although the trends highlighted are interesting with the mean values of both coefficients, $\bar{c}_p$ and $\bar{\rho}_p$, showing a dependance on oscillation frequency and amplitude, there is a lot of scatter in the data resulting from inter-subject variability. This is highlighted by Fig. 2.28 which shows the mean value of both c_p and $\rho_p \pm$ one standard deviation as a function of oscillation frequency. Without understanding the underlying subject biomechanical behaviour, it is not possible to draw any further conclusions on the HSI mechanism.

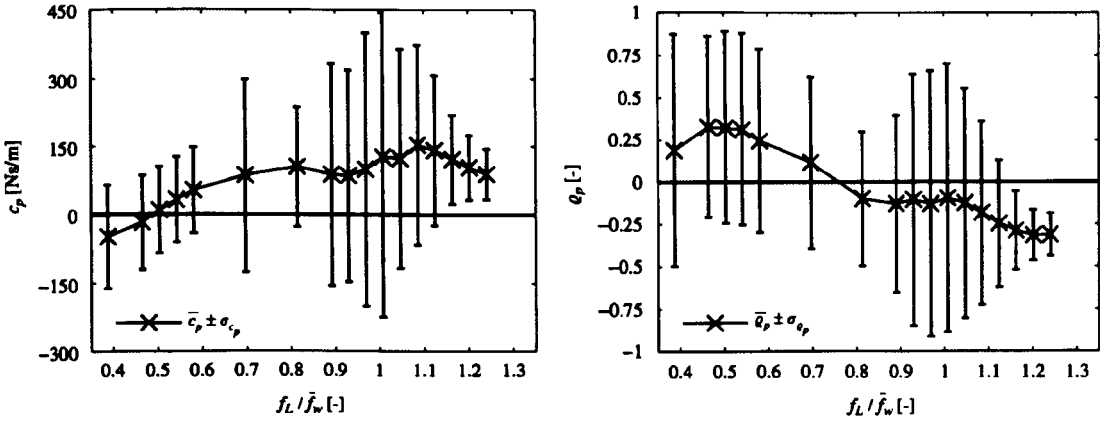

Figure 2.28: Mean value of both c_p and $\rho_p \pm$ one standard deviation as a function of oscillation frequency, after [11].

Despite the lack of analysis regarding the biomechanical behaviour responsible for generating the GRFs, it was established that the self-excited component of the GRF, characterised via the coefficients c_p and ρ_p, do not require any degree of step-synchronisation to occur. Ingólfsson et al. reported results of a typical tests in which a subject walked naturally while the treadmill oscillation frequency increased from 0.33Hz to 1.07Hz in 17 increments [10]. By comparing the lateral oscillation at the waist to that of the treadmill (Fig. 2.29) he showed that pedestrian pacing frequency was unaffected by base motion.

This confirms the earlier field observations of Brownjohn et al. [6] and Macdonald [24] and intensifies the question of how these self-excited forces are developed. A further

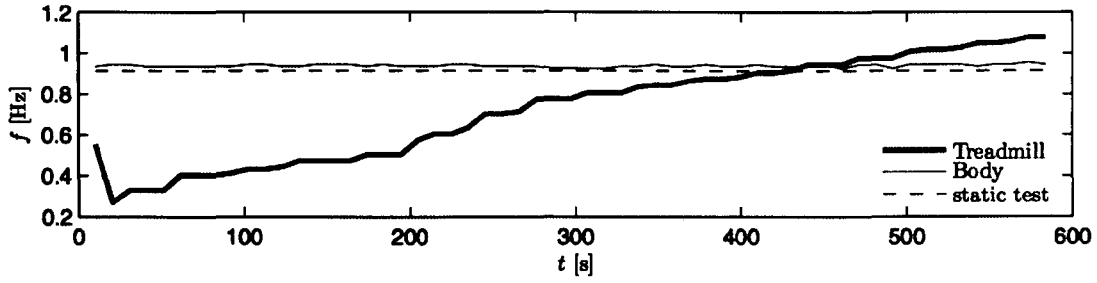

Figure 2.29: Comparison of treadmill and (subject's) waist oscillation frequencies showing the subject's CoM oscillation is not influenced by treadmill motion, after [10].

investigation is required that not only examines the induced GRF, but also the coupled biomechanical behaviour that leads to the generation of the GRF of which the self-excited force is a part.

2.2.3 Optically based data acquisition, Racic et al. 2010

In this subsection, the capture and use of visual marker data to reproduce human GRFs is briefly reviewed. Walking behaviour was not the subject of the investigation discussed below. However, this work has special significance as similar methods are employed in this project to record whole body balance behaviour.

In this paper, Racic et al. use 3D optical motion capture equipment to record the position of tracking markers placed on two test subjects, [12]. The data is used to determine body segment accelerations while the test subjects jump continuously on a force plate. By estimating the mass of each body segment, the vertical GRF was reproduced, Eq. (2.2.10) and compared with that recorded by the force plate,

$$F_{GR} = \sum_{i=1}^{s} m_i(a_i - g) \tag{2.2.10}$$

where m_i and a_i are the mass and acceleration of the centre of mass (CoM) of the i^{th} of s body segments. Fig. 2.32 & 2.31 shows the excellent level of agreement achieved between the reproduced and measured GRFs.

The technique was then used to record two test subjects bouncing and jumping together on a test structure with known modal properties, Fig. 2.32. The GRFs were again reproduced from the recorded marker data and body segment parameters. These forces were applied to a dynamic model of the structure and the simulated response

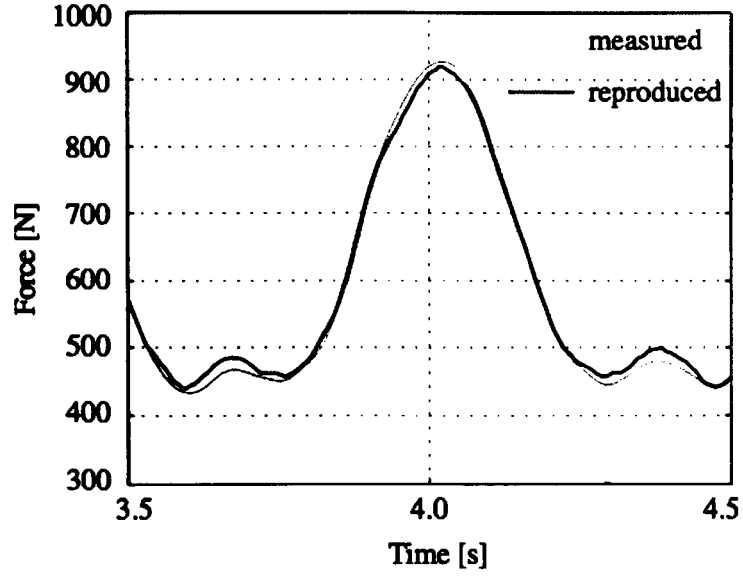

Figure 2.30: Example of reproduced bouncing force for a single person bouncing at 2 Hz, after [12].

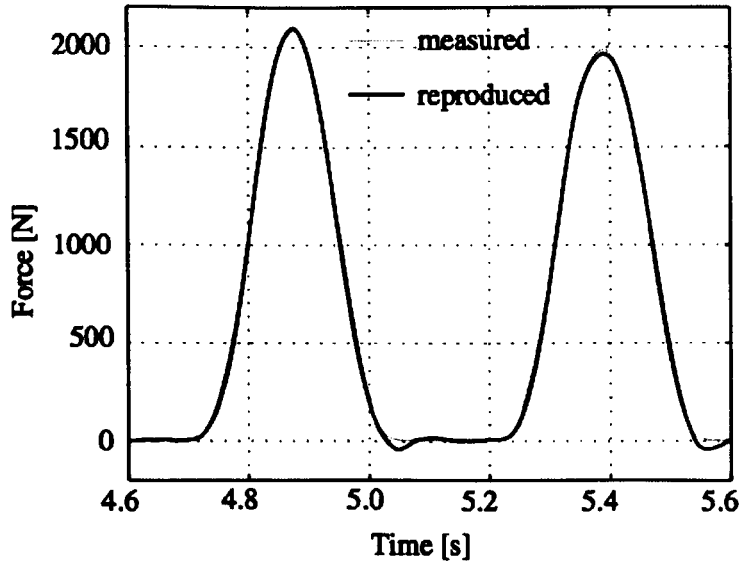

Figure 2.31: Example of reproduced jumping force for a single person jumping at 2 Hz, after [12].

was compared against that recorded during the jumping activity. Excellent agreement is achieved demonstrating that the technique offers a suitable means of recording the data necessary to reproduce human jumping forces.

This work is indicative of an emerging trend in the civil engineering field whereby 'free-field' measurements are used to estimate subject-induced GRFs. This approach

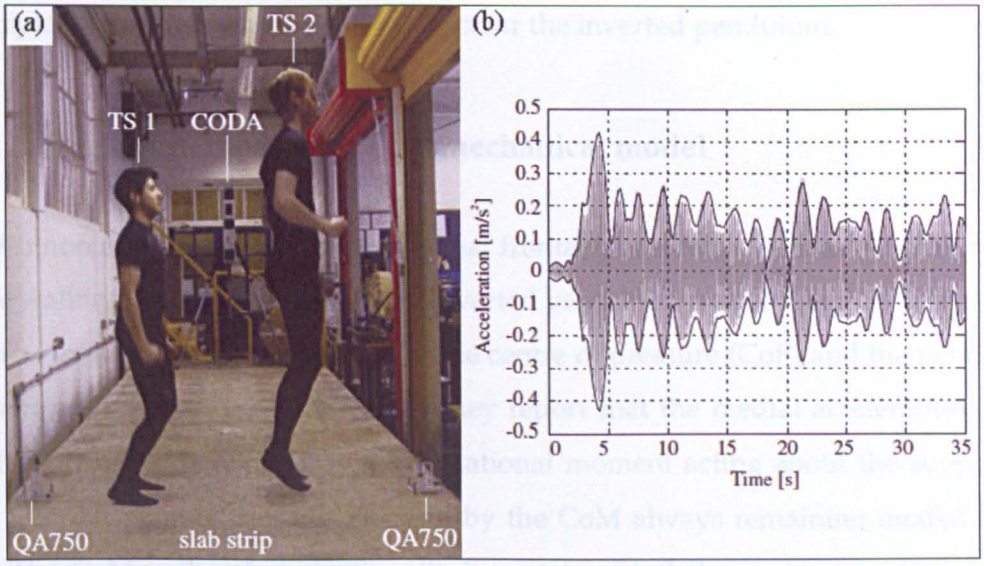

Figure 2.32: (a) Two test subjects jumping together on a test structure, (b) Measured (grey) and envelope of simulated (black) mid-span vibration response of the structure due to two persons jumping together at 2.5 Hz, after [12].

allows the test subject to behave more naturally during data acquisition than would otherwise be possible, eg. by targeting force plates while walking. This method of data acquisition has great potential for the study of HSI due to the unobtrusive nature of the recording equipment, but also due to the data relating to whole body movement that can be captured.

2.3 Biomechanically based load models

The study of human-induced lateral bridge vibration has resulted in the development of many theoretical models. Various excitation mechanisms have been proposed; Piccardo & Tubino proposed a model based on parametric resonance in which the applied force is a function of deck oscillation amplitude [38]. Blekherman proposed that coupling between a vertical mode at twice the frequency of a lateral mode, could result in vertical oscillations initiating large amplitude lateral oscillations [39, 40]. Nakamura proposed a negative damping model similar to that proposed by Arup, in which the self-limiting nature of HSI was simulated [41].

However, the focus herein will be placed on those models that attempt to directly simulate HSI at a biomechanical level, that is to say, those models that are founded on

principled of biomechanics, and in particular the inverted pendulum.

2.3.1 The inverted pendulum biomechanical model

MacKinnon and Winter [42] proposed that frontal plane centre of mass (CoM) motion while walking is well described by an inverted pendulum model in which the centre of rotation (pendulum root) is located at the centre of pressure (CoP) and the pendulum mass corresponds to the body CoM. They report that the medial acceleration of the CoM is primarily generated by a gravitational moment acting about the supporting foot. Frontal plane stability is ensured by the CoM always remaining medial to the CoP. The CoM is therefore continually in a state of imbalance, tending towards the centreline of the frontal plane, a behaviour well described by the inverted pendulum.

A derivation of the dynamic behaviour of the inverted pendulum is now presented, however the generality of the analysis is expanded by considering lateral motion of the structure on which the pendulum is supported.

Consider an inverted pendulum inclined at an angle α to the vertical plane, resting on a structure of mass m, which is free to move laterally, Fig. 2.33. The displacement coordinate of the base structure shall be denoted by U. Thus the vector of generalised coordinates describing the system configuration is $q = [U,\ \alpha]^T$.

The pendulum consists of a single lumped mass m_p at the end of a massless leg of length L_p. The horizontal and vertical coordinates of the pendulum mass are y_m and z_m respectively and are expressed in terms of the generalised coordinates as,

$$y_m = U + L_p \, sin\, \alpha \tag{2.3.1}$$

$$z_m = L_p \, cos\, \alpha \tag{2.3.2}$$

assuming deck level as the vertical datum level. These are differentiated to obtain the corresponding velocity expressions required for the following analysis.

$$\dot{y}_m = \dot{U} + L_p \, \dot{\alpha} \, cos\, \alpha \tag{2.3.3}$$

$$\dot{z}_m = -L_p \, \dot{\alpha} \, sin\, \alpha \tag{2.3.4}$$

The governing equations of motion are derived by considering the Lagrange equation

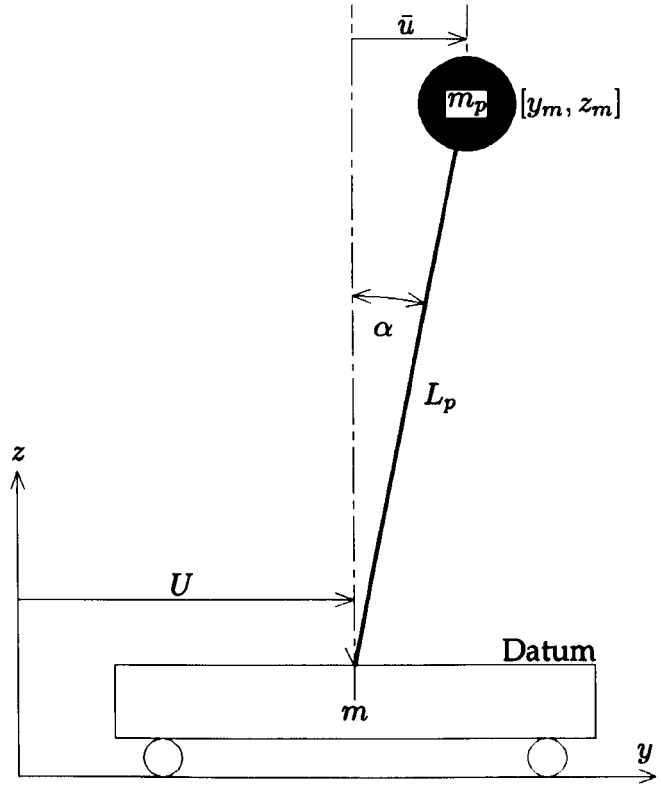

Figure 2.33: Inverted pendulum supported on a structure free to move laterally.

for a conservative system,

$$\frac{d}{dt}\left(\frac{\partial \mathcal{L}}{\partial \dot{q}}\right) - \frac{\partial \mathcal{L}}{\partial q} = 0 \tag{2.3.5}$$

in which the Lagrangian function, $\mathcal{L}$, is the difference between the system kinetic, K and potential energy, V, where,

$$K = \frac{1}{2}\, m\, \dot{U}^2 + \frac{1}{2}\, m_p\, (\dot{y}_m^2 + \dot{z}_m^2) \tag{2.3.6}$$

$$V = m_p\, g\, z_m \tag{2.3.7}$$

Substituting equations (2.3.1) to (2.3.4), into (2.3.6) and (2.3.7), the Lagrangian can be expressed as,

$$\mathcal{L} = \frac{1}{2}\, m\, \dot{U}^2 + \frac{1}{2}\, m_p \left[(\dot{U} + L_p\, \dot{\alpha}\, cos\, \alpha)^2 + (-L_p\, \dot{\alpha}\, sin\, \alpha)^2\right] - m_p\, g\, L_p\, cos\, \alpha \tag{2.3.8}$$

In order to determine the pendulum's equation of motion, the constituent parts of the Lagrange equation, (2.3.5), are evaluated as follows,

$$\frac{d}{dt}\left(\frac{\partial \mathcal{L}}{\partial \dot{\alpha}}\right) = L_p\, m_p \Big[L_p\, \ddot{\alpha} + \ddot{U}\, cos\, \alpha - \dot{U}\dot{\alpha}\, sin\, \alpha\Big] \tag{2.3.9}$$

$$\frac{\partial \mathcal{L}}{\partial \alpha} = L_p\, m_p \left[g - \dot{U}\, \dot{\alpha}\right] sin\, \alpha \tag{2.3.10}$$

Substituting (2.3.9) and (2.3.10) into (2.3.5) and simplifying, results in the non-linear equation of motion for the inverted pendulum on a laterally moving base,

$$\ddot{\alpha} + \frac{\ddot{U}}{L_p} cos\,\alpha - \frac{g}{L_p} sin\,\alpha = 0 \tag{2.3.11}$$

Linearisation

By observing that the pendulum's angle of inclination will remain small during locomotion and defining $\bar{u}$ as the horizontal distance between the pendulum root and pendulum mass positions, Fig. 2.33, the following can be assumed,

$$cos(\alpha) \approx 1 \tag{2.3.12}$$

$$sin(\alpha) = \frac{\bar{u}}{L_p} \tag{2.3.13}$$

Equation (2.3.11) is thus simplified to,

$$L_p\,\ddot{\alpha} = -\ddot{U} + \omega^2\,\bar{u} \tag{2.3.14}$$

where $\omega = \sqrt{g/L_p}$. Again assuming that α remains small, the lateral acceleration, $\ddot{y}_m$, due to a rotational acceleration, $\ddot{\alpha}$, is $\ddot{y}_m = L_p\,\ddot{\alpha}$. Thus (2.3.14) further reduces to,

$$\ddot{y}_m = -\ddot{U} + \omega^2\,\bar{u} \tag{2.3.15}$$

Finally, if y_m is measured with respect to an arbitrary position on the moving support structure and u is defined as the distance from the same arbitrary point to the pendulum root, equation (2.3.15) becomes,

$$\ddot{y}_m = -\ddot{U} - \omega^2\,(u - y_m) \tag{2.3.16}$$

which is the final linearised expression for the lateral acceleration of an inverted pendulum supported on a laterally moving base. This expression can be used to approximate the frontal plane motion of a pedestrian's CoM during the single stance phase of walking.

2.3.2 Hof's support placement stability criterion

It is a well established principal that in order to maintain static balance, the vertical projection of the CoM must remain within the base of support (BoS), where the BoS represents the area through which the resultant GRF may act. While standing on two feet, the lateral limits of the BoS are the lateral edges of the feet, however when balancing on one foot, the BoS is limited to the area beneath the supporting foot. Excursions of the vertical projection of the CoM outside the BoS, result in generation of a destabilising moment about the supporting foot.

Hof et al. [43], acknowledging the inadequacy of this stability criterion for dynamical situations, propose an extension of this rule. The problem is readily visualised in the case of the inverted pendulum model. Immediately after support placement, the CoM will be positioned medially to the CoP, however its velocity will be in the lateral direction. The CoM velocity may be such that the CoM continues travelling laterally beyond the CoP. At this point the CoM acceleration would also be in the lateral direction resulting in instability (the pendulum falling outwards rather than back towards the centreline of the frontal plane).

To avoid this unstable condition, Hof et al. propose that the lateral position of the CoP, u, should be chosen such that given an initial CoM position, y_0, and velocity, $\dot{y}_0$, the CoM will not pass (sway) beyond the CoP. By imposing this condition on the solution of the differential equation describing inverted pendulum motion, the following expression for the lateral position of the CoP is obtained,

$$u \geq y_0 + \frac{\dot{y}_0}{\omega} \tag{2.3.17}$$

in which ω is the angular natural frequency of a hanging pendulum of length L_p. Note that both u and y_0 are measured with respect to the same arbitrary reference point. When the pendulum support position is chosen according to Eq. (2.3.17), the pendulum swings outwards (in the lateral direction), but returns (in the medial direction) before the point of instability is reached. The quantity $y_0 + \frac{\dot{y}_0}{\omega}$ is defined as the extrapolated centre of mass (XCoM). In experiments involving standing and walking, the model was shown to perform well. An additional margin of stability, b_{min}, was experimentally identified as the lateral distance between the XCoM and CoP, Fig. 2.34. Thus Hof et al's

equation describing lateral foot placement position on successive steps is given by:

$$u = y_0 + \frac{\dot{y}_0}{\omega} \pm b_{min} \quad \text{(+ for right foot, - for left foot)} \tag{2.3.18}$$

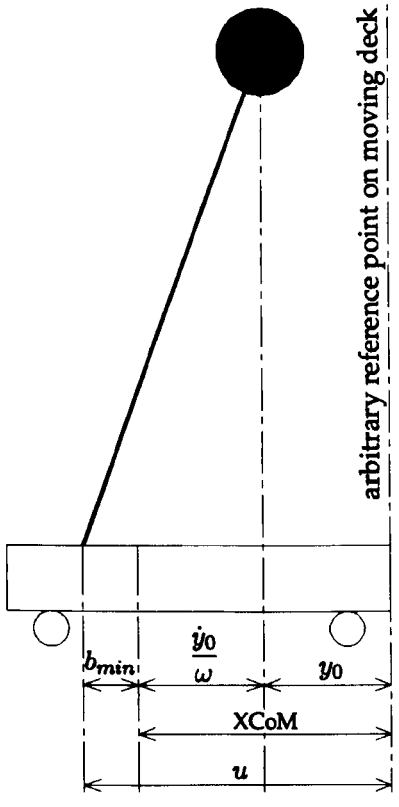

Figure 2.34: Inverted pendulum support placement quantities. The inverted pendulum is supported on the left foot, swinging in the lateral direction (to the left). All distances are measured with respect to an arbitrary reference point on the oscillating deck.

where the sign of b_{min} alternates for successive steps. The authors propose that b_{min} is a measure of subject stability. Hof et al. later attempted to further validate this stability condition and quantify the influence of other balance strategies such as rotation about the hip and ankle [13]. This study compared the walking behaviour of control subjects with that of above-knee amputees, which lacked ankle control in one leg. The study found that the ankle strategy provides fine-tuning of the CoP position during the single stance phase, this correction can be up to 30 mm.

Figure 2.35 compares CoP, XCoM and CoM trajectories for a subject with a left side above-knee prosthesis and their matching control subject. The amputee is shown in

plot (a) with anatomical left towards the bottom of the plot. The influence of ankle control is clearly seen in the non-prosthetic side where the CoP shows much more variability. The influence of active ankle control is even more evident in the control subject. If the CoP is placed within the XCoM, it is moved outwards, conversely if it is placed a sufficient distance beyond the XCoM, it remains a constant distance from the XCoM. Hof et al. conclude that the foot placement balance strategy is the most important for maintaining lateral balance. However the ankle strategy, based on sensory feedback, can provide minor corrections after the foot has been placed.

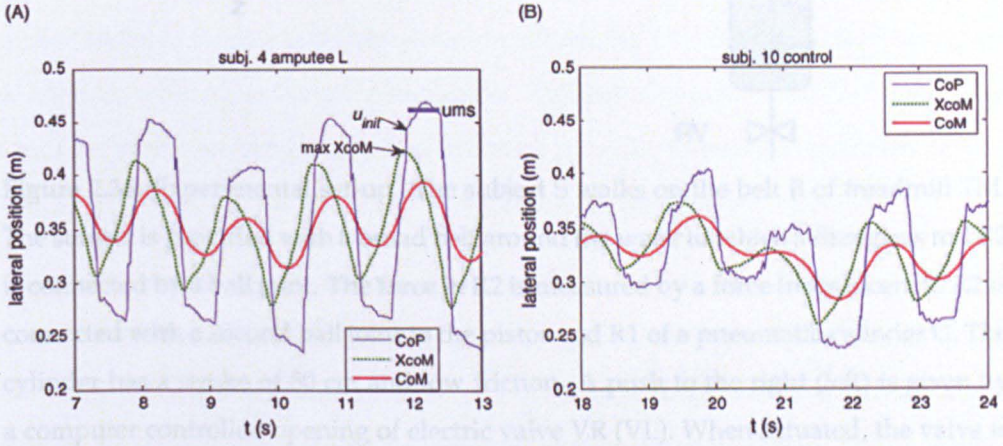

Figure 2.35: Comparison of CoP, XCoM and CoM trajectories for a subject with a left side above-knee prosthesis, plot (a) and their matching control subject, plot (b), after [13].

In order to further test their hypothesis; the CoP is placed a constant distance laterally to the XCoM, the balance response of 10 test subjects was examined after the imposition of a lateral perturbation during walking [14]. Subjects were asked to walk for 5 minutes on an instrumented treadmill during which time 20 lateral perturbations were randomly imposed. The perturbation was delivered via a pneumatically powered rod attached to a belt around the subject's waist, Fig. 2.36. Both the timings of each push (as a % of the gait cycle) and the magnitude of the push force were varied. The authors report that their hypothesis is supported; the margin between XCoM and CoP at the time of foot placement is constant, even after external perturbations.

It is shown that when a perturbation is received during the single stance phase of walking or at a time when it is too late to alter foot placement position, the ankle strategy reduces the imbalance. The ankle strategy was also found to compensate for inaccura-

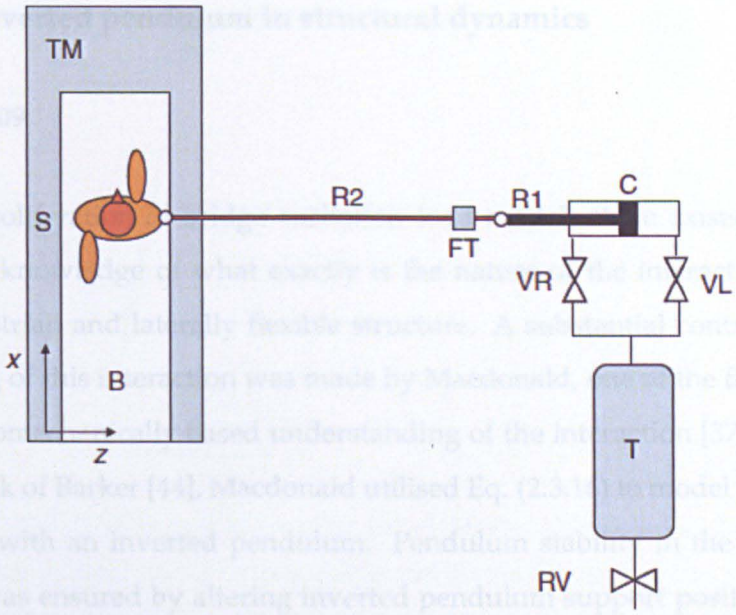

Figure 2.36: Experimental set-up. The subject S walks on the belt B of treadmill TM. The subject is provided with a broad belt around the waist to which a fibreglass rod R2 is connected by a ball joint. The force in R2 is measured by a force transducer FT. R2 is connected with a second ball joint to the piston rod R1 of a pneumatic cylinder C. The cylinder has a stroke of 50 cm and low friction. A push to the right (left) is given by a computer controlled opening of electric valve VR (VL). When actuated, the valve is connected to the pressure tank T, otherwise it is open to the ambient air. Opening time is always 100 ms. The pressure in tank T is regulated by an electric pressure regulator valve RV, after [14].

cies in foot placement under normal undisturbed walking. The interaction between the stepping and ankle strategy is unclear. What determines the degree to which the ankle strategy is employed in parallel with the stepping strategy remains an open question.

This investigation essentially examines the balance response of pedestrians when a lateral motion of the pedestrian CoM is imposed relative to the walking surface. This has obvious significance for the study of HSI in the civil engineering field. The identification of active balance control (via the ankle strategy) suggests that similar active control may be employed while walking on a laterally oscillating bridge deck.

2.3.3 The inverted pendulum in structural dynamics

Macdonald 2009

Despite the proliferation of bridge excitation load models there exists a fundamental gap in the knowledge of what exactly is the nature of the interaction between a walking pedestrian and laterally flexible structure. A substantial contribution to the understanding of this interaction was made by Macdonald, one of the first in the field to pursue a biomechanically based understanding of the interaction [37]. Building on the earlier work of Barker [44], Macdonald utilised Eq. (2.3.16) to model human frontal plane motion with an inverted pendulum. Pendulum stability in the face of lateral base motion was ensured by altering inverted pendulum support position on successive steps, in accordance with Hof et al's stability condition, Eq. (2.3.18).

The inverted pendulum's reaction to base motion is as follows; the influence of bridge acceleration on the pendulum mass is represented by an equivalent inertia force[1] applied to the inverted pendulum mass, $-m_p\ddot{U}$, altering its motion during each step, thus altering its final position, y_0, and velocity, $\dot{y}_0$, at the end of the step. This in turn feeds into the CoP placement law, Eq. (2.3.18), altering the position of the CoP, u, for the next step. Note again that u and y_0 are measured with respect to some arbitrary reference point on the moving structure.

It should also be noted that when using Eq. (2.3.18) there are two possible mass velocities, $\dot{y}_0$, that may be used; (i) the velocity measured in the stationary global reference frame or (ii) the velocity measured with respect to a reference frame moving with the oscillating support structure, Fig. 2.37. The latter option results in a measure of velocity relative to the moving support structure. Macdonald suggests that for walking on a footbridge the CoM velocity relative to the moving structure is likely to be most appropriate on account of the importance of visual feedback in maintaining lateral stability.

[1] From D'Alembert's Principle, the inertia force is a fictitious force that is equal in magnitude and opposite in sign to the resultant of the directly applied external forces. Thus the influence of external forces on a mass, induced by base acceleration, is represented by an equivalent inertia force applied to or *experienced by* the mass.

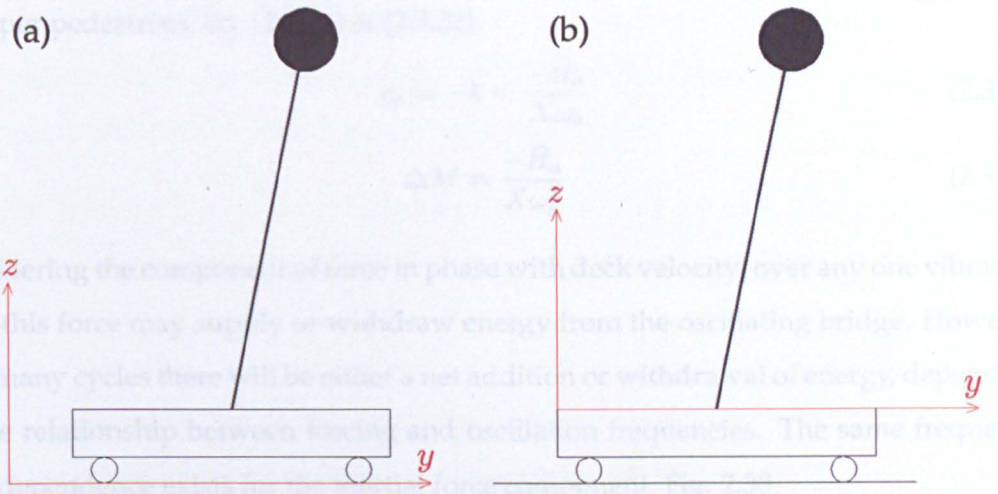

Figure 2.37: Plot (a) shows a stationary or global reference frame independent of support structure motion, plot (b) shows a reference frame that moves laterally with the support structure. Pendulum velocity measured with respect to reference frame (b) is velocity relative to the moving structure, this is therefore referred to as a relative or local reference frame.

Macdonald simulated an inverted pendulum walking with a lateral forcing frequency of 0.9 Hz on a structure undergoing a predefined harmonic oscillation of amplitude 2 mm and frequency 1.11 Hz. Examination of the frequency content of the GRF, $H = -m_p(\ddot{y}_m + \ddot{U})$, imposed by the inverted pendulum revealed harmonics at the base oscillation frequency, ω_b. This was termed a self-excited harmonic due to its dependence on the interaction between the inverted pendulum and oscillating structure. The component of this self-excited harmonic force in phase with deck velocity, H_v, and acceleration H_a, was identified for each vibration cycle, Eq. (2.3.19) & (2.3.20).

$$H_v = \frac{2}{T}\int_{T_0}^{T_0+T} H\, cos\Big(\omega_b(t-\tau)\Big)\, \mathrm{d}t \tag{2.3.19}$$

$$H_a = -\frac{2}{T}\int_{T_0}^{T_0+T} H\, sin\Big(\omega_b(t-\tau)\Big)\, \mathrm{d}t \tag{2.3.20}$$

where $T_0 \leq t \leq (T_0 + T)$ denotes the duration of a vibration cycle and τ is the time lag between the gait and oscillation cycles. The average of each force component was then obtained for a large number of oscillation cycles. The mean value of each component was used to characterise the self-excited force as an equivalent damping and added

mass per pedestrian, Eq. (2.3.21) & (2.3.22).

$$c_p = -k = \frac{-\bar{H}_v}{X\omega_b} \tag{2.3.21}$$

$$\Delta M = \frac{-\bar{H}_a}{X\omega_b^2} \tag{2.3.22}$$

Considering the component of force in phase with deck velocity; over any one vibration cycle this force may supply or withdraw energy from the oscillating bridge. However over many cycles there will be either a net addition or withdrawal of energy, depending on the relationship between forcing and oscillation frequencies. The same frequency ratio dependence exists for the inertial force component, Fig. 2.38.

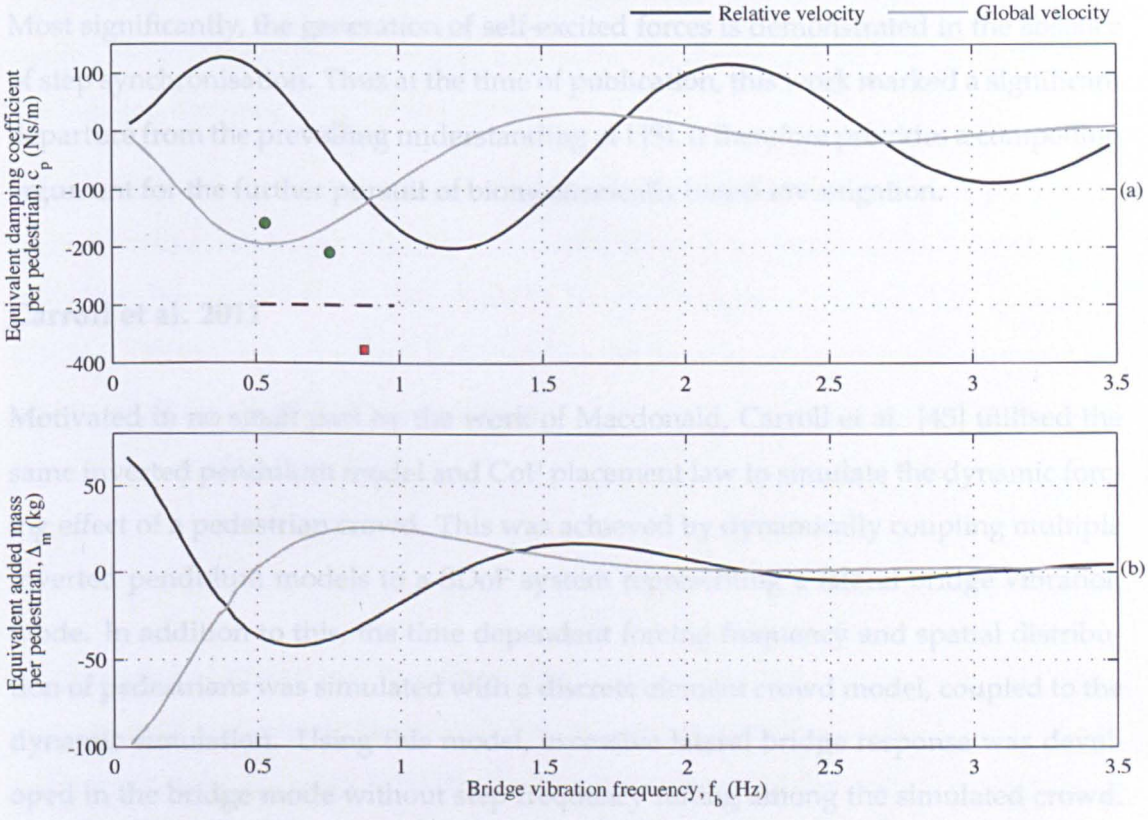

Figure 2.38: Plot (a), equivalent damping coefficient per pedestrian. Inverted pendulum support placement based on relative velocity (solid black line) and global velocity (solid grey line). Also shown are estimates of equivalent damping obtained from field observations of (i) CSB [24] (green circles), LMB [2] (dashed black line) and CMB [6] (red square). Plot (b), equivalent added mass per pedestrian with inverted pendulum support placement based on relative and global velocity. Plot reproduced from [37].

With reference to Fig. 2.38, the continuous black curve represents simulations in which the foot placement law was based on CoM velocity relative to the deck. The continuous

grey curve represents simulations in which the foot placement law was based on global CoM velocity. The significance of this will be further discussed in section 7.1 with reference to the test campaign carried out in this project.

Fig. 2.38 reveals that for frequencies between about 0.75 Hz and 1.75 Hz the inverted pendulum model acts as a negative damper, in agreement with Dallard et al. [2]. Furthermore the self-excited force can be characterised as an effective mass reduction for vibration frequencies between approximately 0.3 Hz and 1.3 Hz (assuming a lateral forcing frequency of 0.9 Hz and using the relative CoM velocity in the CoP placement law). This is in agreement with observations of the CSB [24].

Most significantly, the generation of self-excited forces is demonstrated in the absence of step synchronisation. Thus at the time of publication, this work marked a significant departure from the prevailing understanding of HSI. It therefore provides a compelling argument for the further pursuit of biomechanically based investigation.

Carroll et al. 2011

Motivated in no small part by the work of Macdonald, Carroll et al. [45] utilised the same inverted pendulum model and CoP placement law to simulate the dynamic forcing effect of a pedestrian crowd. This was achieved by dynamically coupling multiple inverted pendulum models to a SDoF system representing a lateral bridge vibration mode. In addition to this, the time dependent forcing frequency and spatial distribution of pedestrians was simulated with a discrete element crowd model, coupled to the dynamic simulation. Using this model, excessive lateral bridge response was developed in the bridge mode without step frequency tuning among the simulated crowd. This model is discussed in detail in chapter 8 and is mentioned here for chronological completeness.

Bocian et al. 2012

Bocian et al. [15], extended the earlier work of Macdonald and investigated the influence of pendulum length, walking frequency, bridge oscillation frequency and margin of stability b_{min}. Interestingly it was reported that the self-excited force was found

via simulation to be independent of stability margin, b_{min}. This is somewhat surprising considering the magnitude of the GRF of which the self-excited force is a part, is directly related to b_{min}, i.e. a wider gait width results in larger magnitude lateral GRFs. The analysis also confirmed the strong frequency dependence of the inverted pendulum-induced damping and mass effects. Simulation values for inverted pendulum negative damping showed particularly good agreement with those reported for the LMB, CSB and CMB for simulated forcing frequencies of 0.6 Hz and 0.7 Hz, corresponding to a relatively slow walking velocity.

According to the inverted pendulum model, a bridge oscillating under the actions of a pedestrian crowd will experience an apparent mass alteration, by virtue of the self-excited force. This alters the response frequency of the system and in turn influences the induced damping effect of the self-excited force.

By assuming a uniform distribution of pedestrians, walking with identical pacing frequencies and considering only the mean self-excited component of the GRF, the mass and damping conditions on the stability boundary were identified, Eq. (2.3.23) & (2.3.24). The stability boundary is defined as the point at which the total damping becomes negative, allowing the development of divergent bridge response amplitudes.

$$\omega_n = \omega_b \sqrt{1 + \frac{\Delta M(\omega_b)}{m_p}\,\mu} \tag{2.3.23}$$

$$\zeta = \frac{c_p(\omega_b)\,\mu}{2\omega_n m_p} \tag{2.3.24}$$

At the outset of an analysis, the modal frequency of the empty structure, ω_n, is known and a ratio of total pedestrian to modal mass, μ, is assumed (m_p is the mass of a single pedestrian). Using Eq. (2.3.23), the response frequency of the occupied structure is determined, ω_b. This is then used in Eq. (2.3.24) to determine the critical structural damping ratio required to maintain overall positive damping. The output for a range of mass ratios and natural frequencies are shown in Fig. 2.39. If the modal damping is below that specified in plot (b) for a given modal frequency and mass ratio, crowd-induced negative damping will overcome the modal damping, provided the model's assumptions are satisfied.

The concept of establishing stability boundaries is beneficial as it gives a clearer view of the scale effects when many inverted pendulums are considered. It also provides

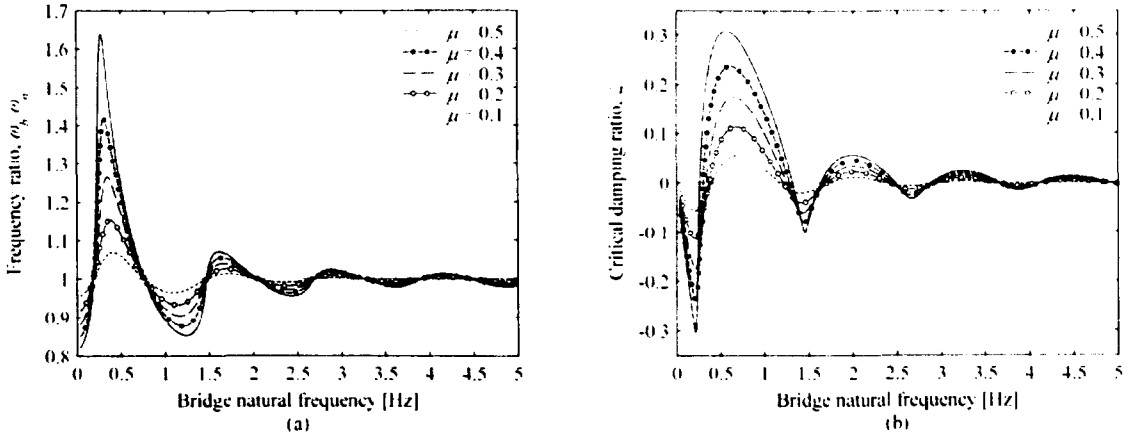

Figure 2.39: Plot (a), response frequency to bridge natural frequency ratio, $\frac{\omega_b}{\omega_n}$, and (b) critical damping ratio, ζ, required for stability, plotted against bridge natural frequency for $f_p = 0.6Hz$ and pendulum length equal to 1.167 m. Data for varying pedestrian to bridge mass ratios, μ is shown, after [15].

a tool for estimating susceptibility to lateral instability. However, as with any model, there exist limiting assumptions. In this case the uniformity of pedestrian distribution (in space and time) and pacing frequencies raise uncertainties regarding the real-world applicability of the predictions.

Furthermore, the validity of the passive inverted pendulum model coupled with Hof et al's balance law has yet to be established for the case of walking on a laterally oscillating structure. Considering the role of sensory feedback in human locomotion, discussed in chapter 3, the inverted pendulum model and balance law should be investigated further.

2.4 Crowd-structure interaction models

As mentioned briefly in chapter 1, one of the most challenging aspects of crowd-induced dynamic loading is the variability in flow characterises and the dependency of structural response on these characteristics. Indeed this is likely the motivation for employing the common simplifying assumption; that pedestrians are uniformly distributed along the bridge deck. In many cases a common or average pacing frequency is also assumed. Among the first to recognise the significance of the interdependency between crowd flow behaviour and structural response were Venuti and Bruno, [46–50].

Although similar concepts were being proposed independently by Bodgi et al. [51].

The continuum crowd modelling approach

Venuti et al. modelled two-way non-linear interaction between a bridge and pedestrian crowd by partitioning them into two subsystems [46]. The bridge was initially modelled as a 1-dimensional beam whose dynamic behaviour was described by a SDoF oscillator. The crowd was modelled as a 1-dimensional compressible fluid by means of the mass conservation equation in its Eulerian form:

$$\frac{\partial \rho}{\partial t} + \frac{\partial}{\partial x}(\rho\, v) = 0 \tag{2.4.1}$$

where ρ is the crowd mass density and v is the crowd velocity. In this manner Venuti et al. modelled the evolving nature of the crowd, identified by Rönnquist [7] as a critical factor when comparing analytical predictions with experimental observations. Furthermore, their model simulated two-way interaction between the pedestrian crowd and bridge oscillation. The bridge lateral velocity envelope was used to modulate the crowd walking speed via a correction factor ($0 \leq h(x,t) \leq 1$). This simulates the tendency for walking speeds to reduce as the magnitude of response increases, an intuitive assumption. In turn, the pedestrian mass distribution was used to alter the bridge modal mass. The force exerted by the pedestrian crowd was the subject of additional work by Venuti et al. in [48].

The force model proposed in [48] is based on a hydrodynamic characterisation of the crowd, i.e. they are defined not as individuals but as a continuum for which a mean walking velocity and therefore step frequency is determined. This fact betrays one of the fundamental weaknesses of the continuum modelling approach, the lack of ISV, one of the defining characteristics of a pedestrian crowd.

According to Venuti et al's model, the force F_c, exerted by a crowd of N individuals consists of three components:

$$F_c = F_{ps} + F_{pp} + F_s \tag{2.4.2}$$

where F_{ps} is the force due to step-synchronisation between the crowd and the bridge, F_{pp} is the force due to step-synchronisation among the crowd and F_s is the force due to

the remaining number of uncorrelated pedestrians. The number of pedestrians participating in the generation of each force component can be summarised as follows:

$$n_{ps} = NS_{ps} \tag{2.4.3}$$

$$n_{pp} = NS_{pp}(1 - S_{ps}) \tag{2.4.4}$$

$$n_s = N - n_{ps} - n_{pp} \tag{2.4.5}$$

where S_{ps} and S_{pp} are synchronisation coefficients in the range [0 1]. S_{ps} is defined as a function of lateral bridge velocity, based on a fitting of Dallard et al's experimental data, [2]. S_{ps} is also a function of the frequency ratio between the pedestrian forcing and structural oscillation frequencies, based on data obtained in [34]. S_{pp} is defined qualitatively as a function of crowd density. The experimental data underpinning this function is extremely limited.

Based on this subdivision of the crowd-induced force, Venuti et al. propose two mechanisms for excessive lateral vibration, one based on pedestrian-structure interaction assuming step-synchronisation and another based on pedestrian-pedestrian synchronisation in situations were the crowd is sufficiently dense.

The artificial subdivision of the crowd-induced load, necessitated by the continuum crowd model, is somewhat problematic; the component F_{ps} is based solely on step synchronisation. Brownjohn et al. [6] and Macdonald [24] have observed excessive lateral vibration on full scale structures in the absence of step synchronisation. Further experimental [10, 11, 52] and analytical [15, 37, 53] work also supports the existence of an alternative HSI mechanism that does not involve step-synchronisation.

The F_{pp} component is based purely on an assumption of inter-pedestrian step synchronisation, with little experimental evidence other than qualitative observations in [8]. Anderson investigated the walking behaviour of test subjects in varying crowd densities up to 1 ped/m^2 [54]. His work revealed that the distribution of pacing phases within the crowd was almost uniform, regardless of the crowd density considered. This contradicts Venuti et al's force model, suggesting inter-pedestrian synchronisation is negligible. However it must be said that with the exception of Brownjohn et al's paper [6], all of the observations cited in the preceding two paragraphs were published after Venuti et al's initial paper [46].

A key element of the interaction model is the relationship relating local crowd density to mean crowd velocity. In [47], Venuti and Bruno propose a fundamental relation for velocity-density based on a phenomenological model of pedestrian walking at the single pedestrian or 'microscopic level'. Essentially the space occupied by a walking pedestrian is derived as a function of walking velocity (via a required forward sensory zone) and lateral bridge velocity (via the required width to allow torso sway). The proposed velocity-density relation is compared with a revised version of the Kladek formula, originally proposed to model vehicular traffic [55]. Both the Kladek formula, (2.4.6) (fitted to experimental data) and the proposed relation (based in microscopic interpretative modelling) show excellent agreement with each other. The Kladek formula revised for use with pedestrian traffic is as follows,

$$v = v_M\left\{1 - exp\Big[-\gamma\Big(\frac{1}{\rho} - \frac{1}{\rho_M}\Big)\Big]\right\} \tag{2.4.6}$$

in which v is the walking speed of the crowd, v_M is the maximum walking speed, ρ is crowd density and ρ_M is the maximum crowd density at which the crowd are forced to stop walking. γ is an empirical parameter used to fit the formula to experimental data. Based on the agreement between both models the authors adopt the more compact revised Kladek formula as a means of relating crowd velocity and density. The derivation of the alternative interpretative relationship (based in microscopic interpretative modelling), according to the authors, serves as a complementary model revealing the underlying microscopic behaviours that contribute to the macroscopic velocity-density relationship.

Following the developments presented [48] and [47], Bruno and Venuti [49] compared simulation results from the updated framework to experimental observations of the TPB [5]. The modelling framework showed good agreement with the experimental data.

The framework proposed by Venuti and Bruno is a novel approach. Its attractiveness as a simulation tool lies mainly in the fundamental concepts it encompasses; the simulation of an evolving crowd and the coupling between crowd behaviour and bridge response. However, the hydrodynamic characterisation of the crowd, in this author's opinion, leads to some fundamental drawbacks with the modelling framework. ISV cannot be facilitated, thus all pedestrians are assigned average parameter values. The

crowd model also requires the assumption of continuity of crowd flow. Satisfying this assumption with low crowd densities, which may prevail in day-to-day traffic may be difficult. Furthermore, the artificial subdivision of the forcing function is somewhat outdated in light of recent contributions to the literature.

2.5 Summary

Experimental campaigns to date have focused on the GRFs developed by pedestrians with little attention paid to the balance behaviour responsible for their generation. There is thus a dearth of data available relating to the kinematics of one half of the HSI system. The use of motion capture technology holds great potential for filling this data 'black spot'.

The literature contains a wide range of modelling techniques. Venuti and Bruno have focused on the influence of crowd behaviour while Macdonald's biomechanical based model focuses on the detail of HSI. There is scope to develop both the understanding of HSI and the modelling tools used to simulate crowd-induced vibration. If existing biomechanical models can be underpinned with experimental data and combined with the advantages offered by an integrated crowd model, a more complete picture of the phenomenon of crowd-induced vibration may be established.

In the following chapter, background material on biomechanics and control of locomotion is briefly discussed. The material discussed in chapters 2 and 3 is then drawn on in chapter 4, in which the aims and objectives of this project are stated.

CHAPTER 3

Bipedal locomotion - background theory

Chapter Summary

In this project, an improved understanding of HSI is sought by analysing whole body behaviour in response to lateral base motion. The discussion and analysis that follows in this thesis therefore extends beyond what may be considered to be 'traditional' civil engineering. An appreciation of key literature in the fields of biomechanics and to a lesser extent, neurology, are required to give context to the analyses and discussion in subsequent chapters.

In sections 3.1 to 3.3, a discussion of human locomotion at a neurological level is presented, setting out the role of the nervous system and sensory feedback in locomotion control. In section 3.4 a review of fundamental concepts and terminology relating to the kinematics of the human gait cycle is presented. In section 3.5 a brief overview of the GRFs generated while walking is provided. Experimental observations relating walking velocity and pacing frequency are reviewed in section 3.6. Finally, in 3.7 the relevance of the preceding discussion to this investigation is briefly summarised.

3.1 The nervous system and sensorimotor coupling

The study of biomechanics and in particular human locomotion has been ongoing since the 19th century. While the physical behaviours and motions involved in locomotion are well documented and understood, there are still many uncertainties regarding how the human brain actually orchestrates the apparently simple task of walking. Despite the inherently unstable human morphology, with its high centre of mass (CoM) and relatively narrow base of support (BoS), human locomotion is remarkably stable and adaptable.

The questions surrounding stable locomotion are interesting in their own right. However they take on a new significance for civil and structural engineers concerned with the problem of human-induced vibration. Of particular interest is the interaction that takes place between a pedestrian, actively balancing as they walk, and the flexible structure beneath them. To investigate this interaction and ultimately design for it, the engineer must understand pedestrian stability and what strategies the 'human system' uses to maintain stable locomotion in the face of external destabilising influences.

In this section, locomotion is considered at a neurological level to provide sufficient context for biomechanical discussions presented later. The components of the nervous system and their part in the generation of biomechanical actions are briefly outlined. This is followed by a short review of motion control and the role of central pattern generators (CPG) in the emergence of rhythmic locomotion. Finally the importance of sensory feedback in bipedal locomotion is outlined. The medical facts pertaining to the nervous system are obtained from *Biomechanical Basis of Human Movement* by J. Hamill and K.M. Knutzen [20], unless otherwise stated.

The nervous system consists of two parts, the Central Nervous System (CNS) and the Peripheral Nervous System (PNS). The brain and spinal cord make up the CNS. It can be considered the central processing unit for human motion control. The PNS is made up of the nerves that lie outside the spinal cord. The PNS links the muscles and organs of the body back into the CNS.

The output from the CNS is transmitted via motor neurons. The motor neuron consists of the cell body located within or just outside the spinal cord, the dendrites which are

fibres that pass information to other neurons (allowing cross communication between neurons) and the axon, a large fibre that connects the cell body to muscle fibres or other neurons. The motor neuron transmission signal takes the form of an electrical potential that travels along the axon down to the motor endplates at the neuromuscular junction. A single action potential causes a twitch type shortening of the muscle. A succession of impulses causes a constant muscle tension. Depending on the type of motor neuron the signal transmission time varies resulting in muscle reaction times between 30 and 70 ms.

The sensory neuron is the means by which the state of the musculoskeletal system and other organs, including the skin, is communicated back to the CNS. This allows the CNS to generate appropriate motor neuron responses based on sensory feedback. Sensory neurons transmit information from sensor systems in the body known as proprioceptors. The proprioceptors associated with the musculoskeletal system are the muscle spindles and the Golgi tendon organ. Muscle spindles are located within the muscle, parallel to the muscle fibres and measure muscle stretch. The golgi tendon organs are located between the muscle fibres and the tendon that connects to the bone and measure muscle tension.

One of the primary sensory systems responsible for spatial orientation and balance is the vestibular system, located in the vestibulum within the inner ear. This consists of the cupula within the semicircular canal system which contains hairs that sense angular acceleration and the utricle and saccule which contain hairs sensitive to linear acceleration. The vestibular system combines with the vision system to provide the sense of spatial orientation, key to maintaining balance.

Interaction between the vestibular and visual systems can be seen in the vestibulo-ocular reflex (VOR). When linear or angular motion of the head is sensed by the vestibular system, a corresponding reflex eye movement is generated in order to stabilise images on the retina. For example, if the head turns to the right while observing a fixed object, the eyes will automatically compensate by rotating left. The VOR is important for stabilising vision and is particularly useful when walking on an unstable or moving structure.

A reflex more generally describes the coupling that takes place between motor neurons

(transmitting *from* the CNS) and sensory neurons (communicated *to* the CNS). Reflexes describe different forms of *sensorimotor* coupling and are categorised as monosynaptic, propriospinal or supraspinal. Monosynaptic reflexes are those in which the sensory input and motor output occur at the same level within the spinal cord. The flexor reflex is a monosynaptic reflex that triggers a rapid withdrawal movement triggered by sensory input indicating pain. Monosynaptic reflexes tend to be experienced as involuntary responses. Propriospinal reflexes process information and initiate responses across multiple levels of the spinal chord. The tonic neck reflex seen in infants is an example of a propriospinal reflex. Here, a rotation of the head to one side results in an extension of the arm on that side and a flexion of the arm on the opposite side. Supraspinal reflexes involve transmission of information to the brain where it is processed to determine an appropriate motor response. Most postural reflexes ensuring overall postural stability and balance require processing by the brain and fall into this category

3.2 Neural control of walking

As pointed out by Nielsen [56], during walking the foot is typically raised 1 to 2 cm from the ground and its position varies by less than 4 mm from step to step. This level of precision is achieved despite the fact that foot position during the swing phase is determined by the position of 5 individual joints while 15 muscles act on the knee joint alone. The number of muscle activation combinations that could be used to achieve this motion control is vast. Thus the question is, how does the CNS solve such a complex inverse kinematic problem without overwhelming the brain and diminishing our ability to perform other complex tasks while walking?

Investigations by Patla [57] and Vaughan et al. [21], examining electromyograph (EMG) data have suggested that complex muscle activity patterns can be deconstructed into only a few basic component patterns. This supports the common theory that muscle activation is generated by a limited number of movement primitives whose combination can generate the full spectrum of human rhythmic motion. The so called central pattern generator, responsible for the initiation and timing of these activation primitives is thought to play a key role in the generation of rhythmic locomotion in humans. Ivanenko et al. [58] reinforced this theory by expanding the work of Patla and Vaughan

et al. to consider EMG records from a wider sample of muscles. They reported that the weighted sum of five component muscle activity patterns could be combined to account for 90 % of the complex patterns seen in the limb and trunk muscles during locomotion.

The existence of these activation primitives means the CNS does not necessarily need to generate the more complex muscle activation patterns observed from EMG recordings, rather it rhythmically combines more basic patterns appropriately to produce complex muscle activation. Ivanenko et al. [16] later reported that the timing of the five component activation bursts is associated with major events in the gait cycle; (1) weight acceptance, (2) loading/propulsion, (3) trunk stabilisation during the double support phase, (4) toe off, and (5) heel strike.

Based on these findings they proposed a hypothetical scheme for motion control in which the CPG initiates a rhythmic spatial and temporal pattern of muscle activation. These activation components are the input into a distributed neural network (NN) where signals are combined and modulated/weighted based on supraspinal and propriospinal feedback. Individual muscles are then activated via motor neurons to produce locomotion, Fig. 3.1.

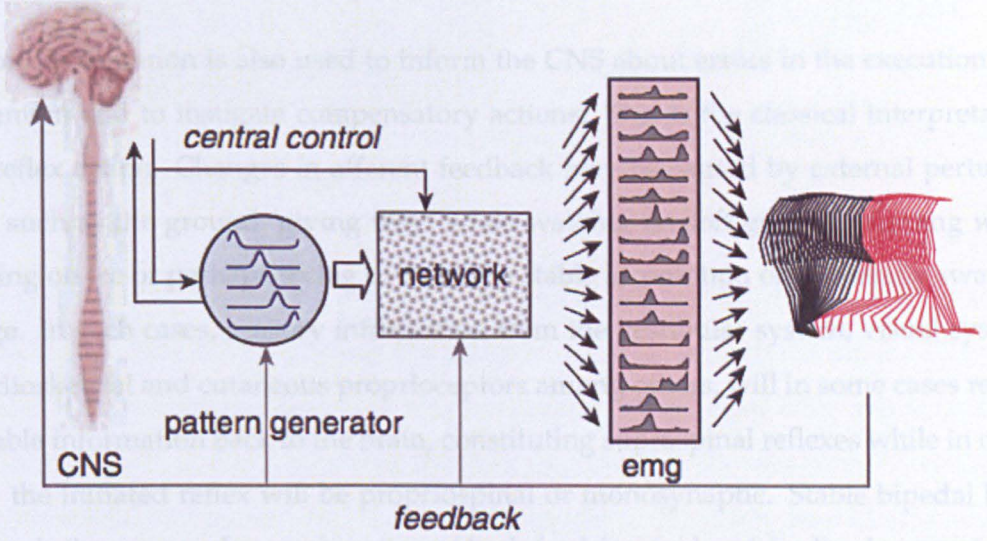

Figure 3.1: Hypothetical scheme of muscle activation in human locomotion, after [16].

3.3 The role of feedback

The CPG and associated spinal NN, sitting within the CNS, is thought to be responsible for generating rhythmic locomotion in humans as well as other vertebrates. However, the motor signals transmitted to muscles from the spinal NN are influenced by supraspinal feedback far more in humans than in other animals [56]. One of the neurological features that sets human locomotion apart from other animals is that the brain is required to process sensory feedback to a far greater extent in order to maintain stable, adaptable bipedal locomotion. In humans (and other primates) a neurological pathway has evolved directly between the motor cortex of the brain and the the spinal motor neurons. This greatly influences muscle activity during walking [56].

Nielsen [59] identifies two fundamentally different ways that sensory or *afferent* feedback contributes to the control of human locomotion. In the first, afferent feedback is used as an information supplement and is integrated into the motor commands which activate the muscles. This feedback information allows the coordination of locomotion to be less centrally driven, i.e. the 'computational overhead' on the brain in driving locomotion is reduced in the presence of sensory feedback. This feedback is anticipated by the CNS and is an integrated part of normal locomotion control.

Sensory information is also used to inform the CNS about errors in the execution of a movement and to instigate compensatory actions. This is the classical interpretation of a reflex action. Changes in afferent feedback may be caused by external perturbations such as the ground 'giving way' when walking on soft ground, slipping while walking on ice or perhaps trying to maintain stable locomotion on a laterally swaying bridge. In such cases, sensory information from the vestibular system, visual system, musclioskeletal and cutaneous proprioceptors among others, will in some cases report valuable information back to the brain, constituting supraspinal reflexes while in other cases the initiated reflex will be propriospinal or monosynaptic. Stable bipedal locomotion is thus a complex combination of both feed forward and feedback control.

Bauby and Kuo [60] investigated both forward-aft and lateral foot placement of 15 subjects during walking trials with both eyes open (EO) and closed (EC). Subjects showed an increase in the variability of lateral foot placement position for EC tests, with rela-

tively little increase in forward-aft variability. This demonstrates the increased sensitivity of lateral balance to visual-vestibular feedback. Bauby and Kuo state that these results are consistent with the hypothesis that lateral balance must be stabilised by visual-vestibular feedback, however forward-aft or sagittal plane balance requires little or no feedback of this type.

A study by Otten [17] investigated the balance strategies employed by subjects balancing on one foot on a narrow beam. This highlighted the inability of the inverted pendulum to model this situation owing to its inherent instability.

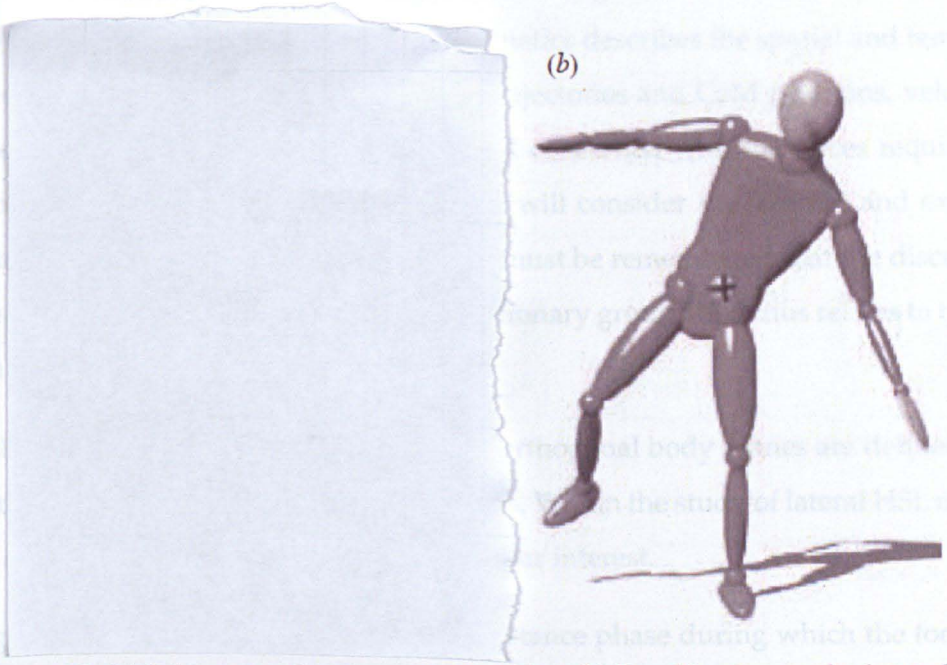

Figure 3.2: (a) Subject standing on a narrow ridge, (b) Resulting human body model, the cross indicates CoM , after [17].

Otten pointed out that balance is maintained by modulating the direction of the lateral component of the GRF by altering the moment applied through the ankle. The ankle moment results from multiple joint rotations made in the upper body while trying to maintain balance. It was found that the joint rotation that showed highest correlation with the lateral component of GRF was hip rotation. Therefore in a case when foot placement cannot be altered, hip and ankle rotation ensure lateral balance.

The situation investigated by Otten is not dissimilar to that of a pedestrian during the single stance phase of walking on a laterally moving bridge deck. During this single stance phase the pedestrian is forced to react (maintain balance) while subject

to base perturbations that where unknown at the instant the foot was placed. In this way, the other balance strategies (hip & ankle) largely ignored for walking on steady ground, may play a bigger role in maintaining balance, particularly considering the single stance phase represents roughly 75 % of the gait cycle.

3.4 Kinematics of the gait cycle

Kinematics of walking refers to the motion of the segments that make up the human body. Within the study of biomechanics, kinematics describes the spatial and temporal features of body movement, including joint trajectories and CoM positions, velocities and accelerations. A kinematic analysis is not concerned with the forces required to produce motion. However a kinetic analysis will consider the internal and external forces and torques involved in the motion. It must be remembered that the discussion in this section is confined to locomotion on stationary ground and thus relates to typical human 'baseline' behaviour.

To facilitate a kinematic analysis, 3 standard orthogonal body planes are defined, Fig. 3.3, within which there are two orthogonal axes. Within the study of lateral HSI, medio-lateral motion in the frontal plane is of particular interest.

During the gait cycle each foot experiences a stance phase during which the foot is in contact with the ground providing vertical support and a swing phase during which the foot is moving through the air and support is provided by the contralateral foot. For healthy individuals with a symmetrical gait the stance phase typically accounts for 62% of the gait cycle with the swing phase accounting for the remaining 38% [21], Fig. 3.4.

The stance phase can be subdivided into the following subphases:

1. *First double support,* (12 %); Both feet are in contact with the ground.
2. *Single limb stance,* (38 %); One foot is swinging while the contralateral foot is in contact with the ground.
3. *Second double support,* (12 %); Both feet are again in contact with the ground.

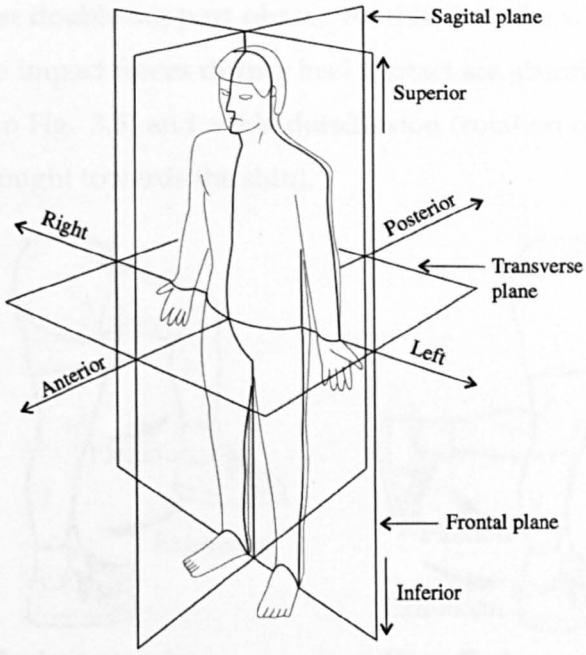

Figure 3.3: 3 orthogonal body planes with associated directionality, after [18].

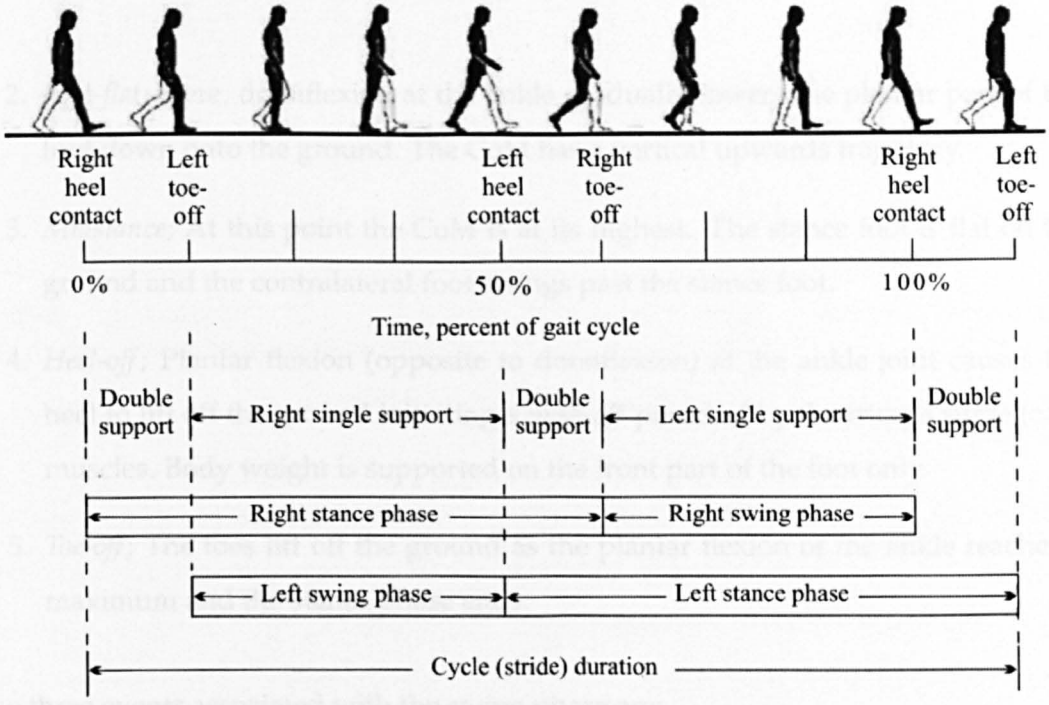

Figure 3.4: Phases of the gait cycle, after [19].

The gait cycle can also be described in terms of *events* that describe discrete movements or behaviours of the foot during the cycle. The events associated with the stance phase are:

1. *Heel-strike*; This conventionally signifies the beginning of the gait cycle and the

start of the first double support phase. At this time the whole body CoM is at its lowest. The impact forces during heel contact are absorbed via hip and knee flexion (refer to Fig. 3.5) and ankle dorsiflexion (rotation of the ankle such that the toes are brought towards the shin).

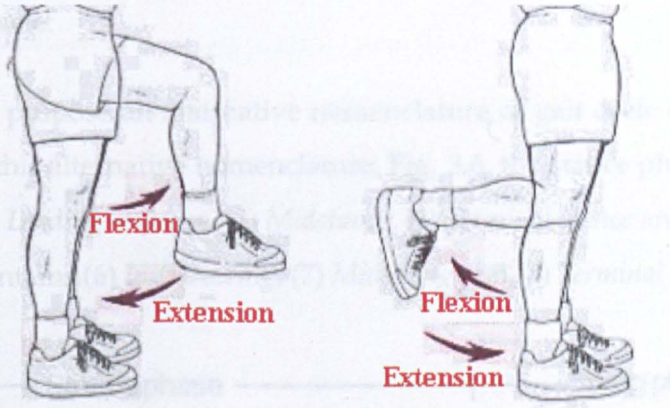

Figure 3.5: Hip and knee flexion and extension, adapted from [20].

2. *Foot-flat*; Here, dorsiflexion at the ankle gradually lowers the plantar part of the foot down onto the ground. The CoM has a vertical upwards trajectory.

3. *Midstance*; At this point the CoM is at its highest. The stance foot is flat on the ground and the contralateral foot swings past the stance foot.

4. *Heel-off*; Plantar flexion (opposite to dorsiflexion) at the ankle joint causes the heel to lift off the ground initiating a *push-off* powered by the triceps surae (calf) muscles. Body weight is supported on the front part of the foot only.

5. *Toe-off*; The toes lift off the ground as the plantar flexion of the ankle reaches a maximum and the stance phase ends.

The three events associated with the swing phase are:

1. *Acceleration*; This immediately follows from the toe-off event. The hip flexor muscles are activated to accelerate the leg forward.

2. *Midswing*; This coincides with the midstance event on the contralateral foot hence the feet are side by side. During the swing phase, hip and knee flexion ensure

adequate ground clearance for the swing foot. Dorsiflexion at the ankle keeps the toes from contacting the ground.

3. *Deceleration*; The leg and hip musculature is employed to slow the leg such that the foot can be stabilised allowing accurate foot placement for the beginning of the next gait cycle.

Vaughan et al. [21] propose an alternative nomenclature of gait cycle events, also in common usage. In this alternative nomenclature, Fig. 3.6, the stance phase consists of (1) *Initial contact*, (2) *Loading response*, (3) *Midstance*, (4) *Terminal stance* and (5) *Preswing*. The swing phase contains (6) *Initial swing*, (7) *Midswing* and (8) *Terminal swing*, Fig. 3.6.

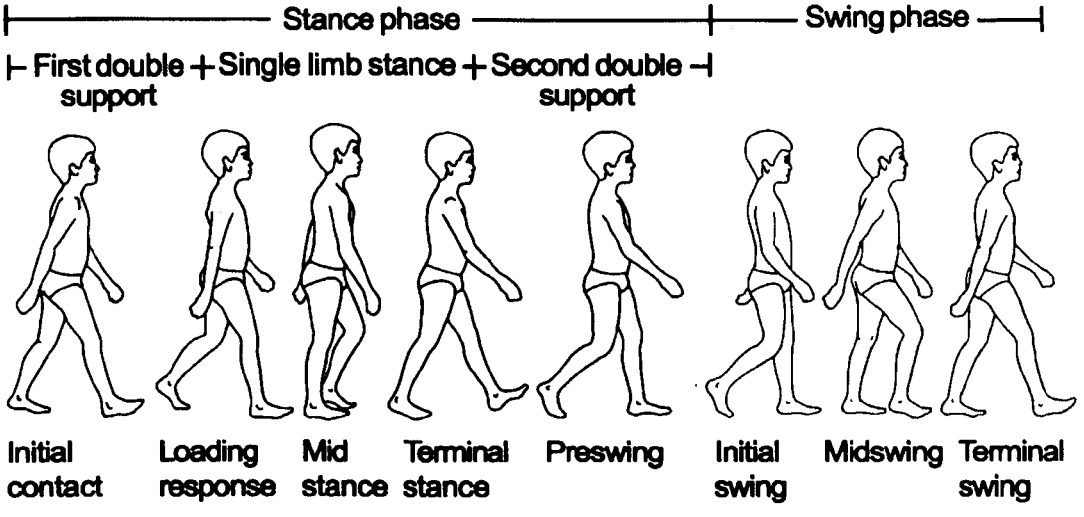

Figure 3.6: Gait cycle events, after [21].

The spatial gait parameters are shown in Fig. 3.7. A stride length is the distance between two successive heel strikes of the same foot. This distance is made up of a (usually equal) right and left step length. The step width describes the medio-lateral distance between the feet. This parameter is of great significance in the study of balance stability in the frontal plane and will be discussed further later.

3.5 Kinetics and the Ground Reaction Force

A kinetic analysis of walking considers the influence of internal and external forces on the human body and its constituent parts. Internal actions, consisting of torques and

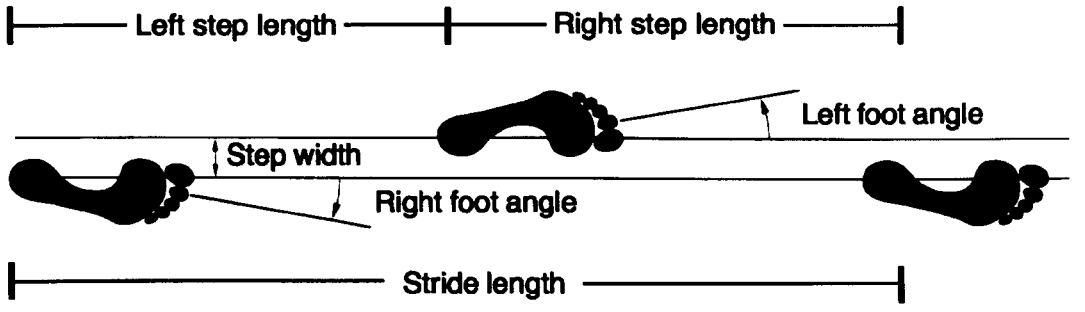

Figure 3.7: Spatial gait parameters, after [21].

forces may include those that are generated between individual body segments as a result of inertia and muscle forces. However of particular interest in this investigation are the external forces generated during foot contact with the ground, known as ground reaction forces (GRF).

The GRF is a 3-dimensional vector quantity, and as such it can be resolved into three orthogonal components; vertical, perpendicular to the transverse plane; longitudinal, perpendicular to the frontal plane; lateral, perpendicular to the sagittal plane. All three components can be seen in Fig. 3.8 which was obtained (during this investigation) as a subject walked over force plates embedded in the walking surface. The force magnitude has been normalised by the subject's body weight, a standard practice in biomechanical analysis, allowing inter-subject comparison.

The GRF force vector acts through a single point under the foot, known as the centre of pressure (CoP). This is identified as the point through which the resultant of the pressure distribution beneath the foot acts. The precise location of the CoP varies during the course of the foot contact.

The vertical component of the force exhibits a characteristic 'M' shape from which key gait cycle events can be identified. The first peak corresponds to weight acceptance, after initial heel contact. The second peak corresponds to the terminal stance or push-off event immediately prior to the foot leaving the ground. The trough between both peaks corresponds to the mid-stance phase. It should be noted that the peak magnitude of the vertical component of the GRF is typically greater than 100% of the subject's body weight, as demonstrated in Fig. 3.8 (a). This is due to the added influence of inertia forces induced by the change in acceleration of body mass immediately after heel contact and prior to toe-off.

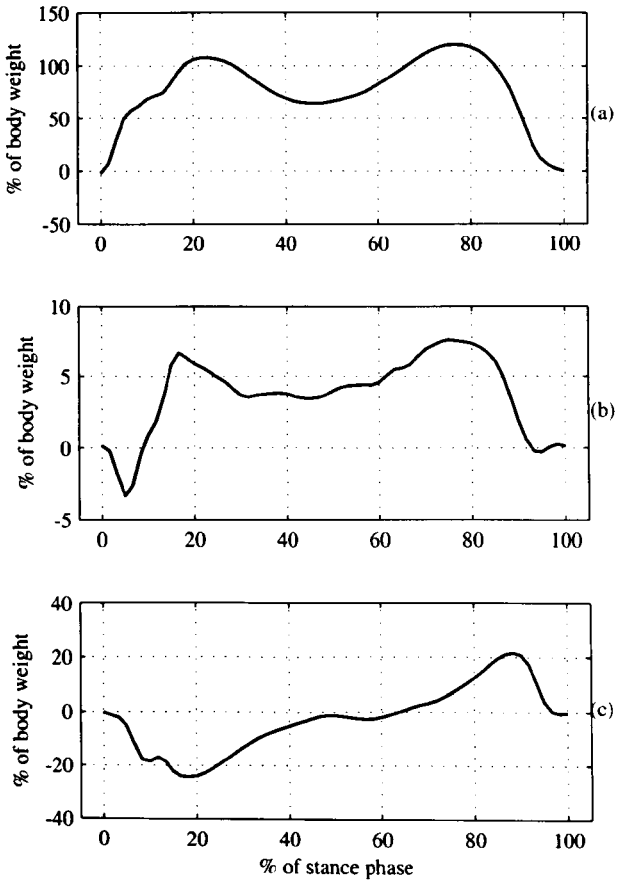

Figure 3.8: Components of the GRF from a single stance phase, normalised by body weight. (a) vertical, (b) lateral and (c) longitudinal force. Data obtained during testing within this project.

The longitudinal force component, Fig. 3.8 (c), varies from positive to negative over the duration of a foot contact and is essentially a friction force developed between the underside of the foot and walking surface. Upon initial foot contact, the longitudinal force imposed on the walking surface is in the anterior direction. However, midway through the stance phase the force direction changes to posterior as the subject's mass is propelled forward.

The lateral force, Fig. 3.8 (b), is the smallest of all three force components and also results from friction between the foot and supporting surface. It too has a characteristic 'M' shape that derives from the inverted-pendulum like motion of the CoM when projected onto the frontal plane. At the beginning of the stance phase, the eccentricity of the CoM with respect to the CoP is at its greatest and therefore the horizontal component of the GRF is at a maximum. During the single stance, this eccentricity reduces to

a minimum, before returning to a maximum at the end of the stance phase. Associated with this variation in eccentricity is a corresponding change in the magnitude of the lateral component of the GRF, resulting in a trough between two peaks.

Figure 3.8 shows the GRF components generated from a single foot contact. However the force imposed on the supporting structure during the double stance phase is equal to the resultant of GRFs from both feet. This is demonstrated in Fig. 3.9.

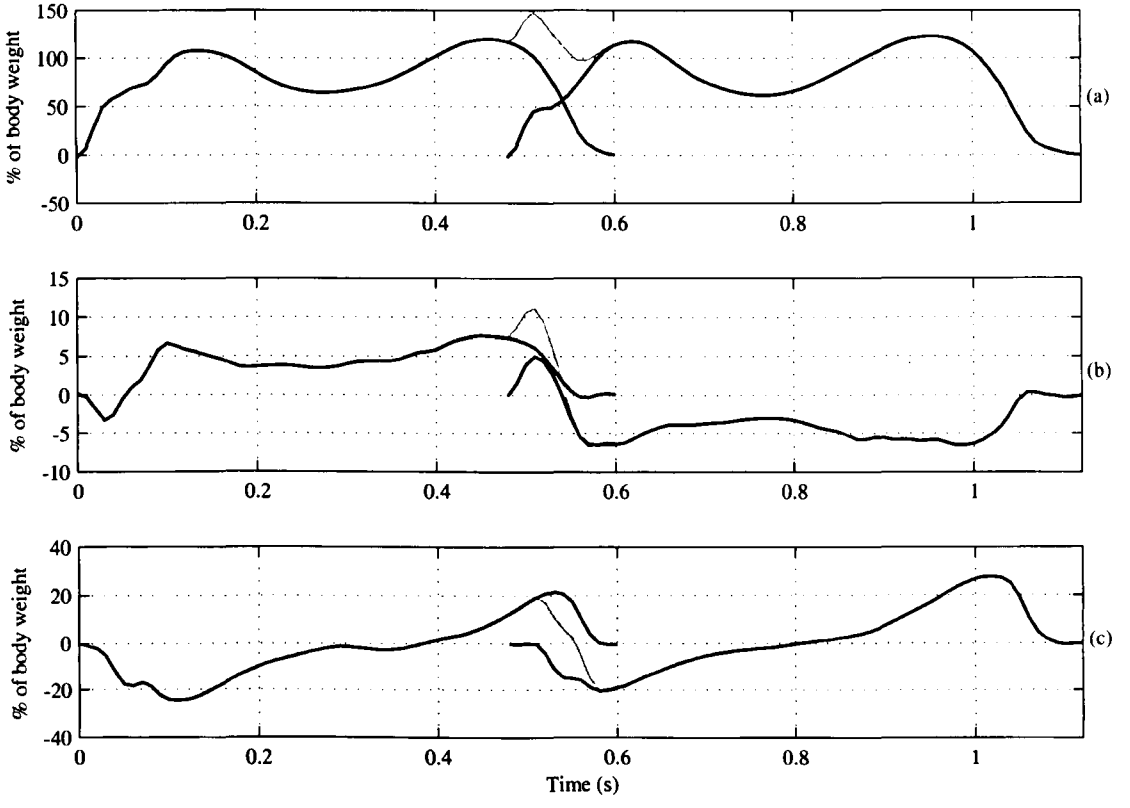

Figure 3.9: GRF generated from 2 successive footsteps (black line) and the resultant force during the double stance phase (grey line), normalised by body weight. (a) vertical, (b) lateral and (c) longitudinal force. Data obtained during testing within this project.

The black lines indicate the individual GRFs recorded from two successive steps on individual force plates. The period of overlap is clearly seen. During this period the resultant force is plotted in grey. The overlap results in a significant peak in the magnitude of the resultant vertical GRF. A peak is also generated in the lateral GRF. This is due to the fact that the lateral GRF is initially directed in the medial direction. It should be remembered that although the resultant GRF may be considered as a continuous function in time, it is discontinuous in space.

3.6 Walking velocity and pacing frequency

The dynamic behaviour of complex civil engineering structures can very often be well characterised by the humble, SDoF oscillator. As is often the case, the difficulty arises when trying to accurately model the excitation. In the case of crowd-induced excitation, one of the most significant parameters in defining the dynamic influence of a crowd is pacing frequency, which is related to walking velocity, a parameter which varies across the population. In wishing to account for this variability, observations and probabilistic analyses have been carried out to help characterise the variability.

From a sample of 505 pedestrians, Matsumoto et al. [61, 62] calculated a mean step frequency of 1.99 Hz with a standard deviation of 0.173 Hz. They also confirmed a normal distribution for the step frequency.

Pachi and Ji [63] studied the effect of pedestrian environment on pacing frequency. They observed the number of steps and the time to cover a set distance for 800 subjects. They proposed a linear relationship between walking speed, v_p, and pacing frequency, f_{vert}:

$$v_p = l_p \, f_{vert} = \begin{cases} 0.75 f_{vert} & \text{for men} \\ 0.67 f_{vert} & \text{for women} \end{cases} \tag{3.6.1}$$

where l_p is step length. By comparing 400 measurements recorded on two footbridges with 400 measurements recorded in urban environments (i.e. not on a footbridge), they reported mean pacing frequencies on footbridges as 1.86 & 1.80Hz versus 2.01 & 1.99Hz for non-footbridge environments. In both cases, a normal distribution was observed. It is important to point out that the subjects in Pachi and Ji's investigation were walking unimpeded at self-selected velocities.

However, as is often the case on crowded footbridges, pedestrians may be subject to velocity constraints due to neighbouring traffic. Bertram and Ruina [22] proposed that if one of the variables: step length, walking velocity or step frequency is constrained, the walking behaviour is altered to optimise metabolic cost per unit transit. By analysing data collected from treadmill tests by Molen et al. [64] in which oxygen consumption was measured, Bertram and Ruina plotted a metabolic cost surface as a function of step frequency and speed, Fig. 3.10. Individual surface contours indicate the combination

of speed and step frequency that demand equal oxygen consumption. Each contour depicts a cost of walking that is less metabolically costly than the contour residing outside. Therefore all contours emanate from the point of least metabolic cost, considered to be the preferred combination of walking speed and step frequency.

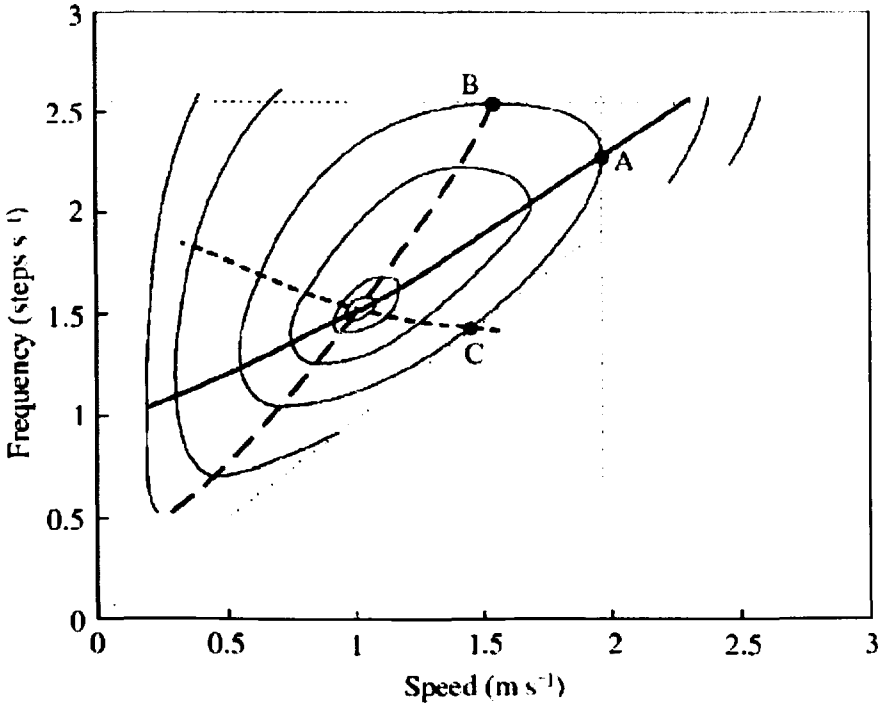

Figure 3.10: Metabolic cost surface showing oxygen consumption above standing still, per unit distance as a function of walking speed, v_p and pacing frequency, f_{vert} , after [22].

The $v_p - f_{vert}$ relationships expected from constrained optimisation of this function are drawn. The curve passing through point A indicates the optimisation to constrained speed v_p in which the curve represents vertically oriented tangents to the cost contours. In other words, for the constrained speed, indicated by the vertical dashed line, point A indicates the optimum combination of walking speed and frequency that minimises oxygen consumption. Similarly, the curve passing through B indicates optimisation to constrained step frequency, f_{vert}, in which the curve represents horizontally oriented tangents to the cost contours. The curve passing through C indicates optimisation to constrained step length, l_p, in which the curve represents tangents of the cost contours and lines emanating from the origin (where each line from the origin indicates a different constant step length.)

They compared the constrained optimisation relationships derived from the metabolic cost surface, to the results of comparative tests. Although their investigation only consisted of 12 test subjects, the theory of constrained optimisation was found to predict the different walking behaviour (under various constraints) with reasonable accuracy. Bruno and Venuti [49] later presented a polynomial fit of Bertram and Ruina's experimental data to produce the following velocity-frequency relationship,

$$f_{vert} = 0.35v_p^3 - 1.59v_p^2 + 2.96v_p \tag{3.6.2}$$

Without directly modelling three-dimensional walking behaviour and fully understanding the physical and psychological motivations during human locomotion, Eq. (3.6.2) represents a feasible and practical means of relating walking velocity and pacing frequency. While this undoubtedly does not consider all possible influences on a pedestrian's pacing rate, it attempts to capture the most significant, walking velocity.

3.7 Closing comment

In this chapter several areas from the broad fields of biomechanics and locomotion control have been briefly discussed with the aim of illustrating the wider biological and biomechanical context of this investigation. Sections 3.1 to 3.3 suggest that the influence of varying inertial stimulus may induce active balance responses while walking on laterally moving surfaces. Sections 3.4 and 3.5 provide the vocabulary necessary for the discussion of gait behaviour. The simple inverted pendulum biomechanical model the work of Hof et al. which will be central to the discussion in following chapters, was explained in 2.3.1. Finally the experimental work relating walking speed with pacing frequency was discussed in 3.6. This too will be significant in the development of numerical models that follow in chapters 5 and 8.

In the next chapter, the material summarised above, along with the literature reviewed in chapter 2, is drawn upon to establish the aims and objectives of this research.

CHAPTER 4

Research motivation and aims

Chapter Summary

The purpose of this chapter is to set out the plan devised for executing the project. This will involve discussion of the research motivation, aims and objectives. Thus a roadmap from this point, chapter 4, to the project conclusions presented in chapter 10, is established.

In section 4.1 conclusions are drawn regarding the literature reviewed in the previous two chapters. Gaps in the state of knowledge are identified from which the aims of this project are drawn. Associated with the aims are a series of lower level objectives which serve as the building blocks required to satisfy each aim. Aims and objectives are discussed in section 4.2.

4.1 Research motivation

The literature pertaining to human-induced lateral bridge vibration is expansive. Despite this, a general consensus has not yet been reached regarding the HSI mechanism. A satisfactory explanation as to why bridges develop excessively large lateral oscillation amplitudes has remained stubbornly ellusive. However, several key field observations [6, 24], have led to the hitherto broadly accepted 'step-synchronisation' mechanism being questioned.

It has since been experimentally demonstrated [11] that step-synchronisation is not necessary for the development of GRF components which resonate with bridge motion. However, one can still not say how or why these force components are generated and thus the interaction mechanism is still unknown.

The work of Macdonald [37] has motivated several researchers [15, 45] to pursue a line of investigation which views the problem from a biomechanical perspective. Application of the inverted pendulum biomechanical model, stabilised via active control of support placement has produced promising results.

The inverted pendulum model is well established in the biomechanics field [65]. The model, coupled with the balance law proposed in [43] can be considered a semi-active model by virtue of the fact that discrete balance corrections are made at the time of support placement. This is known as the foot placement balance strategy. While simulating the single stance phase, motion of the inverted pendulum mass is defined solely by the mass initial conditions and the mechanics of the inverted pendulum. If one considers walking on a stationary surface, foot placement has been shown to be the main balance strategy, with minor corrections provided by rotation of the upper body about the supporting ankle and hip [13]. Therefore the semi-active inverted pendulum model is suitable.

Walking on a laterally moving bridge is fundamentally different from walking on stationary ground. In this case a pedestrian must decide where to place their foot based only on the sensory information they have at the time of foot placement. However, during the single stance phase the bridge oscillates, providing additional sensory stimulus altering the feeling of stability.

On this basis it is logical to hypothesise that external perturbations imposed by a swaying bridge during the single stance phase of walking may be corrected for through some form of active control implemented during the single stance phase. Essentially pedestrians may alter their balance in response to a continuously changing lateral inertial force on the body. Testing of this hypothesis is required to further validate the use of the inverted pendulum model in this context.

Utilisation of motion capture technology to investigate human motion, a well establish practice in many fields, is now being adopted by civil engineers to record and analyse the dynamic influence of people on structures [12]. These techniques offer an excellent opportunity to investigate not only the GRFs generated on a moving structure but also the accompanying biomechanical behaviour. It is the biomechanical response to base motion, correlated with the GRF that is the missing information required to complete the picture of HSI. An optical assessment of pedestrian balance behaviour would also provide a convenient means of establishing the suitability of the inverted pendulum model.

Understanding the detail of the HSI mechanism alone is not sufficient to simulate the dynamic influence of a pedestrian crowd. The work of Venuti et al. has highlighted the potential of considering the pedestrian crowd as an integral part of the dynamic simulation. The crowd-structure interaction modelling approach offers the ability to simulate the effect of more realistic traffic flows. However there are key limitations inherent in a macroscopic characterisation of the crowd:

1. Continuity of flow must be assumed. For low density crowd flows, or the level of traffic a bridge might experience on a daily basis, this assumption may not be satisfied and a continuous flow model is not strictly applicable. A method is required to allow designers to estimate typical bridge response in low and medium density loading events [66].

2. Inter-subject variability refers to the variability in parameters among the crowd. Both the forcing effect and behavioural reactions of individual pedestrian are likely to differ. A macroscopic crowd model cannot reflect this feature of pedestrian traffic.

3. The velocity-density relationship of the crowd is critical in determining the result-

ing dynamic response of the bridge. The mass conservation equation describing crowd flow in a macroscopic model must be accompanied by an equation relating mean crowd velocity to local crowd density [47]. This relationship is difficult to define with confidence in the context of pedestrian traffic.

Accepting the significance of crowd flow behaviour in the dynamic simulation of crowd-induced vibration, there is a need to develop a crowd-structure interaction model that retains the benefits of interaction demonstrated by Venuti et al. and addresses the limitations listed above. Discrete element or agent-based crowd modelling may allow such a model to be developed.

4.2 Aims and objectives

This project has two aims. The first is to improve the understanding of the lateral HSI mechanism. In the simplest terms, an answer is sought to the question; *how does pedestrian balance behaviour in response to base motion lead to the generation of self-excited harmonics within the GRF spectrum?*

An essential step in answering this question is establishing the significance (if any) of active balance control within the HSI mechanism. To that end, based on the reviewed literature in chapter 3, and the reasoning set out in section 4.1, the following hypothesis statement is proposed;

> *Active balance control in response to lateral base motion plays a significant role in determining frontal plane CoM motion, to the extent that the passive inverted pendulum alone can not adequately simulate pedestrian CoM motion during the single stance phase.*

It is not disputed that active balance control plays a crucial stabilising role during locomotion on stationary as well as moving structures. However what is of interest here is the extent to which it may cause CoM motion to deviate from that predicted by a passive inverted pendulum. This hypothesis will be considered disproven if it can be established that there is no practical difference between simulated and observed CoM motion.

The second aim is to combine the improved understanding of HSI obtained through the fulfilment of aim one, with a crowd-structure interaction model that addresses the limitations of the continuum crowd modelling technique. Discrete element agent-based crowd modelling will be utilised for this task. The aim is thus to develop a model capable of capturing the dynamic forcing effect of a pedestrian crowd. The model will include a virtual crowd in which each pedestrian is individually 'aware' of both their spatial environment and their dynamic relationship with the flexible bridge on which they walk. Based on this awareness each pedestrian should behave accordingly.

This model will be capable of simulating lateral bridge response under subcritical or 'every day' traffic conditions as well as the initiation of excessive lateral vibrations under critical conditions. The model will be used to further clarify the scale effects of HSI and the initiation of excessive lateral vibrations induced by pedestrian crowds.

Therefore the objectives associated with aim one; *To identify the nature of lateral HSI*, are:

- Design a test campaign suitable for the investigation of lateral HSI.
- Build a test rig which allows a subject to walk while experiencing lateral deck oscillations of varying amplitudes and frequencies. This will allow subject balance behaviour to be observed under varying conditions. The test rig should be capable of recording the lateral component of the subject's GRF.
- Use motion capture equipment to record the subject's whole body balance behaviour while walking on the laterally oscillating deck. This will allow body movements to be correlated with the recorded (lateral) GRF.
- Use inverse dynamic analysis to reproduce the lateral GRF from visual marker data. This will serve as a validation of the marker data and the body model (mass subdivision) employed in the analyses. This will also give greater insight into the contribution of different body masses to the GRF.
- Analyse the recorded data with the aim of identifying the features of body motion that give rise to the self-excited component of the GRF force.
- Carry out a comparative analysis between inverted pendulum simulated and observed CoM motion to test the active balance control hypothesis. This will allow

the suitability of the inverted pendulum model, for use in the final model (aim 2) to be determined.

Objectives associated with aim two; *development of the simulation tool discussed above* are:

- Investigate the potential of discrete element crowd modelling for use in bridge dynamic analysis. This will be achieved by developing an exploratory model that utilises a discretely defined crowd to determine the characteristics of the dynamic force applied to a single bridge mode.
- Expand the above model in such a manner that individual pedestrians within the crowd are characterised by a suitable biomechanical model dynamically coupled to the structure. This development will allow for the direct simulation of HSI, thereby utilising the improved understanding obtained from the analysis associated with aim one.
- Validate the final model against observations of the Clifton Suspension Bridge, reported in the literature.

The first modelling objective, investigation of agent-based crowd modelling as a means of characterising the dynamic force, will be addressed in the following chapter. The three limitations of hydrodynamic crowd modelling, listed above, will be discussed in more detail therein.

CHAPTER 5

Discrete Crowd - Structure interaction

Chapter Summary

A review of the literature has revealed the use of hydrodynamic or continuum crowd models applied to the simulation of crowd-induced bridge vibration. The purpose of the work presented in this chapter is to explore an alternative discrete crowd characterisation. What follows in this chapter can be considered an exploratory model that demonstrates that a discretely modelled crowd does indeed offer worthwhile advantages over existing continuum crowd models.

Section 5.1 first discusses the fundamental relationship between crowd density and velocity, underlining its significance in the context of human-induced vibration. Section 5.2 discusses the development and implementation of the discrete crowd-structure interaction model in detail. The final section in this chapter, 5.3, summarises the conclusions drawn from this modelling exercise.

5.1 The velocity-density relationship

An emergent phenomena is a crowd behaviour typically observable at a macro scale, i.e. it becomes apparent when one observes the crowd as a whole. It arises due to interactions between pedestrians within the crowd and thus does not result from the actions of any one pedestrian.

The velocity-density relationship for pedestrian traffic is a fundamental emergent crowd behaviour. Stated simply, the speed of pedestrians walking within a crowd reduces as the density of the crowd increases. As a pedestrian is constrained by neighbours, the free space around them is reduced. This forces the pedestrian to walk at a slower speed to avoid potential collisions. Furthermore the opportunity for overtaking slower moving pedestrians is reduced, thus a relatively small number of slow moving pedestrians can cause 'rolling blockages' reducing the speed of the whole crowd.

One of the most significant contributions to the study of pedestrian flow behaviour was made by John J. Fruin [67]. He determined a velocity-density relationship by analysing time lapse photography of pedestrians travelling along a city street. Fruin's data was obtained by observing relatively low density crowds ($<\approx 2$ ped/m^2) walking along a 3 m wide footpath. This data is an excellent benchmark against which to validate the emergent velocity-density relationship produced by the crowd model utilised in this study. This will be discussed further in subsection 5.2.8.

When considering the dynamic influence of a pedestrian crowd traversing a bridge, the spatial and temporal variation of crowd velocity and density is of particulary interest. In order to determine the structural response consistent with a particular traffic

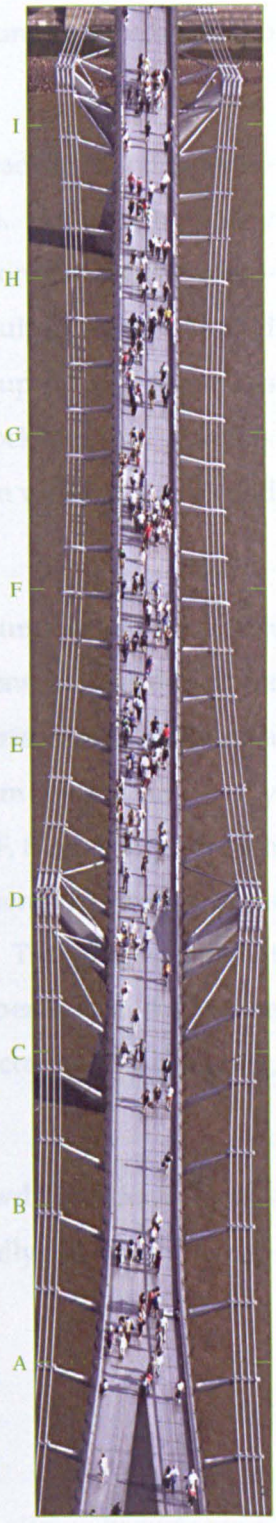

Figure 5.1: LMB.

loading, one must know how the crowd is distributed across the structure, i.e. the density distribution. Equally important is knowledge of the forcing frequency imposed by each walking pedestrian, directly related to walking speed. Furthermore one must know how this information varies with time if the evolving nature of the crowd is to be considered.

It is commonly assumed when modelling pedestrian dynamic loading that the pedestrians in the crowd are uniformly distributed across the bridge. For a high density loading event, this assumption is reasonable. However, when considering more typical everyday loading conditions this assumption is more difficult to satisfy. Crowd density distributions are rarely uniform in space or time. The 'supply' of pedestrians onto the bridge may vary, furthermore subgroups and rolling blockages may develop. All of these influences on crowd density have a knock-on effect on walking speeds and therefore the forcing frequencies imposed on the bridge.

Figure 5.1, shows an arial snapshot of pedestrians on the Millennium Bridge. The south span, between grids A and D has a noticeably lower crowd density than the centre span between grids D and I. Within the centre span, 142 pedestrians, occupy an area of approximately 576 m^2. This equates to en equivalent uniform pedestrian density of 0.25 ped/m^2. However locally, eg. between grid lines G and F, the density is much higher ($\approx$ 0.71 ped/m^2). Thus one can expect the forcing frequencies between grids G and F to be lower than those between C and D, for example. This single snapshot demonstrates the spatial variation in density. It must be remembered than during the course of any dynamic analysis, this density distribution will be continually changing, directly influencing the dynamic force imposed on the structure.

Based on the above reasoning and observations, modelling crowd behaviour directly within a dynamic analysis offers powerful advantages, principally, the ability to capture the dynamic influence of an evolving pedestrian crowd.

5.2 Modelling crowd-bridge dynamic interaction with a discretely defined crowd

This section presents a novel method of modelling crowd-bridge interaction using discrete element theory to model the pedestrian crowd. Discrete element theory, also known as agent-based modelling, is commonly used in the simulation of pedestrian movement, particularly in cases where building evacuation is critical or potentially problematic. Pedestrians are modelled as individual elements subject to global behavioural rules.

In this section a discrete element crowd model is coupled with a dynamic bridge model in a time-stepping framework. Feedback takes place between both models at each time-step. An additional pedestrian stimulus is introduced that is a function of bridge lateral dynamic behaviour. The pedestrians' relationship with the vibrating bridge as well as the pedestrians around them is thus simulated. The lateral response of the bridge is modelled as a damped SDoF oscillator. The excitation and mass enhancement of the dynamic system is determined as the sum of individual pedestrian contributions at each time-step.

Previous crowd-structure interaction modelling, reviewed in 2.4, has utilised a continuum hydrodynamic crowd model. The limitations inherent in the continuum approach have been identified in 4.1. Results are presented that demonstrate the ability of discrete element theory to address these limitations. Simulation results demonstrate the model's ability to consider low density traffic flows and ISV. The emergence of the crowd's velocity-density relationship is also demonstrated and validated against Fruin's observations.

5.2.1 Introduction

Based on their investigation of the LMB, Dallard et al. [2] proposed that pedestrians when influenced by lateral bridge motion, behave as negative dampers, producing a lateral driving force proportional to bridge velocity. Their model predicts the onset of lateral instability as the point at which pedestrian-induced negative damping over-

comes the structure's inherent damping. The model assumes the crowd is uniformly distributed on the bridge deck and all pedestrians contribute equally to the modal excitation.

In reality the pedestrian crowd may not be uniformly distributed, particularly when vibration becomes perceptible. Pedestrians may react by slowing down or stopping depending on their perceived level of bridge response [7]. Furthermore not all pedestrians will contribute equally to the modal excitation due to variability in pacing frequencies while those that stop walking have negligible dynamic force effect.

As already discussed, existing crowd-structure interaction models which utilise a continuum crowd model are limited in several respects by the nature of the crowd model. These limitations are again summarised below for convenience:

1. Continuity of crowd flow must be assumed.
2. Intersubject variability cannot be accommodated.
3. The velocity density relationship for the crowd must be 'hard-coded' into the simulation.

Nevertheless, this approach does allow the coupled evolution of crowd and bridge behaviour to be observed.

The aim of the work presented in this chapter is to address the limitations described above while maintaining the advantages of a time-evolving description of bridge response. By utilising a discrete element crowd model in which pedestrians are individually defined, pedestrian parameters and behavioural rules can be defined individually for each pedestrian. In doing so the problem of trying to model overall crowd behaviour is avoided. Instead it is allowed to emerge 'naturally' as the result of multiple pedestrian interactions. The discrete crowd model allows:

1. low density traffic to be simulated without any loss of accuracy resulting from the crowd characterisation.
2. individual pedestrian parameters such as walking velocity and acceleration perception thresholds to be defined, reflecting ISV among the crowd.

3. crowd behaviour to emerge in a pseudo-natural way eliminating the need to define a relationship between crowd velocity and density, governing macroscopic crowd behaviour.

In subsections 5.2.2 and 5.2.3 the crowd and bridge models are discussed. Interaction between both models is explained in subsection 5.2.4. The complete interaction model is demonstrated for the simple case of a single pedestrian crossing the bridge in 5.2.5. The probabilistic treatment of simulation data is discussed in 5.2.6. Subsection 5.2.7 explores the model's ability to simulate ISV. The emergence of a pseudo-natural velocity-density relationship is demonstrated in 5.2.8. The emergent velocity-density relationship is also validated through comparison with empirical data obtained by Fruin [67].

5.2.2 Crowd model

Discrete element crowd models are often utilised at design stage to allow designers to asses the efficiency and suitability of various building/structure layouts. In spaces where large crowds are expected, they can be crucial in reducing the likelihood of injury or death resulting from a crowd panic or flight response [68].

Crowd modelling and flow analysis has developed into a significant research area in its own right. Various modelling techniques ranging in complexity have been developed [69]. A mark of the maturity of the research in this field is the widespread adoption of crowd modelling techniques in engineering industry. Several large engineering consultancies now maintain their own in house modelling software [70–72]. Despite this, there is no evidence of their use as a means of simulating the nature or location of dynamic loads on a structure, as proposed herein.

In the selection of a specific discrete modelling technique for this work, the features of the pedestrian environment must be considered. Pedestrians travelling across a bridge, are typically concerned with reaching the opposite side with as little obstruction as possible. The environment can be described as linear. With the exception of navigating around their neighbours, pedestrians are not required to select from a range of alternative routes. Therefore algorithms involving the assessment and weighting of alternative travel routes (in order to select the most efficient) can be avoided in favour of

a physics based force model, described below.

A pedestrian walking within a crowd is subject to various stimuli. Helbing and Molnar [73] described these stimuli as social forces and proposed a crowd modelling approach based on Newtonian mechanics. Behavioural rules are modelled as forces. The resultant of all force vectors $\mathbf{F}_{\text{res}}^{(i)}$ (hereafter capital bold font indicates a vector quantity) acting on a pedestrian during an iteration i represents their total motivation. By defining a pedestrian mass m_p, an acceleration vector $\mathbf{A}_p^{(i)}$ is determined using Eq. (5.2.1). The pedestrian velocity $\mathbf{V}_p^{(i+1)}$ and location $\mathbf{X}_p^{(i+1)}$ vectors at the start of the next iteration $i+1$ are determined by solving equations of motion, (5.2.2) & (5.2.3). A simplified pseudocode implementation of the discrete element crowd model is depicted in algorithm 1.

$$\mathbf{A}_p^{(i)} = \frac{\mathbf{F}_{\text{res}}^{(i)}}{m_p} \tag{5.2.1}$$

$$\mathbf{V}_p^{(i+1)} = \mathbf{V}_p^{(i)} + \mathbf{A}_p^{(i)}\Delta t \tag{5.2.2}$$

$$\mathbf{X}_p^{(i+1)} = \mathbf{X}_p^{(i)} + \mathbf{V}_p^{(i)}\Delta t + \frac{1}{2}\mathbf{A}_p^{(i)}\Delta t^2 \tag{5.2.3}$$

The crowd model utilised in this work is adapted from that originally proposed by Langston et al. [74] which is itself based on the original social force model by Helbing et al. [75]. However a significant development upon Langston et al's model, made in this work, is the inclusion of pedestrian anisotropic perception, discussed below.

Herein, two dimensional pedestrian movement is modelled. Individual pedestrians are subject to the force $\mathbf{F}_{\text{res}}^{(i)}$ which is obtained as the sum of a motive force $\mathbf{F}_m^{(i)}$, inter-pedestrian force $\mathbf{F}_p^{(i)}$ and boundary force $\mathbf{F}_b^{(i)}$ acting on each pedestrian. A motive moment, M_m is applied to model rotational motion, simulating a pedestrian's tendency to orientate themselves towards the direction of travel.

Motive Force $\mathbf{F}_m$*:*

A pedestrian will try to maintain a predefined desired velocity $\mathbf{V}_d$. Their actual velocity $\mathbf{V}_p$ may deviate from this due to traffic or other obstructions. $\mathbf{F}_m$ represents their motivation to reach their desired velocity,

$$\mathbf{F}_m = m_p \frac{\mathbf{V}_d - \mathbf{V}_p}{t_r} \tag{5.2.4}$$

in which t_r is an empirical reaction time defined by Helbing et al. [75].

Algorithm 1: Simplified pseudocode implementation of the discrete element crowd model. Δ_t is the simulation time step, *population* is the number of pedestrians in the simulation and *max iteration* is the number of iteration in the simulation.

Data: simulation initial conditions

Result: Emergent crowd flow behaviour

for *i = 1:max iteration* **do**

  for *n = 1:population* **do**

    //Determine inter-pedestrian forces, boundary forces and motive forces

    $F_{p,x}(n) = ...$; //Resultant inter-ped x force experienced by ped n, see Eq. 5.2.5

    $F_{p,y}(n) = ...$; //Resultant inter-ped y force experienced by ped n, see Eq. 5.2.5

    $F_{b,x}(n) = ...$; //Resultant boundary x force experienced by ped n, see Eq. 5.2.6

    $F_{b,y}(n) = ...$; //Resultant boundary y force experienced by ped n, see Eq. 5.2.6

    $F_{m,x}(n) = ...$; //Resultant motive x force experienced by ped n, see Eq. 5.2.4

    $F_{m,y}(n) = ...$; //Resultant motive y force experienced by ped n, see Eq. 5.2.4

  end

  $Fx_{sum} = F_{p,x} + F_{b,x} + F_{m,x}$; //Matrix of resultant x forces experienced by each ped

  $Fy_{sum} = F_{p,y} + F_{b,y} + F_{m,y}$; //Matrix of resultant y forces experienced by each ped

  $acc_x = Fx_{sum}/mass$; //Matrix of ped accelerations in x-direction, see Eq. 5.2.1

  $acc_y = Fy_{sum}/mass$; //Matrix of ped accelerations in y-direction, see Eq. 5.2.1

  $vel_x = vel_x + acc_x * \Delta_t$; //Matrix of new velocities in the x-direction, see Eq. 5.2.2

  $vel_y = vel_y + acc_y * \Delta_t$; //Matrix of new velocities in the y-direction, see Eq. 5.2.2

  $pos_x = pos_x + vel_x * \Delta_t + 0.5 * acc_x * (\Delta_t^2)$; //Matrix of new x-positions, see Eq. 5.2.3

  $pos_y = pos_y + vel_y * \Delta_t + 0.5 * acc_y * (\Delta_t^2)$; //Matrix of new y-positions, see Eq. 5.2.3

end

Inter-Pedestrian Force $\mathbf{F}_p$*:*

This repulsive force acts directly between pedestrians and reflects the fact that pedestrians feel increasingly uncomfortable the closer they get to other unknown pedestrians,

$$|\mathbf{F}_p| = k_1 \, e^{(2\, r_{psy} - d)/k_2} \tag{5.2.5}$$

in which r_{psy} is a psychological radius representing a pedestrian's 'personal space', d is the distance between pedestrians' centres and k_1 and k_2 are a force and distance constants defined in [75] and detailed in table 5.1. When multiple neighbouring pedes-

trians are present, the total inter-pedestrian force experienced by the subject pedestrian is the vector sum of individual direct repulsion forces.

Boundary Force $\mathbf{F}_b$*:*

This force, Eq. (5.2.6), is similar to the inter-pedestrian force and acts directly between a pedestrian and the nearest point on the relevant obstacle. It models a pedestrian's desire to maintain a minimum distance from any obstacle, as to walk too close may result in accidental injury if there was an unexpected collision,

$$|\mathbf{F}_b| = k_1 \, \mathrm{e}^{(2\, r_{\mathrm{psy}} - d_w)/k_2} \tag{5.2.6}$$

in which d_w is the distance between the pedestrian and the nearest point on the obstacle. When multiple obstacles are considered, the total boundary force experienced by the subject pedestrian is the vector sum of individual direct repulsion forces.

Motive Moment M_m*:*

This moment (5.2.7) models a pedestrian's tendency to orientate themselves in the direction in which they are walking. The orientation of the motive force vector $\mathbf{F}_m$ acting on each pedestrian determines their desired orientation angle, θ_d. Thus as a pedestrian's aim point (and therefore $\mathbf{V}_d$) changes, a motive moment is induced such that they orientate themself towards their new aim point,

$$M_m = k_m \, (\theta_p - \theta_d) \tag{5.2.7}$$

in which k_m is the rotational stiffness and θ_p is an angle denoting the pedestrian's current orientation. The equations determining rotational motion are analogous to equations (5.2.1), (5.2.2) & (5.2.3). The mass moment of inertia (MMI) is calculated by multiplying the pedestrian mass by the square of the radius of their enclosing circle (corresponding to the MMI of a circular hoop). The value of k_m and thus the resulting rotational motion is tuned based on a subjective judgement of what appears reasonably realistic.

Anisotropic perception:

A pedestrian will typically be influenced more by pedestrians in front than those behind. This anisotropy of perception is introduced into the crowd model by using a reduction factor proposed by this author, f_{per}, Eq. (5.2.8). If the inter-pedestrian forces

acting on pedestrian p are considered, those arising from pedestrians to the rear are multiplied by the dimensionless reduction factor f_{per},

$$f_{\text{per}} = \frac{1}{1+e^{-k_p b}} \qquad (-\infty \leq b \leq 0) \tag{5.2.8}$$

where k_p is an empirically defined factor with units of m^{-1}. Pedestrians to the rear are defined as those behind a line projecting normal to the direction of travel of pedestrian p. b is the perpendicular distance of a neighbouring pedestrian behind this line, Fig. 5.2.

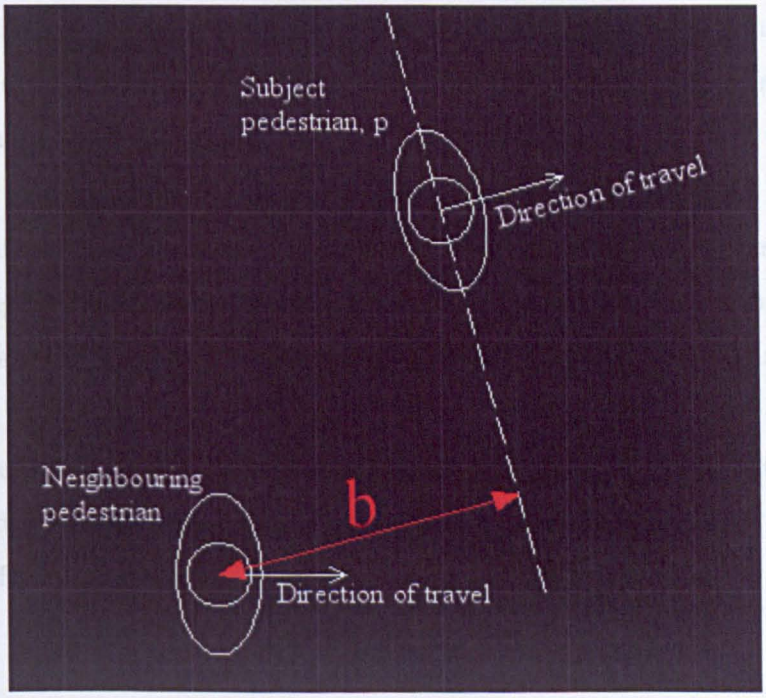

Figure 5.2: Pedestrian to the rear, defined as being behind a line projecting normal to the direction of travel of the subject pedestrian p. b is the perpendicular distance of a neighbouring pedestrian behind this line and defines the magnitude of perception reduction factor.

Eq. (5.2.8) implies that two pedestrians of equal distance to the rear of pedestrian p are equally perceptible even if one is 1 m to the right and the other is 10 m to the right of p. However in the relatively narrow confines of the bridge deck this is a reasonable approximation. Anisotropic perception differentiates a discrete crowd model from a more general discrete particle model and results in markedly different flow behaviour.

Input/Output:

The initial conditions on the crowd model are pedestrians' orientation angles, loca-

tion coordinates, desired velocity magnitudes and start times. Pedestrian orientation and location are randomly selected while desired walking velocities are normally distributed based on observations by Pachi and Ji [63]. To ensure pedestrians do not begin walking 'in-time' with each other, each pedestrian is assigned a start time, t_{start}. Start times are uniformly distributed in a 5 s window at the start of the simulation. The Matlab programming/computing environment is used to implement the simulation and all random parameters are determined using its pseudo random number generator.

At each iteration the crowd model outputs pedestrian orientation angle, location coordinates and realised walking velocity. The velocity magnitude is converted into a pacing frequency, f_{vert} using the empirical relationship (5.2.9) reported in [49]. This is based on a study by Bertram and Ruina [22], investigating constrained walking on a treadmill. By observing fixed velocity walking, test-subject's preferred (constrained) walking frequency was determined. Although this relationship results from observations lasting many seconds, it is used here to update the pedestrian walking frequency on a step-by-step basis. Any transient behaviour that may occur as a pedestrian changes from one walking frequency to another is ignored and it is assumed that changes in pedestrian velocity lead to instantaneous changes in walking frequency. This assumption is reasonable, considering the discrete step-like (rather than continuous) nature of walking.

$$f_{\text{vert}} = 0.35|\mathbf{V}_p|^3 - 1.59|\mathbf{V}_p|^2 + 2.93|\mathbf{V}_p| \tag{5.2.9}$$

The pedestrian-induced lateral force, F_p (discussed in section 5.2.4) is applied at half the pacing frequency, therefore the forcing frequency associated with each pedestrian $f_p = f_{\text{vert}}/2$.

5.2.3 Bridge model

The bridge modelled in this chapter has a span L, deck width W and a mass per unit length M. Only lateral bridge excitation is considered therefore the bridge is modelled as a simply supported (laterally) Euler-Bernoulli beam. Motion in the fundamental mode is described by the standard equation of motion for a SDoF system,

$$m_n\ddot{U}(t) + c_n\dot{U}(t) + k_nU(t) = F_n \tag{5.2.10}$$

in which m_n, c_n, k_n and F_n represent the modal mass, damping, stiffness and excitation respectively. $U(t)$ represents the system displacement while $\dot{U}(t)$ and $\ddot{U}(t)$ represent velocity and acceleration respectively. The equation of motion is solved using the piecewise exact method [76].

The contribution of N pedestrians to the modal mass of the system is considered at each iteration, Eq. (5.2.11), such that the presence of pedestrians reduces the fundamental frequency of oscillation ω_n, Eq. (5.2.12),

$$m_n = \int_0^L M(x_b)\,\phi_n(x_b)^2 \mathrm{d}x_b \quad + \quad \sum_{p=1}^{N} m_p\,\phi_n(x_p)^2 \tag{5.2.11}$$

$$\omega_n = \sqrt{\frac{k_n}{m_n}} \tag{5.2.12}$$

where $\phi_n(x_p)$ is the mode shape ordinate corresponding to the location of pedestrian p and x_b is the longitudinal bridge coordinate. Although the modal mass varies, the deviation from a half-sine mode shape for the fundamental mode due to the addition of pedestrian mass was found to be negligible. Therefore a half-sine mode shape is maintained.

The modal stiffness, k_n, is defined as,

$$k_n = \int_0^L k(x_b)\,\ddot{\phi}_n(x_b)^2\,\mathrm{d}x_b \tag{5.2.13}$$

in which $k(x_b)$ represents the flexural rigidity of the bridge in the lateral direction. A viscous damping coefficient, c_n, is assumed that is consistent with field observations from the literature.

The modal excitation F_n is defined as the sum of the force contributions from N pedestrians on the bridge,

$$F_n = \sum_{p=1}^{N} F_p\,\phi_n(x_p) \tag{5.2.14}$$

in which F_p is the pedestrian induced lateral footfall force and is further discussed below.

5.2.4 Crowd-bridge system interaction

The complete model proposed consists of two individual models, one for the crowd and another for the bridge dynamic behaviour. Rather than the crowd model directly generating the dynamic forcing effect of the crowd, it is utilised here as a behavioural model. It provides a description of individual pedestrian behaviour (positions, orientations and walking velocities) such that overall crowd behaviour emerges and its influence on the dynamic simulation is captured. In order to interpret and map these behaviours to the dynamic simulation, intermediate models are used. In this way the existing body of HSI research can be exploited.

The most notable consequence of separating the crowd and bridge models is that the acceleration of pedestrian mass, simulated within the crowd model through Eq. (5.2.1), does not result in the direct application of a GRF on the bridge. For these forces to be considered in a meaningful way, some form of biomechanical model would be required such that the GRFs are representative of a walking person. The inclusion of a suitable biomechanical model is considered in chapter 8.

The effect of lateral bridge acceleration on the crowd is first discussed followed by the effect of the crowd on the dynamic behaviour of the bridge. The coupled bridge-crowd system is henceforth referred to as the modelling framework. The two-way interaction is summarised graphically in Fig. 5.3.

Effect of bridge acceleration on pedestrians

Local bridge acceleration at each pedestrian's location is defined as,

$$a_l = \ddot{U}(t)\,\phi_n(x_p) \tag{5.2.15}$$

Peak acceleration values are extracted from a_l and used to construct the envelope of acceleration experienced by each pedestrian as they cross the bridge, a_{env}, Fig. 5.4. This envelope is compared against acceleration threshold values and individual pedestrian behaviour is altered accordingly in the crowd model.

ISV suggests that acceleration thresholds should have an associated level of variability. There is little guidance in the literature to suggest how thresholds should be dis-

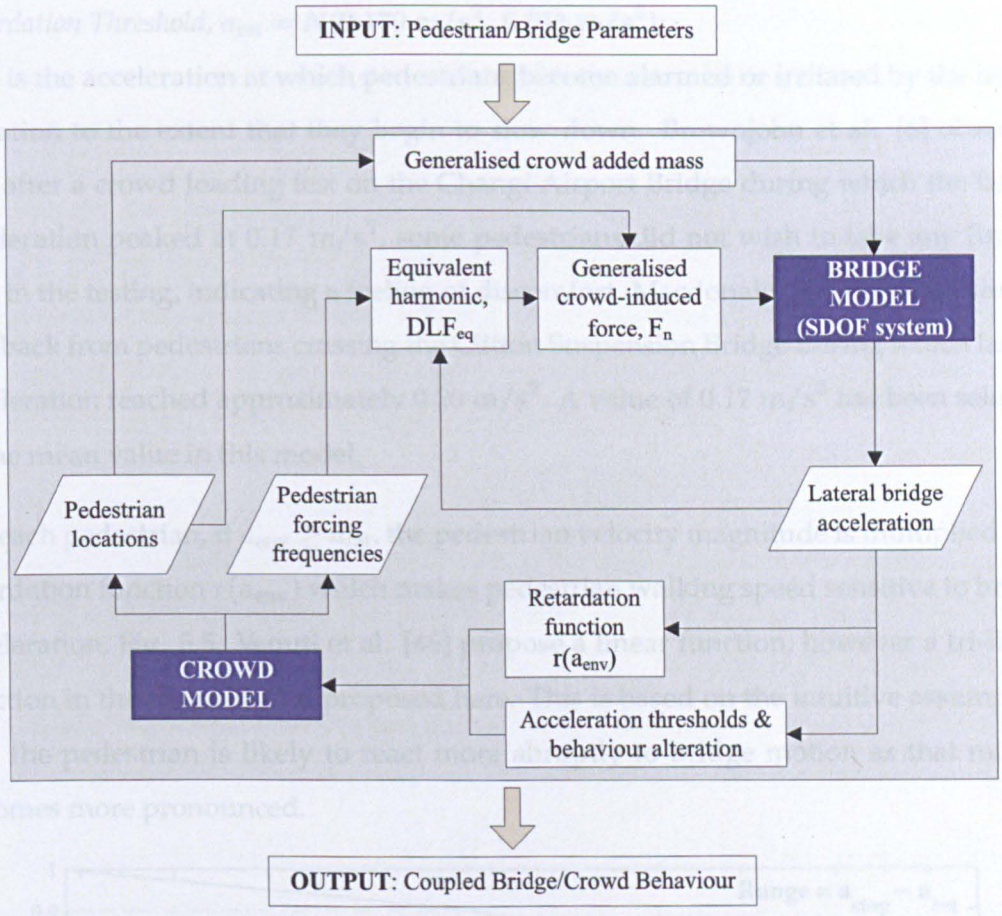

Figure 5.3: Interaction summary flowchart.

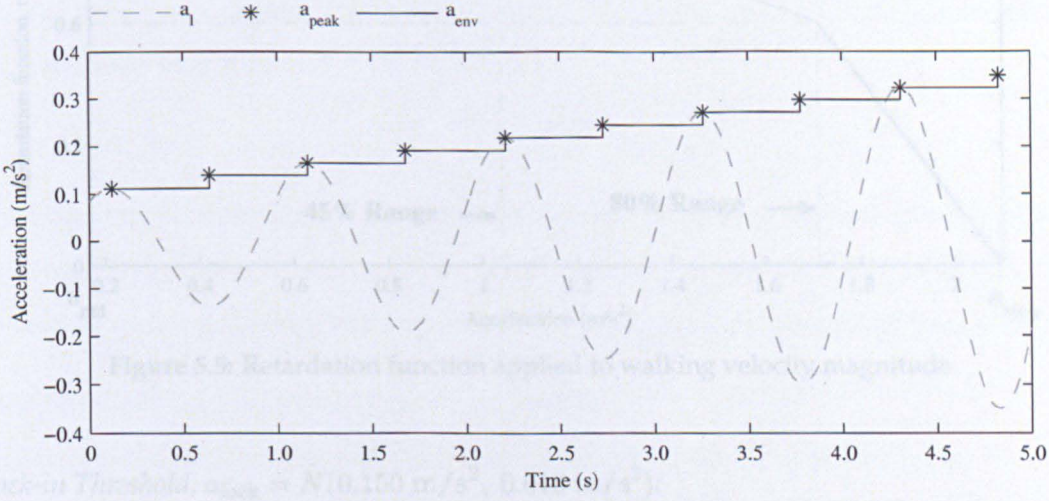

Figure 5.4: Stepped peak acceleration envelope a_{env}.

tributed, therefore for the purposes of demonstrating the capability of this model, thresholds are assumed to be normally distributed $N(\mu, \sigma)$ with a coefficient of variation of 6.7 %.

Retardation Threshold, $a_{\text{ret}} = N(0.170\ \text{m/s}^2,\ 0.011\ \text{m/s}^2)$:

This is the acceleration at which pedestrians become alarmed or irritated by the lateral vibration to the extent that they begin to slow down. Brownjohn et al. [6] observed that after a crowd loading test on the Changi Airport Bridge during which the lateral acceleration peaked at $0.17\ \text{m/s}^2$, some pedestrians did not wish to take any further part in the testing, indicating a feeling of discomfort. Macdonald [24], reported similar feedback from pedestrians crossing the Clifton Suspension Bridge during which lateral acceleration reached approximately $0.20\ \text{m/s}^2$. A value of $0.17\ \text{m/s}^2$ has been selected as the mean value in this model.

For each pedestrian, if $a_{\text{env}} \geq a_{\text{ret}}$, the pedestrian velocity magnitude is multiplied by a retardation function $r(a_{\text{env}})$ which makes pedestrian walking speed sensitive to bridge acceleration, Fig. 5.5. Venuti et al. [46] propose a linear function, however a tri-linear function in the range [0-1] is proposed here. This is based on the intuitive assumption that the pedestrian is likely to react more abruptly to bridge motion as that motion becomes more pronounced.

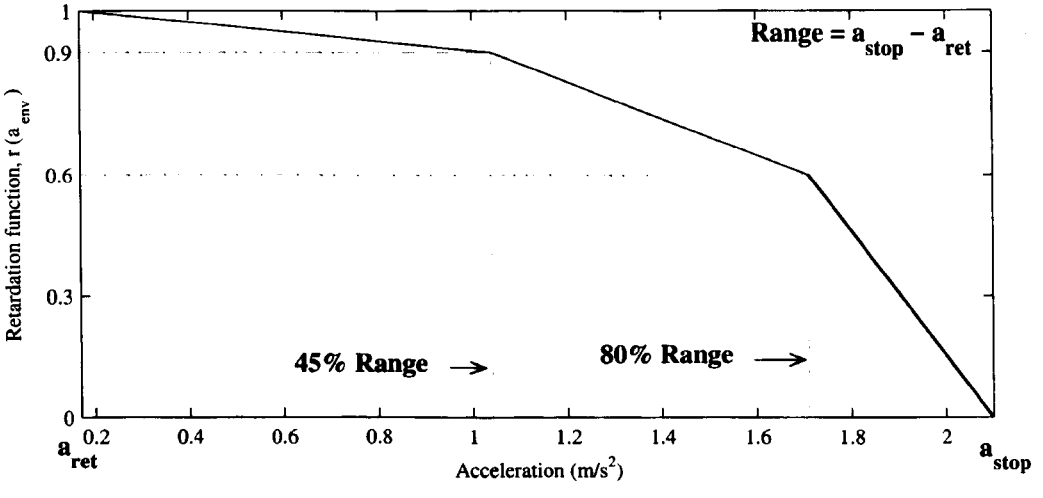

Figure 5.5: Retardation function applied to walking velocity magnitude.

Lock-in Threshold, $a_{\text{lock}} = N(0.150\ \text{m/s}^2,\ 0.010\ \text{m/s}^2)$:

The distinction is made here between pre-lock-in, HSI, demonstrated analytically by Macdonald [37] and experimentally by Ingólfsson [11], and human-structure synchronisation or lock-in observed on the Millennium Bridge. It is proposed here that lock-in is a phenomena which occurs under certain conditions *after* HSI has reached a well developed stage. The inclusion of HSI in this model is discussed below when the crowd

force is presented. Considering that the thrust of this chapter is to explore the capabilities of discrete element crowd modelling, HSI is more thoroughly dealt with in the following chapters.

According to the French Sétra guideline [27], at a threshold value of lateral acceleration found to be approximately 0.1 m/s^2 to 0.15 m/s^2, pedestrians are susceptible to lock-in. In tests examining walking behaviour on an oscillating platform, Rönnquist also reported that the pacing frequency tended to synchronise with the platform oscillation if it was within ± 10 % of the relevant modal frequency [7].

It is therefore assumed in this model that if a pedestrian's lateral forcing frequency f_p is within ± 10 % of the structure's natural frequency f_n, and if $a_{env} \geq a_{lock}$, f_p is altered to match f_n and phase synchronised with bridge velocity. Thus the pedestrian is 'locked-in' and adds energy to the dynamic system. The pedestrian will only resume their normal walking frequency and thereby drop out of lock-in, if the acceleration stop threshold is reached or the bridge acceleration subsides, below the lock-in threshold.

It is possible for the pedestrian to be locked-in to the bridge motion, walking with a defined frequency and also walk at a reducing speed. The pedestrian's walking velocity is still governed by the crowd model and subject to the retardation function described above. When we consider that walking speed $|\mathbf{V}_p|$ is the product of pacing frequency f_{vert} and step length l_p,

$$|\mathbf{V}_p| = f_{vert}\, l_p \tag{5.2.16}$$

it is apparent that step length must remain as a free variable to maintain the above relationship. Therefore is it assumed here that pedestrians reduce their step length in order to reduce walking speed while step frequency is locked-in to the bridge frequency.

Stop Threshold, $a_{stop} = N(2.100\ m/s^2,\ 0.140\ m/s^2)$*:*
Pedestrian-induced lateral excitation is a self-limiting behaviour [4], as the acceleration becomes too large, pedestrians must stop walking to maintain balance. Therefore when $a_{env} \geq a_{stop}$ for any pedestrian, they stop walking and remain stopped until the acceleration level reduces. The mean value of a_{stop} is based on experimental observations by Nakamura [4].

As $a_{env} \rightarrow a_{stop}$, the retardation function, $r(a_{env}) \rightarrow 0$. However to avoid meaninglessly

small walking velocities, as $r(a_{\text{env}}) \rightarrow 0$ a practical lower limit on walking velocity magnitude $v_{\text{lower}} = 0.1\ |\mathbf{V}_d|$ is imposed, thus

$$|\mathbf{V}_p| = \begin{cases} 0.1\ |\mathbf{V}_d| & \text{if } a_{\text{env}} < a_{\text{stop}} \cap |\mathbf{V}_p| \leq v_{\text{lower}} \\ 0 & \text{if } a_{\text{env}} \geq a_{\text{stop}} \end{cases} \tag{5.2.17}$$

After a pedestrian has stopped walking, they are assumed to remain stationary for a duration of time, t_{stop}, in order to allow conditions to improve before trying to continue walking.

Pedestrian(s) effect on the bridge response

Pedestrians influence the bridge by means of their added mass and applied stepping force, both of which are discussed below.

Crowd mass:

Ingólfsson et al. [11] demonstrated that the contribution of a walking pedestrian's mass is more complex than merely adding passively to the system modal mass. However in the frequency range under consideration ($\approx 0.8 - 1.25 \times$ base oscillation frequency), it was shown that walking pedestrians typically make a positive contribution to modal mass. It is difficult to capture the crowd mass effect without modelling HSI directly via some form of biomechanical model. Therefore in this model pedestrians are considered to contribute passively to the modal mass of the system as per Eq. (5.2.11), which is qualitatively in line with [11]. This allows any distribution dependent mass effects to emerge.

Crowd force:

The modal excitation as described by Eq. (5.2.14) is the sum of the contributions from N pedestrians on the bridge in which $\mathrm{F_p}$ is the pedestrian-induced lateral footfall force, individually determined for each pedestrian as,

$$F_p = G_p\ \mathrm{DLF_{eq}}\ \sin[2\pi\ f_p\ (t - t_{start})]\ \cos(\theta_p) \tag{5.2.18}$$

where G_p, f_p and θ_p are the static weight, forcing frequency and orientation angle (measured with respect to the longitudinal axis of the bridge) of pedestrian p. It should be remembered that the crowd-induced modal force results from the summation of these

force models (5.2.18), rather than the inertia effect of the pedestrian masses, m_p in the crowd model.

DLF_{eq}, Eq. (5.2.19) is the equivalent lateral dynamic load factor providing the magnitude of the lateral footfall force as a proportion of body weight, proposed by Rönnquist [7]. He recorded the resultant lateral force from 1087 foot-pair samples while individual subjects crossed a suspended platform. By noting that the footfall force is approximately periodic, it may be decomposed into a series of harmonic components. Rönnquist modelled the force produced during each 50 % of the gait cycle with a single equivalent harmonic possessing the same impulse energy as its multi-harmonic representation. The amplitude of the equivalent harmonic was empirically determined as a function of local platform acceleration a_l and the difference between the platform's natural frequency f_n and the lateral forcing frequency f_p, Eq. (5.2.19). This model's input parameters and its foundation on an experimental campaign justify its use here.

$$DLF_{eq} = 0.145 - 0.1 \exp\left[- \left(0.45 + 1.5 \exp\left[- \frac{1}{2} \left(\frac{f_p - f_n}{0.07} \right)^2 \right] \right) a_l^{1.35} \right] \qquad (5.2.19)$$

The resultant footfall force is thus applied in a step-by-step manner, with the single footstep force duration t_f determined by the lateral forcing frequency, $t_f = 1/2f_p$. The instantaneous lateral acceleration at the time and location of application of the footstep, $a_l(t, x_p)$ is used to determine the force magnitude. In order to determine a discrete value of $a_l(t, x_p)$, applicable to each half sinusoid representing a single footfall force, an instantaneous transfer from one foot to the other is assumed. It is through the implementation of Eq. (5.2.19) that HSI is considered in the modelling framework.

Pedestrian avoidance behaviours result in deviations in direction of travel. Only force components perpendicular to the bridge axis perform work on the lateral dynamic system. Therefore pedestrian orientation (determined from the crowd model) is included in Eq. (5.2.18). This suggests the inclusion of additional force components; the anterior-posterior (longitudinal) force component as well as impulse forces resulting from changes in pedestrian walking velocity. The anterior-posterior force transitions from positive to negative over the duration of a footstep and typically produces a symmetrical force-time history. It is therefore a dynamic force at twice the frequency of the lateral component. It is de-tuned from the frequency of interest and of little significance. Forces resulting from changes in velocity are omitted because they are analogous

to impulses and have little dynamic effect against a dominant background of periodic lateral forces.

The time-step for the modelling framework is governed by the crowd model. Simulations were carried out with varying time-steps increasing from 0.002 s to 0.05 s. The variation in pedestrian locations at the end of each simulation was observed. A time-step of 0.01 s provided a maximum deviation of less than 90 mm, after travelling 50 m. Balancing the need for accuracy and computational efficiency, 0.01 s was selected as a suitable time-step.

5.2.5 Single pedestrian interaction simulations

The parameters selected for the crowd model and generic bridge model are summarised in table 5.1.

Table 5.1: Summary of simulation parameters.

Parameter	Value
m_p	80 kg
Δt_{crowd}	0.01 s
t_r	0.5 s
t_{stop}	2.0 s
r_{psy}	0.35 m
k_1	2000 N
k_2	0.08 m
k_m	5000 N m/rad
k_p	6
L	100 m
W	4 m
M	2000 kg/m
f_n	0.80 Hz
ζ	0.5 %
l_p	0.75 m

In order to clearly demonstrate the interactions within the model, interaction between

the bridge and a single pedestrian is first presented. Three cases are discussed;

1. A single pedestrian crossing the bridge; the lateral acceleration is imperceptible (below the retardation threshold) at all times. Interaction between the pedestrian and bridge is via the response dependent GRF magnitude, given by Eq. (5.2.19).
2. A single pedestrian crossing when lateral acceleration is perceptible (above the retardation threshold).
3. A pedestrian crossing when lock-in is triggered.

The lateral acceleration thresholds in these three case studies are artificially reduced to $a_{\text{ret}} = 2 \times 10^{-3}$ m/s^2, $a_{\text{stop}} = 15 \times 10^{-3}$ m/s^2 and $a_{\text{lock}} = 1.5 \times 10^{-3}$ m/s^2 in order to generate the desired behaviour for demonstration purposes.

Case 1

The pedestrian desired velocity magnitude is $|\mathbf{V}_d| = 1.3$ m/s resulting in a lateral pacing frequency of 0.95 Hz. The peak acceleration envelope a_{env} does not exceed the retardation threshold and therefore bridge motion does not influence the pedestrian's walking velocity, Fig. 5.6. The pedestrian is not obstructed by traffic therefore the realised velocity magnitude $|\mathbf{V}_p|$ equals the desired velocity magnitude $|\mathbf{V}_d|$.

Case 2

In this case $|\mathbf{V}_d| = 1.15$ m/s, yielding a lateral pacing frequency of 0.9 Hz. The simulation proceeds similarly to Case 1, however at $t = 46$ s, a_{env} exceeds the retardation threshold a_{ret}. The pedestrian begins to slow down due to the retardation function $r(a_{env})$, with an associated drop in lateral forcing frequency f_p. As f_p approaches f_n, the vibration amplitude felt by the pedestrian increases, as seen by the sharp rise in a_{env} at $50 \text{ s} \leq t \leq 58$ s, Fig. 5.7.

As the pedestrian approaches the mid-span at approximately $60 \text{ s} \leq t \leq 90$ s, a_{env} enters an oscillatory pattern. As the pedestrian slows down under the influence of $r(a_{env})$, f_p moves away from f_n and excitation amplitude is reduced, however this has the effect of reducing $r(a_{env})$, allowing the pedestrian to speed up, bringing f_p closer to

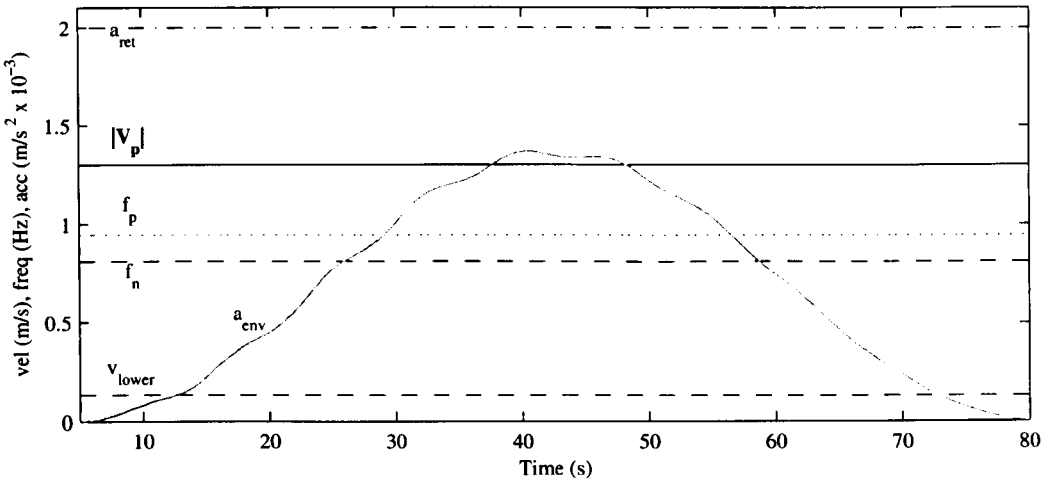

Figure 5.6: Envelope of peak acceleration experienced by pedestrian, a_{env} and associated retardation threshold, a_{ret}, realised pedestrian walking velocity, $|V_p|$ and lower velocity cut-off limit, v_{lower}, lateral forcing frequency, f_p and bridge modal frequency, f_n, Case 1.

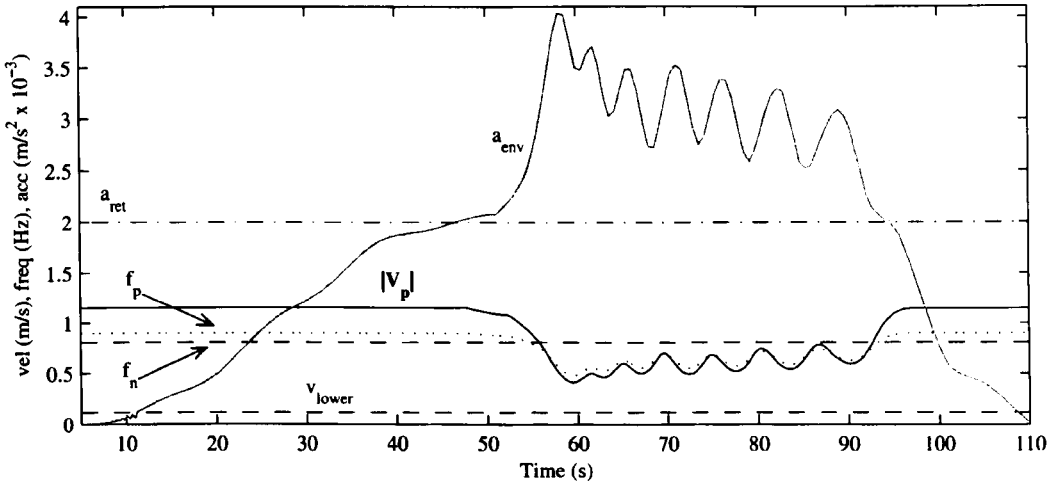

Figure 5.7: Envelope of peak acceleration experienced by pedestrian, a_{env} and associated retardation threshold, a_{ret}, realised pedestrian walking velocity, $|V_p|$ and lower velocity cut-off limit, v_{lower}, lateral pacing frequency, f_p and bridge modal frequency, f_n, Case 2.

resonance with the bridge once more. The pedestrian is periodically slowing down and speeding up while experiencing the undulating vibration profile. This cycle continues until the pedestrian moves away from the location of excessive vibration amplitude.

When a_{env} falls below a_{ret} the pedestrian behaviour resumes its 'normal' pattern. It is noted that even after accounting for the difference in $|V_d|$ between Case 1 and 2, the

pedestrian crossing takes about 18 % longer in Case 2 due to the fluctuations in walking velocity $|\mathbf{V}_p|$.

Case 3

In this case $|\mathbf{V}_d| = 1.0$ m/s, therefore $f_p = 0.845$ Hz. At this frequency the pedestrian is susceptible to lock-in ($0.9f_n \leq f_p \leq 1.1f_n$) if a_{env} exceeds a_{lock}, Fig. 5.8. At $t = 24$ s, $a_{env} > a_{lock}$ and the pedestrian locks in to the bridge vibration. f_p is altered to match f_n and phase synchronised with bridge velocity for subsequent footsteps. This is seen in Fig. 5.9 at $t = 25$ s, F_p is temporarily (≈ 0.25 s) reduced to zero to allow the footfall force to phase synchronise with the local bridge velocity, $v_l = \dot{x}(t)\,\phi(x_p)$. It should be noted that although the footfall force is temporarily reduced to zero, the pedestrian walking velocity is not. Due to the very short time required to achieve phase synchronisation it is more realistic to allow the pedestrian to continue moving rather than imposing a 'hard stop'. This can be phenomenologically explained as a pedestrian continuing their forward motion while momentarily hesitating before placing their foot in time with the bridge. After lock-in is achieved the slope of a_{env} increases as the pedestrian-induced force is now synchronised with the structure.

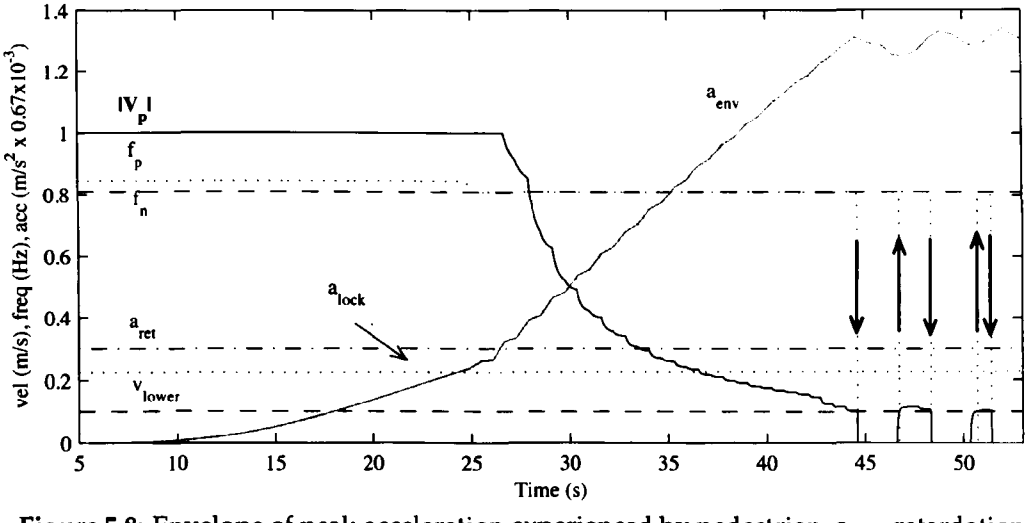

Figure 5.8: Envelope of peak acceleration experienced by pedestrian, a_{env}, retardation threshold, a_{ret} and lock-in threshold, a_{lock}, realised pedestrian walking velocity, $|\mathbf{V}_p|$ and lower velocity cut-off limit, v_{lower}, lateral pacing frequency, f_p and bridge modal frequency, f_n, Case 3.

When a_{env} exceeds a_{ret} the pedestrian walking velocity reduces due to $r(a_{env})$, how-

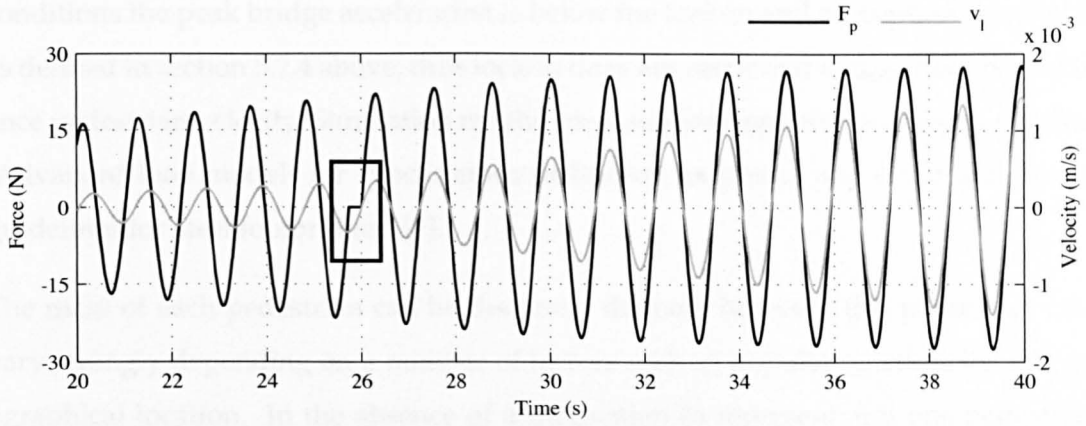

Figure 5.9: Generalised pedestrian-induced lateral force F_p & local velocity v_l.

ever because the pacing frequency is locked into the modal frequency, it is assumed that step length is reducing in line with the velocity, Eq. (5.2.16). The pedestrian velocity $|\mathbf{V}_p|$ continues to reduce until v_{lower} is reached at approximately $t = 45$ s. $|\mathbf{V}_p|$ is now considered to be unrealistically small and it is assumed the pedestrian will stop walking and remain stopped for a period of time, t_{stop}. After t_{stop} has elapsed $|\mathbf{V}_p|$ increases, however the pedestrian does not actually move forward and begin generating a stepping force until $|\mathbf{V}_p|$ exceeds v_{lower} (see Eq. (5.2.17)). It is assumed that if the pedestrian stopped while locked-in, when they recommence walking, if the acceleration level is still in excess of the lock-in threshold $a_{env} \geq a_{lock}$, their walking behaviour will automatically tune into the bridge, thus $f_p = f_n$.

After the pedestrian has locked-in a pattern of behaviour is entered similar to Case 2. While the pedestrian is stopped, energy input into the system is zero and response level reduces, thus $r(a_{env})$ is reduced and the pedestrian begins walking again. Once walking/force input has resumed vibration levels increase and the pedestrian is forced to stop walking once more. The pattern continues until the pedestrian has moved away from the zone of excess vibration amplitude.

5.2.6 Low density traffic

The three case studies above have demonstrated pedestrian-structure interaction for a single pedestrian. This is now expanded to consider a low-density crowd crossing the bridge, thus the effect of pedestrian interaction is introduced. Under these traffic

conditions the peak bridge acceleration is below the lock-in and perception thresholds as defined in section 5.2.4 above, thus lock-in does not occur and $r(a_{\text{env}})$ does not influence pedestrian velocity. Simulation results are compared against the design guideline 'Advanced load models for synchronous pedestrian excitation and optimised design guidelines for steel footbridges' [9].

The mass of each pedestrian can be discretely defined, however this parameter may vary strongly depending on a number of factors such as population ethnicity and geographical location. In the absence of a motivation to represent any one pedestrian group, all pedestrians are assumed to have a mass $m_p = 80$ kg.

Pedestrian desired velocities $|\mathbf{V}_{\text{d}}|$ are drawn from a normal distribution $N(\mu, \sigma) = N(1.3 \text{ m/s}, 0.125 \text{ m/s})$ [63]. Simulations involve one-way flow of traffic across the bridge, initial pedestrian position coordinates are drawn from a uniform distribution confined to an area to one side of the bridge. A random distribution of step phases is ensured by the uniform distribution of start times. Entry times onto the bridge are a function of initial position coordinates, desired velocity and start time, therefore bridge entry time is a random variable. The crowd model is used to simulate pedestrian behaviour while pedestrians are both on and off the bridge, thus after the initial randomness has been determined from the distributions above, the flow rate of pedestrians is governed by the crowd model.

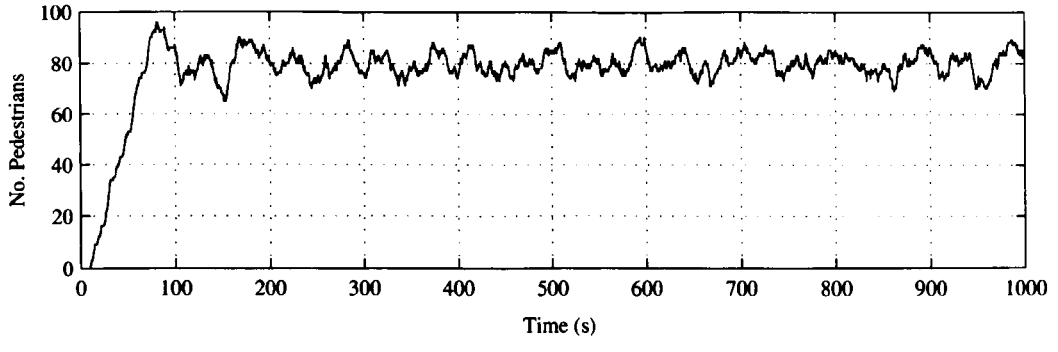

Figure 5.10: Number of pedestrians present on the bridge throughout one simulation.

The number of pedestrians present on the bridge is shown in Fig. 5.10. For $0 \ s \leq t \leq 80$ s, pedestrians are populating the bridge, thereafter the occupancy fluctuates about a mean level of 80 due to non-coincident pedestrian entries and exits from the bridge. 80 pedestrians equate to an equivalent uniform density of 0.2 ped/m^2, however

the actual distribution at $t = 100$ s, Fig. 5.11, reveals the non-uniform nature of the distribution with areas of high traffic density punctuated by empty areas of bridge deck. The assumption of continuity of flow, required by a hydrodynamic crowd model would appear difficult to satisfy in this case.

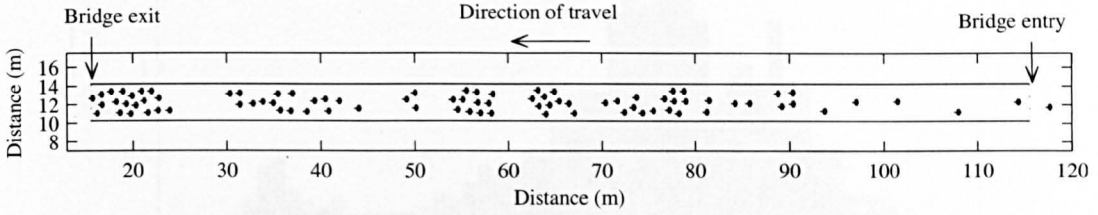

Figure 5.11: Pedestrian distribution across the bridge at $t = 100$ s, flow from right to left.

The lateral acceleration at mid-span is shown in Fig. 5.12 for the time period corresponding to approximately stable occupancy. Pacing frequencies are normally distributed $N(1.9 \text{ Hz}, 0.18 \text{ Hz})$, resulting in a distribution of lateral forcing frequencies of $N(0.95 \text{ Hz}, 0.09 \text{ Hz})$, commonly observed for footbridge traffic [61–63, 77]. The peak acceleration achieved during the period of observation is 0.023 m/s^2.

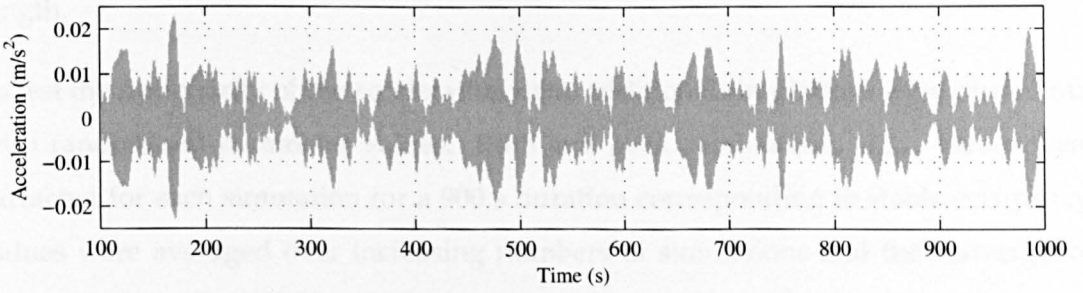

Figure 5.12: Lateral acceleration at mid-span.

Figure 5.13 reveals the frequency content of the lateral acceleration signal. The majority of the spectrum occupies a bandwidth of 0.85 Hz - 1.0 Hz, representing the distribution of lateral forcing frequencies. A smaller peak is visible at 0.79 Hz, corresponding to the bridge natural frequency after the addition of pedestrian mass.

Probabilistic analysis

To draw further conclusions from the simulation data, it must be determined how representative one simulation is of the bridge's overall vibration behaviour under these loading conditions. If the simulation data can be shown to be approximately station-

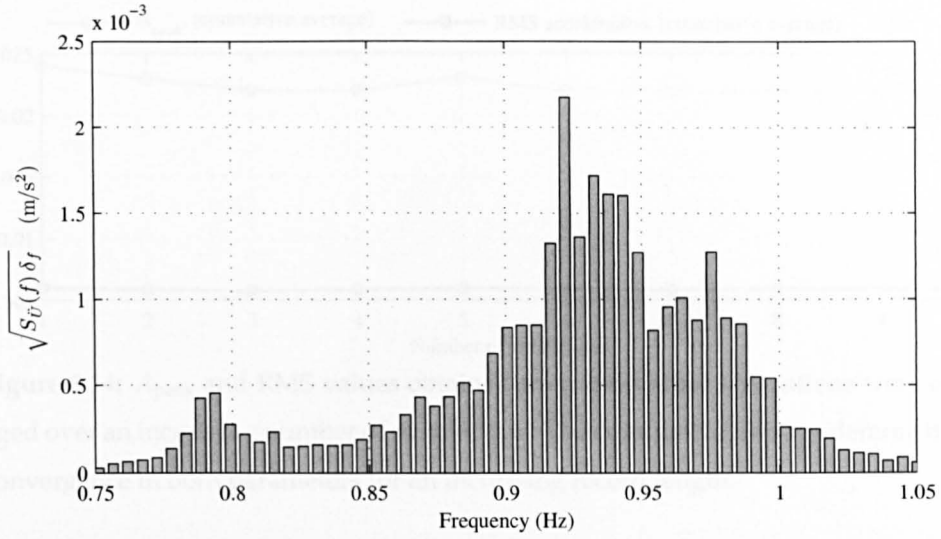

Figure 5.13: The frequency composition of lateral acceleration at mid-span. Bar plots showing the RMS value of frequency contributions over fixed bandwidths. The bandwidths of vertical bars are determined by the frequency resolution ($\delta_f = 0.005$ Hz) of the underlying single sided power spectral density, $\hat{S}_{\ddot{U}}(f)$.

ary, i.e. if its statistical parameters are shown to be time-invariant, bridge behaviour can be considered from a probabilistic point of view based on a relatively short record length.

To test the stationarity of the acceleration data, additional simulations were carried out with randomised parameter values. RMS and peak acceleration, A_{peak} values were extracted for each simulation for a 900 s duration corresponding to stable occupancy. Values were averaged over increasing numbers of simulations and the convergence observed, Fig. 5.14. RMS acceleration converges to 0.006 m/s^2 (CoV = 6 %) and A_{peak} converges to 0.022 m/s^2 (CoV = 9 %). Therefore increasing simulation length does not significantly alter RMS or A_{peak} for the process, these values are thus considered to be the characteristic or 'benchmark' values for the process (under these loading conditions). The low dispersion of individual values about the process RMS and A_{peak} supports the assumption that the resulting acceleration data is representative of an approximately stationary process.

In an alternative analysis, four ensemble RMS values measured *across* 23 records also show very good agreement with those measured *along* individual time-histories. As a result the process can be considered ergodic and therefore stationary [78]. Therefore a relatively short acceleration record length of 4500 s was analysed to determine the

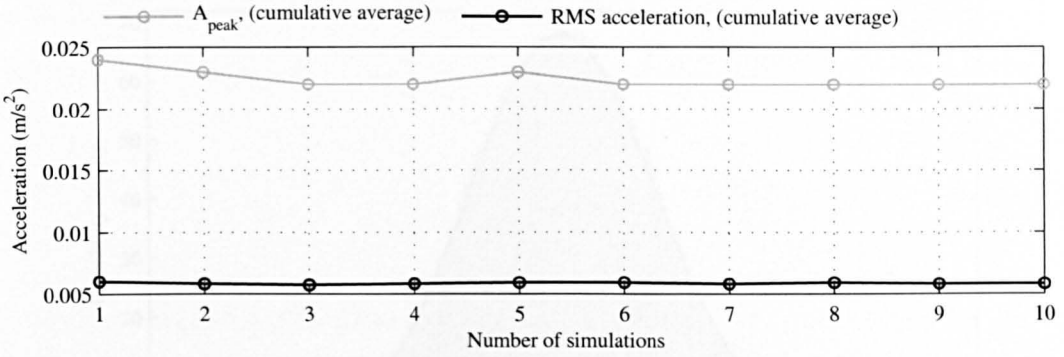

Figure 5.14: A_{peak} and RMS values obtained from individual simulations were averaged over an increasing number of simulations. The cumulative average demonstrates convergence in both parameters for an increasing record length.

probabilistic characteristics.

Acceleration values were sampled at 100 Hz and shown to follow a normal distribution, Fig. 5.15. A Pearson's chi-squared test revealed a fit significance level of 99 %. The distribution of peaks was investigated and shown to be well approximated by a Rayleigh distribution. A goodness of fit test applied to the full range of acceleration peaks results in a significance level < 5 %. However, this is primarily due to the first two data bins, and is most likely a result of relatively few data points being considered in the analysis. Repeating the test on peaks in the range of 0.5×10^{-3} m/s^2 to 18.1×10^{-3} m/s^2, highlighted in Fig. 5.16, increases the significance level beyond the 5 % threshold.

Having determined that the acceleration data is representative of an approximately stationary, ergodic, Gaussian process and noting it is also a narrow-band process, standard probabilistic methods can be employed to determine the likelihood of exceeding any given acceleration limit. It is this statistical processing of raw simulation data that transforms model output into a useable performance measure.

Consider a series of η peak acceleration values each of which is an independent random sample from a distribution with cumulative distribution function (CDF), $F_x(x)$ and probability density function (pdf), $f_x(x)$. The magnitude of the i^{th} sample is x_i and the maximum value of η samples is Y_η,

$$Y_\eta = \max\{x_1, x_2 ... x_\eta\} \tag{5.2.20}$$

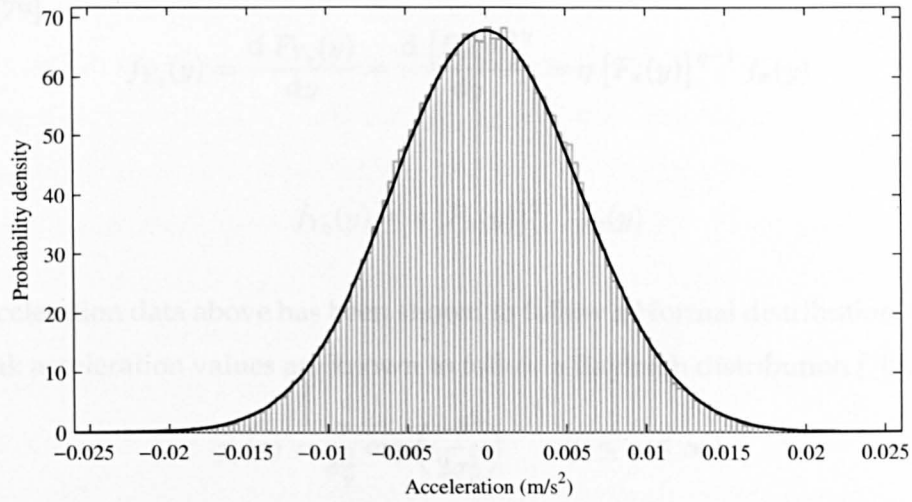

Figure 5.15: Acceleration data was sampled at 100 Hz. The distribution of acceleration values was found to follow a normal distribution with a significance level of 99 %, obtained from a Pearson's chi-squared test.

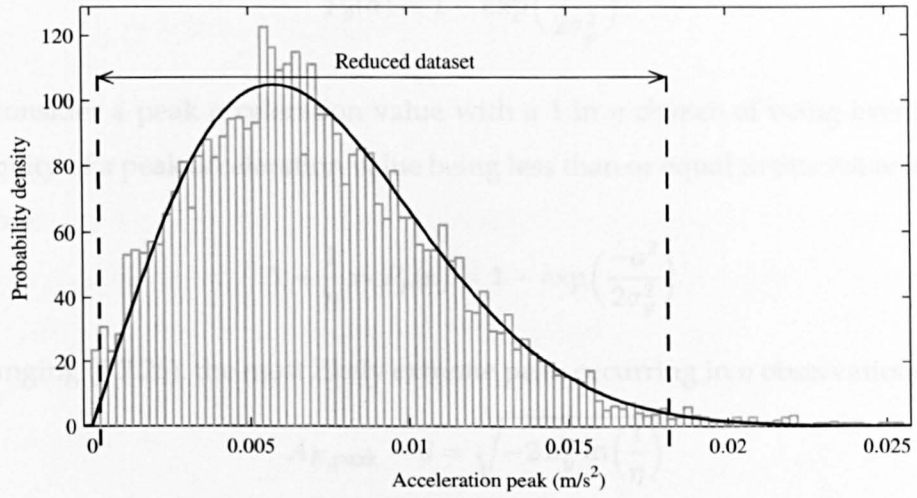

Figure 5.16: The distribution of peak acceleration values was found to follow a Rayleigh distribution. The significance of the full dataset is less than 5 %. However the reduced dataset has a significance greater than 5 %. Significance testing used a Pearson's chi-squared test.

$F_{Y\eta}(y)$ denotes the *extreme value cumulative distribution function* of Y_η [79] and by definition:

$$F_{Y\eta}(y) = \left[F_x(y)\right]^\eta \tag{5.2.21}$$

By differentiating (5.2.21) we obtain the *extreme value probability density function*, $f_{Y_\eta}(y)$

for Y_η [79]:

$$f_{Y_\eta}(y) = \frac{\mathrm{d}\, F_{Y_\eta}(y)}{\mathrm{d}y} = \frac{\mathrm{d}\left[F_x(y)\right]^\eta}{\mathrm{d}y} = \eta\left[F_x(y)\right]^{\eta-1} f_x(y) \tag{5.2.22}$$

$$f_{Y_\eta}(y) = \eta\left[F_x(y)\right]^{\eta-1} f_x(y) \tag{5.2.23}$$

The acceleration data above has been shown to follow a Normal distribution, therefore the peak acceleration values are known to follow a Rayleigh distribution [78], $p_p(a)$:

$$p_p(a) = \frac{a}{\sigma_y^2}\exp\left(\frac{-a^2}{2\sigma_y^2}\right) \qquad (0 \le a \le \infty) \tag{5.2.24}$$

where σ_y is the standard deviation of the underlying Normal distribution. The CDF of the Rayleigh distribution is [80]:

$$P_p(a) = 1 - \exp\left(\frac{-a^2}{2\sigma_y^2}\right) \tag{5.2.25}$$

Now consider a peak acceleration value with a 1 in η chance of being exceeded, the probability of a peak acceleration value being less than or equal to this value is $1 - 1/\eta$, therefore:

$$1 - \frac{1}{\eta} = P_p(a) = 1 - \exp\left(\frac{-a^2}{2\sigma_y^2}\right) \tag{5.2.26}$$

Rearranging (5.2.26), the most likely extreme peak occurring in η observations is:

$$A_{E,\text{peak}} = a = \sqrt{-2\,\sigma_y^2 \ln\left(\frac{1}{\eta}\right)} \tag{5.2.27}$$

To obtain the peak acceleration value from η observations with a 5 % chance of being exceeded:

$$P_p(a) = 0.95 = \left[1 - \exp\left(\frac{-a^2}{2\sigma_y^2}\right)\right]^\eta \tag{5.2.28}$$

$$A_{E,95} = a = \sqrt{-2\,\sigma_y^2 \ln\left(1 - 0.95^{(1/\eta)}\right)} \tag{5.2.29}$$

By substituting (5.2.24) and (5.2.25) into (5.2.23), we obtain the extreme value probability distribution function of $A_{E,\text{peak}}$:

$$fn(A_{E,\text{peak}}) = \eta\left[1 - \exp\left(\frac{-{A_{E,\text{peak}}}^2}{2\sigma_y^2}\right)\right]^{\eta-1}\left[\frac{A_{E,\text{peak}}}{\sigma_y^2}\exp\left(\frac{-{A_{E,\text{peak}}}^2}{2\sigma_y^2}\right)\right] \tag{5.2.30}$$

To illustrate the practical value of this post processing approach, a hypothetical design situation is now considered. Assume the traffic conditions simulated above are representative of peak traffic on a particular bridge and that these conditions prevail for a given period of time, return period T_r equal to 2 hours. This return period may correspond to peak morning/evening usage periods. The most likely peak acceleration value or extreme peak $A_{E,\text{peak}}$ occurring during this return period can be estimated, Eq. (5.2.27). The observed peak acceleration may be more or less than $A_{E,\text{peak}}$, this uncertainty is estimated by the extreme value probability distribution, $fn(A_{E,\text{peak}})$, Eq. (5.2.30). Assuming the highest oscillation frequency, $f_m \approx 1.0$ Hz, during a return period, $T_r = 7200$ s, approximately $\eta = f_m \times T_r$ positive acceleration peaks will be observed. The most likely extreme peak in this return period, $A_{E,\text{peak}}$ is equal to 0.025 m/s^2, increasing only marginally as the return period increases. Of more significance is the peak occurring during this time with a 5 % chance of exceedance $A_{E,95}$, obtained by Eq. (5.2.29) as 0.029 m/s^2.

The process outlined above represents a novel approach to the serviceability design of footbridges in which the estimated traffic profile is considered and discrete loading events of fixed duration (return period) identified. By combining stationary simulation data with an estimate of daily traffic conditions the probability of exceeding any given acceleration value can be determined. Considering the stochastic nature of pedestrian loading this probabilistic treatment seems more appropriate than reporting a single value estimate.

A comparative analysis was carried out in accordance with a recently published design guideline [9]. This guideline proposes N randomly walking pedestrians uniformly distributed over the bridge may be replaced by an equivalent number n_{eq}, all walking in phase at the same frequency as the vibrating mode of interest. Their dynamic effect is represented by the uniformly distributed pulsating force $p(t)$,

$$p(t) = G_f \cos(2\pi\, f_n\, t)\, n_{\text{eq}}\, \psi \tag{5.2.31}$$

in which $G_f = 35$ N and is the magnitude of the lateral component of the footfall force. ψ is a reduction factor applied when the forcing frequency is sufficiently removed from the modal frequency of interest, f_n. The average simulated traffic density of 0.2 per/m^2 corresponds to traffic class 2 which is characterised as 'weak traffic' in which over-

taking is possible and pedestrians can achieve their desired walking velocity. Under these traffic conditions, the equivalent number of frequency and phase synchronised pedestrians is given by,

$$n_{\text{eq}} = 10.8\sqrt{\zeta N} = 6.83 \text{ pedestrians} \tag{5.2.32}$$

where N is the number of pedestrians actually on the bridge, walking with normally distributed pacing frequencies and ζ is the damping ratio. When this force is transferred to modal coordinates the maximum modal acceleration a_{max} is obtained by

$$a_{\text{max}} = \frac{F_n}{m_n\, 2\, \zeta} \tag{5.2.33}$$

in which F_n and m_n are the modal excitation and mass respectively. Application of this load model yields a peak response estimate of 0.152 m/s^2, significantly in excess of both $A_{E,\text{peak}}$ and $A_{E,95}$ determined above.

To highlight the effect of reducing the mean pacing frequency to a less likely value, further simulations were carried out with mean lateral forcing frequencies, $f_{l,\mu}$, of 0.90 Hz and 0.85 Hz. The corresponding extreme value probability distributions are shown in figure 5.17. For $f_{l,\mu} = 0.90$ Hz, $A_{E,\text{peak}} = 0.047$ m/s^2 and $A_{E,95} = 0.055$ m/s^2. For $f_{l,\mu} = 0.85$ Hz, $A_{E,\text{peak}} = 0.155$ m/s^2 and $A_{E,95} = 0.179$ m/s^2. This analysis highlights the sensitivity of lateral acceleration to mean pacing frequency, which itself depends on traffic conditions.

Figure 5.17 shows that peak acceleration predicted using the modelling framework presented herein is roughly in agreement with that proposed in [9] for a mean forcing frequency close to the modal frequency. However considering a mean lateral forcing frequency of 0.95 Hz is more likely than 0.85 Hz in normal uncongested traffic, this case study suggests the model proposed in [9] becomes more conservative as the mean pacing frequency deviates from the modal frequency of interest. It is noted that the model proposed in [9] does not accept mean pacing frequency as an input parameter.

The simulation data above demonstrate that the discrete crowd model utilised in this work allow the dynamic effect of both individual pedestrians and low density traffic to be simulated, thus the assumption of continuity of flow and any potential inaccuracies associated are avoided.

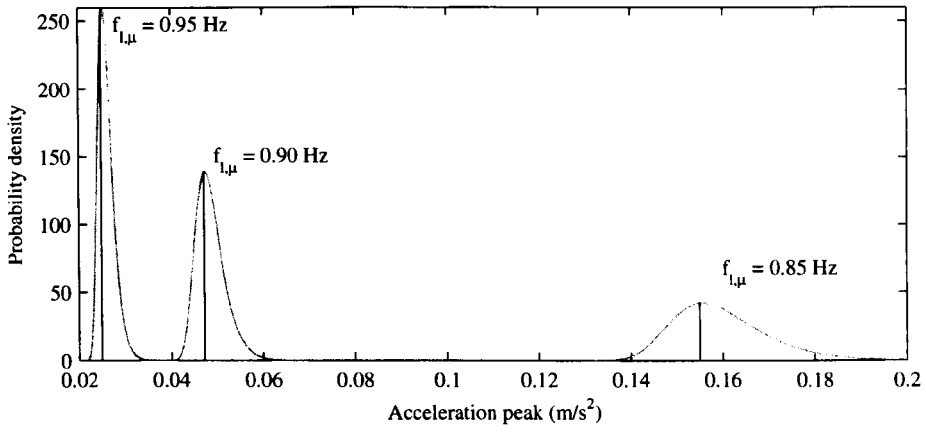

Figure 5.17: Extreme value probability distributions for three simulations with different mean crowd forcing frequencies, $f_{l,\mu}$.

5.2.7 Inter-subject variability

One of the main characteristics of pedestrian-induced loading is the difference in characteristics between individuals, termed ISV. Provided information regarding the statistical distribution of parameters is available, the discrete crowd model utilised herein allows ISV to be modelled. The effect of ISV is now examined by comparing simulations in which all pedestrians are assigned the same parameter values with simulations in which parameters are drawn from probabilistic distributions. Case A considers variability in desired walking velocity. Case B considers the combined effect of ISV in acceleration thresholds ($a_{\text{ret}}, a_{\text{lock}}, a_{\text{stop}}$) and forcing frequency f_p. For all simulations, the number of pedestrians has been increased such that the equivalent uniform pedestrian density reaches a stable value of approximately 0.6 ped/m^2.

Case A: ISV in lateral forcing frequency

Simulation data in which all pedestrians have a desired velocity $|\mathbf{V}_d| = 1.3$ m/s^2, is referred to as *mean value data.* A comparison is provided by simulations in which pedestrians have a desired velocity drawn from the normal distribution, $N(1.3 \text{ m/s}, 0.125 \text{ m/s})$, *distributed value data.*

Figure 5.18 (a) and (b) represent typical peak acceleration envelopes for distributed and mean value simulations respectively. The qualitative difference in plots is explained by considering the frequency content of each. The corresponding plots showing frequency composition are shown in figure 5.19 (a) & (b). The narrow-band spectrum in plot (b)

results from the fact that all pedestrians are walking with approximately the same frequency. In contrast the pedestrians in the distributed value simulation have normally distributed pacing frequencies resulting in a broader spectrum, plot (a). The minor peak in Fig. 5.19 (a) at 0.75 Hz is due to the relatively broader band excitation exciting the fundamental mode, now with a frequency of 0.75 Hz due to the addition of pedestrian mass. Note the different vertical scales in Fig. 5.19 (a) & (b).

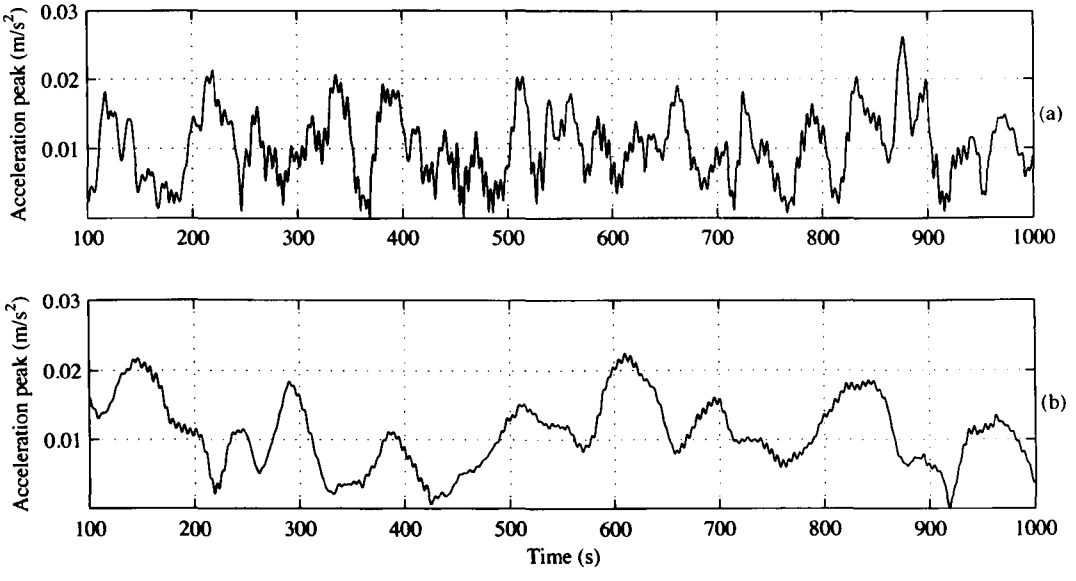

Figure 5.18: Typical peak acceleration-time history at mid-span for (a) distributed value and (b) mean value simulation.

From a probabilistic viewpoint, the analysis to determine stationarity described above was repeated. In the case of distributed value data, RMS and A_{peak} accelerations converged to 0.008 m/s^2 (CoV = 8 %) and 0.026 m/s^2 (CoV = 13 %) respectively. Again, ensemble RMS values show good agreement with values measured along individual records. Thus it is reasonably concluded that the distributed value response data is representative of an approximately stationary ergodic process.

Stationarity for mean value data was not demonstrated. This is due to the lower frequency trending in acceleration peaks visible in Fig. 5.18 (b), resulting from the relatively narrow excitation spectrum. Agreement of RMS values between subsections of the same record, as well as ensemble values show less consistency. Thus if a probabilistic analysis as demonstrated above is selected as a post-processing method, inclusion of ISV is desirable as it widens the excitation spectrum reducing low frequency trend-

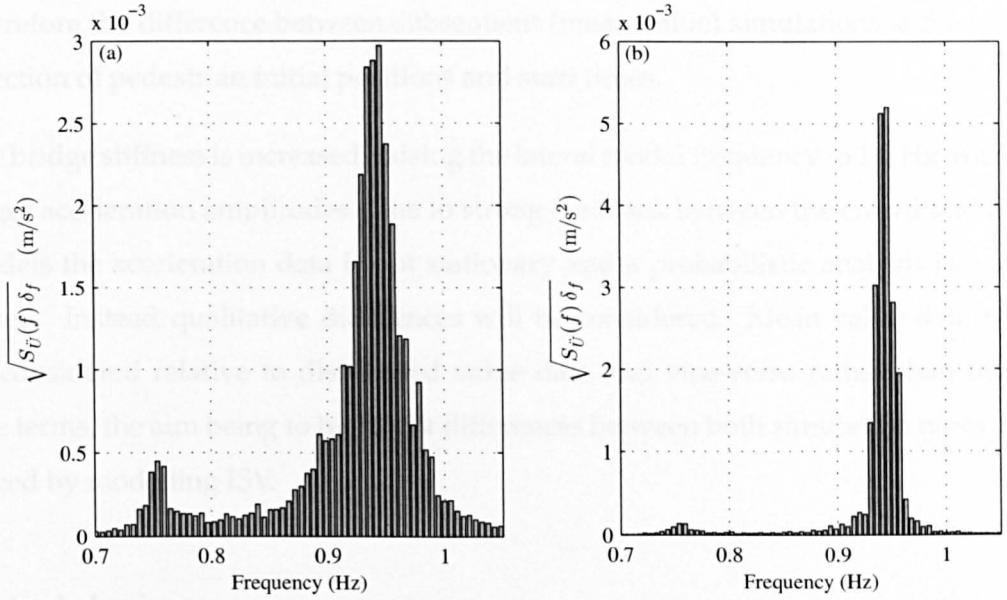

Figure 5.19: The frequency composition of lateral acceleration at mid-span for (a) distributed value and (b) mean value simulations. Bar plots showing the RMS value of frequency contributions over fixed bandwidths. The bandwidths of vertical bars are determined by the frequency resolution ($\delta_f = 0.005$ Hz) of the underlying single sided power spectral density, $\hat{S}_{\ddot{U}}(f)$.

ing in the response data. Alternatively, if the resulting response spectrum is relatively narrow banded, much longer record lengths should be used to investigate response stationarity.

When the $A_{E,95}$ value is calculated for the distributed value data, it becomes apparent that despite the number of pedestrians increasing by a factor of 3 compared with the analysis in section 5.2.6, $A_{E,95}$ has only increased by 34 % from 0.0290 m/s^2 to 0.0389 m/s^2. Because the lateral footfall force alternates in sign with successive steps, additional pedestrians are as likely to attenuate as add to the crowd-induced force. Therefore any assumption of increasing lateral response with increasing crowd density requires careful consideration; particularly as the actual HSI mechanism remains unclear [11]. The general thrust of the work in the following chapters will be to identify this mechanism for inclusion in a crowd-induced bridge excitation model.

Case B: ISV in acceleration thresholds & lateral forcing frequency

In this analysis mean value data is derived from simulations in which a_{ret}, a_{lock}, and a_{stop} are the same for all pedestrians in addition to their desired walking velocity.

Therefore the difference between subsequent (mean value) simulations is the random selection of pedestrian initial positions and start times.

The bridge stiffness is increased, raising the lateral modal frequency to 1.0 Hz to achieve larger acceleration amplitudes. Due to strong feedback between the crowd and bridge models the acceleration data is not stationary and a probabilistic analysis is not proposed. Instead qualitative differences will be considered. Mean value data should be considered relative to distributed value data and vice-versa rather than in absolute terms, the aim being to highlight differences between both simulation types, introduced by modelling ISV.

Bridge behaviour

Figure 5.20 shows 5 peak lateral acceleration envelopes for both distributed and mean value simulations respectively. Five have been selected in order to give an indication of the level of inter-simulation variability; however the same qualitative features are visible in each individual simulation. In all cases acceleration amplitude rises sharply once lock-in has been triggered. Once triggered more pedestrians are drawn into a lock-in state, further increasing bridge response. Acceleration amplitudes increase until the stop threshold (a_{stop}) forces some pedestrians to stop walking and the response amplitude slowly declines thereafter. While pedestrians at mid-span have typically stopped, pedestrians downstream usually start walking again continuing to excite the bridge. These features of crowd behaviour will be discussed in more detail below.

Once lock-in is triggered, the bridge response is largely unaffected by crowd distribution. This is seen by comparing figure 5.20 (a) and (b). In all cases the response rapidly reaches a peak and decays slowly thereafter, regardless of the crowd distribution. After lock-in, the coupled crowd-bridge system enters a pattern of behaviour that is deviated from only if pedestrians vacate the bridge without replacement or all pedestrians stop walking regardless of the acceleration level experienced.

Pre-lock-in responses differ significantly depending on whether ISV is considered. For mean value simulations, Fig. 5.21 (b), all acceleration envelopes follow similar trajectories until lock-in is triggered in all cases at a value of 0.15 m/s^2, within a time window of 45 to 85 seconds. This is expected as all pedestrians have similar pacing frequencies

and identical acceleration thresholds.

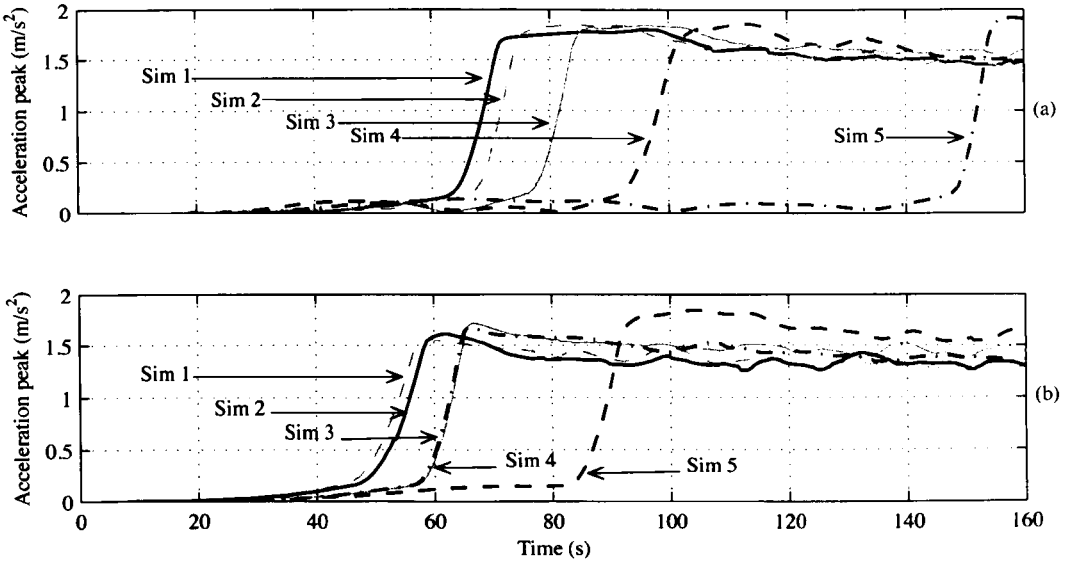

Figure 5.20: Peak mid-span acceleration envelopes for (a) distributed value simulations and (b) mean value simulations. Simulation have been arbitrarily numbered from 1 to 5 and show both pre- and post-lock-in behaviour.

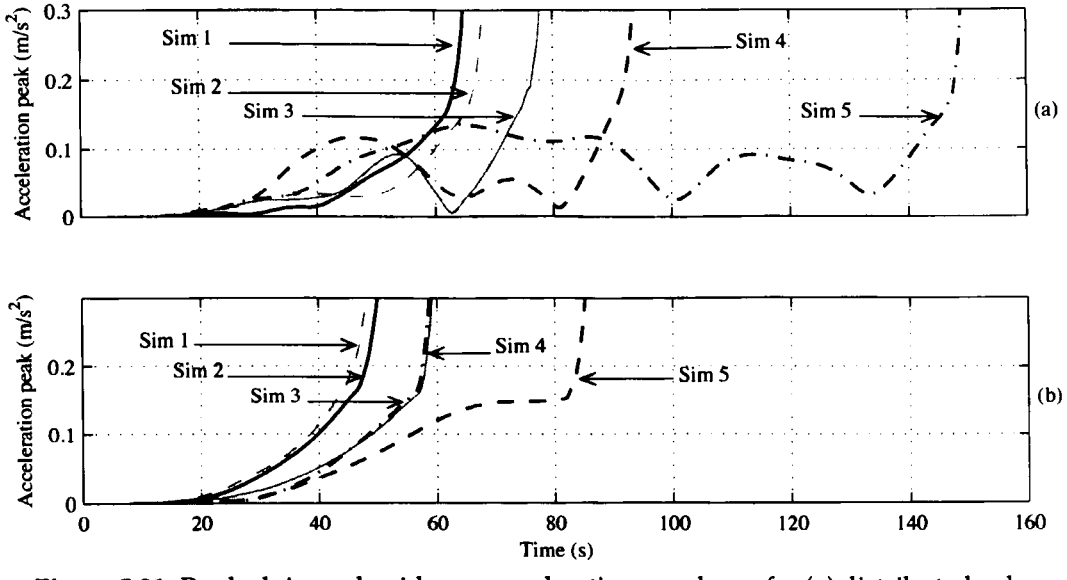

Figure 5.21: Pre-lock-in peak mid-span acceleration envelopes for (a) distributed value simulations and (b) mean value simulations. The inclusion of ISV, plot (a), leads to significant inter-simulation variability compared with mean value simulations, plot (b).

Distributed value simulations, Fig. 5.21 (a), show less similarity due to variability within the crowd. Lock-in is triggered in all 5 cases within a window of 65 to 150 sec-

onds, with the average time required to trigger lock-in noticeably increasing from 58 s to 88 s. Assuming an acceleration threshold exists for pedestrian lock-in (as assumed in this framework), this observation suggests ISV in this threshold makes lock-in less likely to occur.

It should be noted that mean forcing frequency ($\approx$ 0.95 Hz) and bridge modal frequency (1.0 Hz) were closely matched, in cases where these frequencies are not so closely matched, ISV is expected to be a more significant factor in inhibiting the development of lateral instability.

Crowd behaviour

The pedestrian distribution for a typical distributed value simulation is shown in Fig. 5.22, with the crowd walking from right to left. Pedestrians coloured green are unaffected by bridge motion, those in orange are locked-in and those in red are stationary, either due to bridge motion or traffic conditions. The peak mid-span acceleration is shown in Fig. 5.23. Red dashed lines correspond to the times for which the crowd distribution is shown in Fig. 5.22.

A common simplification when dealing with crowd dynamic loading is that the crowd remains uniformly distributed across the bridge throughout the simulation. However, when a homogeneous crowd crosses a perceptibly moving structure, the crowd is likely to fragment as pedestrians at different locations experience different levels of acceleration. Some pedestrians slow down and may stop while others continue unaffected. This leads to crowd fragmentation [7]. A discrete crowd model allows this crowd behaviour to develop, as demonstrated below.

At t = 120 s (a), acceleration is imperceptible across the bridge. Crowd density is non-uniform as would be expected from a random uncorrelated crowd. The peak mid-span acceleration is 0.13 m/s^2.

At t = 140 s (b), lock-in has been triggered and the peak acceleration has risen sharply to 1.59 m/s^2. The majority of pedestrians in area B have stopped walking due to their individual stop thresholds being exceeded. In area C, most pedestrians are still walking but are locked-in to the bridge motion. Those downstream of the congestion in area A continue to walk off the bridge but are also locked-in.

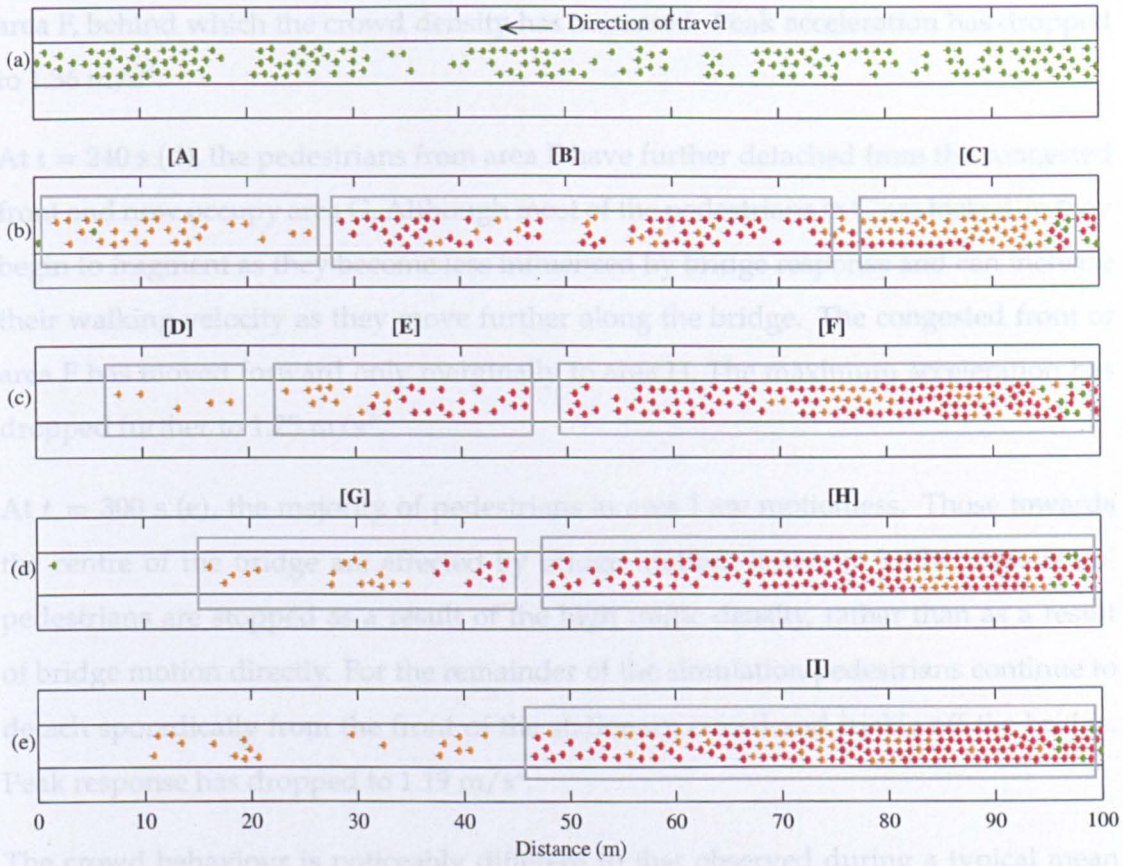

Figure 5.22: Crowd distribution during a typical distributed value simulation at (a) $t = 120$ s, (b) $t = 140$ s, (c) $t = 170$ s, (d) $t = 240$ s, (e) $t = 300$ s. Green pedestrians are unaffected by bridge motion, yellow pedestrians are locked-in and red pedestrians are stationary.

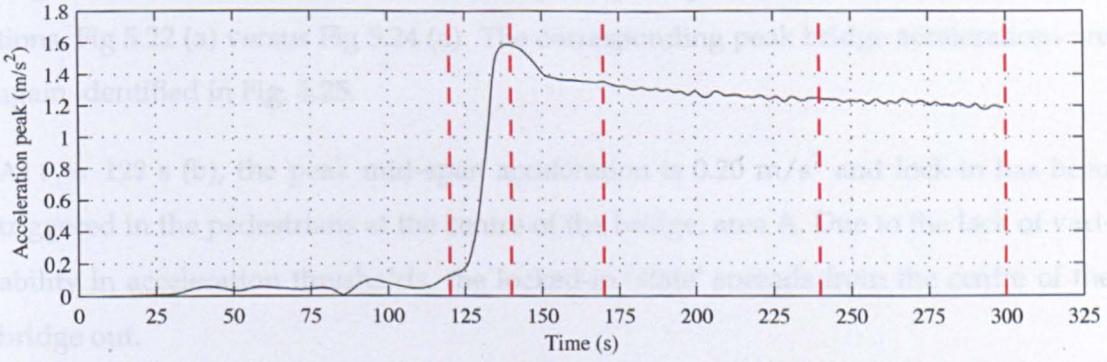

Figure 5.23: Peak mid-span acceleration. The red dashed lines indicate the times $t =$ [120, 140, 170, 240, 300] s corresponding to the crowd distributions shown in Fig. 5.22.

At $t = 170$ s (c), most of the pedestrians that were in area A have left the bridge except the rearward five, who are still making their way off, area D. Those that were towards the front of area B, now occupy area E where the front half are locked-in while the rear half have stopped walking. A congested front has now been established at the front of

area F, behind which the crowd density has increased. Peak acceleration has dropped to 1.36 m/s^2.

At $t = 240$ s (d), the pedestrians from area E have further detached from the congested front and now occupy area G. Although most of the pedestrians in G are locked-in they begin to fragment as they become less influenced by bridge response and can increase their walking velocity as they move further along the bridge. The congested front of area F has moved forward only marginally to area H. The maximum acceleration has dropped further to 1.25 m/s^2.

At $t = 300$ s (e), the majority of pedestrians in area I are motionless. Those towards the centre of the bridge are affected by bridge motion, however further 'upstream' pedestrians are stopped as a result of the high traffic density, rather than as a result of bridge motion directly. For the remainder of the simulation pedestrians continue to detach sporadically from the front of the stationary crowd and trickle off the bridge. Peak response has dropped to 1.19 m/s^2.

The crowd behaviour is noticeably different to that observed during a typical mean value simulation, Fig 5.24. The pre-lock-in distribution at $t = 100$ s is seen in Fig 5.24 (a). The crowd density is much higher due to the uniform desired velocity applied to all pedestrians. Varying the desired walking velocity in the crowd encourages natural fragmentation to occur, this can be seen by comparing the pre-lock-in crowd distributions, Fig 5.22 (a) versus Fig 5.24 (a). The corresponding peak bridge accelerations are again identified in Fig. 5.25.

At $t = 122$ s (b), the peak mid-span acceleration is 0.20 m/s^2 and lock-in has been triggered in the pedestrians at the centre of the bridge, area A. Due to the lack of variability in acceleration thresholds, the locked-in 'state' spreads from the centre of the bridge out.

At $t = 125$ s (c), the locked-in 'state' has spread further to include all pedestrians in area B. As a result, the peak response has increased to 0.54 m/s^2. The peak response continues to rise until a maximum value of 1.79 m/s^2 is reached at $t = 132$.

At $t = 170$ s (d), the peak response has fallen to 1.46 m/s^2 however walking velocities are still strongly influenced by the retardation function. The low walking velocities

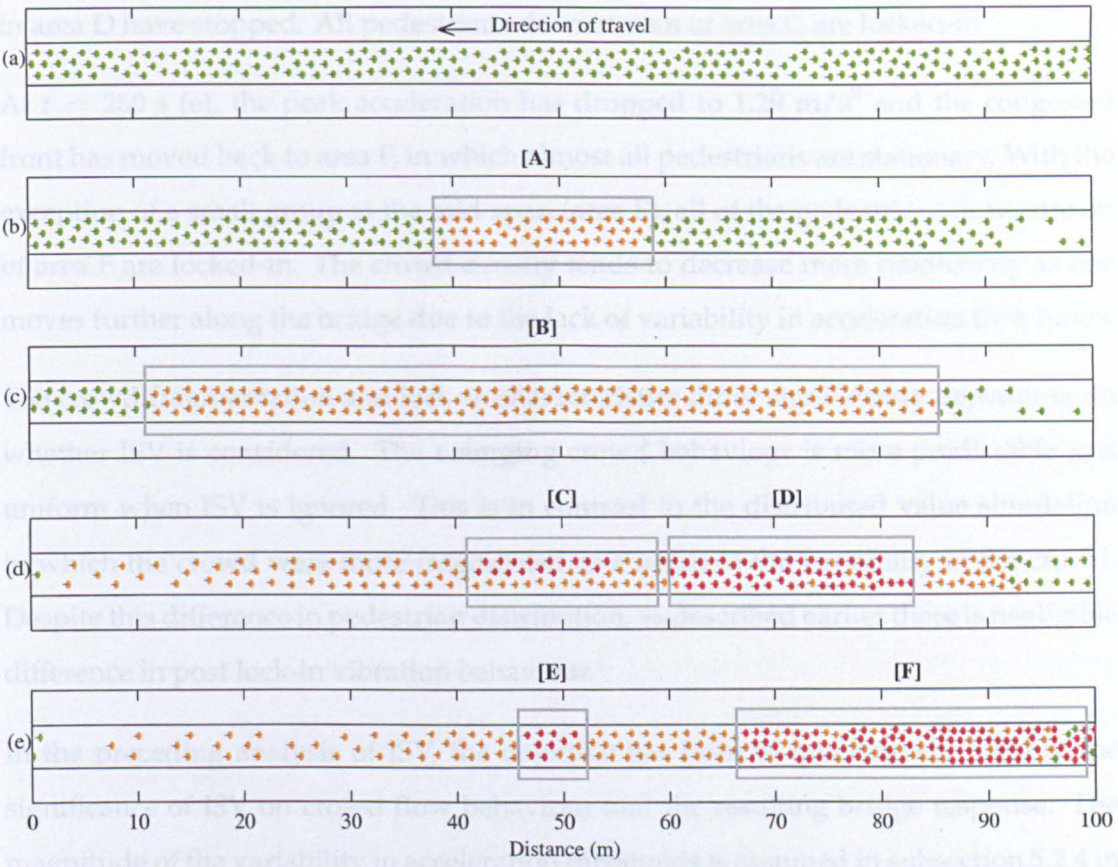

Figure 5.24: Crowd distribution during a typical mean value simulation at (a) $t = 100$ s, (b) $t = 122$ s, (c) $t = 125$ s, (d) $t = 170$ s, (e) $t = 250$ s. Green pedestrians are unaffected by bridge motion, yellow pedestrians are locked-in and red pedestrians are stationary.

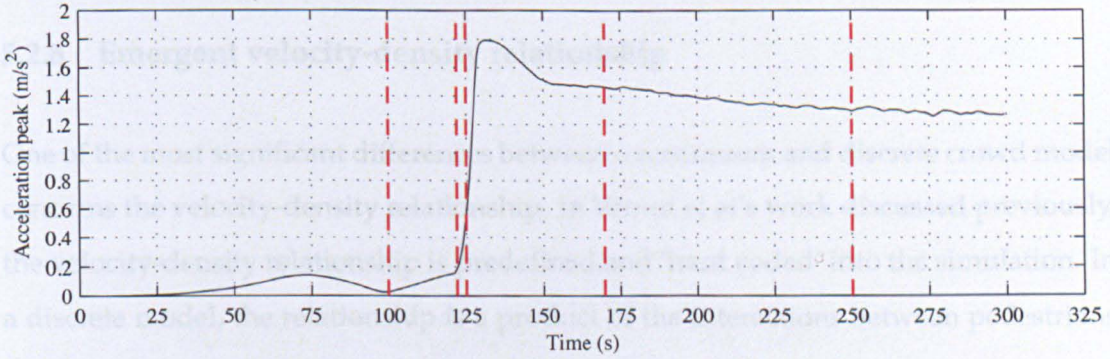

Figure 5.25: Peak mid-span acceleration. The red dashed lines indicate the times $t =$ [100, 122, 125, 170, 250] s corresponding to the crowd distributions shown in Fig. 5.24.

have caused congestion to increase upstream of the mid-span as more pedestrians continue to walk onto the bridge. As a result of the crowding and congestion brought about by the high level of acceleration, approximately half of the pedestrians in area C have stopped walking (the remaining half are locked-in) and practically all pedestrians

in area D have stopped. All pedestrians downstream of area C are locked-in.

At $t = 250$ s (e), the peak acceleration has dropped to 1.29 m/s^2 and the congested front has moved back to area F, in which almost all pedestrians are stationary. With the exception of a small group at the mid-span (area E), all of the pedestrians downstream of area F are locked-in. The crowd density tends to decrease more predictably as one moves further along the bridge due to the lack of variability in acceleration thresholds.

The crowd fragmentation and lock-in characteristics differ significantly depending on whether ISV is considered. The emerging crowd behaviour is more predictable and uniform when ISV is ignored. This is in contrast to the distributed value simulation in which the crowd were more fragmented as a result of the variability in the crowd. Despite this difference in pedestrian distribution, as described earlier there is negligible difference in post lock-in vibration behaviour.

In the preceding analysis of ISV, the objective has been to qualitatively identify the significance of ISV on crowd flow behaviour and the resulting bridge response. The magnitude of the variability in acceleration thresholds is assumed in subsection 5.2.4 in the absence of guidance in the literature. Therefore any further analysis to investigate the influence of the degree of ISV is of little practical value until variability can be judged with more accuracy.

5.2.8 Emergent velocity-density relationship

One of the most significant differences between a continuum and discrete crowd model concerns the velocity-density relationship. In Venuti et al's work discussed previously, the velocity-density relationship is predefined and 'hard coded' into the simulation. In a discrete model, the relationship is a product of the interactions between pedestrians and is an emergent property of the model.

In this subsection the emerging crowd velocity-density relationship is examined. Constrictions analogous to barriers are first introduced along the bridge as a means of inducing abrupt changes in the flow characteristics of the crowd, for demonstration purposes. The bridge is divided into 15 zones. Each pedestrian's walking velocity, $|V_p|$ is normalised by their desired walking velocity $|V_d|$ and the average for each zone,

$v_{z,\text{avg}}$, is determined. The equivalent uniform density, $d_{z,\text{eq}}$ within each zone is also calculated.

This is followed by an analysis of the velocity-density relationship in an obstruction free channel. Simulated data is compared against empirical observations as a means of validating the crowd model employed in this investigation.

Crowd behaviour

Figure 5.26 shows the typical variation of crowd velocity and density along the bridge without barriers. The traffic density across the majority of the bridge is in excess of 0.5 ped/m^2, as a result $v_{z,\text{avg}}$ has fallen below the mean desired level. The presence of a reasonably dense crowd results in all pedestrians walking slower than they would otherwise choose. This is a subtle example of emergent crowd behaviour. As the density reduces towards the end of the bridge, $v_{z,\text{avg}}$ recovers as pedestrians are free to increase their walking velocity.

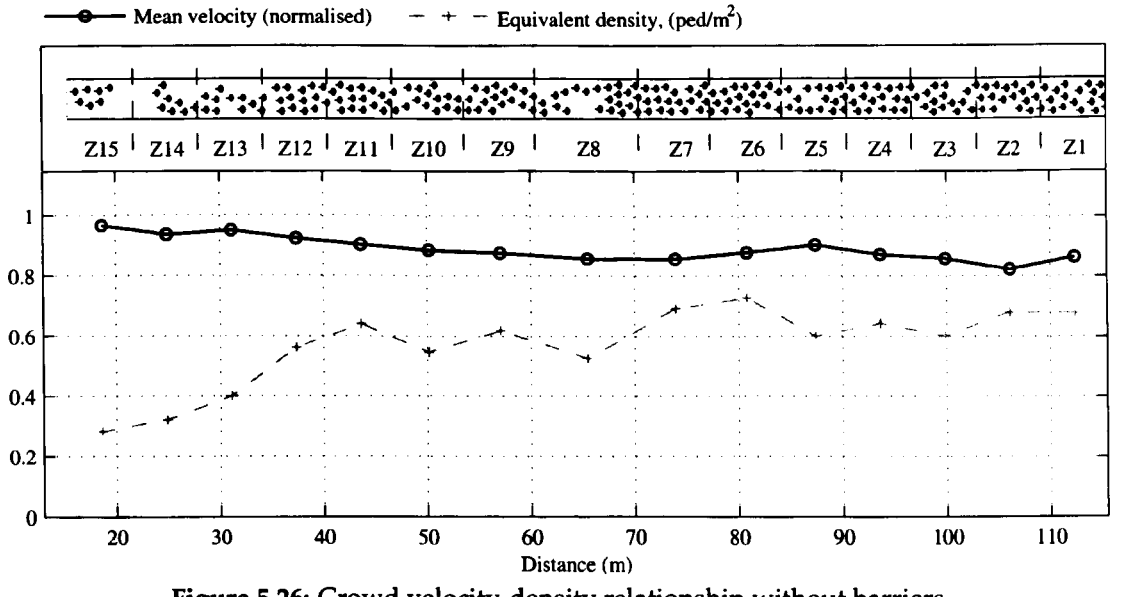

Figure 5.26: Crowd velocity-density relationship without barriers.

In figure 5.27 barriers are introduced. The crowd density increases as pedestrians meet the constrictions (zones 2,7 & 12), causing a corresponding drop in $v_{z,\text{avg}}$. Immediately downstream of each constriction (zones 3,8 & 13) $v_{z,\text{avg}}$ begins to recover as the 'bottleneck' has been passed. However the overall drop in velocity observed in Fig 5.26 due to traffic is maintained across the full span. The emergent velocity-density relationship

for the crowd is clearly demonstrated in Figs. 5.26 and 5.27.

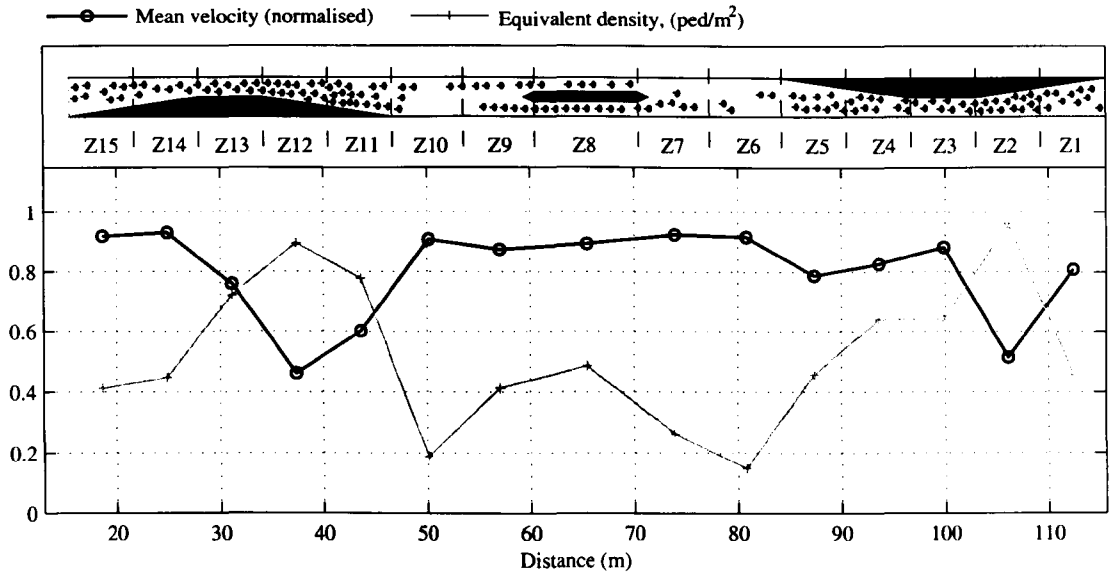

Figure 5.27: Crowd velocity-density relationship with barriers.

When pedestrian behaviour upstream of a constriction is examined the emerging crowd behaviour exhibits granular as opposed to fluid flow characteristics. Flow is often temporarily halted by a 'jam' of pedestrians. A temporary stop of one pedestrian has an influence 'upstream' if the crowd is sufficiently dense, as illustrated in Fig. 5.28.

Crowd behaviour for a period of 1.75 s is presented in 0.25 s increments. Pedestrians that are stopped are coloured in red and circled. The effect of a single pedestrian stopping at $t = 0$ s results in the crowd density upstream increasing, causing others to stop. This stop-start behaviour tends to exacerbate the jamming effect at the constriction, increasing the time required to pass, further increasing upstream density.

Bridge behaviour

The introduction of 'temporary barriers' above has a significant effect on the flow behaviour of the crowd. A strength of crowd-structure interaction modelling is that the bridge response resulting from this augmented flow can be inspected. Although barriers are an effective means of reducing the number of pedestrians on a bridge, they have the duel effect of slowing pedestrians down resulting in a reduction in lateral forcing frequencies. Averaging the pedestrian forcing frequencies for two simulations, one without and one with barriers on the bridge, the average forcing frequency is reduced

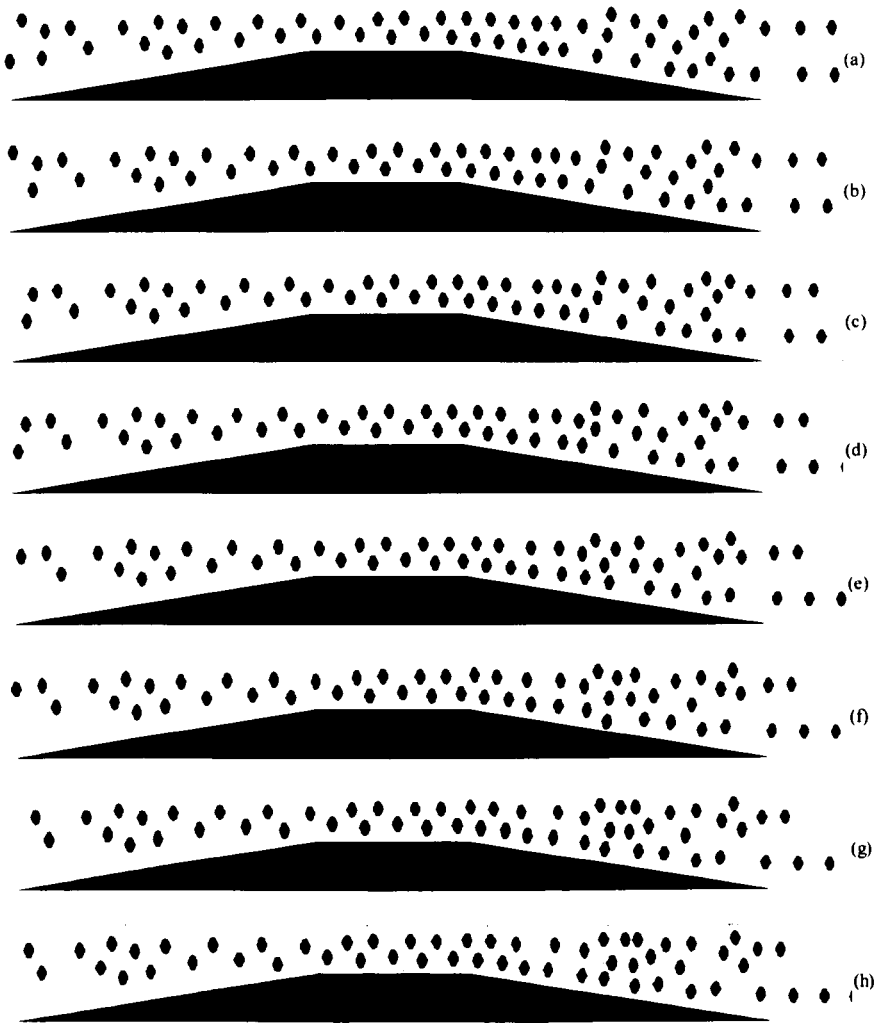

Figure 5.28: Pedestrian behaviour at constriction at 0.25 s increments (a)-(h).

from 0.96 Hz to 0.89 Hz.

The effect of this reduction is highlighted when one compares the RMS and peak lateral acceleration, A_{peak} values from both simulations;

$$\left.\begin{aligned} \text{RMS} &= 0.033 \text{ m/s}^2 \\ A_{peak} &= 0.092 \text{ m/s}^2 \end{aligned}\right\} \text{Barriers} \tag{5.2.34}$$

$$\left.\begin{aligned} \text{RMS} &= 0.008 \text{ m/s}^2 \\ A_{peak} &= 0.025 \text{ m/s}^2 \end{aligned}\right\} \text{No barriers} \tag{5.2.35}$$

Although there are considerably fewer people on the bridge, the lateral acceleration is higher after barriers are introduced because the crowd are forced to slow down bringing them closer to resonance with the structure's modal frequency of interest. This

suggests in cases where a bridge's lateral (or vertical) frequency is close to or above the mean crowd pacing frequency, temporary barriers may be an effective means of modifying pedestrian flow such that bridge response is reduced.

This may be particularly advantageous during a bridge's opening day when it will experience traffic levels well in excess of daily norms. It may be more cost effective to place temporary barriers (potentially in the guise of deck furniture such as large potted trees) rather than design structural damping measures for a once in a lifetime loading event. This single simulation merely indicates the mitigation potential of temporary barriers. A more thorough investigation is required before a more widely applicable conclusion can be reached.

Comparison with Fruin

In order to validate the simulated emergent crowd behaviour, a comparison is provided between the emergent velocity-density relationship and Fruin's empirical data [67], Fig. 5.29. A continuous flow of pedestrians was simulated walking through a (barrier free) channel 100 m long × 3 m wide for a period of 1000 s. The channel was divided longitudinally into 20 zones each with an area of 15 m^2. The equivalent uniform density, $d_{z,\text{eq}}$, mean normalised velocity, $v_{z,\text{avg}}$ and mean velocity, $\bar{v}_{z,\text{avg}}$, was determined for each zone at 5 s intervals. The mean and standard deviation of $v_{z,\text{avg}}$ and $\bar{v}_{z,\text{avg}}$ were determined for each discrete value of $d_{z,\text{eq}}$ observed, plots (a) and (b) respectively. Plot (a) indicates the degree to which pedestrians deviate from the desired walking velocity. Plot (b) represents the trend in terms of actual walking velocities.

Figure 5.29 shows that the simulated crowd velocities are higher than those observed by Fruin, particularly so as the crowd density increases. Within the simulation, a mean desired velocity of 1.4 m/s was set for the crowd, in order to match Fruin's unobstructed walking velocity. However the standard deviation of desired velocities, σ, was obtained from [63]. To investigate the influence of this parameter, repeat simulation were carried out with varying values of σ = [0.083, 0.125, 0.167, 0.208, 0.250, 0.292, 0.333, 0.375, 0.417] m/s. The linear fit to mean value data can be seen for each simulation in Fig. 5.30.

It can be seen that as the variability in desired velocities increases, the influence of

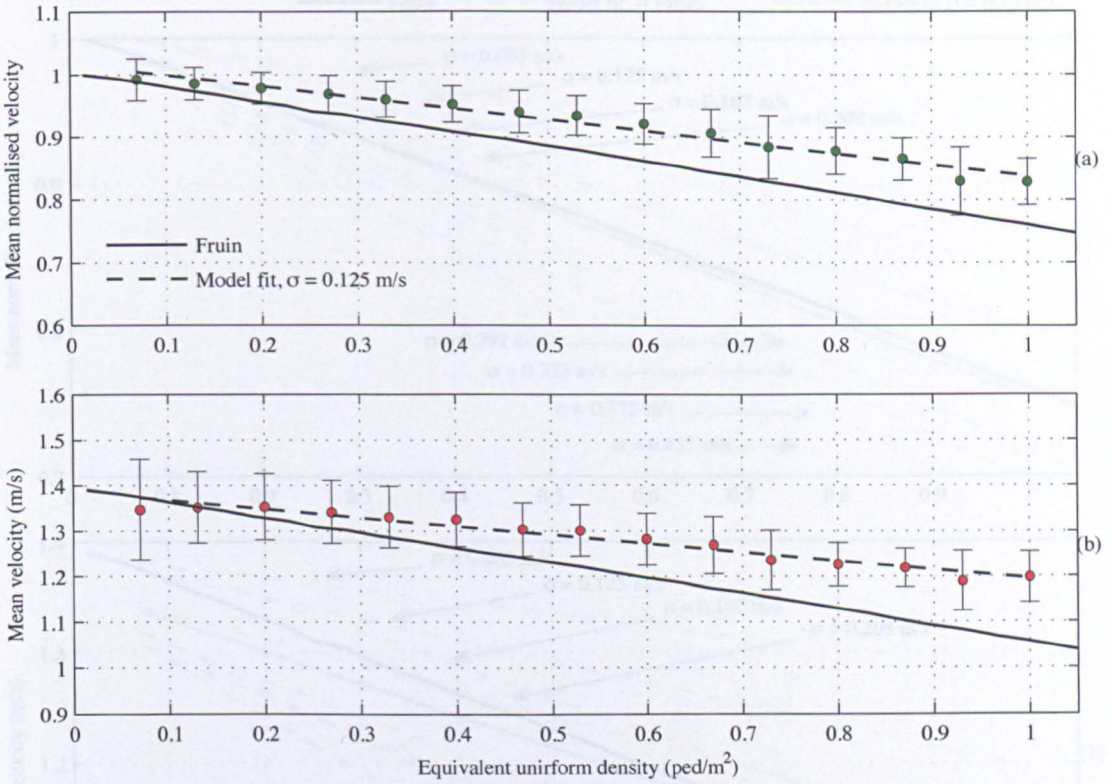

Figure 5.29: Comparison between the emergent velocity-density relationship and Fruin's empirical data. The standard deviation of desired velocities, σ, is 0.125 m/s, from [63]. In plot (a), mean velocities are normalised by pedestrian desired velocities and plotted against equivalent uniform density. In plot (b), realised walking velocities are plotted against equivalent uniform density. Circles and error bars indicate the mean and $\pm$ one standard deviation boundary for all data points observed at a given density. Note that the dashed black line represent a linear fit to mean value data.

higher crowd densities on mean velocity and mean normalised velocity becomes more significant. In other words, as the variability in desired velocities increases, the chances of becoming blocked by a slower moving pedestrian are increased. Due to the anisotropic nature of perception in a unidirectional flow, slower moving pedestrians tend to slow those behind them. This is further exacerbated as the crowd density increases.

It is clear that the simulation showing greatest agreement with Fruin is that for which $\sigma = 0.25$ m/s, shown in more detail in Fig. 5.31. It should be remembered that Fruin's data was obtained by observing pedestrians on a city street. It is reasonable to suggest that in such an environment the degree of 'visual distraction' among pedestrians may have been higher than Pachi and Ji observed in their study of footbridge environments [63]. A greater level of distraction is consistent with greater variability in desired

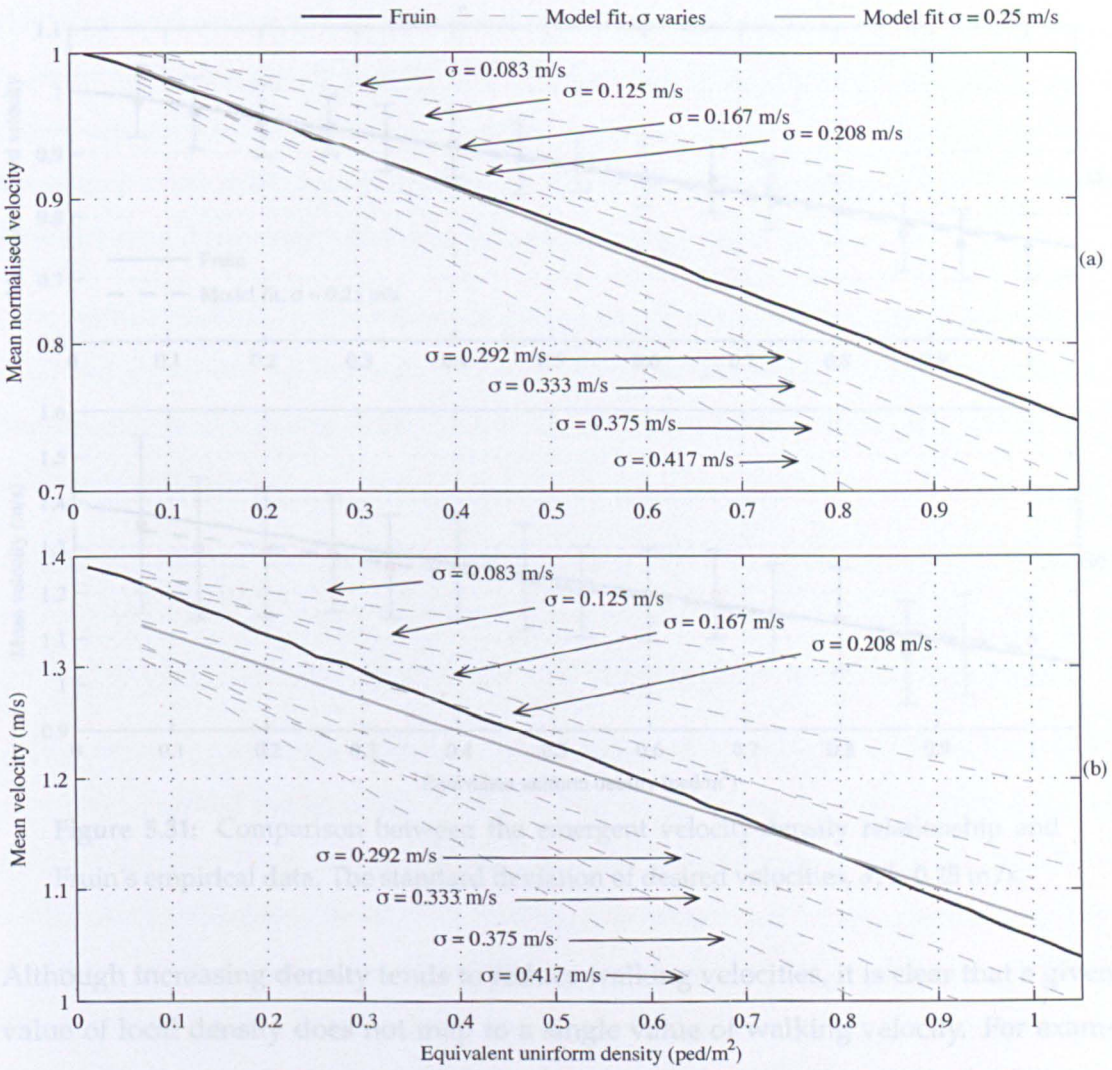

Figure 5.30: Comparison between the emergent velocity-density relationship and Fruin's empirical data. Linear fits to mean value data are shown for 9 simulations with values of σ = [0.083, 0.125, 0.167, 0.208, 0.250, 0.292, 0.333, 0.375, 0.417] m/s. Simulation showing the closest fit (σ = 0.25) is shown with a solid grey line, while the remaining fits are shown with dashed grey lines.

walking velocities; when this is simulated by increasing the standard deviation of desired velocities, the agreement with Fruin's data is considerably improved. The precise amount by which σ can be justifiably increased to account for different environments can only be speculated, however an increase is logical and justifiable. On this basis it is concluded that the crowd model simulates emergent crowd behaviour in reasonably agreement with empirical observations and its continued use is justified.

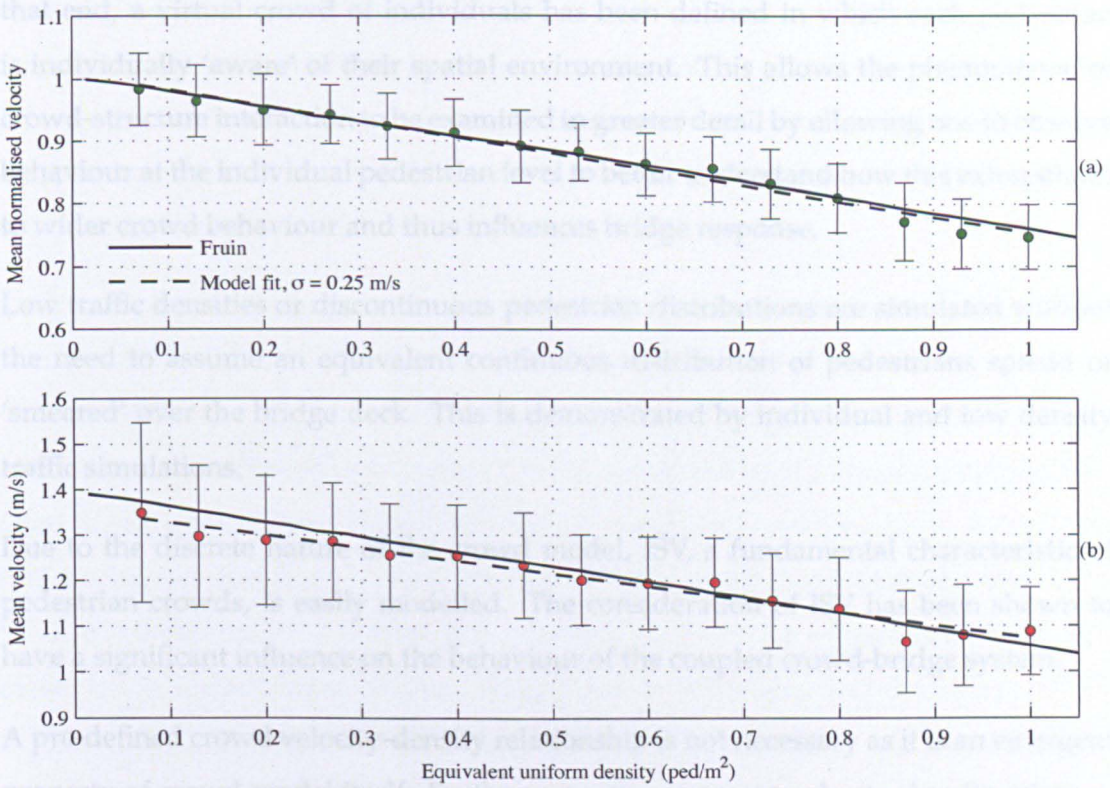

Figure 5.31: Comparison between the emergent velocity-density relationship and Fruin's empirical data. The standard deviation of desired velocities, σ, is 0.25 m/s.

Although increasing density tends to reduce walking velocities, it is clear that a given value of local density does not map to a single value of walking velocity. For example, a pedestrian at the front of a dense subgroup may potentially experience the same local density as a pedestrian to the rear of the same subgroup. However the pedestrian to the front is more likely to approach their desired velocity. It is also noted that this variability in walking velocities reduces as the crowd density increases and realised walking velocities are forces to converge, eg. Fig. 5.31, plot (b). Reliance on a strict velocity-density relationship is therefore too restrictive in the context of human-induced dynamic loading. This is especially so considering walking velocity is directly related to forcing frequency, a key parameter.

5.3 Conclusions

The aim of the work presented in this chapter has been to explore the potential offered by a discretely defined crowd in the simulation of crowd-induced vibration. To

that end, a virtual crowd of individuals has been defined in which each pedestrian is individually 'aware' of their spatial environment. This allows the phenomenon of crowd-structure interaction to be examined in greater detail by allowing one to observe behaviour at the individual pedestrian level to better understand how this extrapolates to wider crowd behaviour and thus influences bridge response.

Low traffic densities or discontinuous pedestrian distributions are simulated without the need to assume an equivalent continuous distribution of pedestrians spread or 'smeared' over the bridge deck. This is demonstrated by individual and low density traffic simulations.

Due to the discrete nature of the crowd model, ISV, a fundamental characteristic of pedestrian crowds, is easily modelled. The consideration of ISV has been shown to have a significant influence on the behaviour of the coupled crowd-bridge system.

A pre-defined crowd velocity-density relationship is not necessary as it is an emergent property of crowd model itself. Furthermore, the emergent velocity-density relationship exhibited by the crowd model has been validated through successful comparison with Fruin's field observations. This analysis also reveals that for any given crowd density there exists a distribution of pacing frequencies, i.e. a single value of crowd density does not map to a single value of walking velocity. Considering the dependance of forcing frequency on walking velocity, reliance on a pre-defined velocity-density relationship is too simplistic.

It is therefore concluded that using a discrete crowd model to predict emergent crowd behaviour, for the purposes of simulating bridge response, has distinct advantages over earlier hydrodynamic models. It can capture key phenomena, reveal underlying physics and is flexible enough to be expanded further.

The modelling in this chapter is built on many assumptions. However the two areas of greatest uncertainty relate to:

1. Pedestrian vibration thresholds, the ISV associated with these thresholds and resulting behavioural alterations.
2. The treatment of HSI and the assumption of a lock-in state, characterised by step frequency tuning.

Further investigation of the existence and potential variability in acceleration vibration thresholds is beyond what can be achieved in this project and is left as the subject of future work. In the following chapters, the focus will be on investigating the HSI mechanism. As suggested by other researchers [37, 81], biomechanical modelling would appear to be the most logical way to proceed.

As discussed previously in section 2.3, other authors have adopted an inverted pendulum biomechanical model to simulate HSI. However, there are outstanding questions and uncertainties regarding the suitability of the inverted pendulum model. In light of the literature reviewed in sections 3.1 to 3.3, and based on the simple reasoning outlined in section 4.1, there are two principle question to be addressed; (i) what is the HSI mechanism and (ii), how well does the inverted pendulum model and associated balance law capture it? It is these questions that motivate the experimental campaign presented in the following chapter. After these are addressed and the nature of HSI is more fully understood, the modelling framework presented in this chapter can be expanded to simulate biomechanically based HSI in chapter 8.

CHAPTER 6

Experimental campaign

Chapter Summary

In this chapter the experimental campaign and related data processing and analysis are discussed. An outline of the test campaign is presented in section 6.1. This is followed by a description of the oscillating treadmill test rig in section 6.2. The active motion capture system is detailed in section 6.3.

The reproduction of lateral GRFs from visual marker data is demonstrated in section 6.4. This is followed by an analysis of typical gait behaviour in section 6.5. The relationship between balance behaviour and the generation of self-excited GRFs is also discussed in this section. The conclusions from the experimental campaign are set out in section 6.6.

6.1 Campaign outline

Based on both field [6, 24] and laboratory observations [11], the process of step synchronisation between pedestrians and an oscillating bridge deck is now thought to be preceded by a more subtle interaction. This HSI (as opposed to human-structure synchronisation) results in force harmonics within the GRF spectrum, that resonate with the bridge deck oscillation. Fundamental to the production of these resonant force harmonics is the pedestrian's balance response to base motion. As such, to further understand HSI, one must first consider pedestrian stability and balance behaviour during locomotion.

A review of the literature has shown that much work has been done to examine and characterise lateral GRFs [11, 81]. However, within the civil engineering discipline, there has been relatively little experimental investigation of the biomechanical behaviour that ultimately produces these forces. On this basis, the logical next step in the investigation of HSI is to look 'further up the load path', and try to understand a pedestrian's kinematic behaviour when subject to lateral base motion.

As the understanding of pedestrian-induced vibration has progressed, so too have the means and methods of investigation. The use of optically based motion capture equipment has recently been demonstrated as a potentially useful means of reproducing GRFs. Inverse dynamics was used in [12] to reproduce human bouncing and jumping forces from visual marker data. If successfully applied to the reproduction of lateral GRFs while walking, this would allow an analysis of how the whole body responds to base motion and contributes to the GRF. It is this information that is currently lacking and may reveal more about the nature of HSI, ultimately enabling better modelling, simulation and prediction of structural response.

One of the central questions posed in this thesis is, how well does the inverted pendulum model coupled with Hof et al's balance law [43] (hereafter referred to as the *CoP law*), approximate human locomotion on a laterally oscillating structure? Based on the discussion presented in section 3.1, it is reasonable to suggest the potential significance of active balance control. In any event, further validation of the CoP law for the specific case of walking on a laterally oscillating bridge is required. A more complete picture

of human response to base motion provided by the use of motion capture equipment offers an excellent opportunity to address these uncertainties.

To this end, an experimental campaign was designed in which test subjects walk individually on a laterally oscillating treadmill similar to that reported in [11]. A range of tests were carried out, with varying oscillation frequencies and amplitudes imposed on the deck. GRFs were directly measured using deck mounted load cells. In addition, each subject was instrumented with 31 active visual markers in order to record 3-dimensional whole body motion.

The experimental campaign was carried out between March and May of 2012, in the Human Performance Laboratory, at the University of Nottingham. The test protocol received ethical approval from the Faculty (of Engineering) Research Ethics Committee within the University of Nottingham. Subjects were tested in isolation on separate days. The test protocol for an individual subject was as follows;

- The subject was familiarised with the oscillating treadmill rig (discussed in section 6.2 below) and all safety procedures (emergency stop etc.).
- The subject was instrumented with gait analysis wands and visual markers (discussed in section 6.3 below).
- The subject had a further unrecorded period of familiarisation walking on the treadmill without lateral motion, lasting approximately 10 minutes. During this time a comfortable walking speed was selected by the subject
- The subject was then recorded for three individual periods of 20 s each walking without lateral motion imposed on the deck. This data served as a baseline for the subject's walking behaviour.
- After baseline tests were completed, the subject was recorded walking while lateral oscillations were imposed on the deck, referred to hereafter as dynamic tests. Each individual dynamic test lasted for 20 s (limited by the motion capture system, discussed below). At the beginning of each dynamic test prior to data recording, subjects were asked (while walking on the oscillating deck) if they wished to alter the treadmill belt speed to maintain a comfortable feeling of stability. If they wished, the belt speed was altered and the test commenced.

- Rest breaks were imposed every 2-3 minutes during the course of the test session.

During each test, the lateral GRF was measured directly via 4 deck mounted Zemic bending beam load cells (490 N capacity each). For the duration of each dynamic test, the lateral deck displacement and acceleration were also recorded via a linear variable differential transformer (LVDT) and Schaevitz linear servo accelerometer. A sampling rate of 250 Hz was selected for all treadmill-borne data to provide good time domain resolution. A National Instruments SCXI-1000 chassis, housing a SCXI-1100, 32 channel multiplexer amplifier (receiving LVDT and accelerometer signals) and SCXI-1520 strain bridge (receiving load cell signals) was used to coordinate data logging and signal conditioning. The chassis was also used to trigger simultaneous logging of the marker data. All marker data was sampled at 100 Hz using a CODA ActiveHub computer from Charnwood Dynamics Ltd. Sampling 31 markers at 100 Hz, limited acquisition time to 20 s, this governed individual test durations.

To allow potential comparison with the extensive data set obtained by Ingólfsson et al. [11], a similar range of amplitudes and frequencies were chosen for dynamic tests. Therefore 5 oscillation amplitudes were tested, 5 mm, 10 mm, 20 mm, 35 mm and 50 mm. Within each amplitude, 9 oscillation frequencies were tested ranging from 0.3 Hz to 1.1 Hz in 0.1 Hz increments, resulting in a 45 point test matrix.

In order to establish the significance of ISV within the various behaviours observed, it was decided that 10 subjects would be tested. This is considerably fewer subjects than took part in Ingólfsson et al's study [11]. However the quantity of data recorded for each subject in this investigation is substantially greater, thus there is inevitably a trade-off between the number of subjects tested and the amount of data per subject. The approach taken here is to study fewer subjects, but in greater detail.

The age, height and weight of all participants is shown in table 6.1. The majority of anthropometric data in the literature has been obtained from male subjects. In order to utilise this data as effectively as possible only male subjects were recruited for this campaign. This is justifiable when one considers that there is no reason to suspect that male subjects will behave (statistically) significantly differently to female subjects. Furthermore, to test for statistical differences between males and females would require a much larger sample size than can be achieved within this work. It is therefore as-

sumed (until proven otherwise) that the behaviours observed and conclusions drawn are equally applicable to both sexes.

Table 6.1: Test subject data.

Subject	Height (m)	Mass (kg)	Age (Years)
1	1.73	82.05	28
2	1.82	96.20	30
3	1.74	63.05	27
4	1.84	98.95	28
5	1.68	85.45	34
6	1.88	90.95	21
7	1.82	87.20	26
8	1.61	75.00	31
9	1.80	74.05	28
10	1.76	82.70	34
Mean	1.77	83.11	28.7

6.2 Oscillating treadmill test rig

In order to meet the requirements of the test campaign, a treadmill capable of oscillating laterally with various frequencies and amplitudes was designed and constructed by the author, Fig. 6.1 (a). The design is similar to that constructed by Pizzimenti [34] and used more recently by Ingólfsson [11]. What marks this test campaign as a further development of what has gone before is the use of motion capture equipment, discussed in section 6.3.

6.2.1 Construction

The treadmill structure consists of three steel frames arranged as follows (refer to Fig. 6.2):

1. The base frame is the lowermost frame and remains stationary. The motor pro-

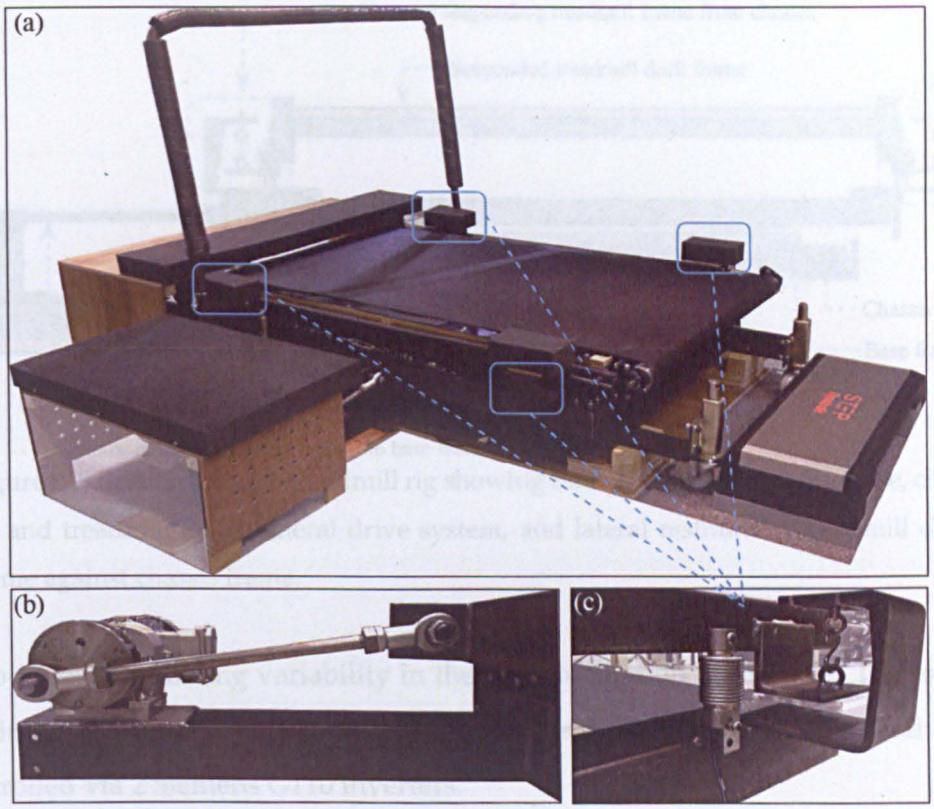

Figure 6.1: (a) Oscillating treadmill test rig, (b) Motor and lateral drive arm producing reciprocating sinusoidal motion from rotary motion, (c) Hanger and load cell arrangement (1 of 4), the treadmill deck is supported vertically by hangers and restrained laterally by bending beam load cells.

viding lateral motion is connected to this frame.

2. The chassis frame sits on 4 carriages that travel along linear guide rails fixed to the base frame. The chassis frame is driven laterally by a drive arm connected to the motor, see Fig. 6.1 (b). Thus rotational motion, provided by the motor is converted, through the drive arm, to sinusoidal reciprocating motion.

3. The uppermost treadmill frame is suspended from the chassis frame by 4 hangers, Fig. 6.1 (c). The self weight of the treadmill frame and any vertical imposed loads are resisted by the hangers. The treadmill frame is restrained laterally by 4 bending beam load cells, the means through which the lateral GRF is recorded. The treadmill belt is driven by a second motor mounted on the chassis frame.

The chassis frame is driven laterally by a Nordbloc 0.55 kW geared motor. A specifically designed coupling is used to allow the drive arm to be fitted at different radii from

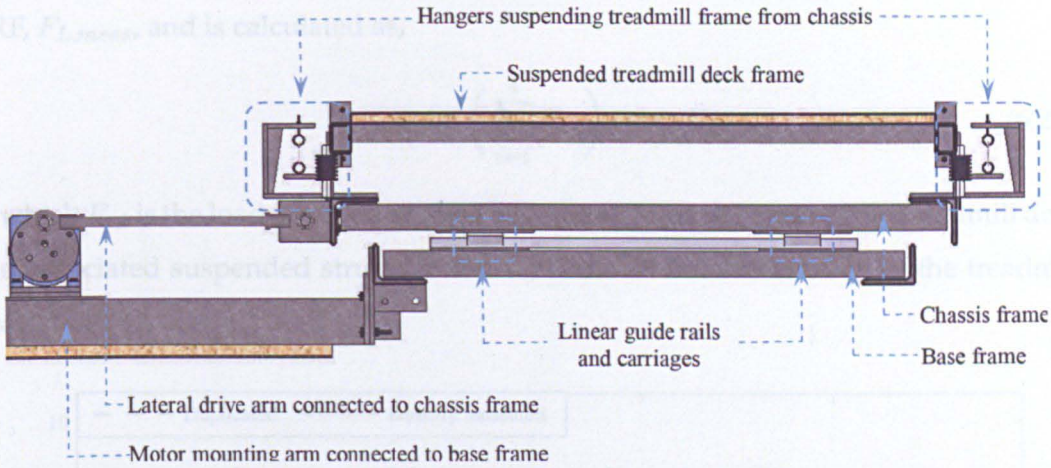

Figure 6.2: Section through treadmill rig showing three constituent frames (base, chassis and treadmill deck), lateral drive system, and lateral restraint of treadmill deck frame against chassis frame.

the motor shaft, allowing variability in the deck oscillation amplitude. The treadmill belt is itself belt driven by a Nordbloc 0.75 kW geared motor. The speed of both motors is controlled via 2 Siemens G110 inverters.

The deck walking area measures 1 m wide $\times$ 1.5 m long. A horizontal bar/handle was placed across the front of the treadmill to provide extra stability should a test subject feel particularly unstable. Subjects were instructed not to touch the bar unless absolutely necessary, after which the test data was discounted. The front-mounted bar is obviously not in keeping with what one would experience on a real bridge, however side rails could not be provided without obscuring marker visibility.

6.2.2 Data acquisition and rig validation

Considering a sampling frequency of 250 Hz was selected, all analogue signals were filtered at 100 Hz to avoid aliasing. The accelerometer and LVDT recording deck motion were further digitally low pass filtered with 4th order Butterworth (BW4) filters. A cutoff frequency of 2 Hz was deemed sufficient for deck displacement as deck oscillations do not exceed 1.1 Hz. Because deck acceleration data is used to reproduce GRFs, a higher cutoff frequency of 5 Hz was selected to allow reproduction of higher force harmonics. The load cells were digitally low pass filtered at 6 Hz (BW4).

The lateral GRF obtained from the treadmill rig shall be referred to as the measured

GRF, $F_{L,meas}$, and is calculated as,

$$F_{L,meas} = \left(\sum_{i=1}^{4} F_{c,i} \right) - m_d \ddot{U}_d \tag{6.2.1}$$

in which $F_{c,i}$ is the load imposed on the i^{th} load cell, m_d is the mass of the treadmill deck and associated suspended structure and $\ddot{U}_d$ is the lateral acceleration of the treadmill deck.

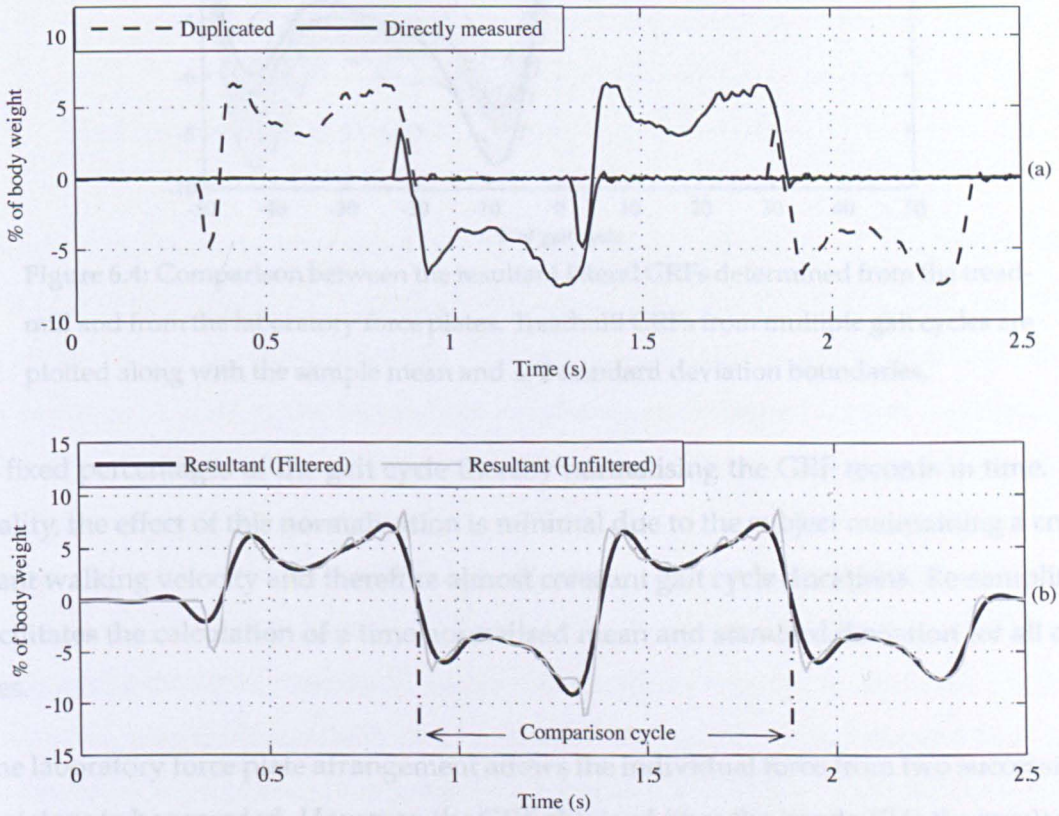

Figure 6.3: (a), GRFs measured individually for both feet (solid black line) and the duplicated records (dashed black line) to provide a periodic signal, both unfiltered. (b), The resultant GRF obtained from the periodic record (grey line) and the filtered resultant GRF.

$F_{L,meas}$ was validated against GRFs recorded from independently calibrated Kistler force plates (in-situ in the Human Performance Lab). The GRF time series obtained from the rig, $F_{L,meas}$, was divided into windows, each covering two successive steps. The beginning and end of each window was determined as the point at which the GRF was zero, the middle of a double stance phase. This period of time defines the individual gait cycle time for the following analysis. Each data window was re-sampled

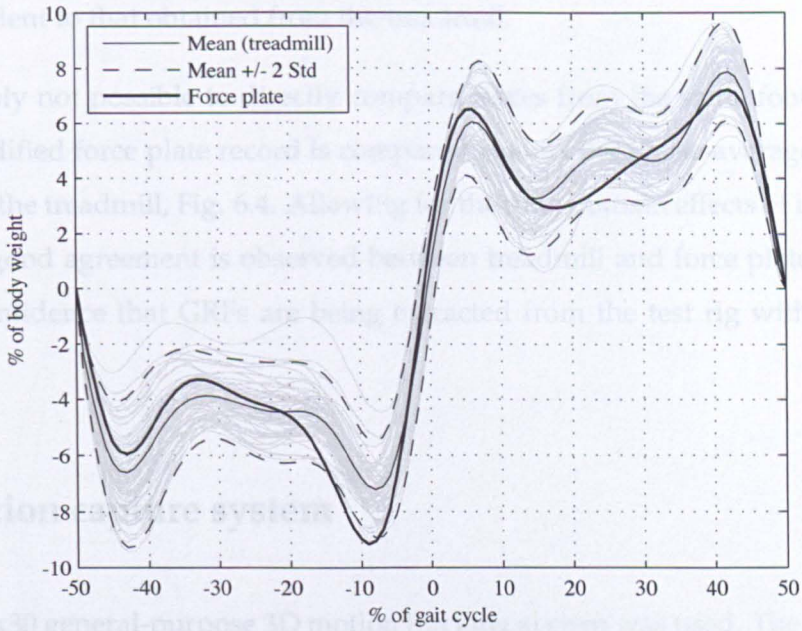

Figure 6.4: Comparison between the resultant lateral GRFs determined from the treadmill and from the laboratory force plates. Treadmill GRFs from multiple gait cycles are plotted along with the sample mean and $\pm$ 2 standard deviation boundaries.

at fixed percentages of the gait cycle thereby normalising the GRF records in time. In reality, the effect of this normalisation is minimal due to the subject maintaining a constant walking velocity and therefore almost constant gait cycle durations. Re-sampling facilitates the calculation of a time normalised mean and standard deviation for all cycles.

The laboratory force plate arrangement allows the individual force from two successive footsteps to be recorded. However, the GRF obtained from the treadmill is the resultant of forces from both feet (during the double stance phase). Therefore the resultant of both force plate records was determined in order to provide a comparable time series. To further improve comparability, the force plate records for each foot were duplicated and appended to the beginning and end of the original data. This creates an artificially periodic GRF record, Fig. 6.3 (a). The resultant of this periodic force plate record was then determined and a single cycle extracted for comparison with the treadmill data, Fig. 6.3 (b). There is inevitably some inaccuracy involved in duplicating the force plate records to obtain a periodic time series, as the 'energy spreading' effect of intra-subject variability in ignored. However in this case the influence of this error is minimal. The main purpose of generating a periodic signal is to allow the extraction of a time domain

cycle equivalent to that obtained from the treadmill.

It is obviously not possible to directly compare forces from the same footstep, therefore the modified force plate record is compared against the phase-averaged cycle obtained from the treadmill, Fig. 6.4. Allowing for the time domain effects of intra-subject variability, good agreement is observed between treadmill and force plate data. This provides confidence that GRFs are being extracted from the test rig with acceptable accuracy.

6.3 Motion capture system

A Coda mpx30 general-purpose 3D motion tracking system was used. The system consists of 2 measurement units, each containing 3, pre-aligned cameras, wall mounted on either side of the treadmill deck. The cameras track the position of active markers (infra-red LEDs) in the measurement volume, achieving a position resolution of 0.1 mm horizontally and vertically and a distance resolution of 0.3 mm. Each subject was instrumented with 31 active markers, placed directly on the skin (over bony landmarks) and attached to gait analysis wands strapped to the body, Fig. 6.5 (b). The use of gait analysis wands improves marker visibility. However they also facilitate the calculation of joint centres and body segment embedded vector bases (EVB). By locating three noncollinear markers with known spatial relationships to the relevant anatomical landmarks or reference points, basic vector analysis is used to locate the joint centre and associated EVB.

6.3.1 Marker placement

During testing subjects wore a sleeveless shirt and shorts. Subjects were not permitted to wear any form of footwear. This may at first appear odd as pedestrians walking on a bridge rarely walk barefoot. However, the emphasis in this campaign is on understanding biomechanical response in the face of lateral base motion. The direct equivalence of the test environment to the footbridge environment is secondary to this. The somatosensory information received through the sole of the foot is undoubtedly altered if a person wears shoes. Whether or not this information is altered to the extent

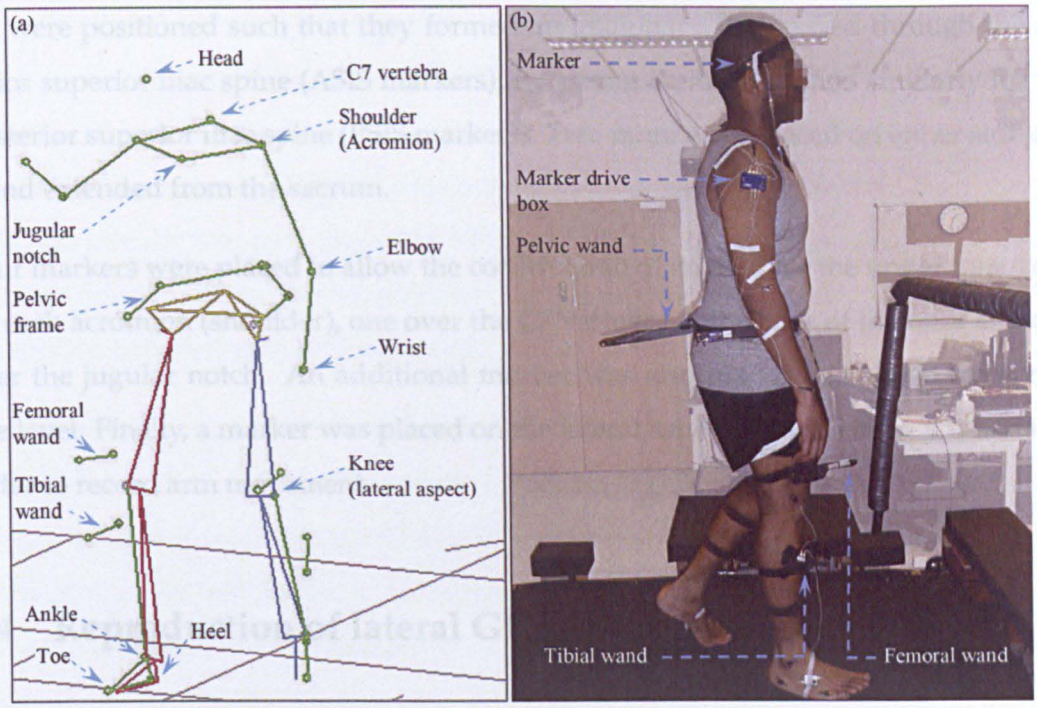

Figure 6.5: (a) Marker arrangement showing locations of 31 active markers, (b) Test subject instrumented with markers and gait analysis wands.

that it has an influence on the actual balance behaviour is less certain. It was therefore decided to remove any potential variability introduced by footwear.

The positioning of all markers placed at or below hip level was determined by the marker placement protocol set out in the Coda mpx30 user guide [82]. Hip, knee and ankle joint centres are calculated relative to marker positions as per the procedure set out in [82]. Markers placed on the upper torso, arm and head were placed based on the specific requirements of this test campaign. Namely to allow quantification of upper torso rotation and head and arm movement allowing accurate calculation of the CoM trajectory.

More specifically, markers were positioned at the heel, at the end of the 5^{th} metatarsal (toe), both facing laterally, at the lateral malleolus (ankle) and on the lateral aspect of the medio-lateral knee axis. Tibial and femoral wands, containing two additional markers each, were strapped to the subject's lower leg and thigh. The purpose of the wands is primarily to facilitate the construction of an embedded vector basis (EVB) for the thigh and shank segments, facilitating the calculation of joint rotation angles.

A pelvic frame containing 6 markers allows a pelvis EVB to be constructed. Two mark-

ers were positioned such that they formed an imaginary line passed through the anterior superior iliac spine (ASIS markers), two more were positioned similarly for the posterior superior iliac spine (PSIS markers). Two more were placed on either side of a wand extended from the sacrum.

Four markers were placed to allow the construction of an EVB for the upper torso; one on each acromion (shoulder), one over the C7 vertebra at the back of the neck and one over the jugular notch. An additional marker was also placed just above the ear, at eye level. Finally, a marker was placed on the lateral aspect of each elbow and wrist in order to record arm movement.

6.4 Reproduction of lateral GRFs - background theory

In the context of this work, inverse dynamics refers to the process whereby the acceleration of a rigid body combined with knowledge of the body's inertial parameters (mass and location of CoM) is used to determine the force required to produce the observed motion. This is achieved through the application of Newton's second law [83]. Thus, if the human body is considered as a connected linkage of rigid bodies, by combining individual body segment accelerations with their associated inertial parameters, it is possible to determine the resultant, external GRF. When confined to accelerations and forces in the lateral direction/frontal plane only, this relationship is stated mathematically as,

$$F_{lat} = \sum_{i=1}^{N} m_i \, \ddot{x}_i \tag{6.4.1}$$

in which F_{lat} is the lateral/frontal plane component of the GRF, while m_i and $\ddot{x}_i$ are the mass and frontal plane acceleration (measured at the CoM) of the i^{th} of N body segments.

The success of this technique was recently demonstrated for human bouncing and jumping forces [12]. However, body segment accelerations must be determined through the double differentiation of marker displacement data. As such the derived accelerations are susceptible to high frequency noise in the original signal, such as can arise due to movement of the marker relative to the underlying bony structure. This is often termed soft-tissue artifact and results from the relative movement of the soft tissue

on which the marker is placed, particularly during heel contact. The range of frontal plane motion during locomotion is relatively low compared to bouncing or jumping, therefore the marker displacement signal-to-noise ratio makes accurate reproduction of the GRF potentially problematic, requiring judicious post-processing. The raw marker data was initially low pass filtered at 6 Hz (BW4). Marker accelerations were obtained through double differentiation of marker displacements with the same 6 Hz (BW4) filter applied between each differentiation step.

The remaining requirement is to determine a suitable kinematic model of the human body in order that individual segment masses and CoM locations can be determined. There is extensive anthropometric data in the literature dating back to cadaver studies in the mid to late 19^{th} century. More recently, Zatsiorsky et al. [84] used gamma-ray scanning techniques to determine body segment masses and CoM locations relative to nearby bony landmarks. Zatsiorsky et al's data set contains 115 (100 male & 15 female) Caucasian subjects with mean ages of 24 and 19 years respectively. In order to increase the useability of Zatsiorsky et al's data, de Leva [25] referenced the mean CoM locations to the relevant proximal and distal joint centres, Fig. 6.6, a more practical option for the kinetic analysis presented herein.

In this work the subject's body model will be divided into 15 segments as follows: feet, shanks, thighs, pelvis, trunk consisting of abdomen and thorax regions, hands, forearms, upper arms and head. Due to the comprehensive data set upon which de Leva's body model is based [84], the segment masses as a proportion of overall subject mass and segment CoM location, used in this study, will as per de Leva's proposal [25].

The reproduced GRF, $F_{L,rep}$ is therefore obtained as,

$$F_{L,rep} = \sum_{i=1}^{15} m_{s,i}\, \ddot{x}_{s,i} \tag{6.4.2}$$

in which $m_{s,i}$ and $\ddot{x}_{s,i}$ are the mass and CoM (frontal plane) acceleration of the i^{th} of 15 body segments described previously.

In the following section (6.4.1) the above method of force reproduction is demonstrated for subjects walking on both a static and oscillating test rig. Representative data sets relating to subjects 1 and 3 is resented.

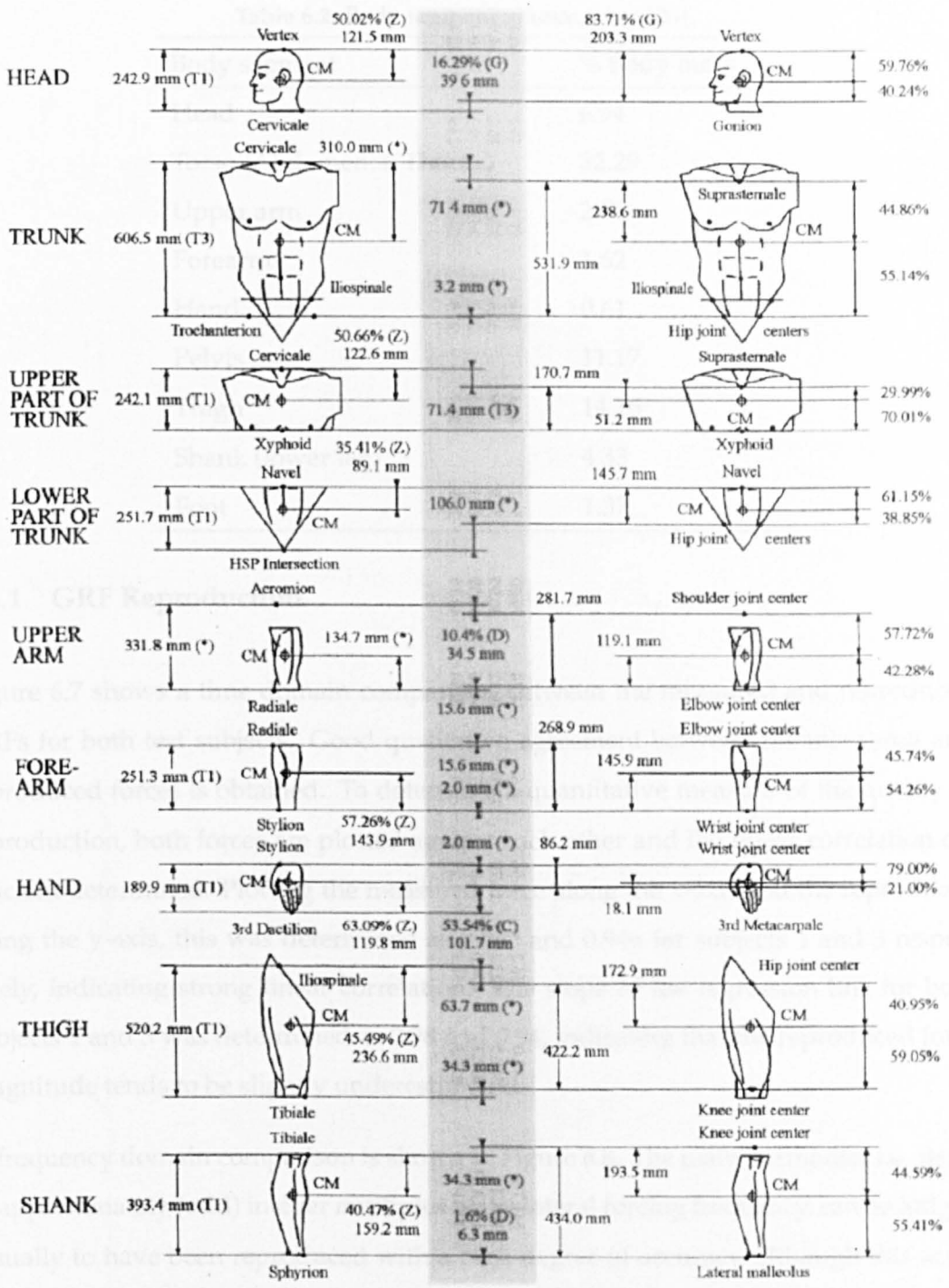

Figure 6.6: A graphic description of the main adjustments to the relative CoM positions for males. The adjusted distances are shown on the right of the shaded area. For all segments, except trunk and upper arm, the shaded area indicates the longitudinal distance between original (on its left) and new (on its right) reference points. All percent values are relative to the segment lengths indicated on their left, after [25].

Table 6.2: Body segment masses, after [25].

Body segment	% Body mass
Head	6.94
Torso (Abdomen + Thorax)	32.29
Upper arm	2.71
Forearm	1.62
Hand	0.61
Pelvis	11.17
Thigh	14.16
Shank (lower leg)	4.33
Foot	1.37

6.4.1 GRF Reproduction

Figure 6.7 shows a time domain comparison between the measured and reproduced GRFs for both test subjects. Good qualitative agreement between the measured and reproduced forces is obtained. To determine a quantitative measure of the quality of reproduction, both forces are plotted against each other and the linear correlation coefficient determined. Plotting the measured force along the x-axis and the reproduced along the y-axis, this was determined as 0.950 and 0.946 for subjects 1 and 3 respectively, indicating strong linear correlation. The slope of the regression line for both subjects 1 and 3 was determined as 0.98 and 0.94, indicating that the reproduced force magnitude tends to be slightly underestimated.

A frequency domain comparison is shown in Figure 6.8. The main harmonics i.e. those at approximately (odd) integer multiples of the lateral forcing frequency, can be judged visually to have been reproduced with a high degree of accuracy, although this accuracy diminishes for higher frequencies. In the case of human-induced lateral bridge vibration, these higher frequency force components beyond a narrow bandwidth centred on the fundamental harmonic, are of little practical interest. The percentage difference in the area under the full spectrum (up to 5 Hz) for the measured and reproduced forces was 7.4 % and 5.5 % for subjects 1 and 3 respectively. Table 6.3 summarises the percentage difference in the most significant harmonics for each subject. The good agreement observed again underlines the quality of force reproduction. This increases confidence

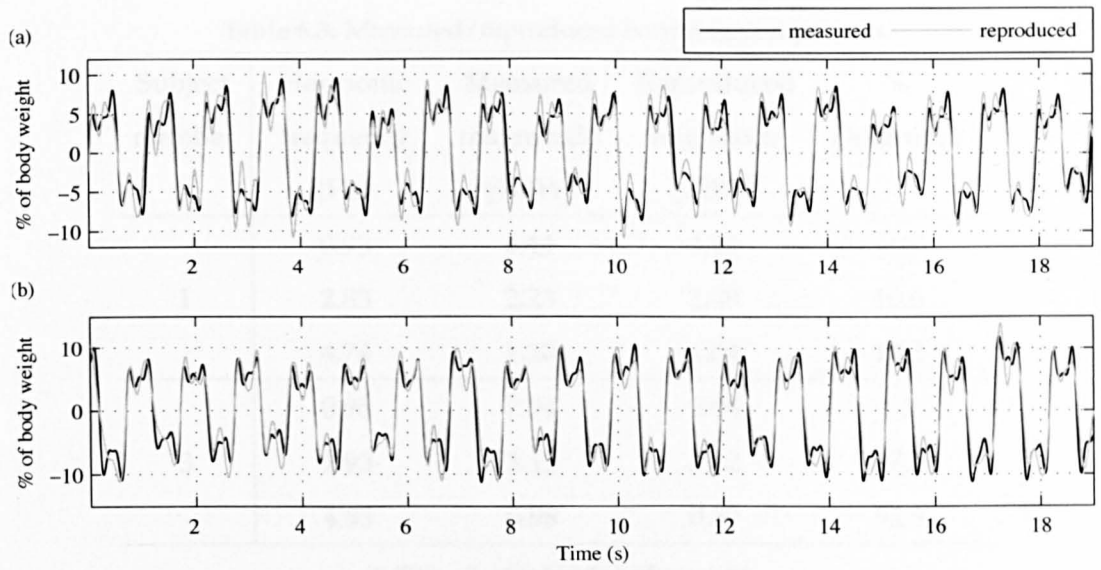

Figure 6.7: Comparison between the measured and reproduced GRFs while walking on a static deck for (a), subject 1 and (b), subject 3.

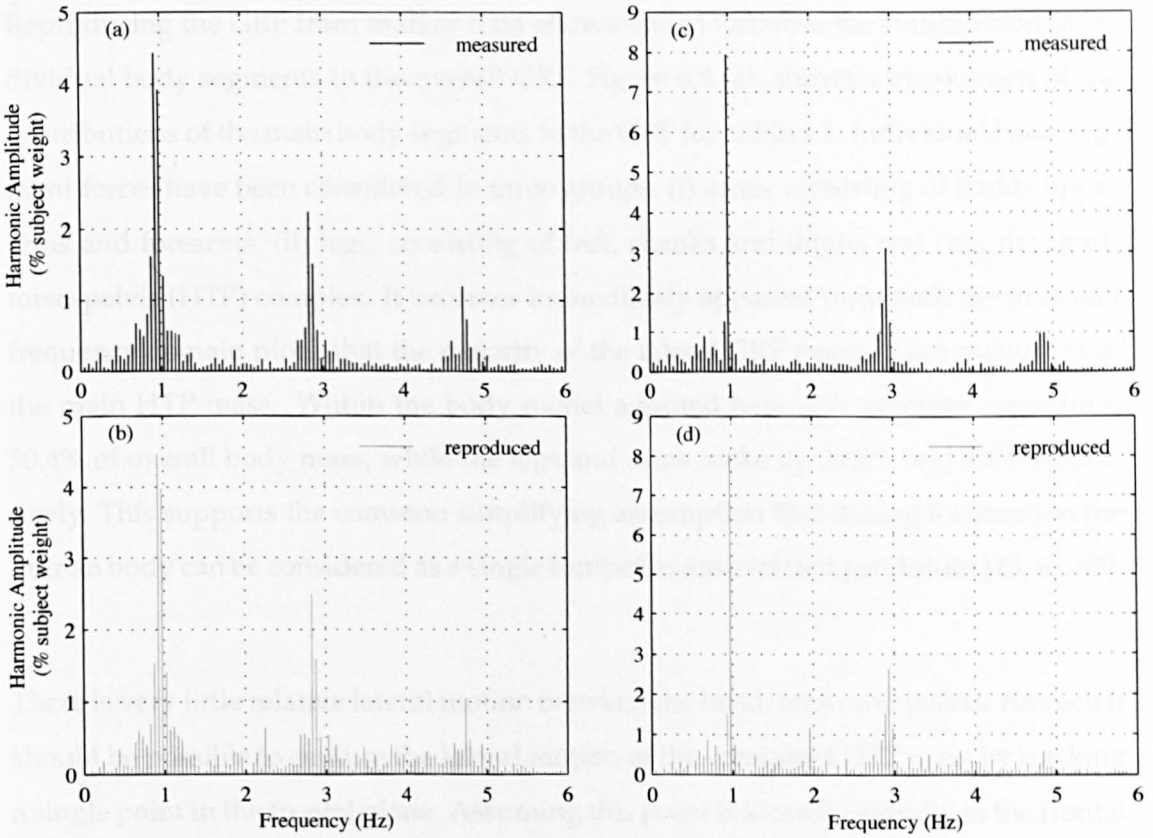

Figure 6.8: Discrete harmonic components of the measured and reproduced GRF for subject 1, (a) & (b) and subject 3, (c) & (d).

in both the quality of marker data obtained and the validity of the 15 segment body

Table 6.3: Measured/reproduced harmonic comparison.

Subject number	Harmonic frequency (Hz)	Measured magnitude (%BW)	Reproduced magnitude (%BW)	% Difference
1	0.93	4.44	4.44	0.0
	2.83	2.23	2.48	10.6
	4.74	1.20	1.04	14.3
3	0.98	7.94	8.04	1.3
	2.93	3.12	2.62	17.4
	4.83	0.98	0.57	52.9

(%BW) = % of subject's body weight

model used.

Reproducing the GRF from marker data allows one to visualise the contribution of individual body segments to the overall GRF. Figure 6.9 (a), shows a breakdown of the contributions of the main body segments to the GRF for subject 1. Individual body segment forces have been considered in three groups, (i) arms, consisting of hands upper arms and forearms, (ii) legs, consisting of feet, shanks and thighs and (iii), the head-torso-pelvis (HTP) complex. It becomes immediately apparent from both the time and frequency domain plots, that the majority of the lateral GRF results from oscillation of the main HTP mass. Within the body model adopted here, this complex constitutes 50.4% of overall body mass, while the legs and arms make up 39.8% and 9.8% respectively. This supports the common simplifying assumption that during locomotion the human body can be considered as a single lumped mass inverted pendulum [43, 65, 85].

There is very little relative lateral motion between the head, torso and pelvis. As such it should be possible to capture the lateral motion of the combined HTP mass by tracking a single point in the frontal plane. Assuming this point is located centrally in the frontal plane, the remaining task is to identify its vertical coordinate. In a further analysis two additional GRF estimates were produced by multiplying the combined mass of the HTP by the lateral acceleration of (i), the pelvis CoM and (ii), the torso CoM. There was negligible difference between both. Therefore the vertical position of the pelvis was

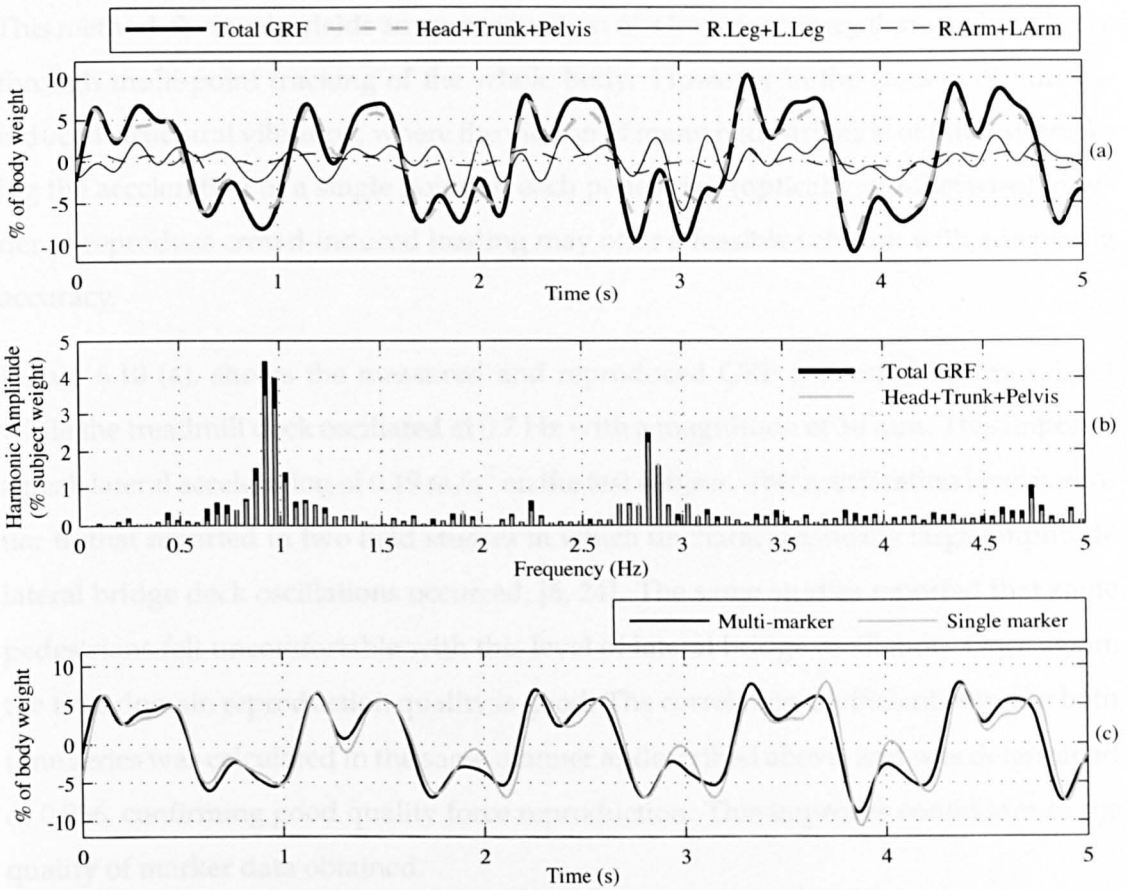

Figure 6.9: (a) Time domain and (b) frequency domain breakdown of body segment contributions to the GRF. (c) The GRF reproduced from multi-marker tracking of the HTP and single point tracking via two ASIS markers.

selected as a suitable vertical coordinate for single point force estimation. Conveniently, this corresponds approximately to a point midway between the two ASIS (anterior superior iliac spine) markers.

Thus, Fig. 6.9 (c) shows a comparison between the force reproduced from multi-point tracking (six markers on the pelvic frame, one on each acromion, one over the C7 vertebra and jugular notch and one on the side of the head) of the HTP and the force reproduced by multiplying the HTP mass with the acceleration of a single point at approximately waist level. The comparison shows reasonably good agreement demonstrating that the GRF can be approximated by associating the central HTP mass with the acceleration of a single point at waist level. It should be noted that when the subject's full body mass is multiplied by the acceleration of this single point, the accuracy of the reproduced GRF deteriorates; it significantly overestimates the actual GRF due largely to the unrealistic contribution from leg mass.

This method obviously yields an approximation of a lower accuracy than can be achieved through multi-point tracking of the whole body. However in the context of human-induced structural vibration, where the motion of many pedestrians is of interest, tracking the acceleration of a single point on each pedestrian (optically or otherwise) in order to reproduce crowd-induced loading may offer a feasible solution with acceptable accuracy.

Figure 6.10 (a), shows the measured and reproduced GRF generated by the subject while the treadmill deck oscillated at 0.7 Hz with a magnitude of 10 mm. This imposed a peak lateral acceleration of 0.19 m/s^2 on the test subject. This acceleration level is similar to that reported in two field studies in which uncharacteristically large amplitude lateral bridge deck oscillations occurred, [6, 24]. The same studies reported that some pedestrians felt uncomfortable with this level of lateral bridge oscillation. Once again, the time domain reproduction quality is good. The correlation coefficient between both time series was calculated in the same manner as described above, and was determined as 0.936, confirming good quality force reproduction. This improves confidence in the quality of marker data obtained.

In figure 6.10 (b), the contribution to the GRF from the three body segment groups, previously described, is shown. This again demonstrates that the majority of the GRF results from oscillation of the central head, torso, pelvis body mass. This supports use of the *'single lumped mass simplification'* while walking on an oscillating surface, i.e. in this instance, the net contribution to the GRF from arm movement is negligible. The GRF comparison between multi-point tracking and single-point tracking of the HTP is demonstrated in plot (c). The agreement demonstrated in this case supports the use of single point tracking in situations were an approximation of the GRF is sufficient rather than a full picture of whole body balance.

In their work, Ricciardelli and Pizzimenti [86] and Ingólfsson [11] identified the presence of an additional GRF component that arises due to interaction between the walking pedestrian an the oscillating deck. This additional interaction force is manifested as additional force harmonics on either side of the main walking force harmonics, although typically only those around the fundamental force harmonic are well defined. One of the additional harmonics always occurs at the base oscillation frequency and

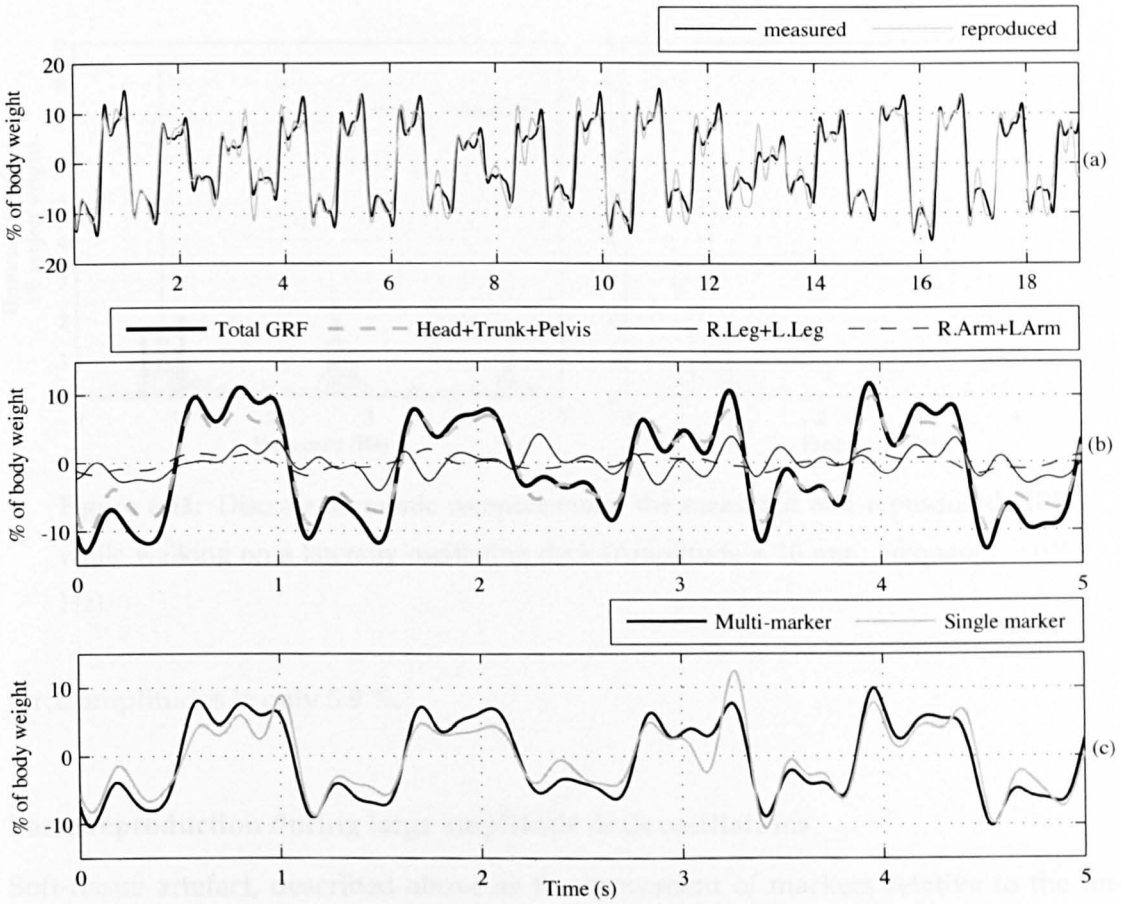

Figure 6.10: (a) Comparison between the measured and reproduced GRFs while walking on a laterally oscillating deck (Amplitude = 10 mm, Frequency = 0.7 Hz) (b) Time domain breakdown of body segment contributions to the GRF. (c) The GRF reproduced from multi-marker tracking of the HTP and single point tracking via two ASIS markers.

crucially, arises in the absence of step frequency tuning. This harmonic is often referred to as a self-excited GRF and is thought to be responsible for initiating large amplitude lateral bridge oscillations. The equivalent mass and damping effects of this force have been comprehensively characterised in [11].

Figure 6.11 (a) & (b) shows the measured and reproduced FFT of the GRF for the above mentioned dynamic test. In both instances the interaction force is shown by the heavy lines. The self-excited force, resonating with deck motion can be seen at 0.7 Hz in the spectrum. Comparing (a) and (b), it can be seen that individual force harmonics are reproduced with a reasonable degree of accuracy. The percentage difference between the measured (1.65 % body weight) and reproduced (1.75 % body weight) self-excited

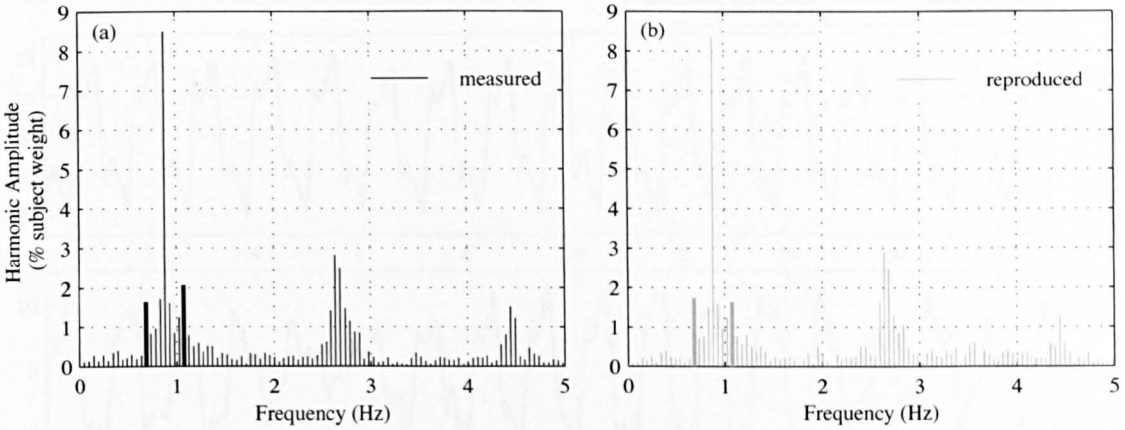

Figure 6.11: Discrete harmonic components of the measured and reproduced GRF while walking on a laterally oscillating deck (Amplitude = 10 mm, Frequency = 0.7 Hz).

force amplitudes is only 5.9 %.

Force reproduction during large amplitude deck oscillations

Soft-tissue artefact, described above as the movement of markers relative to the underlying bone structure is typically more prevalent a higher pacing rates and during jogging or running which include a flight phase during which the body is no longer in contact with the ground. When the foot strikes the ground, particularly after the flight phase, the peak acceleration experienced results in inertia forces that induce marker movement. This suggests that reproducing GRFs from marker data may be less successful for tests involving larger peak deck accelerations.

However, when the force reproduction method was employed for tests in which the largest peak deck accelerations were imposed, there was found to be no deterioration in the quality of reproduction. Figure 6.12 shows a comparison between measured and reproduced GRFs for subject 1 during which the deck was driven laterally with an amplitude of 50 mm at frequencies of 0.9, 1.0, & 1.1 Hz. The correlation coefficients determined were 0.967, 0.969 and 0.962 respectively. This indicates that when walking on a laterally oscillating structure, soft-tissue artefact does not limit the application of the force reproduction methods described herein.

The preceding discussion has clearly demonstrated that visual marker data can be used

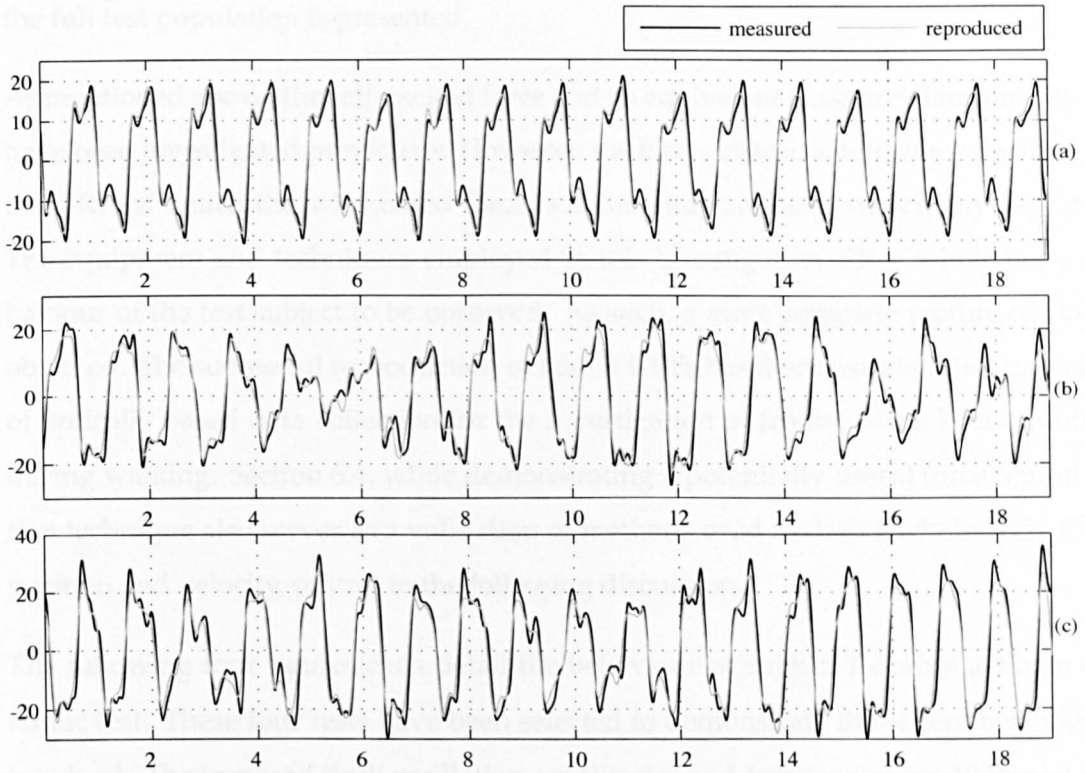

Figure 6.12: Comparison between the measured and reproduced GRFs while walking on a laterally oscillating deck with amplitude 50 mm and frequency (a) 0.9 Hz (correlation coefficient = 0.967), (b) 1.0 Hz (correlation coefficient = 0.969) and (c) 1.1 Hz (correlation coefficient = 0.962).

to successfully reproduce lateral GRFs. Furthermore, this serves as a validation of sorts, conforming the quality of marker data and the applicability of the 15 segment body model used. As such there can be an enhanced level of confidence in the analyses that follow.

6.5 Gait behaviour and the self-excited force

In this section, an analysis of the balance behaviour exhibited by test subjects while walking on the laterally oscillating treadmill is presented. For brevity, and owing to the behaviours presented being typical, data from test subject 1 is discussed in detail. Furthermore, a subset of the full test matrix is sufficient to demonstrate the key biomechanical behaviours. The generality of the observations is then demonstrated by reporting data relating to all tests in which subject 1 took part. Finally, average data for

the full test population is presented.

As mentioned above, the self-excited force and its equivalent mass and damping effects have been investigated previously. However, the biomechanical behaviour resulting in the GRF, of which the self-excited force is a part, has not been sufficiently explored. The equipment and techniques employed in this investigation allow whole body behaviour of the test subject to be observed. As such, a more complete picture of HSI is obtained. The successful reproduction of lateral GRFs has demonstrated the suitability of optically based data collection for the investigation of frontal plane lateral motion during walking. Section 6.4, while demonstrating a potentially useful force reproduction technique also serves as a validation of methods used to derive whole body CoM position and velocity, central to the following discussion.

The following four figures each detail the behaviour of subject 1 during a single dynamic test. These four tests have been selected to demonstrate the salient behaviours involved. The imposed deck oscillation amplitudes and frequencies are 10 mm at 0.7, 0.9 and 1.1 Hz and 35 mm at 0.6 Hz. In all cases the pedestrian maintained a constant pacing frequency of 1.8 Hz, resulting in a lateral forcing frequency of 0.9 Hz throughout the tests.

Figure 6.13 (a) shows the subject's CoM oscillation relative to the moving deck (solid black line and left scale), the corresponding deck oscillation is also shown (solid grey line and right scale). Note that the underlying deck motion has been removed from all marker data, thus all reported subject motion is relative to the moving deck. Markers on the lateral aspect of the foot, at the heel and toe have been used to determine the position of the foot for each footstep (intermittent black lines), the position is calculated as the median point between both markers. It should be noted that this does not correspond to the CoP which is positioned approximately 30 to 40 mm medially of this point. The circle at each foot position, marks the average foot position for the duration of the footstep.

Plot (b) shows the step widths for successive steps, defined as the lateral distance between the mean foot position marks. The x-axis position of each vertical stem is determined as the mid-time between the foot positions used to calculate that step width. Plot (c) shows the directly measured GRF and plot (d) shows its harmonic components.

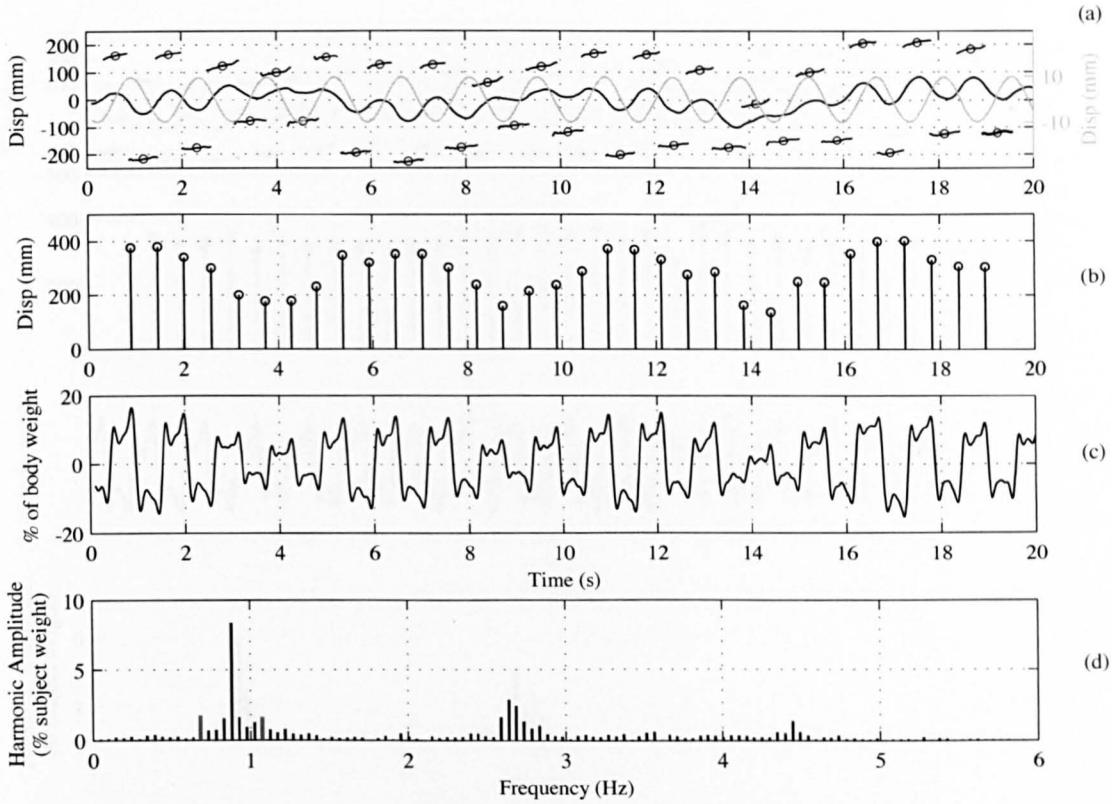

Figure 6.13: Deck oscillation amplitude = 10 mm, frequency = 0.7 Hz. (a) CoM oscillation (continuous black line and left scale), deck oscillation (continuous grey line and right scale) and lateral foot position (intermittent black line), (b) step widths, (c) directly measured GRF, (d) harmonic components of the directly measured GRF (interaction forces shown in red).

The most striking feature of the subject's behaviour is the alteration of their gait width. Closer inspection of plot (a) reveals that if the subject steps to the left in time with the rig's maximum leftward displacement (and vice versa on the right), the CoM oscillation amplitude is a minimum, eg. at $t \approx 4.5$ s. Conversely, when the subject steps in a direction opposite to the deck's motion and in time with the peak deck displacement, the CoM amplitude is at a maximum, eg. at ≈ 7.5 s. This is a direct result of the sinusoidally varying inertia force experienced by the subject due to the base acceleration. Owing to the different pacing and oscillation frequencies, this results in a periodic modulation of the CoM oscillation amplitude. Coincident with this, is a narrowing and widening of the subject's gait and as a result, modulation of the GRF occurs.

When the whole body behaviour responsible for the GRF is examined, it becomes apparent that the gait width and therefore the GRF is being modulated at a fixed fre-

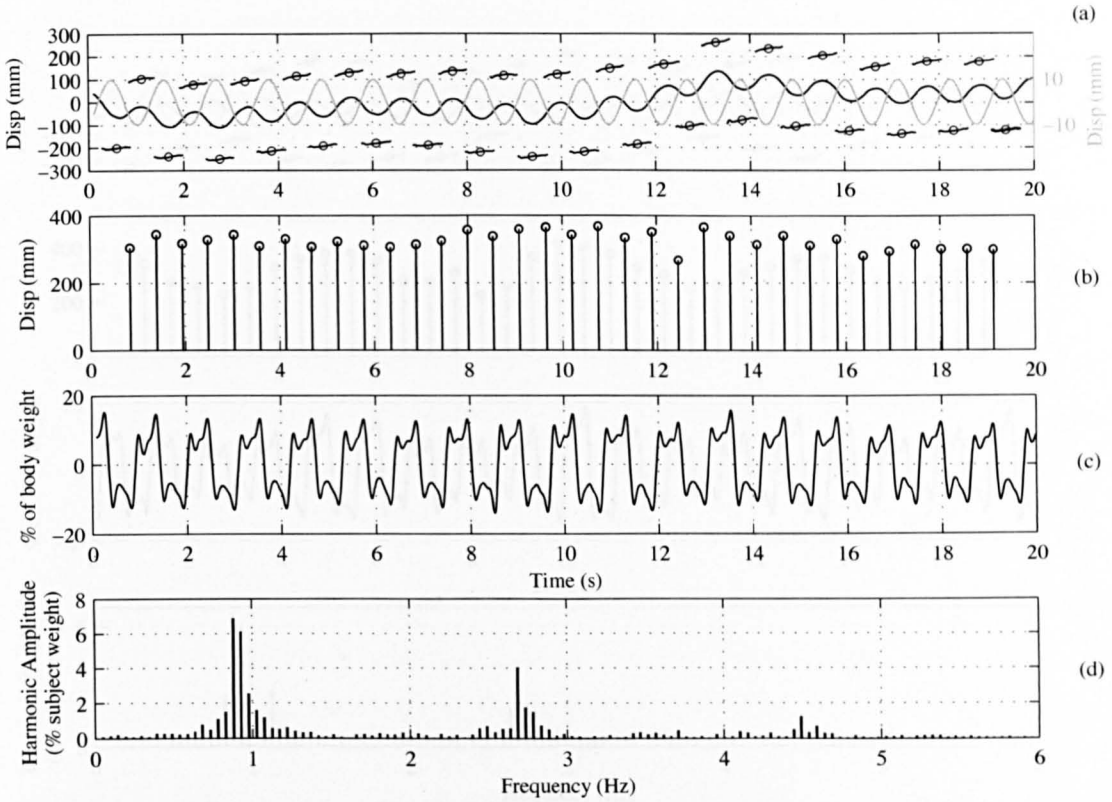

Figure 6.14: Deck oscillation amplitude = 10 mm, frequency = 0.9 Hz. (a) CoM oscillation (continuous black line and left scale), deck oscillation (continuous grey line and right scale) and lateral foot position (intermittent black line), (b) step widths, (c) directly measured GRF, (d) harmonic components of the directly measured GRF.

quency equal to the modulus of the difference between the lateral forcing frequency and the base oscillation frequency, in this case approximately 0.2 Hz or every 5 seconds. The gait width modulation is quantified through the percentage modulation depth, MD:

$$\text{MD} = 100 \times \frac{\text{wave peak} - \text{wave trough}}{\text{wave peak} + \text{wave trough}} \tag{6.5.1}$$

The wave peak was determined by discarding the maximum value of gait width and obtaining the average of the next two largest values. The corresponding procedure was applied to the minimum gait widths to determine the wave trough. In the case of Fig. 6.13, MD = 42%

Plot (d) shows the harmonic components of the GRF, the interaction force is shown in red. Notably, these are also spaced approximately 0.2 Hz on either side of the fundamental force harmonic, a measure predicted by the biomechanical behaviour described

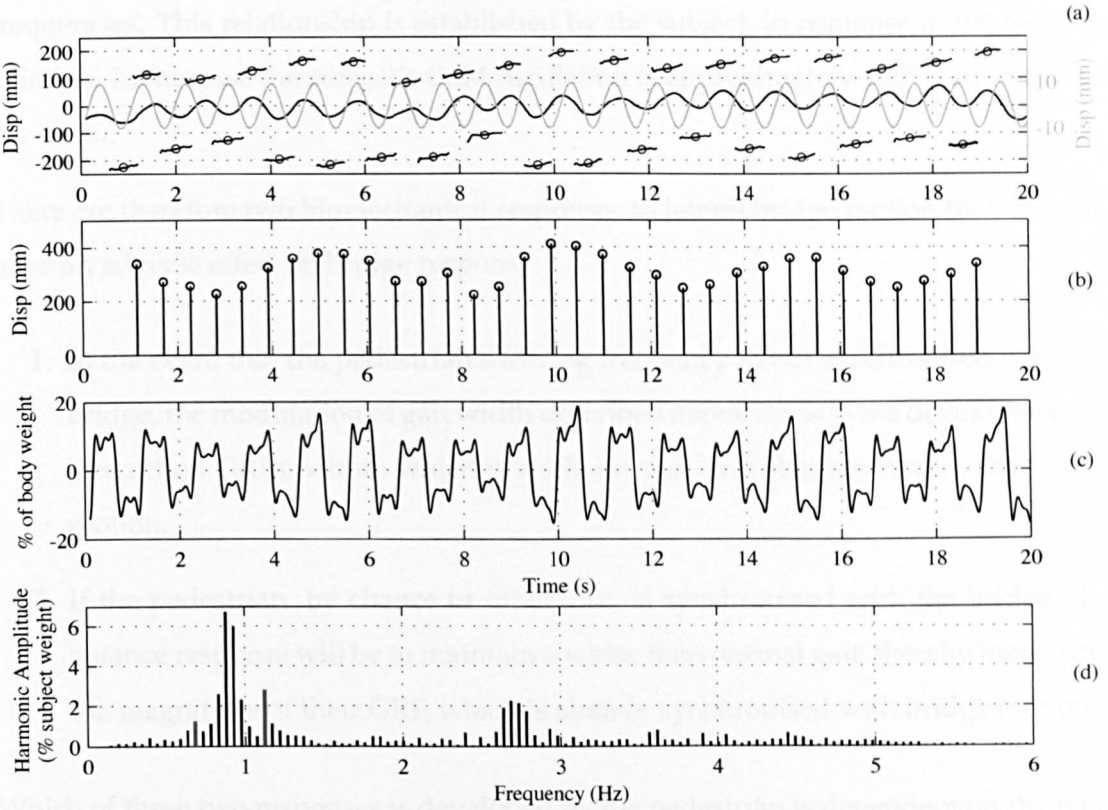

Figure 6.15: Deck oscillation amplitude = 10 mm, frequency = 1.1 Hz. (a) CoM oscillation (continuous black line and left scale), deck oscillation (continuous grey line and right scale) and lateral foot position (intermittent black line), (b) step widths, (c) directly measured GRF, (d) harmonic components of the directly measured GRF (interaction forces shown in red).

above.

In Fig. 6.14, the base oscillation amplitude is 10 mm but the frequency is increased to 0.9 Hz (peak lateral acceleration of 0.32 m/s^2). The alterations in gait width previously observed are notably absent, plot (a) and (b). CoM oscillation amplitude, gait width and GRF amplitude all remain relatively stable during the test. Due to the constant phase relationship between the subject's lateral forcing frequency and the deck oscillation frequency, the inertia force experienced by the subject remains the same from gait cycle to gait cycle. This eliminates the need to periodically alter foot placement position to maintain frontal plane stability, instead, the subject adopts a wider gait sufficient to deal with the imposed inertia force, leading to a scale increase in the GRF. The magnitude of the inertia force experienced by the subject at the time of foot placement is directly related to the phase relationship between lateral forcing and base oscillation

frequencies. This relationship is established by the subject, in response to the base oscillation. In this case the subject's CoM oscillation is approximately 155° behind that of the deck.

There are therefore two biomechanical responses to lateral bridge motion that, in turn, have an adverse effect on bridge response:

1. In the event that the pedestrian's forcing frequency in not synchronised with the bridge, the modulation of gait width described above leads to the development of interaction GRFs, within which is a self-excited force that resonates with bridge motion.

2. If the pedestrian, by chance or otherwise, is synchronised with the bridge, the balance response will be to maintain a wider than normal gait, thereby increasing the magnitude of their GRF, which is already synchronised with bridge motion.

Which of these two responses is developed by the pedestrian is dependent on the relationship between their lateral forcing frequency and the deck oscillation frequency. It should be noted that both responses can occur once pedestrian stability in the frontal plane is influenced by deck motion. Due to the sensitivity of the visual-vestibular system to frontal plane motion, this can occur for very low lateral acceleration amplitudes.

Figure 6.15 demonstrates the return of the gait width modulation behaviour (MD = 24%) after synchronisation is disturbed. Still oscillating with an amplitude of 10 mm but at a frequency of 1.1 Hz (0.48 m/s^2 peak acceleration), the familiar pattern of biomechanical behaviour is observed, as is the return of the self-excited component of the GRF, plot (d).

When the deck amplitude is increased to 35 mm, oscillating at 0.6 Hz (0.5 m/s^2 peak acceleration), Figure 6.16, the MD increases to MD = 42%. The minimum gait with observed is approximately 170 mm while the maximum is 510 mm. This compares to a maximum not exceeding 400 mm in the tests discussed previously. Associated with this is a corresponding increase in the MD of the GRF, plot (c). The frequency relationship between base oscillation and pedestrian pacing is demonstrated again in plot (b). The period of modulation is between 3 and 3.5 seconds, predicted by the modulus of the

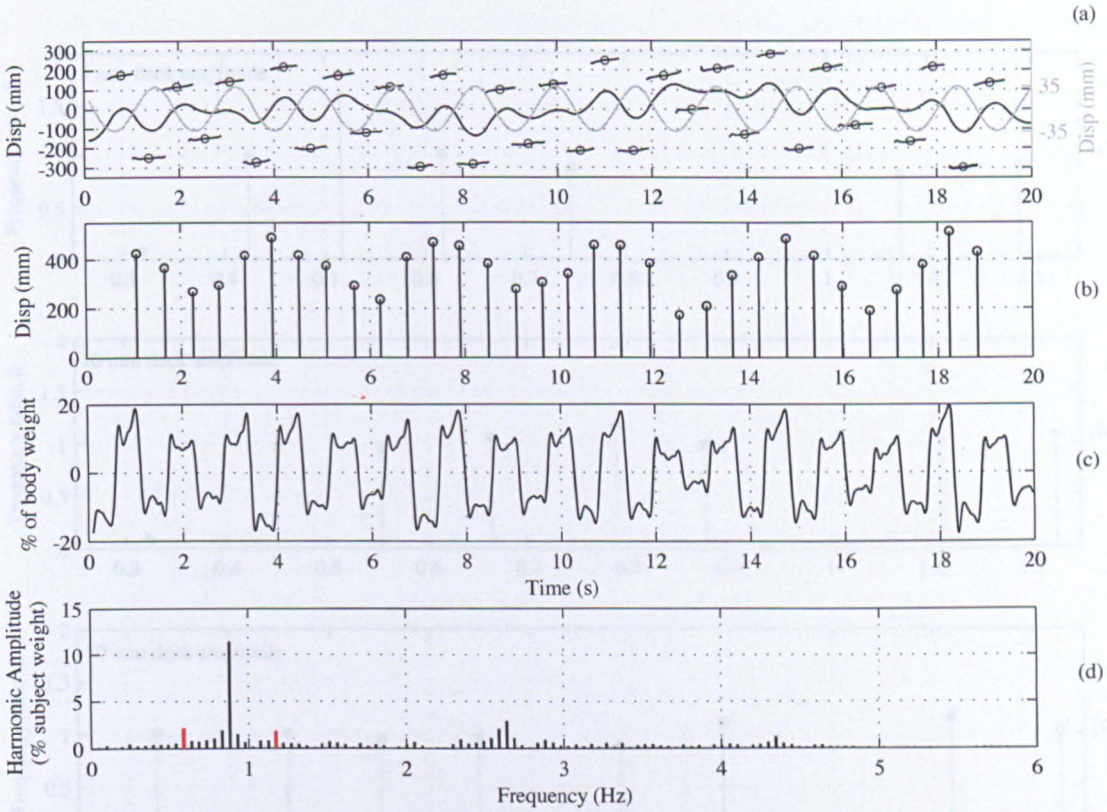

Figure 6.16: Deck oscillation amplitude = 35 mm, frequency = 0.6 Hz. (a) CoM oscillation (continuous black line and left scale), deck oscillation (continuous grey line and right scale) and lateral foot position (intermittent black line), (b) step widths, (c) directly measured GRF, (d) harmonic components of the directly measured GRF (interaction forces shown in red).

difference between the oscillation and lateral forcing frequencies, 0.3 Hz.

To investigate the generality of this frequency relationship, the factor β is defined as the ratio of observed modulation frequency to the modulation frequency predicted by the base oscillation and forcing frequency relationship:

$$\beta = \frac{\text{Observed modulation frequency}}{|f_{\text{base}} - f_{\text{subject}}|} \tag{6.5.2}$$

where f_{base} is the base oscillation frequency and f_{subject} is the frequency of the lateral GRF imposed by the subject. All frequencies required for the calculation of β are determined as the maximum amplitude harmonics obtained from a fast Fourier transform (FFT) of the underlying data. Figure 6.17 show the ratio β calculated for each test completed by subject 1. Note that β values for which $f_{\text{base}} \approx f_{\text{subject}}$ have been omitted as the parameter is not applicable under this frequency regime.

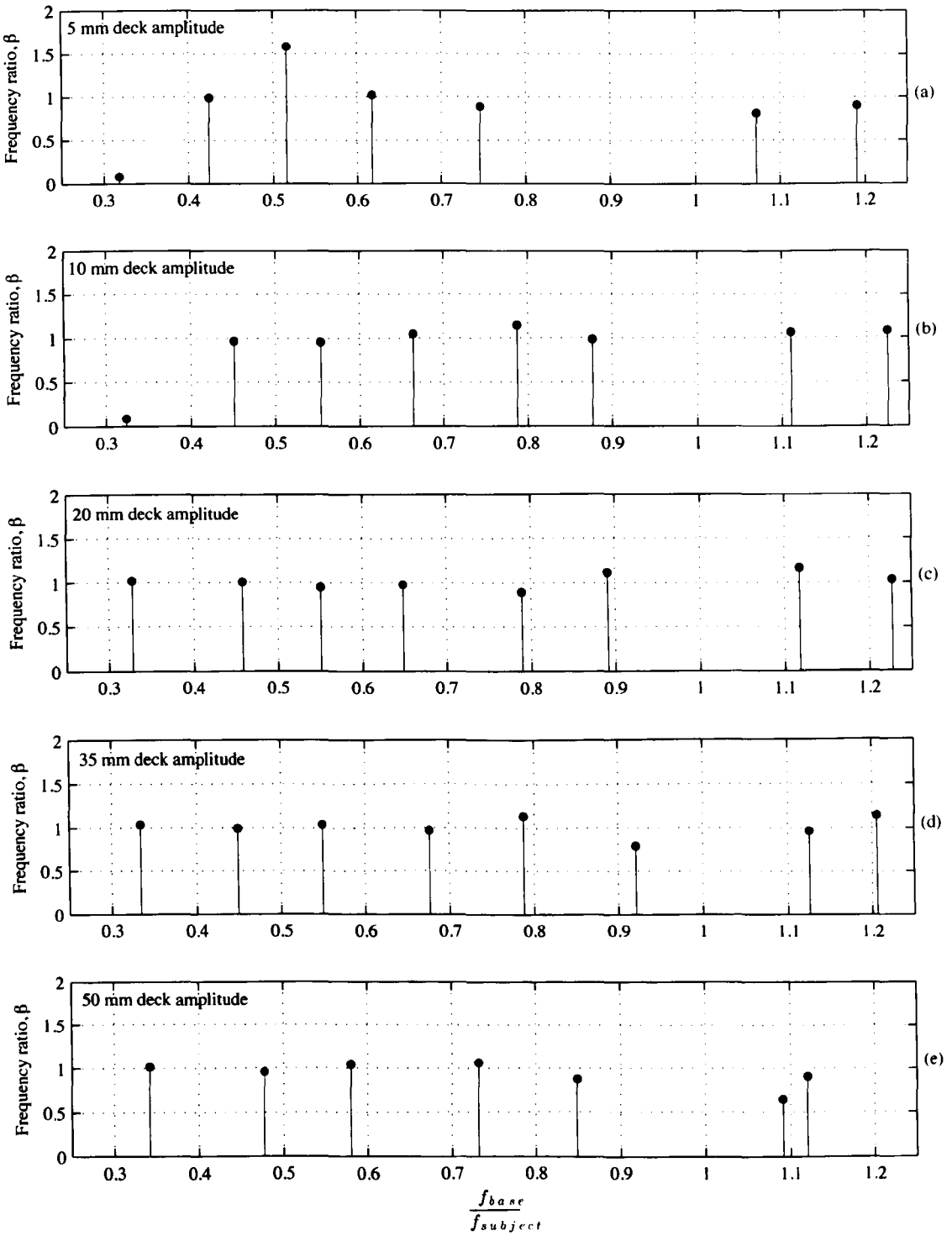

Figure 6.17: The ratio of observed gait width modulation frequency to that predicted by the expression, $|f_{\text{base}} - f_{\text{subject}}|$. Data shown for 5 mm (a), 10 mm (b), 20 mm (c), 35 mm (d) and 50 mm (e) amplitude tests, completed by test subject 1.

It can be seen that in the majority of cases $\beta \approx 1$, indicating that a periodic gait width modulation is generally occurring at a frequency equal to $|f_{\text{base}} - f_{\text{subject}}|$. The biome-

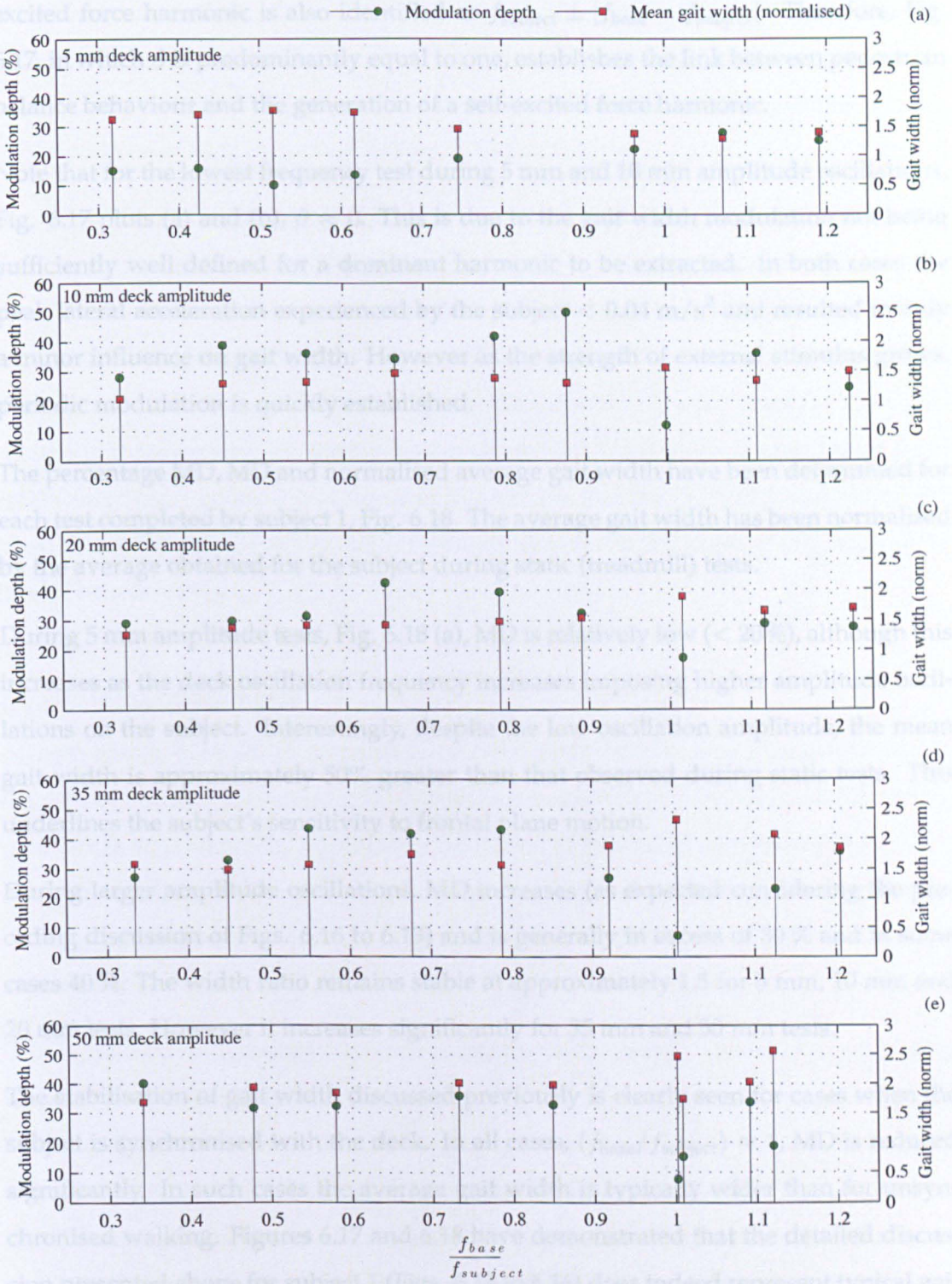

Figure 6.18: The percentage MD and normalised average gait width for each test completed by subject 1. Data shown for 5 mm (a), 10 mm (b), 20 mm (c), 35 mm (d) and 50 mm (e) amplitude tests.

chanical motivation for alteration of foot position has been identified as being a response to a sinusoidally varying inertia force. Furthermore, the frequency of the self-

excited force harmonic is also identified as $f_{subject} \pm |f_{base} - f_{subject}|$. Therefore, Fig. 6.17, in which β is predominantly equal to one, establishes the link between pedestrian balance behaviour and the generation of a self-excited force harmonic.

Note that for the lowest frequency test during 5 mm and 10 mm amplitude oscillations, Fig. 6.17 plots (a) and (b), $\beta \approx 0$. This is due to the gait width modulation not being sufficiently well defined for a dominant harmonic to be extracted. In both cases the peak lateral acceleration experienced by the subject $< 0.04\ m/s^2$ and resulted in only a minor influence on gait width. However as the strength of external stimulus grows, periodic modulation is quickly established.

The percentage MD, MD and normalised average gait width have been determined for each test completed by subject 1, Fig. 6.18. The average gait width has been normalised by the average obtained for the subject during static (treadmill) tests.

During 5 mm amplitude tests, Fig. 6.18 (a), MD is relatively low ($< 20\%$), although this increases as the deck oscillation frequency increases imposing higher amplitude oscillations on the subject. Interestingly, despite the low oscillation amplitude, the mean gait width is approximately 50% greater than that observed during static tests. This underlines the subject's sensitivity to frontal plane motion.

During larger amplitude oscillations, MD increases (as expected considering the preceding discussion of Figs. 6.16 to 6.13) and is generally in excess of 30 % and in some cases 40 %. The width ratio remains stable at approximately 1.5 for 5 mm, 10 mm and 20 mm tests. However it increases significantly for 35 mm and 50 mm tests.

The stabilisation of gait width discussed previously is clearly seen for cases when the subject is synchronised with the deck. In all cases, $(f_{base}/f_{subject}) \approx 1$, MD is reduced significantly. In such cases the average gait width is typically wider than for unsynchronised walking. Figures 6.17 and 6.18 have demonstrated that the detailed discussion presented above for subject 1 (Figs. 6.13 to 6.16) does indeed represent typical gait behaviour for that subject.

These analyses have been carried out for the remaining 9 subjects and average values of MD, Fig. 6.19 and normalised mean gait width, Figure 6.20, have been determined. The data has been sorted into frequency bins arranged as follows: Bins = [(0.25 - 0.35),

(0.36 - 0.45), (0.46 - 0.55), (0.56 - 0.65), (0.66 - 0.75), (0.76 - 0.85), (0.86 - 0.95), (0.96 - 1.05), (1.06 - 1.15), (1.16 - 1.25)]. The mean and standard deviation of data points in each bin was then determined. The mean frequency ratio in each bin is used to determine the x-axis position of each data point in Figs. 6.19 and 6.20.

The population average data for MD is in agreement with that presented for subject 1. For 5 mm amplitude tests, MD is approximately 20 % with very little ISV. However as the stimulus increases, so too does the MD. The tendency for gait widths to stabilise at a constant value and therefore reduce MD during synchronisation is also visible in the population data. Figure 6.20 also clearly demonstrated the tendency for mean gait widths to increase with increasing base acceleration. Despite ISV increasing as oscillation amplitude grows, it is reasonable to conclude that the biomechanical behaviour identified at the start of section 6.5 is representative of the test populations response to lateral base motion.

Equivalent square wave

As seen above, the balance response to external perturbations is to alter gait width. In the case of a sinusoidal lateral base motion, a sinusoidal gait width modulation develops; this in turn results in amplitude modulation of the lateral component of the GRF. It is this variation in foot placement that generates the interaction force of which the self-excited harmonic is a part, rather than the behaviour of the CoM during the single stance phase.

This is clearly demonstrated when one examines the frequency content of an equivalent square wave, mimicking foot placement positions but excluding any variation in GRF resulting from CoM motion during the single stance phase. Figure 6.21 (a), shows such a wave mimicking foot placements for the previous dynamic test (35 mm at 0.6 Hz). The harmonics components of the square-like wave are shown in plot (b). The interaction force harmonics are clearly visible at approximately $\pm$ 0.3 Hz of the main pacing frequency harmonics. This confirms the significance of frontal plane balance behaviour and the resulting alterations in foot placement as being central to the development of self-excited excitation forces in the absence of step frequency tuning.

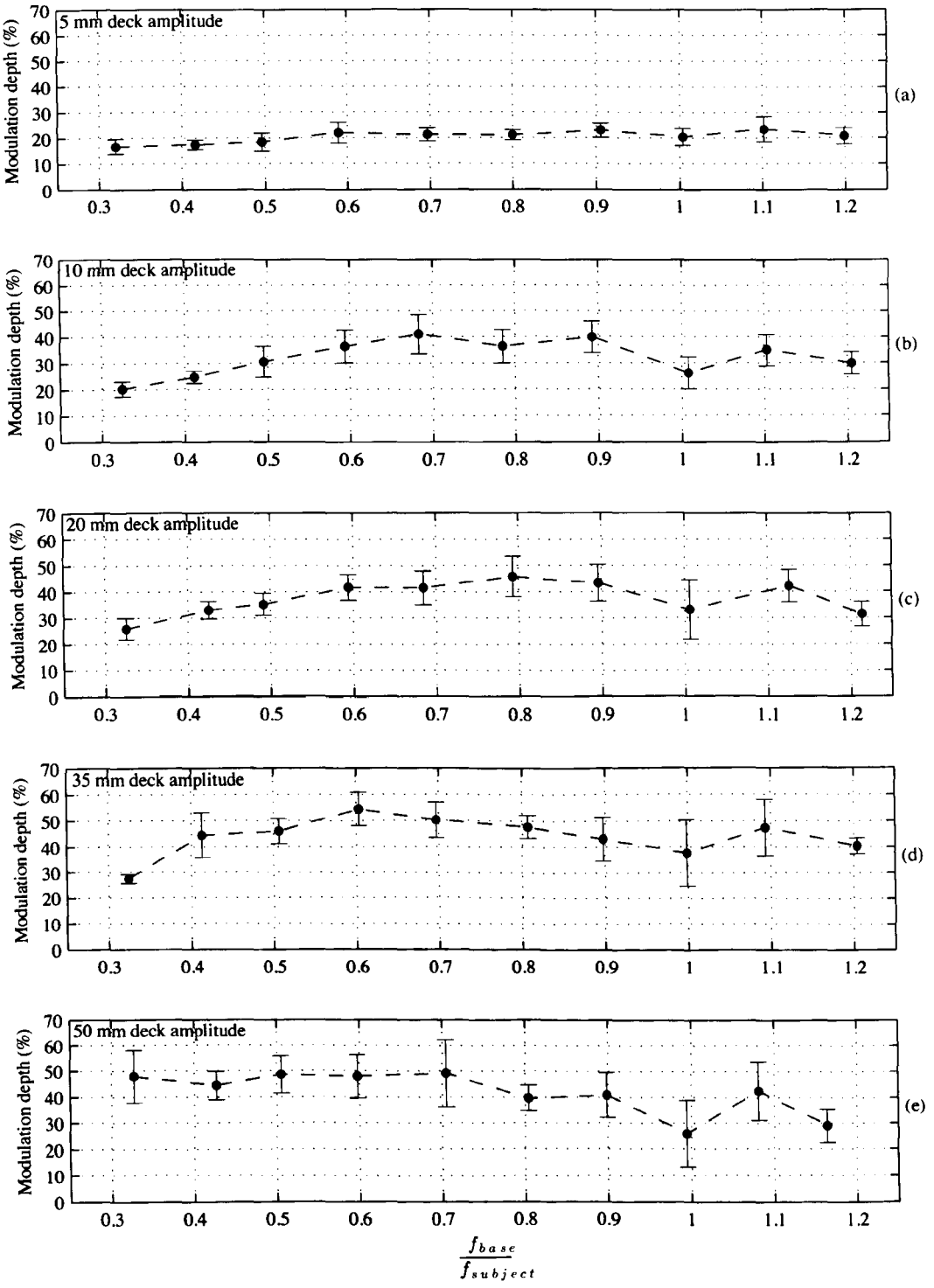

Figure 6.19: The percentage MD for 10 subjects. The mean ±0.5 standard deviations (i.e. full bar height = 1 SD) is plotted for each frequency bin within (a) 5 mm, (b) 10 mm, (c) 20 mm, (d) 35 mm and (e) 50 mm amplitude tests.

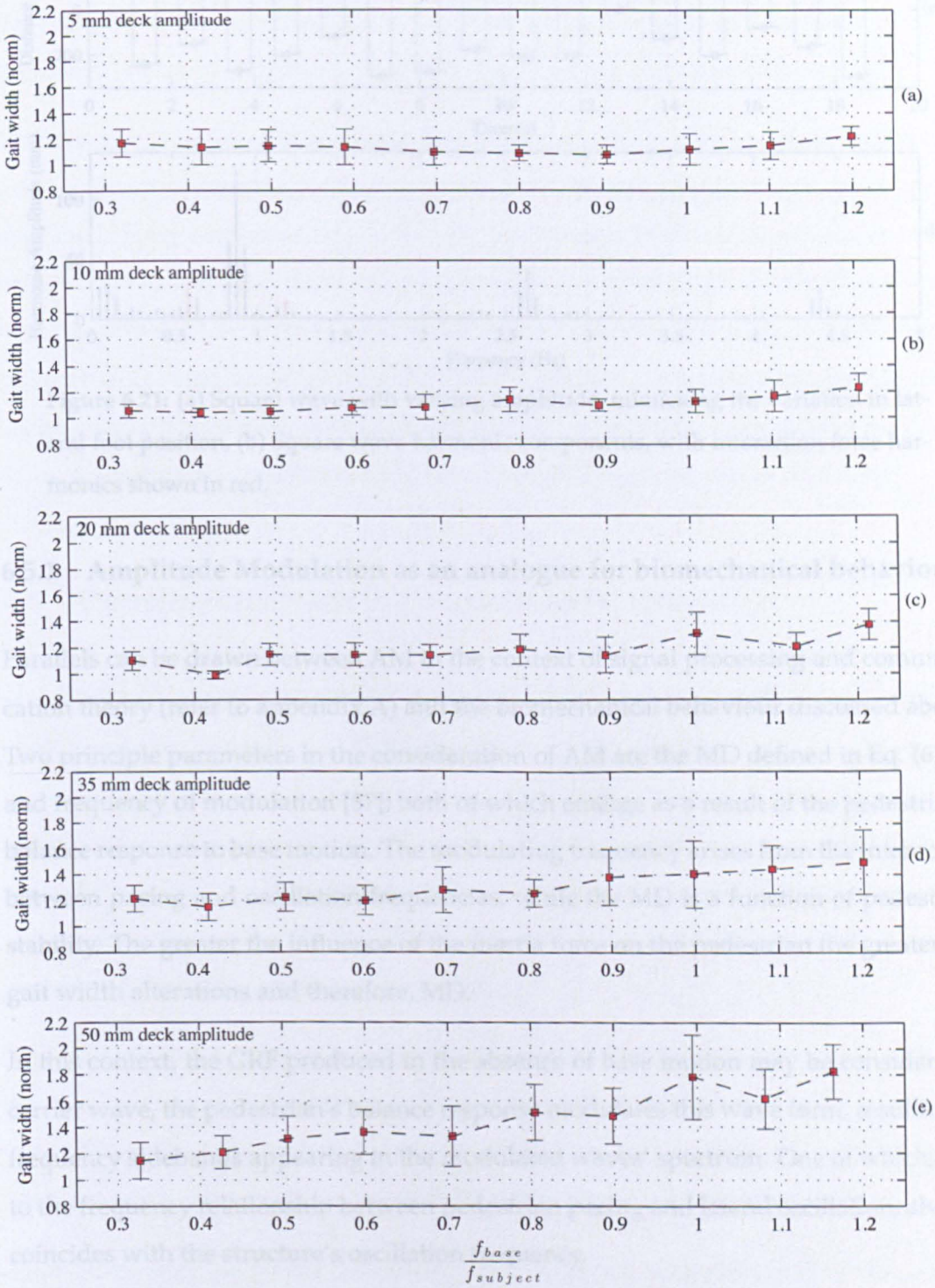

Figure 6.20: The mean normalised gait width for 10 subjects. The mean ± 0.5 standard deviations (i.e. full bar height = 1 SD) is plotted for each frequency bin within (a) 5 mm, (b) 10 mm, (c) 20 mm, (d) 35 mm and (e) 50 mm amplitude tests.

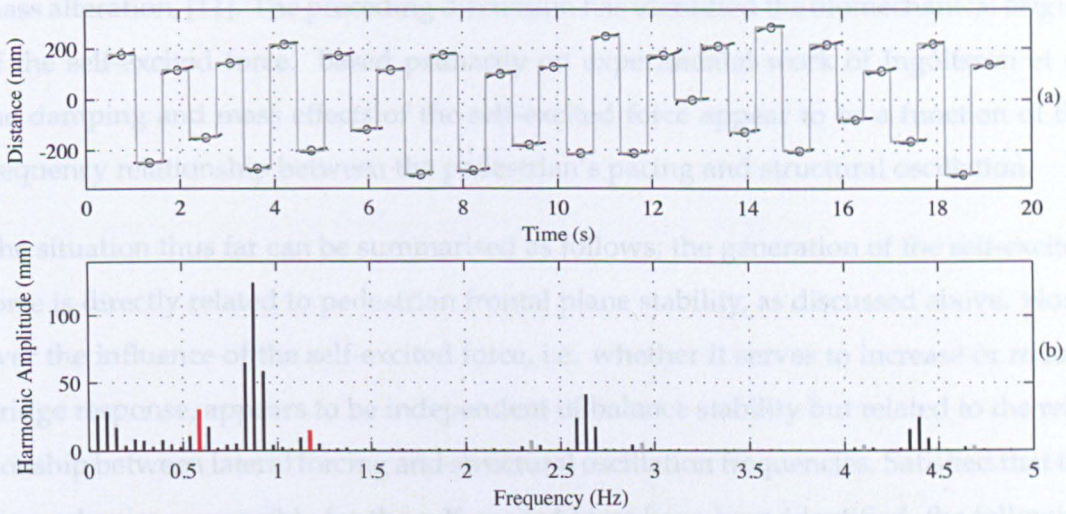

Figure 6.21: (a) Square wave with varying amplitude, mimicking the variation in lateral foot position, (b) Square wave harmonic components, with interaction force harmonics shown in red.

6.5.1 Amplitude Modulation as an analogue for biomechanical behaviour

Parallels can be drawn between AM in the context of signal processing and communication theory (refer to appendix A) and the biomechanical behaviour discussed above. Two principle parameters in the consideration of AM are the MD defined in Eq. (6.5.1) and frequency of modulation [87]; both of which emerge as a result of the pedestrian's balance response to base motion. The modulating frequency arises from the interaction between pacing and oscillation frequencies, while the MD is a function of pedestrian stability. The greater the influence of the inertia force on the pedestrian the greater the gait width alterations and therefore, MD.

In this context, the GRF produced in the absence of base motion may be considered a carrier wave, the pedestrian's balance response modulates this wave form, resulting in frequency sidebands appearing in the modulated waves' spectrum. One of which, due to the frequency relationship between pedestrian pacing and lateral oscillation, always coincides with the structure's oscillation frequency.

The influence of the self-excited force on the structure is of course dependent on the phase relationship between the force and structural motion. A common approach is to identify the component of the self-excited force in phase with structural velocity and acceleration and therefore characterise its influence as a structural damping and

mass alteration, [11]. The preceding discussion has identified the biomechanical origins of the self-excited force. Based primarily on experimental work of Ingólfsson et al. the damping and mass effects of the self-excited force appear to be a function of the frequency relationship between the pedestrian's pacing and structural oscillation.

The situation thus far can be summarised as follows; the generation of the self-excited force is directly related to pedestrian frontal plane stability, as discussed above. However the influence of the self-excited force, i.e. whether it serves to increase or reduce bridge response, appears to be independent of balance stability but related to the relationship between lateral forcing and structural oscillation frequencies. Satisfied that the biomechanics responsible for the self-excited force have been identified, the following chapter seeks to assess the suitability of the inverted pendulum model used in chapter 8, for simulating the pedestrian CoM behaviour and resulting self-excited force.

6.6 Conclusions from the experimental campaign

In this experimental investigation, subject balance behaviour while walking on both a stationary and laterally oscillating treadmill was investigated with the aid of a 3D motion tracking camera system. The approach in this campaign was to investigate the behaviour of a relatively small number of subjects, but in greater detail than has typically been the case in the literature thus far. A more statistically robust investigation aiming to further generalise the above observations and conclusions made herein, is considered the next evolution of this work.

The analysis and discussion of experimental data is divided into two sections. In section 6.4, validation of the inverse dynamics method used to reproduce the lateral GRF is presented. In section 6.5, subject balance behaviour was analysed in order to better understand the root cause or source of the self-excited GRF, identified in 6.4.

Reproduction of the lateral GRF proved successful for both static and dynamic tests. The agreement between directly measured and reproduced GRFs validates the method and increases confidence in the further use of the marker data to analyse subject biomechanics. More broadly, this suggests that continued use of optical techniques in the analysis of HSI, may continue to offer much greater insight.

The subject's balance response to deck oscillation is dominated by changes to lateral foot placement position. It has been confirmed that the interaction forces arise directly as a result of the foot placement position, which itself is a function of pedestrian stability. Furthermore, AM, from the field of communication theory has been identified as a mathematical analogue for the biomechanical behaviour observed.

The frequency of gait width modulation was identified as the modulus of the difference between the lateral forcing and deck oscillation frequencies. The underlying reason for this was revealed by examining the subject's CoM oscillation and recognising the influence of a sinusoidally varying inertia force imposed on the subject. Furthermore, the degree to which the subject alters their gait is determined by the degree to which their frontal plane stability is impaired by base motion. Thus the link between frontal plane balance behaviour and the generation of the self-excited component of the lateral GRF has been established.

It has also been identified that, when lateral forcing and deck oscillation frequencies are synchronised, the gait width stabilises to a width greater than would be observed on a stationary base. Thus two discrete biomechanical responses to lateral base motion have been identified that have an adverse influence on bridge response;

1. Modulation of gait width (and therefore GRF) leading to the development of interaction GRFs, within which is a self-excited force that resonates with bridge motion.

2. A stable increase in gait width when the forcing frequency is synchronised with the base oscillation frequency, increasing the magnitude of the GRF already synchronised with bridge motion.

Although there is a large degree of ISV, the fundamental HSI mechanism identified, namely periodic gait width modulation resulting in AM of the GRF, can be considered typical for the full test population.

Limitations within the campaign.

Throughout the execution of testing and the data analysis that followed, several limitations of the test campaign have been identified. They are briefly discussed here as

a cautionary note to future investigators. The influence of visual stimulus on a subject's behaviour is significant and should be considered. At the very least it should be monitored but if at all possible, should be controlled during testing.

Feedback between treadmill belt speed and subject walking velocity was identified during the rig design process as a desirable feature. However due to time and budget constraints this could not be achieved. Such a feature combined with longer test durations would allow one to investigate a subject's tendency to step synchronise with the oscillating deck. In this campaign, the subject's need to maintain a constant walking speed (to match the belt speed) biases any step synchronisation behaviour. As such no conclusions can be drawn regarding the subject's tendency to synchronise with the oscillating deck.

Despite these limitations, the principal aim of this test campaign, to identify the interaction mechanism through the novel use of motion capture equipment, has been satisfied. Thus a worthwhile contribution to the understanding of HSI has been made.

CHAPTER 7

Inverted pendulum model assessment

Chapter Summary

In this chapter the suitability of the inverted pendulum (abbreviated to IP in the remaining chapters) model, first presented in section 2.3, is assessed. The hypothesis regarding active CoM motion control is tested. This is achieved by comparing subject behaviour observed during testing with that predicted by the IP model.

CoM motion is discussed in section 7.1. The accuracy of the simulated GRF is considered in sections 7.2 and 7.3. Finally, conclusions are drawn in 7.4 regarding the suitability of the semi-active IP model for use in the context of civil engineering dynamics.

7.1 Passive versus active control

To investigate the suitability of the passive IP, a simple comparison between observed subject behaviour and model output is considered. Data relating to subject number 4 is discussed in detail before results for the test population are presented.

To facilitate the comparison, an IP model equivalent to the subject in question was established. The IP length was determined as the vertical distance to the subject's CoM (based on marker data and de Leva's model [25]), while the IP mass was equal to the subject's body mass.

7.1.1 IP-subject comparison: Stationary deck

The IP was first tuned to match the subject's observed behaviour during a stationary test in which no treadmill oscillation was imposed. IP initial mass position, velocity and support position were chosen to match the subject at the beginning of the simulation. In order to tune the IP behaviour to match the subject, the minimum stability margin, b_{min} from Eq. (2.3.18) was used as a tuning parameter. The cumulative area under the (absolute) GRF time history was compared for the IP and subject and b_{min} altered until the difference in areas was a minimum. Note that the subject's measured rather than reproduced GRF was considered. The final value selected for b_{min} in this case was 0.026 m resulting in an area difference of 1.1 %. Figure 7.1 shows the result of this tuning process for CoM position, velocity and acceleration, plots (a) to (c). Plot (d) shows a comparison between XCoM and CoP position for the subject and IP.

The initial drift in IP CoM trajectory results from a discrepancy between the IP and subject's (assumed) initial CoP position. The influence of this discrepancy is dissipated within the first two steps and has no bearing on the comparison thereafter. To facilitate the comparison, the mean value offset (determined after the first two steps have occurred) has been removed from both sets of data in plot (a). This removes the influence of the initial drift in simulated CoM motion, arising due to the initial CoP position inaccuracy. The same offsets have also been removed from the simulated and observed data in plot (d).

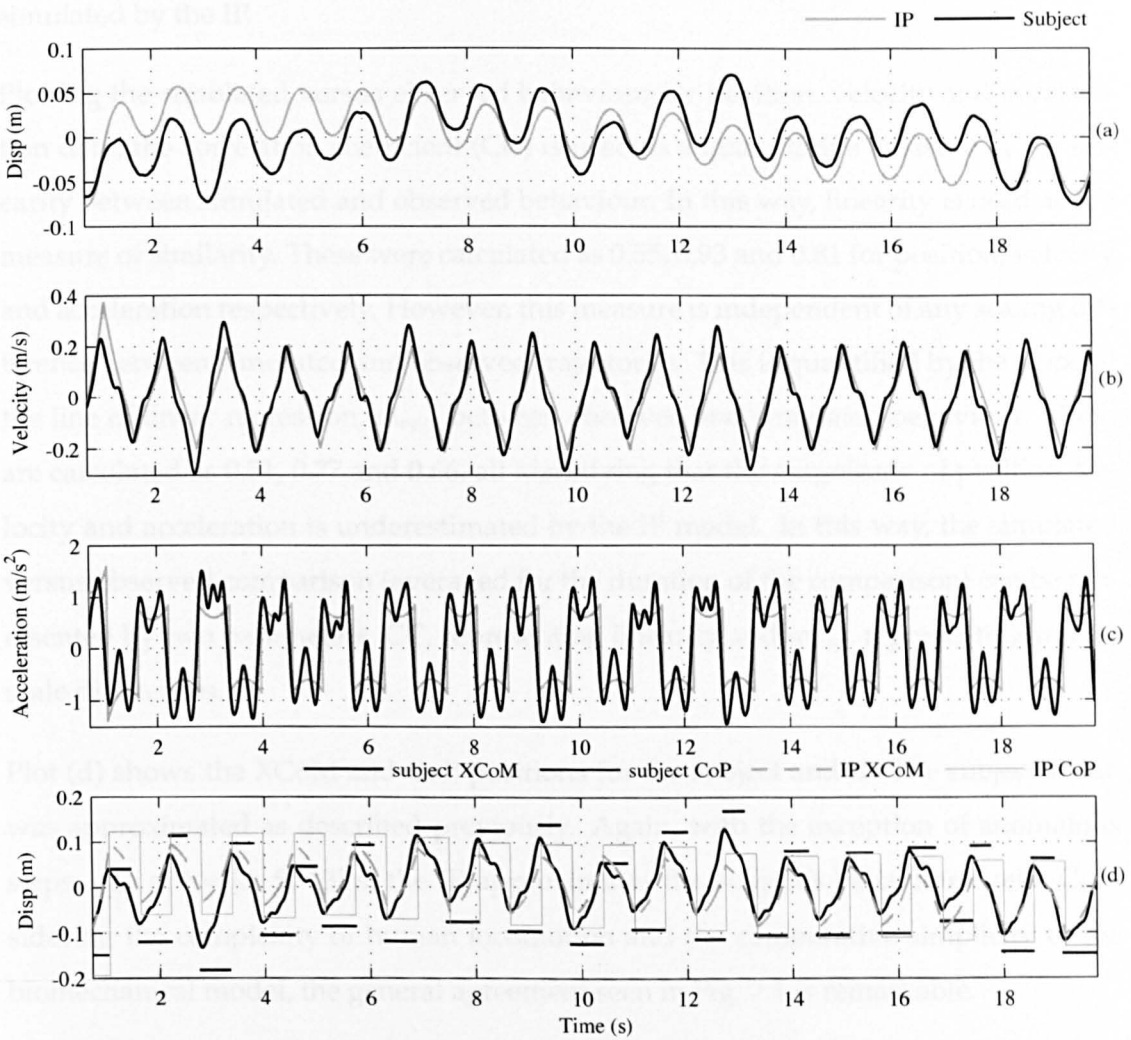

Figure 7.1: Comparison between subject and equivalent IP, (a) CoM position (correlation coefficient, CC = 0.55, slope of the linear regression line, m_{reg}= 0.51), (b) CoM velocity (CC/m_{reg} = 0.93/0.77), (c) CoM acceleration (CC/m_{reg} = 0.81/0.66) and (d) XCoM and CoP position. A constant medial offset of 35 mm has been applied to the recorded foot position to approximate the average position of the subject's CoP.

Considering the CoM position, velocity and acceleration comparisons in plots (a), (b) and (c), the IP appears to simulate the CoM trajectory quite well, particularly in the case of the CoM velocity, plot (b). With reference to plot (a), it is apparent that the IP model is unable to simulate 'atypical' CoM oscillations such as arise from the subject drifting across the treadmill deck as they walk. Nevertheless, the general character of the oscillatory behaviour agrees quite well. The CoM accelerations in plot (c) show good amplitude agreement (ensured by the b_{min} tuning process), although the subject's acceleration during the mid-stance deviates significantly from the smooth trajectory

simulated by the IP.

Plotting the simulated versus observed behaviour for position, velocity and acceleration data, the correlation coefficient (CC) is used as a quantitative measure of the linearity between simulated and observed behaviour. In this way, linearity is used as the measure of similarity. These were calculated as 0.55, 0.93 and 0.81 for position, velocity and acceleration respectively. However, this measure is independent of any scaling difference between simulated and observed trajectories. This is quantified by the slope of the line of linear regression, m_{reg}, between observed and simulated behaviour. These are calculated as 0.51, 0.77 and 0.66, all identifying that the magnitude of position, velocity and acceleration is underestimated by the IP model. In this way, the simulated versus observed comparison (averaged for the duration of the comparison) can be represented by two parameters, CC, representing linearity and m_{reg}, representing purely scale differences.

Plot (d) shows the XCoM and CoP positions for the subject and IP. The subject's CoP was approximated as described previously. Again, with the exception of anomalous steps, eg. at t = [3, 5, 13] s, the IP approximates the subject's behaviour well. Considering the complexity of human locomotion and the comparative simplicity of the biomechanical model, the general agreement seen in Fig. 7.1 is remarkable.

Figure 7.2 shows the GRF comparison. After tuning via the b_{min} parameter, the IP model reproduces the GRF amplitude with a good degree of accuracy. The red line, referred to as the *residual GRF*, indicates the difference between the subject's measured force and the IP simulated force. Due to the assumption of an instantaneous transfer between supporting legs, the simulated GRF deviates significantly from the measured force during the double stance phase. Furthermore since it is the single stance phase behaviour that is of interest in this investigation, the residual GRF has been set to zero during the double stance phase.

For static tests the residual force may be considered to represent the additional force resulting from the combination of intra-subject variability and the organic nature of human-behaviour. This is in contrast with the strict, repeatable mechanical behaviour produced by the IP model. Figure 7.3 (a) shows the frequency composition of the subject's GRF while plot (b) shows that of the residual GRF. It is clear from plot (b) that

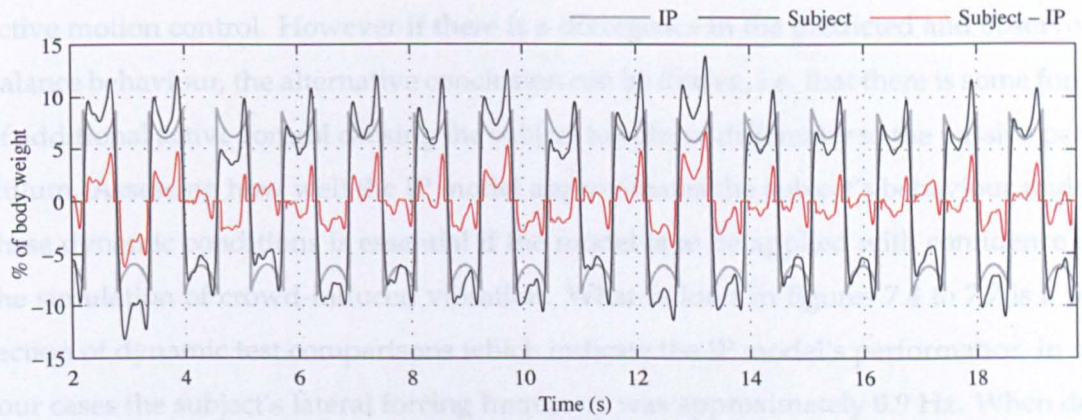

Figure 7.2: GRF comparison, measured GRF, IP simulated GRF and the difference between both during the single stance phase.

there are no dominant harmonics within the residual GRF and it's contribution to the measured GRF can be characterised as relatively low power noise.

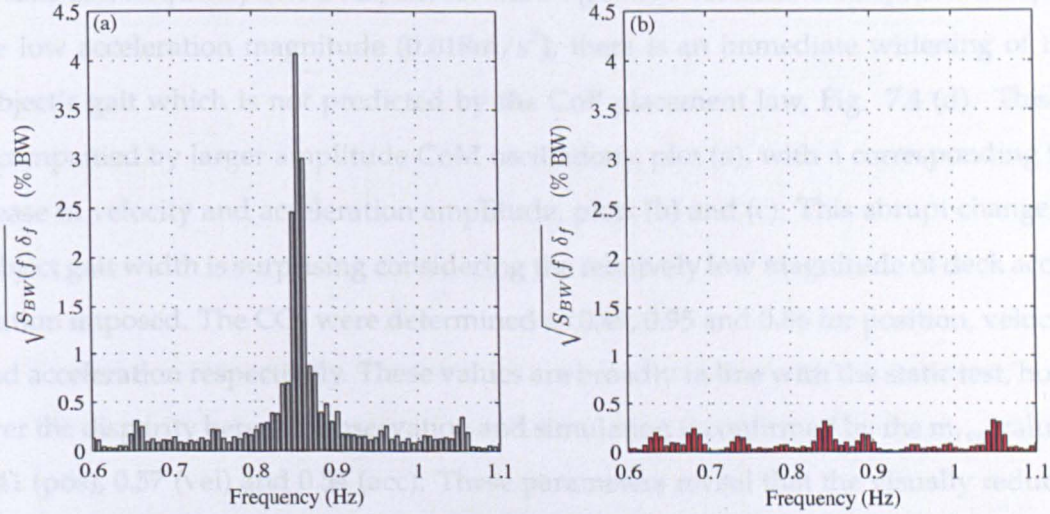

Figure 7.3: The frequency composition of (a), the subject's measured GRF and (b), the residual GRF. Bar plots show the RMS value of frequency contributions over fixed bandwidths. The bandwidths of vertical bars are determined by the frequency resolution ($\delta_f = 0.007$ Hz) of the underlying single sided power spectral density, $\hat{S}_{BW}(f)$.

7.1.2 IP-subject comparison: Oscillating deck

Having tuned the IP model to the specific subject under consideration, the comparison is now repeated for dynamic tests. If the model performs well, it can be concluded that a passive IP is sufficient to describe CoM motion and there is no need to implement

active motion control. However if there is a divergence in the predicted and observed balance behaviour, the alternative conclusion can be drawn, i.e. that there is some form of additional active control causing the subject to behave differently to the passive pendulum. Assessing how well the IP model approximates the subject's behaviour under these dynamic conditions is essential if the model is to be applied with confidence in the simulation of crowd-induced vibration. What follows in figures 7.4 to 7.7 is a selection of dynamic test comparisons which indicate the IP model's performance. In all four cases the subject's lateral forcing frequency was approximately 0.9 Hz. When determining the IP support placement position from Eq. (2.3.18), the CoM velocity *relative* to the moving deck was found to be appropriate. The significance of the velocity term is further discussed below.

Figure 7.4 represents the IP/subject comparison during lateral oscillations of 5 mm amplitude at a frequency of 0.3 Hz, the lowest magnitude acceleration imposed. Despite the low acceleration magnitude ($0.018 m/s^2$), there is an immediate widening of the subject's gait which is not predicted by the CoP placement law, Fig. 7.4 (d). This is accompanied by larger amplitude CoM oscillations, plot (a), with a corresponding increase in velocity and acceleration amplitude, plots (b) and (c). This abrupt change in subject gait width is surprising considering the relatively low magnitude of deck acceleration imposed. The CCs were determined as 0.49, 0.95 and 0.86 for position, velocity and acceleration respectively. These values are broadly in line with the static test, however the disparity between observation and simulation is confirmed by the m_{reg} values, 0.41 (pos), 0.57 (vel) and 0.54 (acc). These parameters reveal that the visually reduced agreement results from scaling differences due to the subject's wider gait, rather than any fundamentally different oscillatory behaviour. Indeed, the CCs for velocity and acceleration are marginally higher than those obtained during the static test

Figure 7.5 shows the comparison during lateral oscillations of 10 mm amplitude at a frequency of 0.5 Hz. The passive dynamics of the IP appear to predict reasonably well the subject's oscillatory behaviour in the face of this strengthening stimulus. This is particularly the case between $4s <= t <= 12s$, during which position, velocity and acceleration are well predicted. However atypical behaviour, eg. between $13s <= t <= 14s$ obviously cannot be predicted by the IP. The correlation and regression data was calculated as CC/m_{reg} = 0.64/0.34 (pos), 0.93/0.66 (vel) and 0.81/0.59 (acc). Both velocity

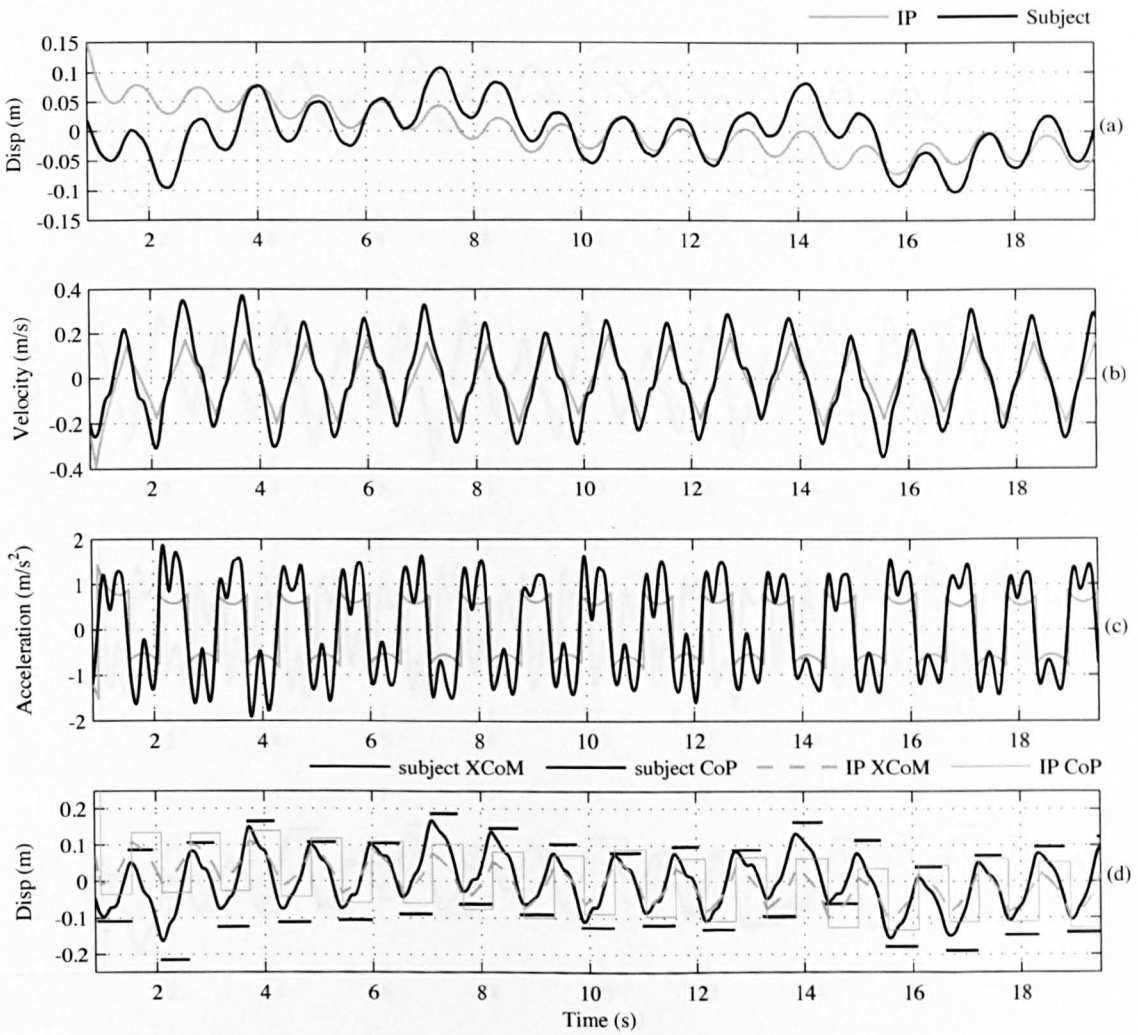

Figure 7.4: Comparison between subject and equivalent IP, deck oscillation 5 mm amplitude at 0.3 Hz. (a) CoM position (CC/m_{reg} = 0.49/0.41), (b) CoM velocity (CC/m_{reg} = 0.95/0.57), (c) CoM acceleration (CC/m_{reg} = 0.86/0.54) and (d) XCoM and CoP position. A constant medial offset of 35 mm has been applied to the recorded foot position to approximate the average position of the subject's CoP.

and acceleration simulation show similar parameter values to the tests discussed previously, however the position CC is noticeably improved, although significantly underestimated in terms of amplitude.

It can be postulated that the strengthening external stimulus leads to a convergence in simulated and observed CoM motion, i.e. the stronger the inertia force experienced by the subject, the more like a passive IP they behave during the single stance phase. It is at least reasonable to suggest that the passive nature of the IP model **is** sufficient to describe the subject's CoM oscillation in the presence of lateral base motion. That is

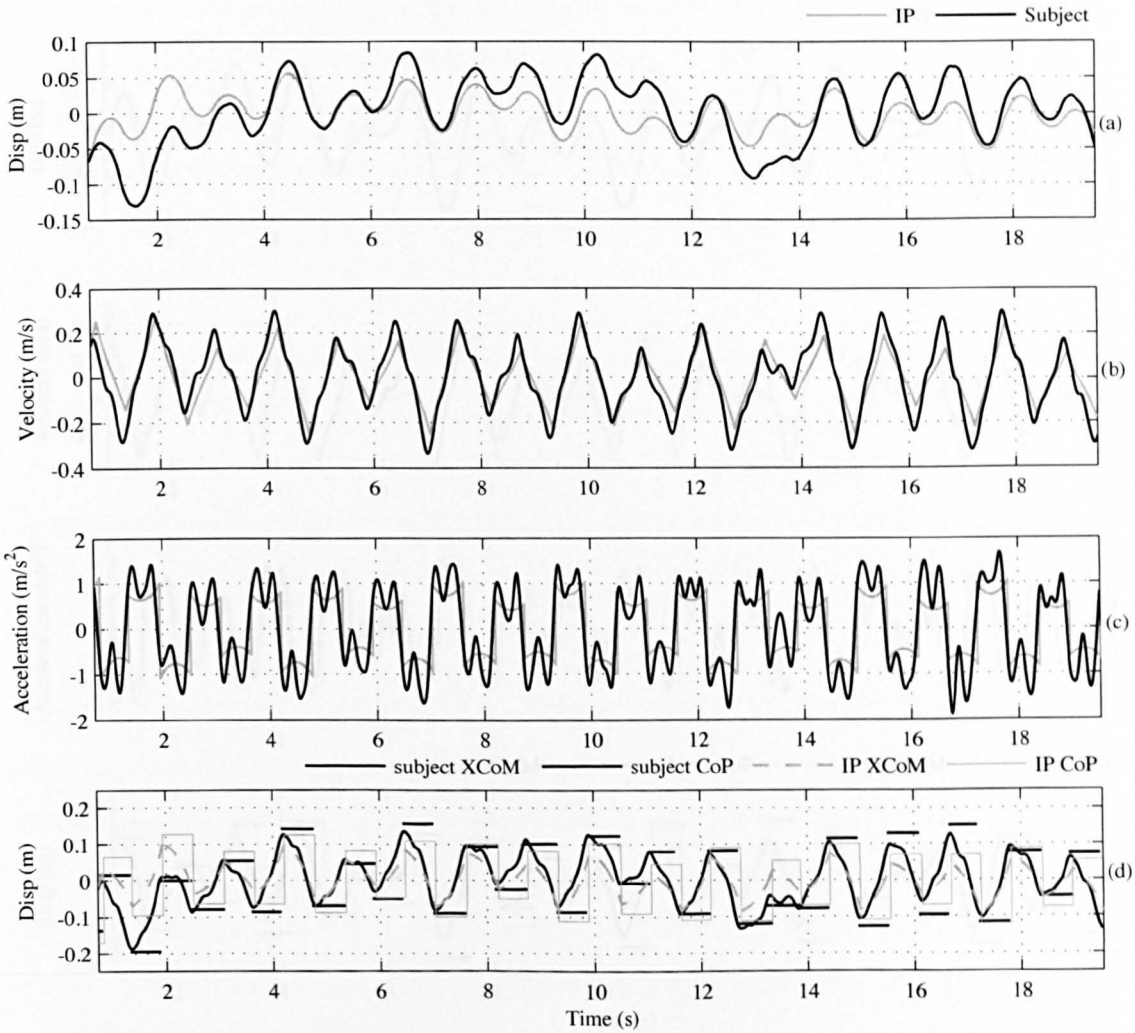

Figure 7.5: Comparison between subject and equivalent IP, deck oscillation 10 mm amplitude at 0.5 Hz. (a) CoM position (CC/m_{reg} = 0.64/0.34), (b) CoM velocity (CC/m_{reg} = 0.93/0.66), (c) CoM acceleration (CC/m_{reg} = 0.81/0.59) and (d) XCoM and CoP position. A constant medial offset of 35 mm has been applied to the recorded foot position to approximate the average position of the subject's CoP.

to say the addition of a further active control element on CoM does not appear to be warranted. On this basis (and considering that similar behaviour is observed across all subject comparisons), it can be tentatively concluded that the hypothesis in section 4.2 is disproven. While active balance control certainly plays a role in maintaining stability during locomotion on a laterally oscillating deck, the CoM behaviour is adequately described by the dynamics of a passive IP.

Examining the IP/subject comparison for a larger oscillation amplitude and frequency, 20 mm at 0.6 Hz, the inaccuracy in CoP position prediction is highlighted, Fig. 7.6.

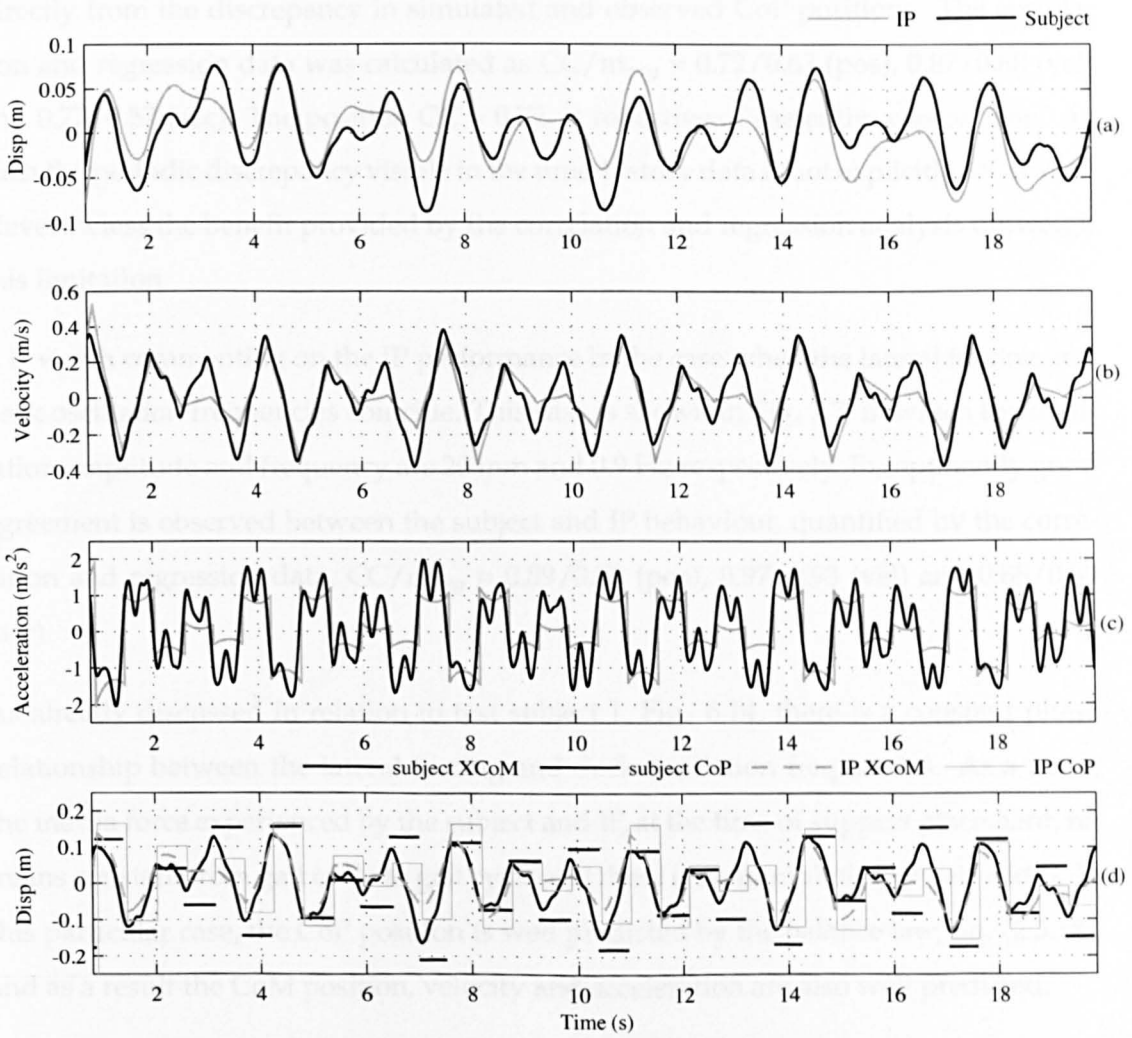

Figure 7.6: Comparison between subject and equivalent IP, deck oscillation 20 mm amplitude at 0.6 Hz. (a) CoM position (CC/m_{reg} = 0.72/0.67), (b) CoM velocity (CC/m_{reg} = 0.87/0.68), (c) CoM acceleration (CC = 0.77/0.57) and (d) XCoM and CoP position. A constant medial offset of 35 mm has been applied to the recorded foot position to approximate the average position of the subject's CoP.

Gait width modulation is correctly simulated, however the lateral position of the CoP is consistently underestimated by the CoP law. This results in an unrealistically narrow gait width being simulated, 7.6 (d). The consequence of this can be seen in 7.6 (a) - (c). Between $7s <= t <= 8s$, when the gait width is a maximum, the CoM position, velocity and acceleration are reasonably well predicted, although the simulated oscillation amplitude is underestimated due to the narrower gait of the IP, relative to the subject. However when the simulated gait narrows to a minimum, $9s <= t <= 10s$, the CoM oscillation flattens out, significantly departing from the subject's. This results

directly from the discrepancy in simulated and observed CoP positions. The correlation and regression data was calculated as CC/m_{reg} = 0.72/0.67 (pos), 0.87/0.68 (vel) and 0.77/0.57 (acc). The position CC = 0.72, is reflective of the entire comparison. As such the periodic discrepancy visible in the time-history data is not explicitly identified. Nevertheless the benefit provided by the correlation and regression analysis outweigh this limitation.

It is worth commenting on the IP performance in the case when the lateral forcing and deck oscillation frequencies coincide. This case is shown in Fig. 7.7, in which the oscillation amplitude and frequency are 20 mm and 0.9 Hz respectively. Exceptionally good agreement is observed between the subject and IP behaviour, quantified by the correlation and regression data, CC/m_{reg} = 0.89/0.78 (pos), 0.97/0.93 (vel) and 0.88/0.89 (acc).

As already discussed in relation to test subject 1, Fig. 6.14, there is a constant phase relationship between the lateral forcing and deck oscillation frequencies. As a result the inertia force experienced by the subject and IP, at the time of support placement, remains constant from gait cycle to gait cycle and there is no modulation of gait width. In this particular case, the CoP position is well predicted by the balance law, Eq. (2.3.18), and as a result the CoM position, velocity and acceleration are also well predicted.

Not withstanding the inaccuracy of support placement position, exemplified by Figs. 7.4 to 7.6, Fig. 7.7 further confirms the suitability of a passive model for CoM oscillatory behaviour. Regarding the original hypothesis:

> *Active balance control in response to lateral base motion plays a significant role in determining frontal plane CoM motion, to the extent that the passive inverted pendulum alone can not adequately simulate pedestrian CoM motion during the single stance phase.*

the situation can be summarised by stating that; human frontal-plane CoM motion, while walking on a laterally oscillating surface is well described by the passive IP. Thus in this case, clarity is provided by disproving the original hypothesis.

A limitation of the CoP placement law becomes apparent as the magnitude of deck velocity experienced by the IP grows. According to Eq. (2.3.18), repeated below, the

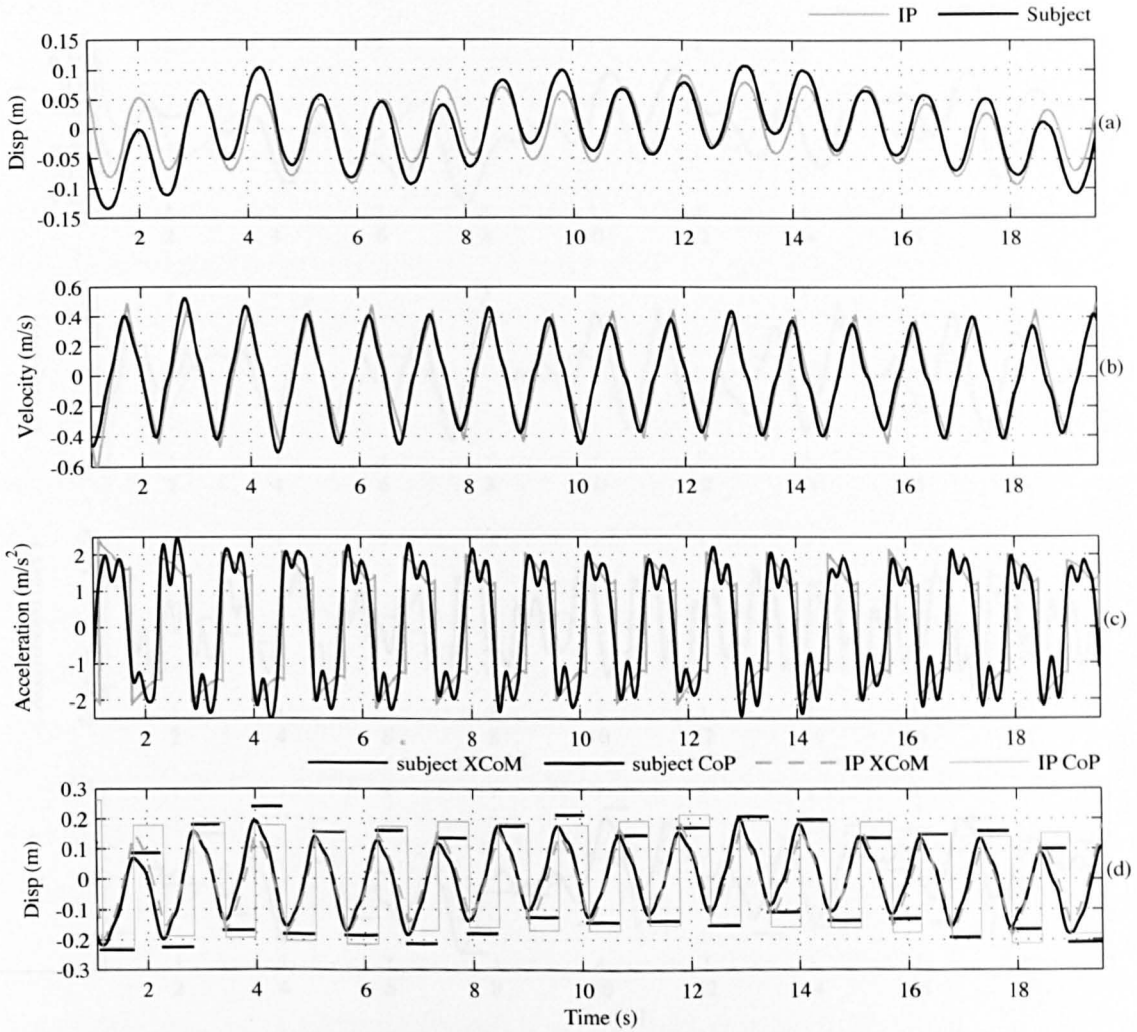

Figure 7.7: Comparison between subject and equivalent IP, deck oscillation 20 mm amplitude at 0.9 Hz. (a) CoM position (CC/m$_{reg}$ = 0.89/0.78), (b) CoM velocity (CC/m$_{reg}$ = 0.97/0.93), (c) CoM acceleration (CC/m$_{reg}$ = 0.88/0.89) and (d) XCoM and CoP position A constant medial offset of 35 mm has been applied to the recorded foot position to approximate the average position of the subject's CoP.

lateral position of the CoP contains a term proportional to CoM velocity, $\frac{\dot{y}_0}{\omega}$, and the additional stability margin, b_{min},

$$u = y_0 + \frac{\dot{y}_0}{\omega} \pm b_{min}$$

In the event that the IP and deck have global velocities in the same direction but the deck velocity magnitude is greater than the absolute velocity of the IP, the velocity of the IP relative to the deck will be in the medial direction. As a result, the term $\frac{\dot{y}_0}{\omega}$ will

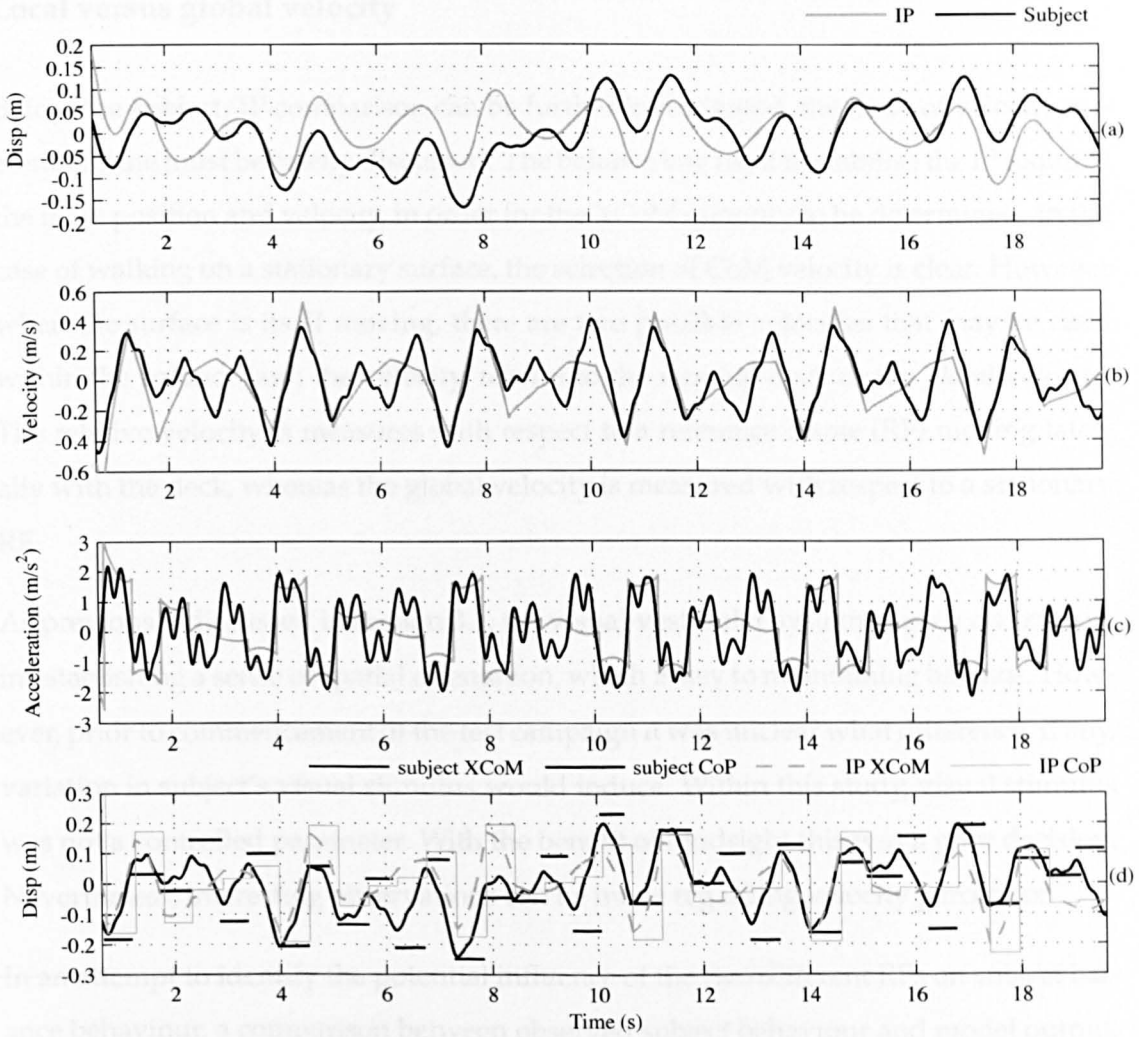

Figure 7.8: Comparison between subject and equivalent IP, deck oscillation 35 mm amplitude at 0.6 Hz demonstrating the occurrence of crossover steps. (a) CoM position, (b) CoM velocity, (c) CoM acceleration and (d) XCoM and CoP position A constant medial offset of 35 mm has been applied to the recorded foot position to approximate the average position of the subject's CoP.

be opposite in sign to b_{min}. As deck velocity magnitude increases, b_{min} is effectively eroded by $\frac{\dot{y}_0}{\omega}$ and a 'crossover' step occurs. A crossover step describes the situation in which the IP CoP is placed on the 'wrong' side of the CoM for the imminent step. Figure 7.8 shows the IP/subject comparison for deck oscillation amplitude and frequency, 35 mm at 0.6 Hz. The occurrence of crossover steps can be seen in plot (d). This behaviour, although ensuring IP stability, signals the breakdown of the balance law as the IP behaviour no longer resembles human locomotion. For this reason, comparisons have not been presented for 35 mm and 50 mm amplitude tests.

Local versus global velocity

Before the subject/IP comparison can be further investigated, the issue of velocity reference frame must be briefly discussed. The balance law used to stabilise the IP requires the mass position and velocity, in order for the XCoM quantity to be determined. In the case of walking on a stationary surface, the selection of CoM velocity is clear. However when the surface is itself moving, there are two possible velocities that may be used within the balance law; the velocity, *relative* to the moving deck or the *global* velocity. The relative velocity is measures with respect to a reference frame (RF) moving laterally with the deck, whereas the global velocity is measured with respect to a stationary RF.

As previously discussed in section 3.1, the visual-vestibular system plays a central role in establishing a sense of spatial orientation, which is key to maintaining balance. However, prior to commencement of the test campaign it was unclear what difference, if any, variation in subject's visual stimulus would induce. Within this study, visual stimulus was not a controlled parameter. With the benefit of hindsight this was a poor decision. Nevertheless, interesting observations can be made regarding velocity perception.

In an attempt to identify the potential influence of the two different RFs on subject balance behaviour, a comparison between observed subject behaviour and model output, similar to that described above, was repeated. Two simulation sets were performed, in one, the relative or local velocity was used in the balance law, while the global velocity was used in the other. On a footbridge, it is reasonable to assume that the relative velocity would be more relevant, however in the laboratory test environment this is not necessarily the case.

Figure 7.9 shows the results of one such simulation considered to be particularly interesting. In this case, test subject 1 experienced lateral deck oscillations of 20 mm amplitude at 1.0 Hz. There appears to be a transition between relative and global velocity which is particularly apparent for CoM velocity. Between approximately $0s <= t <= 5s$, a simulation based on relative velocity, plot (b), appears to approximate the observed behaviour quite well. However, between $5s <= t <= 11s$, the agreement deteriorates and a global velocity simulation performs considerably better, plot (d). The situation is again reversed between $11s <= t <= 16s$.

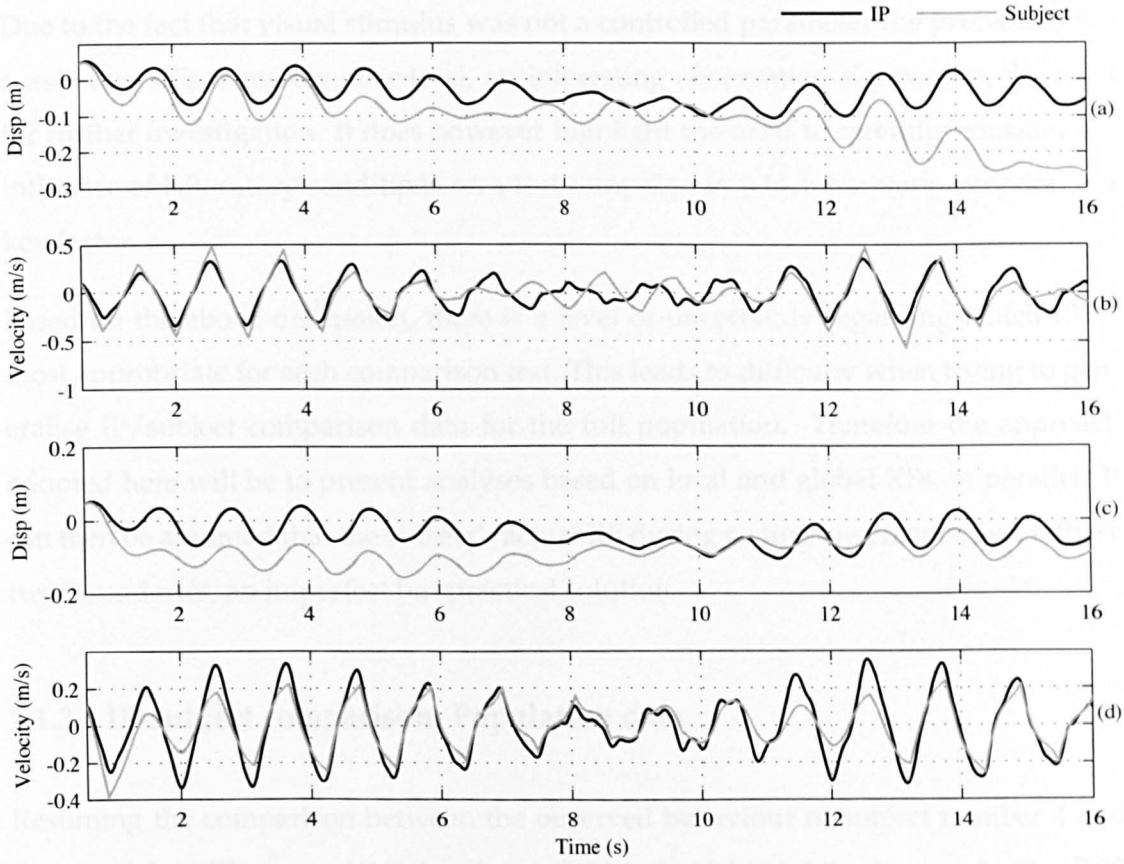

Figure 7.9: Comparison between subject and IP behaviour; CoM position (plots (a) and (c)) and CoM velocity (plots (b) and (c)). In plot (a) and (b) the CoM velocity relative to the moving deck has been used in the balance law. In plots (c) and (d) the global velocity has been used.

It appears that the subject's balance behaviour was such that during part of the test they perceived velocity in the local treadmill RF, this is followed by a change in perception to the global RF, followed by a reversion to the local RF. It is not possible to say with certainty, what the cause of this transition was, however it can be postulated that it may have coincided with a change in the subject's visual stimulus. For example, when focusing on a fixed reference point in the laboratory, the subject may have perceived their CoM velocity in the global RF. However when looking down at their feet moving relative to the treadmill deck (or the horizontal stabilising bar in front of them), they may have perceived velocity in the local RF. A change in RF perception may have resulted in a change of balance behaviour, potentially explaining the CoM motion observed in Fig. 7.9. Although each test was visually recorded (from the subject's rear), it was not possible to correlate the subject's visual focus with transitions in the data, a limitation within the test campaign.

Due to the fact that visual stimulus was not a controlled parameter the preceding discussion on RFs is merely anecdotal, an interesting observation signposting the need for further investigation. It does however highlight the need to carefully consider the influence of laboratory conditions on a test campaign in which human perception is a key factor.

Based on the above discussion, there is a level of uncertainty regarding which RF is most appropriate for each comparison test. This leads to difficulty when trying to generalise IP/subject comparison data for the full population. Therefore the approach adopted here will be to present analyses based on local and global RFs, in parallel. It can then be assumed that the subject's actual RF during testing lay on or between these two boundaries, an imperfect but practical solution.

7.1.3 IP-subject comparison: Population data

Resuming the comparison between the observed behaviour of subject number 4 and the equivalent IP, comparison data from all tests for subject 4 can be seen in Fig. 7.10 which show the subject versus equivalent IP behaviour for CoM position (plot a, d, g), velocity (plot b, e, h) and acceleration (plot c, f, i). All comparison data has been combined for 5mm tests (plots a - c), 10mm tests (plots d - f) and 20mm tests (h - i). As above, IP CoP placement is based on CoM velocity in the moving treadmill (local) reference frame. The same comparison exercise was repeated, Fig. 7.11, however the local IP velocity was replaced with the mass velocity measured in a stationary global reference frame.

With reference to Fig. 7.10, the behaviours and level of agreement discussed above appears to be typical for the entire text matrix for subject 4. In all cases the slope of the regression lines show that the magnitude of CoM motion is underestimated by the IP model, however in the case of velocity and acceleration all CCs are ≥ 0.77 indicating strong linearity. CoM position however shows weaker linearity with CC between 0.36 and 0.42. This is due to the tendency for the subject (and IP) to drift laterally on the deck during testing (simulation) whereas the velocity and position data is zero-centred throughout the test. Comparing figures 7.10 and 7.11, there appears to be little difference between simulations based on global and local velocity for 5 mm and 10 mm

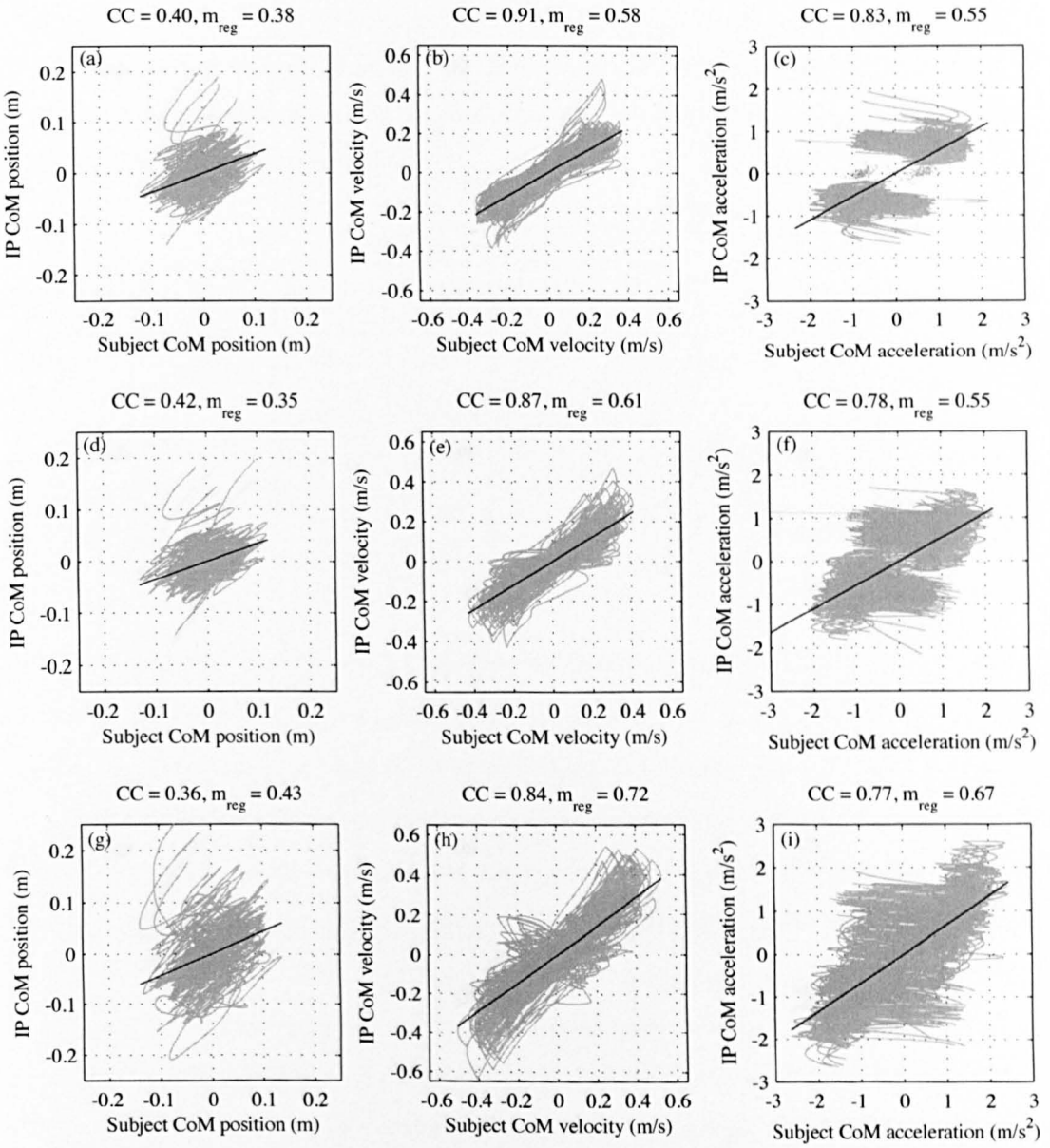

Figure 7.10: Plot of subject (No. 4) versus equivalent IP behaviour for CoM position (plot a, d, g), velocity (plot b, e, h) and acceleration (plot c, f, i). Plots (a - c) contain all data relating to 5 mm amplitude tests, plots (d - f) contain all data relating to 10 mm amplitude tests and plots (h - i) contain all data relating to 20 mm amplitude tests. Corresponding correlation coefficients are shown above the relevant plot. IP CoP placement based on local CoM velocity.

amplitude tests. However the differences become more apparent for 20 mm tests, plots (g - i). In particular, simulations based on local velocity appear to provide better amplitude estimation, indicated by notably higher m_{reg} values. An observable difference between local and global simulation performance is not surprising, considering the in-

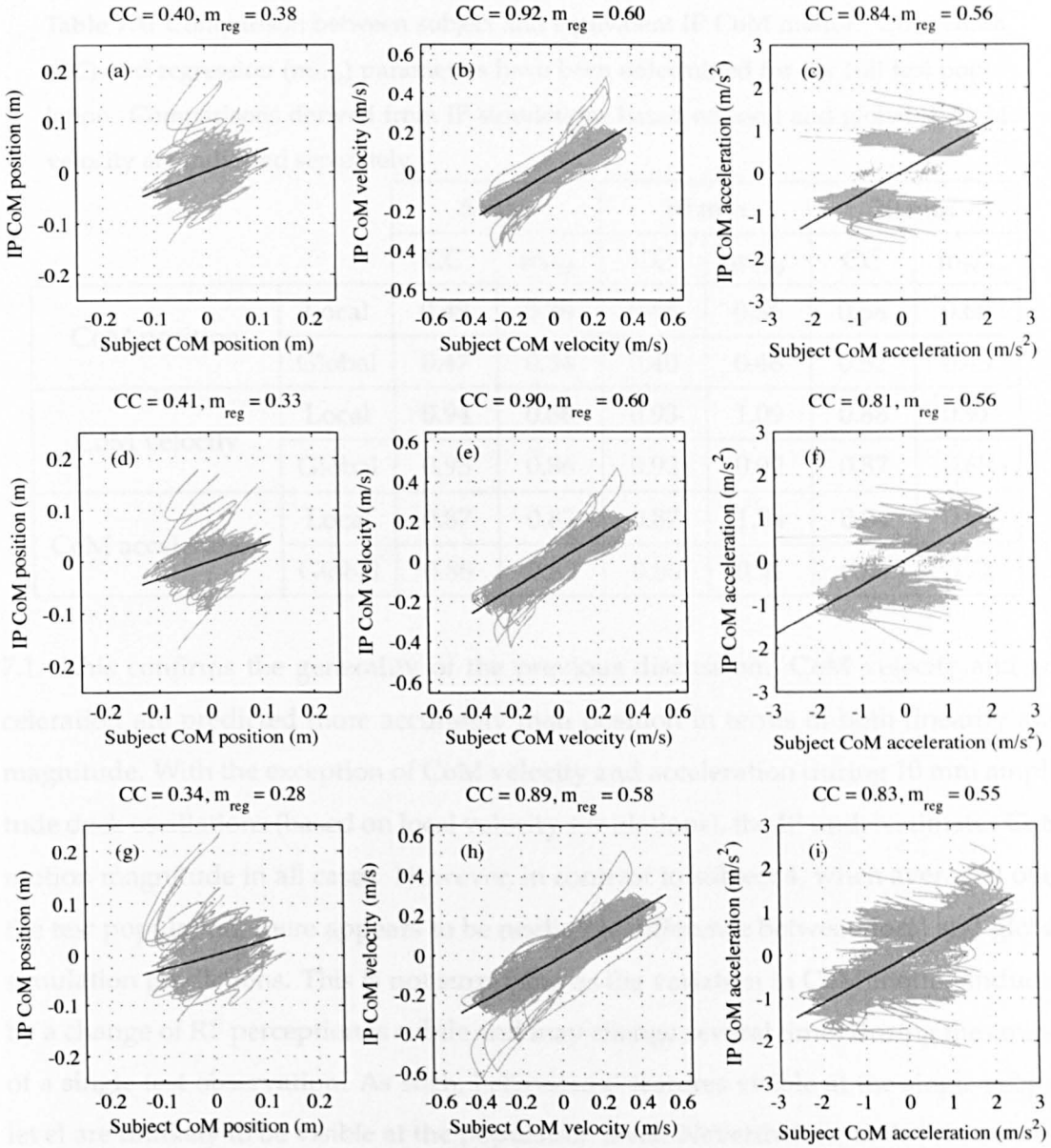

Figure 7.11: Plot of subject (No. 4) versus equivalent IP behaviour for CoM position (plot a, d, g), velocity (plot b, e, h) and acceleration (plot c, f, i). Plots (a - c) contain all data relating to 5 mm amplitude tests, plots (d - f) contain all data relating to 10 mm amplitude tests and plots (h - i) contain all data relating to 20 mm amplitude tests. Corresponding correlation coefficients are shown above the relevant plot. IP CoP placement based on global CoM velocity.

creasing magnitude (and therefore influence) of deck velocity experienced during 20 mm tests.

This analysis is expanded to consider data from all 10 test subjects; the correlation and regression data for both local and global velocity simulations is summarised in table

Table 7.1: Comparison between subject and equivalent IP CoM motion. Correlation (CC) and regression (m_{reg}) parameters have been determined for the full test population. Comparisons derived from IP simulations based on local and global IP CoM velocity are indicated separately.

		5 mm		10 mm		20 mm	
		CC	m_{reg}	CC	m_{reg}	CC	m_{reg}
CoM position	Local	0.48	0.36	0.45	0.56	0.58	0.68
	Global	0.47	0.34	0.40	0.46	0.52	0.43
CoM velocity	Local	0.94	0.86	0.93	1.09	0.88	0.91
	Global	0.95	0.86	0.92	0.92	0.87	0.69
CoM acceleration	Local	0.87	0.83	0.87	1.04	0.84	0.89
	Global	0.88	0.83	0.86	0.91	0.85	0.72

7.1. This confirms the generality of the previous discussion. CoM velocity and acceleration are predicted more accurately than position in terms of both linearity and magnitude. With the exception of CoM velocity and acceleration during 10 mm amplitude deck oscillations (based on local velocity simulations), the IP underestimates CoM motion magnitude in all cases. However, in contrast to subject 4, when averaged over the test population, there appears to be negligible difference between local and global simulation predictions. This is not surprising as the variation in CoM motion induced by a change of RF perception is subtle and may change several times during the course of a single test observation. As such, behavioural features visible at the single subject level are unlikely to be visible at the population level. Nevertheless, table 7.1 confirms the suitability of a passive IP model for CoM motion in the frontal plane.

In the context of human-induced bridge vibration, the raison d'être of the IP model is to generate GRFs consistent with HSI. In light of the discussion above it can be stated that the gait behaviour simulated is consistent with HSI, i.e. self-excited forces are generated through the modulation of IP gait width, Figs. 7.4 to 7.7. The same mechanism has been confirmed for test subjects, Figs. 6.13 to 6.16 and thus a further qualitative validation of the IP model for use on an oscillating structure is established.

7.2 Simulated versus observed GRF

The discussion in section 7.1 above, confirms the suitability of the passive IP model in simulating CoM motion. The following analysis investigates the accuracy of the GRF simulated.

GRFs generated while walking on an oscillating deck are typically analysed to determine the component in phase with oscillation velocity and acceleration. By averaging the values of the respective force components over a large number of oscillation cycles, the dynamic influence of the GRF can be characterised as an alteration to the modal mass and damping of the oscillating structure, [11, 15, 37]. The question now arises; how much does the mass and damping influence of the IP-generated self-excited force differ from that of a human subject?

The simulated and observed GRFs have been analysed to determine the equivalent damping and mass coefficients for each test, as per the procedure outlined in [37] and previously described in section 2.3. It is important to stress that in this analysis it is not the absolute value of the simulated/observed mass and damping coefficients that is of interest. The test durations are too short (approximately 18-20 s) for statistically meaningful coefficients to be determined. Of more interest is the relationship between coefficient magnitudes, as this indicates the degree to which the IP behaviour deviates from the subject's.

Figure 7.12 shows the ratio of subject to IP-induced damping coefficients for test subject 4. For each test, the ratio of base oscillation to lateral forcing frequency has been determined. Bearing in mind that the vector of test frequencies [0.3, 0.4, 0.5, 0.6, 0.7, 0.8, 0.9, 1.0, 1.1] Hz, the subject's lateral forcing frequency is easily identified for each test. Comparisons in which the simulation was based on a local RF are indicated in red, those based on a global RF are indicated in green. In cases where the change in RF has negligible influence on the coefficient ratio, only the relative data point is visible.

Those tests in which the lateral displacement amplitude was 35 mm and 50 mm have been excluded from the comparison due to poor performance of the IP model, resulting from the simulation of crossover steps discussed above.

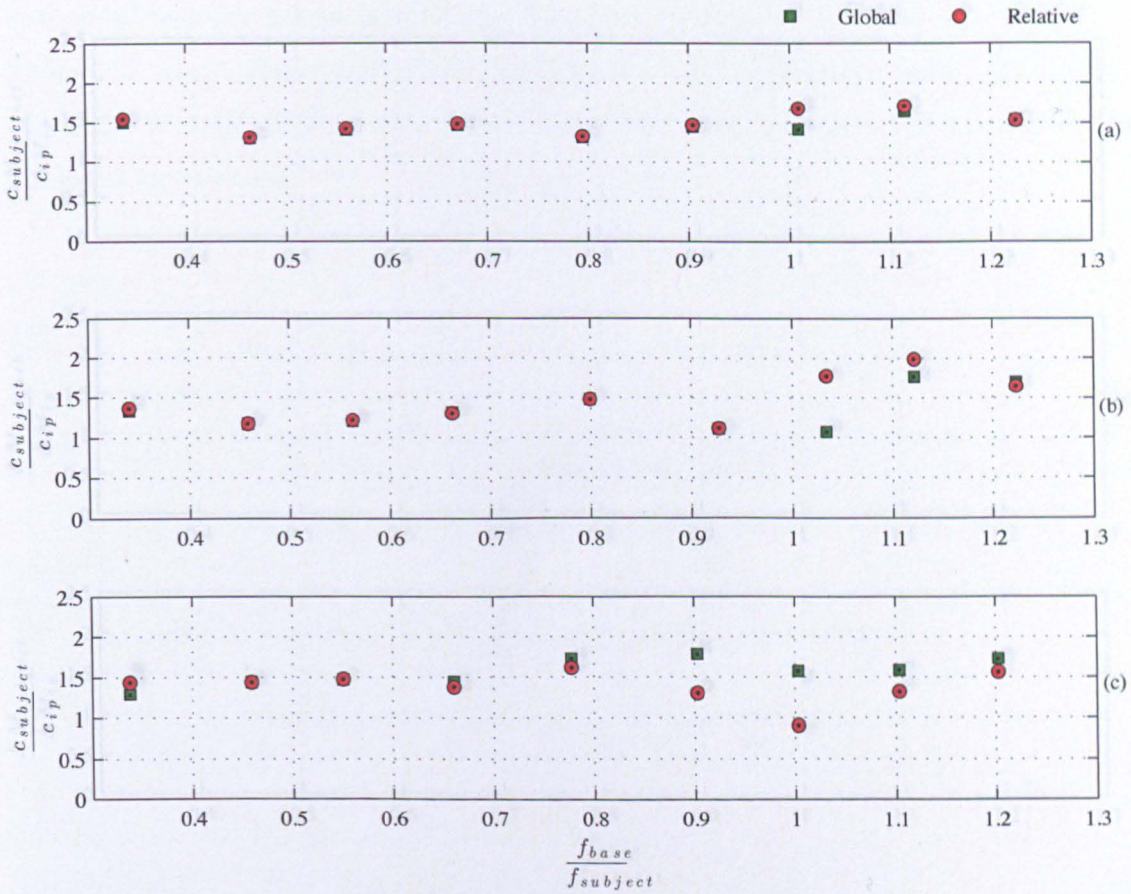

Figure 7.12: The ratio of subject to IP-induced damping coefficients for test subject 4 for tests with a lateral displacement amplitude of (a) 5 mm, (b) 10 mm and (c) 20 mm. Simulations based on global velocity are indicated in green, relative velocity in red.

It is immediately clear that the IP underestimates the damping influence of the subject in almost all cases, with the exception of the (20 mm / 0.9 Hz) test discussed previously. In this particular case the agreement between damping coefficients is remarkably good (as one might expect based on Fig. 7.7) when a relative RF is assumed. It is also clear that the forcing and oscillation frequencies are almost perfectly matched. This results in the stabilisation of gait width discussed previously. However, this particular test is not representative of the IP 's general performance.

The discrepancy between simulated and observed coefficients results from the fact that the gait width of the IP is consistently underestimated and as a result so too is the magnitude of the GRF. It is therefore not surprising that almost identical ratios are produced when considering the mass coefficients, Fig. 7.13.

The difference between simulations based on a local and global RF is minimal for all

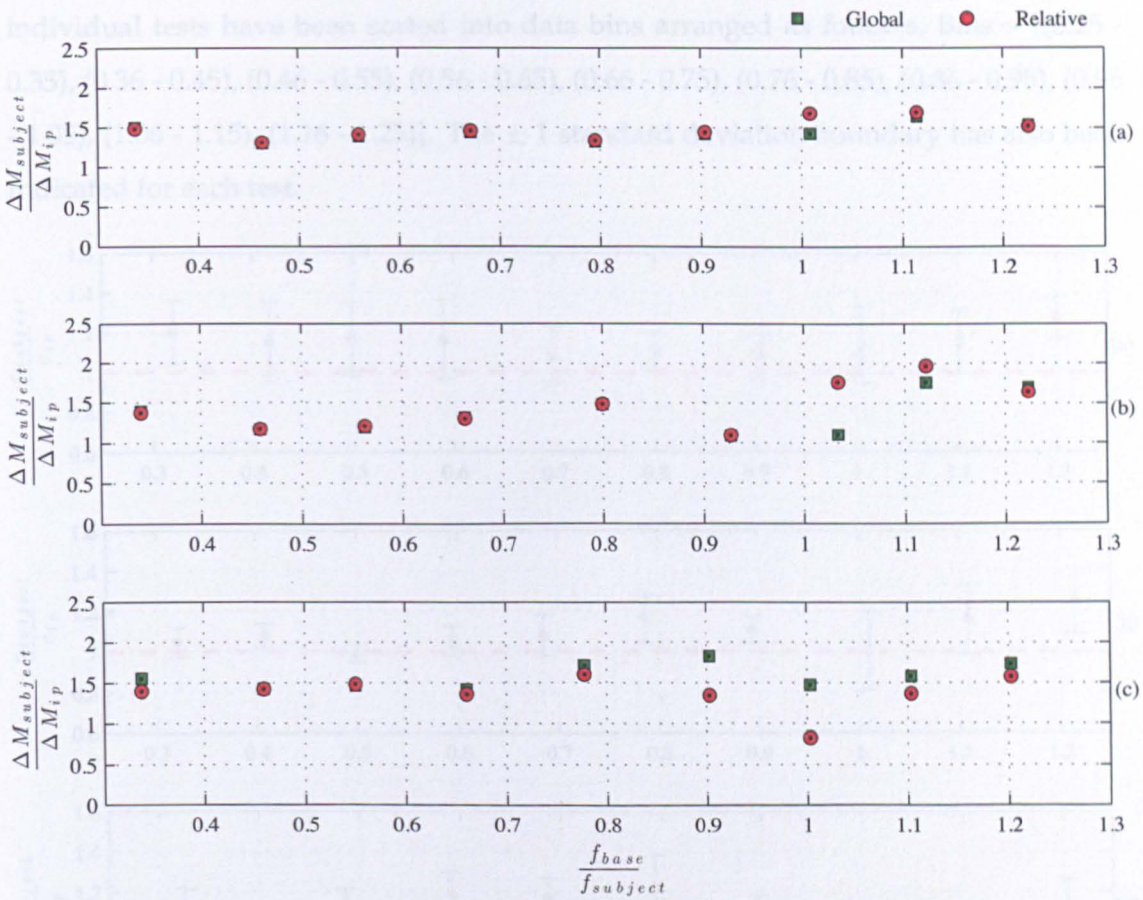

Figure 7.13: The ratio of subject to IP-induced mass coefficients for test subject 4 for tests with a lateral displacement amplitude of (a) 5 mm, (b) 10 mm and (c) 20 mm. Simulations based on global velocity are indicated in green, relative velocity in red.

5 mm amplitude tests, plot (a). Due to the relatively low magnitude of deck velocity the difference between IP velocity measured in the global or local RF is minimal and therefore both equally underestimate the GRF. With reference to 10 mm and 20 mm amplitude tests, plots (b) & (c), as the influence of deck velocity increases so too does the difference between relative and global RF based simulations.

It should be remembered that the relevant RF may change during the course of an individual test, as demonstrated in Fig. 7.9. As such, the relevant RF cannot conclusively be identified from Figs. 7.12 & 7.13. These figures merely indicate, on average, during the course of a test, which RF is likely to have been relevant to the subject.

The same analysis has been repeated for all test subjects and the average coefficient ratios determined. Fig. 7.14 is based on relative RF simulations while Fig. 7.15 is based on global RF simulations. The average frequency ratio has also been determined and

individual tests have been sorted into data bins arranged as follows, Bins = [(0.25 - 0.35), (0.36 - 0.45), (0.46 - 0.55), (0.56 - 0.65), (0.66 - 0.75), (0.76 - 0.85), (0.86 - 0.95), (0.96 - 1.05), (1.06 - 1.15), (1.16 - 1.25)]. The ± 1 standard deviation boundary has also been indicated for each test.

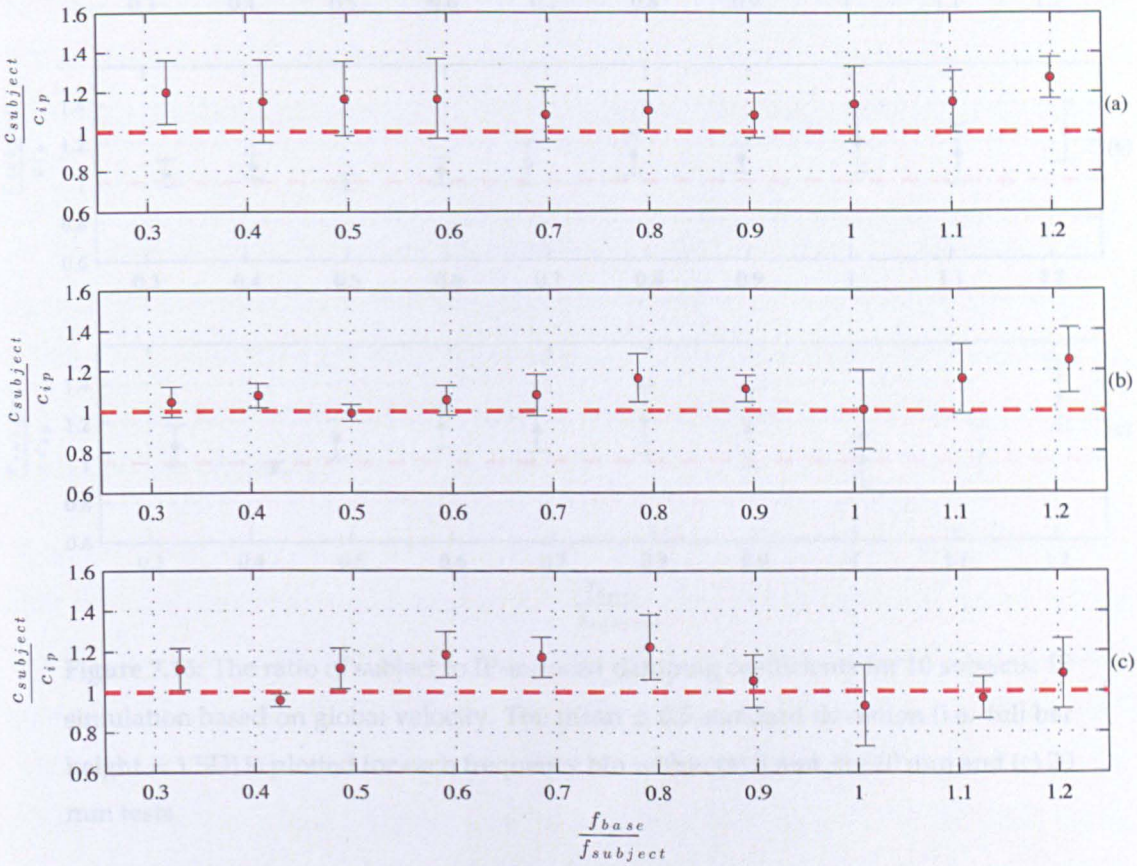

Figure 7.14: The ratio of subject to IP-induced damping coefficients for 10 subjects. IP simulation based on local velocity. The mean ± 0.5 standard deviation (i.e. full bar height = 1 SD) is plotted for each frequency bin within (a) 5 mm, (b) 10 mm and (c) 20 mm tests

With reference to both figures, the most obvious feature is the lack of variability between relative and global RF simulation sets. Although a change in RF alters IP behaviour eg. Figs 7.12 & 7.13, when averaged over the population, the difference is negligible. It should be remembered that the actual value of the margin ratio is not of interest due to the limited simulation duration.

Data points above the horizontal dashed red lines indicate tests in which, on average, the IP model stabilised by the CoP law, underestimates the average damping coefficient

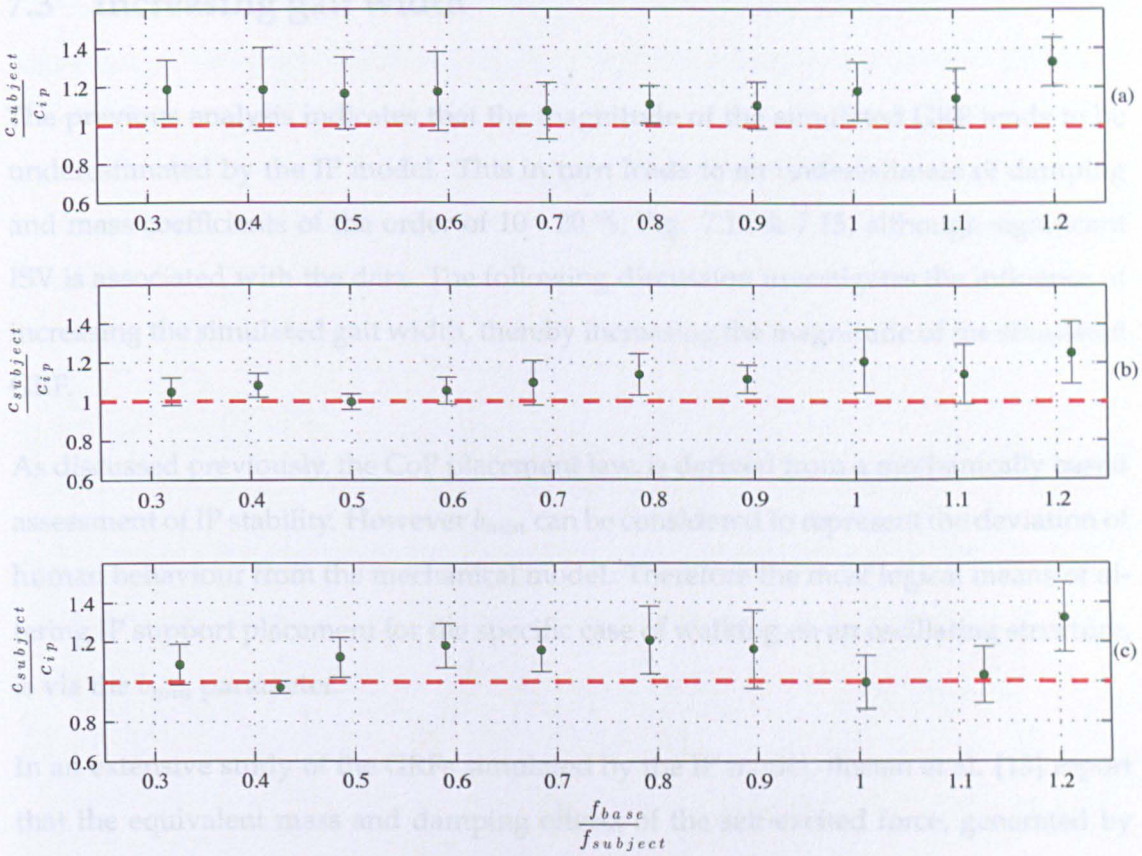

Figure 7.15: The ratio of subject to IP-induced damping coefficients for 10 subjects. IP simulation based on global velocity. The mean $\pm$ 0.5 standard deviation (i.e. full bar height = 1 SD) is plotted for each frequency bin within (a) 5 mm, (b) 10 mm and (c) 20 mm tests

and vice versa. In almost all cases the IP, on average, underestimates the damping coefficient. For the same reason that Fig. 7.13 closely resembles 7.12, the corresponding plot showing the mass coefficients for the population is almost identical to Fig. 7.14 and is therefore omitted.

For the 5 mm amplitude tests, the underestimation is reasonably uniform across the full frequency range at approximately 15 %. The degree to which the IP underestimates $c_{subject}$ varies more for 10 mm and 20 mm amplitude tests with no discernable trend. Bearing in mind the philosophy of this test campaign, to investigate fewer subjects but in greater detail, little more can be gleaned from Figs. 7.14 and 7.15 (with any degree of statistical significance) regarding population wide conclusions.

7.3 Increasing gait width

The previous analysis indicates that the magnitude of the simulated GRF tends to be underestimated by the IP model. This in turn leads to an underestimate of damping and mass coefficients of the order of 10 - 20 %, Fig. 7.14 & 7.15, although significant ISV is associated with the data. The following discussion investigates the influence of increasing the simulated gait width, thereby increasing the magnitude of the simulated GRF.

As discussed previously, the CoP placement law, is derived from a mechanically based assessment of IP stability. However b_{min} can be considered to represent the deviation of human behaviour from the mechanical model. Therefore the most logical means of altering IP support placement for the specific case of walking on an oscillating structure, is via the b_{min} parameter.

In an extensive study of the GRFs simulated by the IP model, Bocian et al. [15] report that the equivalent mass and damping effects of the self-excited force, generated by the IP model, are independent of b_{min}. Therefore, alterations of the type discussed here should not alter the underlying damping and inertial characteristics of the self-excited force, when averaged over many bridge oscillation cycles. The objective in what follows is to present a more general measure of the accuracy of the GRF, rather than the self-excited force discussed in section 7.2.

To obtain a comparison between simulated and observed GRFs, the area under the absolute GRF was determined for simulated and observed force-time histories. This indicates, on average over the course of a single test, whether the GRF magnitude was under or overestimated. Rather than reporting percentage differences in the GRF, the IP in each comparison was tuned such that the percentage difference in cumulative area under the GRFs was reduced to $\leq \pm 1\%$. This was achieved by applying a constant alteration to b_{min}, for the duration of the test. In the event that the area under the recorded GRF was greater than that simulated, b_{min} was incrementally increased until the area difference was within $\pm 1\%$.

To facilitate the discussion, the parameter b_{fac} is defined,

$$b_{fac} = \frac{b_{dyn}}{b_{min}} \tag{7.3.1}$$

where b_{min} is the minimum stability margin obtained after tuning the IP to subject behaviour on a stationary deck and b_{dyn} is the stability margin obtained from tuning on an oscillating deck. The results of this tuning process can be seen in Fig. 7.16 for which b_{fac} was found to be 1.4. The red line indicates IP behaviour after the stability margin has been optimised to reduce the residual GRF. The grey line indicates the original IP simulation.

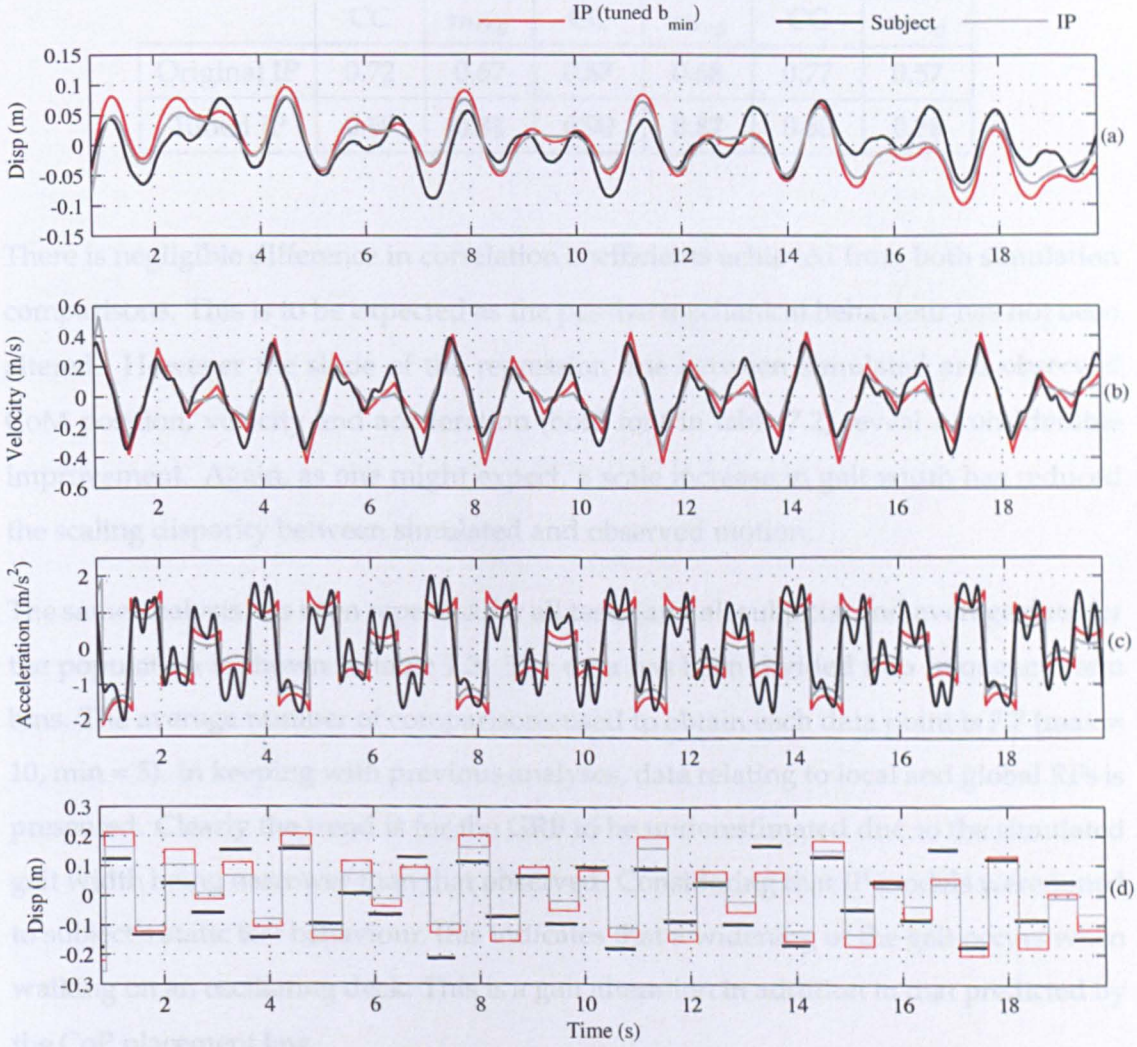

Figure 7.16: Comparison between subject (No. 4) and equivalent IP during deck oscillations of 20 mm amplitude at 0.6 Hz, (a) CoM position, (b) CoM velocity, (c) CoM acceleration and (d) CoP position. A constant medial offset of 35 mm has been applied to the recorded foot position to approximate the average position of the subject's CoP.

It can be seen that the flattening out of IP CoM position and velocity, plots (a) and (b), when gait width is at a minimum, has been reduced due to the increase in b_{min} and resulting wider gait. This is accompanied by an expected scale increase in IP CoM

acceleration magnitude, plot (c). The improved CoM motion is more clearly seen by comparing correlation and regression data for standard and tuned IP behaviour, table 7.2

Table 7.2: Correlation and regression parameters for the original IP simulation against observed behaviour and the tuned IP simulation against observed behaviour.

	Position		Velocity		Acceleration	
	CC	m_{reg}	CC	m_{reg}	CC	m_{reg}
Original IP	0.72	0.67	0.87	0.68	0.77	0.57
Tuned IP	0.69	**0.81**	0.90	**0.87**	0.80	**0.78**

There is negligible difference in correlation coefficients achieved from both simulation comparisons. This is to be expected as the passive mechanical behaviour has not been altered. However the slope of the regression line between simulated and observed CoM position, velocity and acceleration (bold font in table 7.2) reveal a considerable improvement. Again, as one might expect, a scale increase in gait width has reduced the scaling disparity between simulated and observed motion.

The same analysis has been repeated for all tests (and all subjects) and average data for the population is shown in table 7.3. The data has been divided into frequency ratio bins. The average number of comparisons used to obtain each data point is 7.7 (max = 10, min = 5). In keeping with previous analyses, data relating to local and global RFs is presented. Clearly the trend is for the GRF to be underestimated due to the simulated gait width being narrower than that observed. Considering that IP models were tuned to subject's static test behaviour, this indicates that a widening of the gait occurs when walking on an oscillating deck. This is a gait alteration in addition to that predicted by the CoP placement law.

Trends in the data are more clearly seen in Fig. 7.17 plots (a) and (b), which are contour plot representations of the data in table 7.3. Note that linear interpolation has been used between data points. The y-coordinate of each data point has been taken as the midpoint of the frequency ratio bin. Plots (c) and (d) show the corresponding coefficient of variation as a percentage, indicating the variability associated with the b_{fac} data.

Table 7.3: Average values of b_{fac} obtained for for the test population. Average and standard deviation values across all amplitudes are shown in the two rightmost columns, average and standard deviation values across all frequencies are shown in the lowermost row. Average and standard deviation values across all tests are shown in the red in the bottom right.

	5 mm		10 mm		20 mm		Mean	
$\frac{f_{base}}{f_{subject}}$	Local	Global	Local	Global	Local	Global	Local	Global
0.25-0.35	1.26	1.26	1.08	1.08	1.14	1.14	**1.16/0.09**	1.16/0.09
0.36-0.45	1.21	1.21	1.13	1.13	1.02	1.04	**1.12/0.09**	1.12/0.08
0.46-0.55	1.19	1.19	1.02	1.02	1.17	1.18	**1.13/0.09**	1.13/0.09
0.56-0.65	1.19	1.18	1.11	1.13	1.23	1.25	**1.18/0.06**	1.19/0.06
0.66-0.75	1.11	1.11	1.13	1.14	1.25	1.26	**1.16/0.08**	1.17/0.08
0.76-0.85	1.13	1.12	1.21	1.18	1.28	1.26	**1.21/0.07**	1.19/0.07
0.86-0.95	1.13	1.12	1.10	1.14	1.12	1.13	**0.12/0.01**	1.13/0.01
0.96-1.05	1.21	1.20	1.01	1.23	1.09	1.10	**1.11/0.10**	1.18/0.07
1.06-1.15	1.23	1.19	1.17	1.15	1.05	1.00	**1.15/0.09**	1.11/0.11
1.16-1.25	1.31	1.30	1.34	1.30	1.28	1.36	**1.31/0.03**	1.32/0.03
Mean/Std	**1.20/0.06**	1.19/0.06	**1.13/0.10**	1.15/0.08	**1.16/0.09**	1.17/0.11	1.16/0.09	1.17/0.09

With reference to plots (a) and (b), there is relatively little difference between local and global velocity simulations except when the subject is synchronised with the structure. Plots (c) and (d) show that the level of variability associated with the b_{fac} data is relatively low, $\leq\approx$ 20% across a large area of the parameter space. The exception to this is again, when the subject is synchronised with the structure. As previously discussed, the IP gait width in this case is essentially a function of the phase relationship between the forcing and oscillation frequencies. This explains the high degree of variability in b_{fac} under these conditions.

7.4 Conclusion

Experimental observations and analysis in this chapter reveal that the IP model, originally discussed in section 2.3, is at least qualitatively sound; that is to say the IP model combined with the CoP placement law, [43], generates self-excited forces through the alteration of CoP placement position; a process analogous to AM. Examination of actual subject balance behaviour has revealed the same mechanism at work.

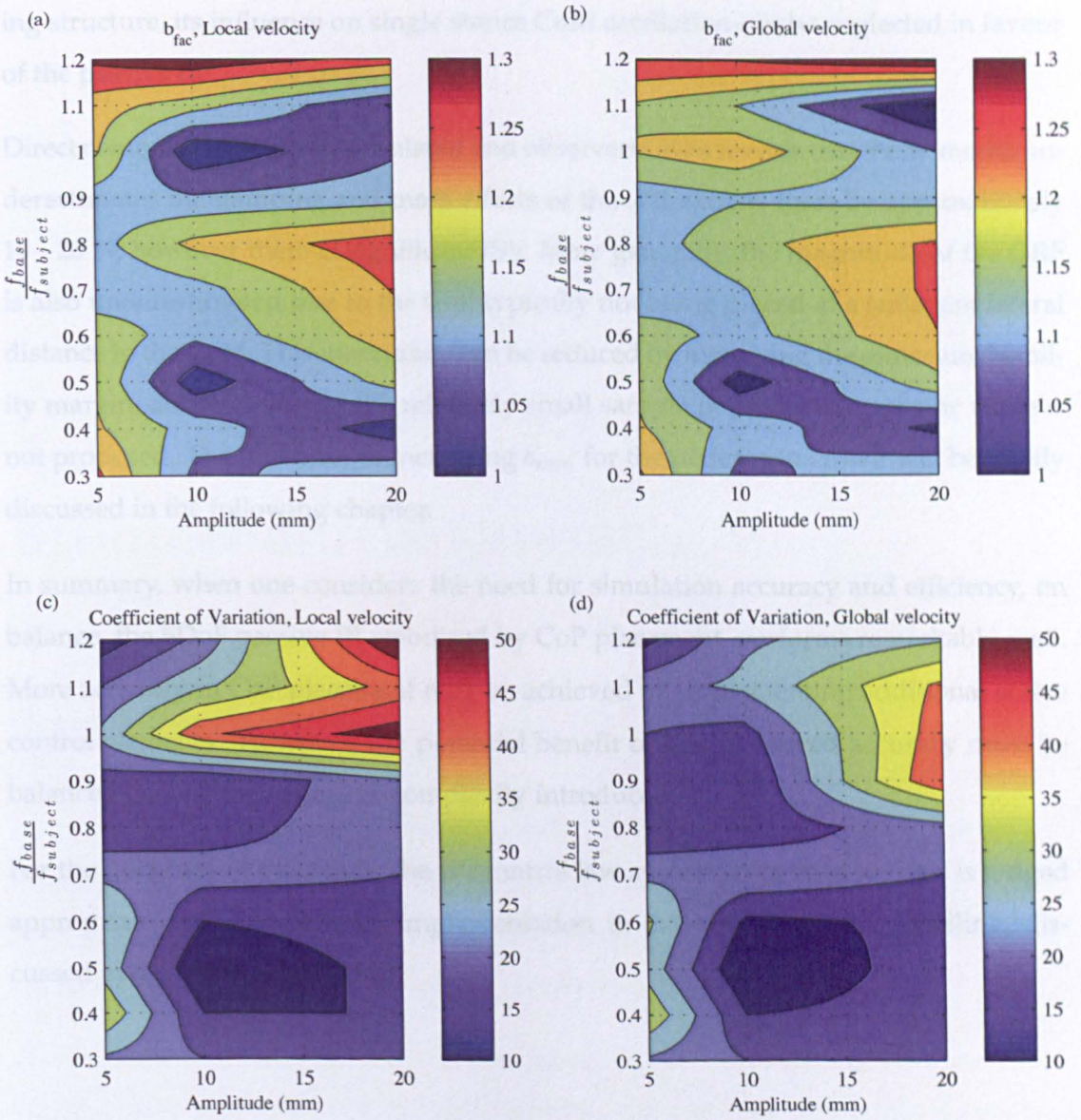

Figure 7.17: Plots (a) and (b), average b_{fac} obtained for the test population in which IP simulations are based on local and global velocity respectively, plots(c) and (d), b_{tac} coefficient of variation (%) for simulations based on local and global velocity respectively.

Furthermore, the single stance oscillatory behaviour of pedestrians walking on laterally oscillating structures is well described by a passive IP model, for the range of amplitudes ($\leq$ 20 mm) and frequencies ($\leq$ 1.1 Hz) discussed. The magnitude of lateral acceleration experienced on full scale structures, including that experienced at the onset of lateral instability, will almost certainly be within this range. Thus the original hypothesis stated in chapter 4 has been disproven. While active balance control based on sensory feedback is certainly utilised in stabilising locomotion on an oscillat-

ing structure, its influence on single stance CoM oscillation can be neglected in favour of the passive IP.

Direct comparison between simulated and observed GRFs reveals that the IP model underestimates the damping and mass effects of the self-excited force by approximately 10 - 20 %, however there is significant ISV. More generally, the magnitude of the GRF is also underestimated due to the CoP typically not being placed at a sufficient lateral distance to the CoM. This inaccuracy can be reduced by increasing the minimum stability margin, although due to the relatively small sample population, a specific value is not proposed. The influence of increasing b_{min} for the pedestrian crowd will be briefly discussed in the following chapter.

In summary, when one considers the need for simulation accuracy and efficiency, on balance, the SDoF passive IP, stabilised by CoP placement, performs remarkably well. More accuracy in CoP placement may be achieved by implementing additional active control elements. However, the potential benefit of this improved accuracy must be balanced against the increased complexity introduced.

For the purposes of this study, the IP/control law system in its current form is judged appropriate and sufficient for implementation in the next phase of modelling, discussed in the following chapter.

CHAPTER 8

Discrete Crowd - Structure - Biomechanical interaction

Chapter Summary

In this chapter, the discrete element modelling framework presented in chapter 5 is developed to more carefully consider HSI. The modelling aim now, is to move away from reliance on empirical load models and directly simulate HSI with a view to developing a better understanding of the phenomenon.

Having validated the use of the IP biomechanical model in the previous chapter, multiple IP models are herein dynamically coupled to the structure, facilitating the study of two-way HSI. In section 8.1, a detailed discussion of the proposed interaction model is presented. Section 8.2 summarises what has been learned from the modelling exercise.

8.1 A coupled biomechanical/discrete crowd interaction model

In this section, human-induced vibration is considered from two viewpoints, (i) the interaction that takes place between individual walking pedestrians and the vibrating bridge, and (ii) the wider crowd behaviour that results from the interactions between pedestrians, initially discussed in chapter 5. The discrete element crowd model previously discussed is coupled with a dynamical system. The dynamical system models interaction between multiple IP biomechanical models and a SDoF system representing a bridge vibration mode. Both the crowd model and dynamical system are coupled in a time-stepping framework with crowd model output used to update the dynamical system at each time-step.

If the emphasis in chapter 5 was on exploring the application of discrete element crowd modelling to this research problem, the emphasis in this chapter is on understanding the macro scale effects of a more carefully considered HSI. Thus, in what follows no acceleration thresholds or predefined pedestrian behaviours will be implemented. At no point in the simulation is pedestrian pacing frequency altered in response to base motion. The proposed model therefore does not simulate crowd-structure synchronisation (as was done in chapter 5), rather the model attempts to simulate crowd-structure interaction, a precursor to potential synchronisation.

8.1.1 Coupled biomechanical-bridge dynamical system

In this subsection coupling between multiple IP models and a SDoF base structure is presented. Lateral acceleration of the IP, $\ddot{y}$ (repeated from Eq. (2.3.16) and dropping the subscript m), is approximated by,

$$\ddot{y} = -\ddot{U} - \omega^2(u - y) \tag{8.1.1}$$

in which $\omega = \sqrt{g/L_p}$, L_p is the IP length, u is the CoP placement position during the oscillation, y is the mass position and $\ddot{U}$ represents the lateral base acceleration [37]. Transfer between supporting legs is assumed to be instantaneous, thus the double support phase of the gait cycle is not considered. It should be noted that the CoP, u, refers to the position of the force resulting from the pressure distribution beneath the foot and is here assumed constant during each single stance phase. u, is calculated

based on the IP position, y_0, and velocity, $\dot{y}_0$, immediately prior to foot placement [43], using Eq. (2.3.18), repeated below,

$$u = y_0 + \frac{\dot{y}_0}{\omega} \pm b_{min} \quad (+ \text{ for right foot, - for left foot})$$

where the quantity, $y_0 + \frac{\dot{y}_0}{\omega}$ defines the minimum outward distance the IP support (CoP) must be placed, in order that the mass does not swing beyond the point of support, resulting in the pendulum falling outward. b_{min} is the additional minimum stability margin [13, 14, 43] discussed in section 2.3 and chapter 7.

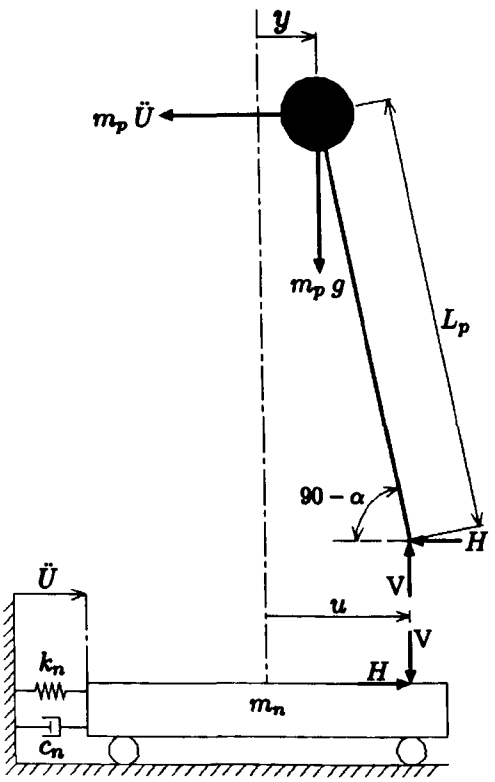

Figure 8.1: Coupled structural-biomechanical IP model.

When simulating walking on a laterally moving surface, the influence of base acceleration, $\ddot{U}$, can be represented by applying a lateral inertia force on the IP mass, altering its motion during the single stance phase. The IP is assumed to maintain lateral balance and therefore correct for base motion by altering its support position, u, for the following step. Thus balance corrections are made only at the time of support placement. Between these discrete corrections, the IP model can be considered passive. This behaviour has been found through analysis of experimental data in chapter 7 to be consistent with human behaviour while walking on a laterally oscillating structure.

Herein the IP model is dynamically coupled to the base structure, thus the lateral force,

H, imparted on the structure by the IP causes a base displacement U which in turn alters the motion of the IP mass during the single stance phase via the inertia force $m_p \ddot{U}$, Fig. 8.1. The lateral inertia force imparted on the base structure is,

$$H = -m_p(\ddot{U} + \ddot{y}) = m_p \omega^2(u - y) \tag{8.1.2}$$

If the base SDoF system represents the n^{th} mode of bridge vibration, then m_n, k_n, and c_n represent the modal mass, stiffness and damping of the bridge while U_n, $\dot{U}_n$ and $\ddot{U}_n$ represent the modal displacement, velocity and acceleration. Thus if N pedestrians are modelled and the location of each along the bridge is denoted by x_p (where p is used as a pedestrian index), the modal equation of motion is,

$$m_n \ddot{U}_n + c_n \dot{U}_n + k_n U_n = \sum_{p=1}^{N} m_{p,p} \omega_p^2 (u_p - y_p) \phi_n(x_p) \tag{8.1.3}$$

in which (assuming a sinusoidal mode shape),

$$\phi_n(x_p) = sin\left(\frac{n \pi x_p}{L}\right) \tag{8.1.4}$$

To account for the introduction of a longitudinal bridge dimension, L, with multiple 'pedestrians' walking simultaneously, the coupled second order differential equations of motion ($2ODE$) become,

$$\ddot{y}_p = -\ddot{U}_n \phi_n(x_p) - \omega_p^2(u_p - y_p) \tag{8.1.5}$$

for $p = 1$ to N, and rearranging Eq. (8.1.3),

$$\ddot{U}_n = \frac{1}{m_n}\left[\left(\sum_{p=1}^{N} m_{p,p} \omega_p^2 (u_p - y_p) \phi_n(x_p)\right) - c_n \dot{U}_n - k_n U_n\right] \tag{8.1.6}$$

Thus an analysis considering N pedestrians requires the solution of N+1 coupled second order differential equations. A solution is sought for the time period during which all IPs are in the single stance phase. When any one of the IPs must switch supporting legs (dictated by their pacing frequency, discussed in section 8.1.4), the coupled 2ODE solution algorithm is temporarily halted and the position and velocity of all masses is saved to form the initial conditions for the next solution period. A new support placement position, u, is calculated for the IP in question, and the system solved for the period until the next IP must switch support legs. The coupled system of differential equations is solved using Matlab's ode45 function which implements a Runge-Kutta algorithm.

8.1.2 Time-step sensitivity

As with the numerical solution of any dynamical system, consideration must be given to the solution time-step. One must balance the competing demands of numerical accuracy and computational efficiency. To choose too large a time-step will result in the system's response deviating from the true behaviour, as a result of the accumulation of small errors in trajectory at each time-step. However, to choose too small a time-step results in unfeasibly long simulation times as the number of calculations grows.

The drift in IP trajectory is demonstrated by simulating a single IP walking, dynamically coupled to a SDoF base structure. By varying the time-step, the growing deviation in IP trajectory (relative to the base) can be observed, Fig. 8.2.

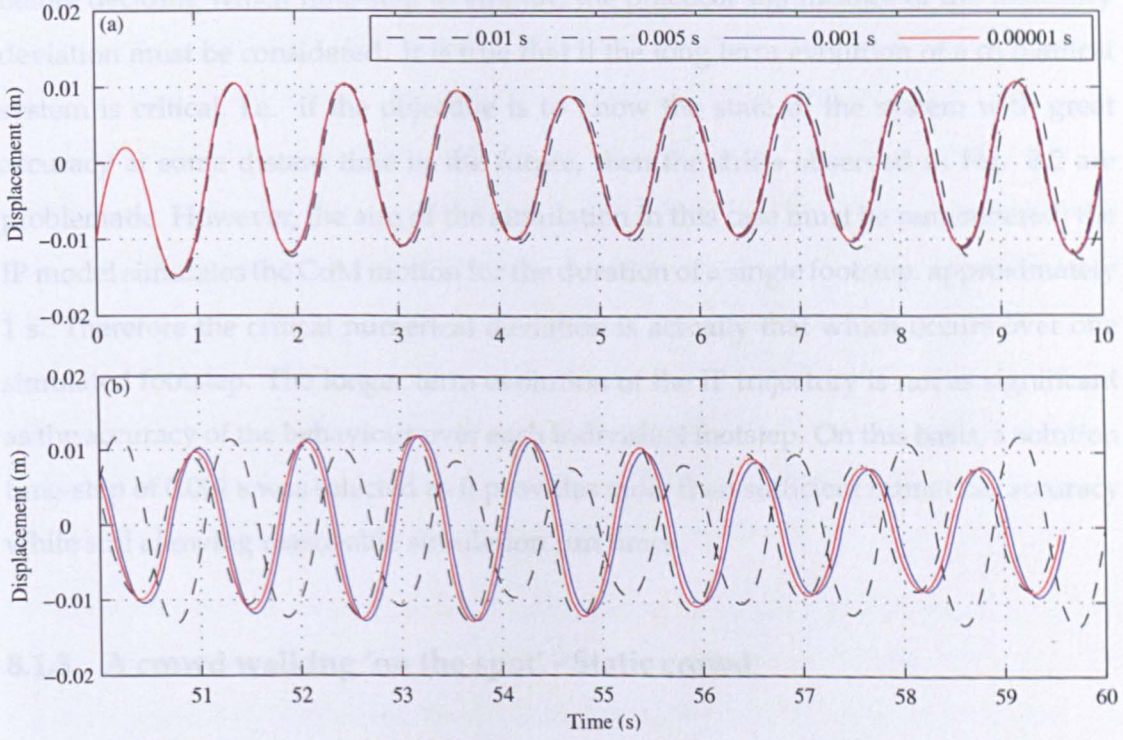

Figure 8.2: IP trajectory for varying time-step, (a) solution period $0\ s < t < 10\ s$ and (b) solution period $50\ s < t < 60\ s$.

Figure 8.2 (a) shows the first 10 s of a 60 s simulation while (b) shows the last 10 s. Four

time-steps have been considered, (8.1.7),

$$\Delta t = \begin{bmatrix} 0.01000\ s \\ 0.00500\ s \\ 0.00100\ s \\ 0.00001\ s \end{bmatrix} \tag{8.1.7}$$

If one considers $\Delta t = 0.00001\ s$ as the benchmark against which the others can be compared, the three larger time-steps appear to perform well initially. However a deviation becomes evident in $\Delta\, t = 0.01\ s$ in the second half of plot (a). Plot (b) shows the extent of the deviation after a further 40 s of simulation. The remaining two time-steps have continued to perform well, closely tracking the benchmark simulation.

Before deciding which time-step to employ, the practical significance of the trajectory deviation must be considered. It is true that if the long term evolution of a dynamical system is critical, i.e. if the objective is to know the state of the system with great accuracy at some distant time in the future, then the drifts observed in Fig. 8.2 are problematic. However, the aim of the simulation in this case must be remembered; the IP model simulates the CoM motion for the duration of a single footstep, approximately 1 s. Therefore the critical numerical deviation is actually that which occurs over one simulated footstep. The longer term evolution of the IP trajectory is not as significant as the accuracy of the behaviour over each individual footstep. On this basis, a solution time-step of 0.001 s was selected as it provides more than sufficient numerical accuracy while still allowing reasonable simulation run times.

8.1.3 A crowd walking 'on the spot' - Static crowd

In order to first demonstrate the behaviour of the dynamical system described in 8.1.1, its solution is now discussed, without the influence of the discrete crowd model. Thus the simplified case of a crowd randomly distributed across a bridge, walking on the spot with constant pacing frequency is simulated. 240 IP models (equivalent to a uniform pedestrian density of 0.6 ped/m^2 on a deck 100 m long × 4 m wide) were coupled with the SDoF bridge model. The location of individual IPs along the deck was randomised by selecting values of x_p drawn from a uniform distribution between 0 and 100, corresponding to the deck length. Lateral forcing frequencies, f_l, governing the

length of the single stance phase for each IP were normally distributed about a mean of 0.95 Hz ($\sigma = 0.09$ Hz), which is typical for pedestrian traffic [61–63, 77].

Initial conditions for the IP model are support position u_0, initial mass position y_0 and velocity $\dot{y}_0$. For 50 % of IPs, initial support positions were drawn from a uniform distribution with values between 0.03 m and 0.05 m, for the remaining 50 %, support positions were drawn from a uniform distribution between -0.03 m and -0.05 m. Initial velocities were also uniformly distributed between 0.06 m/s and 0.1 m/s for 50 % and -0.06m/s and -0.1 m/s for the remaining 50 %. Initial mass position was zero for all IPs. Values for IP initial conditions represent anatomically realistic values, however their influence is dissipated within several 'footsteps' and they do not have a significant effect on the IP's steady state behaviour.

In order for the dynamic behaviour of the IP models to stabilise and the transient effects of initial conditions to dissipate, a minimum of 5 s of dynamic IP behaviour is simulated before any IP is coupled to the bridge. After this initial 5 s has elapsed, individual IPs are coupled to the bridge at random start times. Start times are drawn from a uniform distribution between $t = 5\ s$ and $t = 10\ s$. This ensures IPs do not begin exciting the structure in time. Decoupling individual IP models from the bridge is achieved by setting $\phi_n(x_p) = 0$ in Eqs. (8.1.5) & (8.1.6). This allows solution of the fixed size dynamic system to progress, without any interaction between a (decoupled) IP and the bridge, i.e. the number of degrees of freedom within the dynamical system is constant regardless of the number of IPs actually coupled to the SDoF system.

Multiple simulations were carried out with randomised initial conditions as described above. The remaining simulation parameters are summarised in Table 8.1. Figure 8.3 (a) is a typical example of the lateral bridge acceleration observed at mid-span. In this instance, at approximately 520 s the bridge response begins to increase rapidly. This behaviour, indicated by the vertical dashed line is herein referred to as lateral dynamical instability and is identified by the onset of uncharacteristically large vibration amplitudes. These large vibration amplitudes are developed due to the crowd-induced power input remaining positive for a prolonged period of time allowing feedback between the IP crowd and bridge oscillations to develop. The simulated bridge behaviour approximates quite well the behaviour observed on several full scale bridges [2, 4–

Table 8.1: Simulation parameters.

Parameter	Value	Reference
Δt_{dyn}	0.001 s	
m_n	70×10^3 kg	
k_n	1.996×10^6 N/m	
c_n	3.738×10^3 Ns/m	
ζ	0.5 %	
f_n	0.85 Hz	
m_p	70 kg	[37]
L_p	1.2 m	[37]
b_{min}	0.0157 m	[37]
$f_{l,\mu}$	0.95 Hz	
$f_{l,\sigma}$	0.09 Hz	

6, 24, 26].

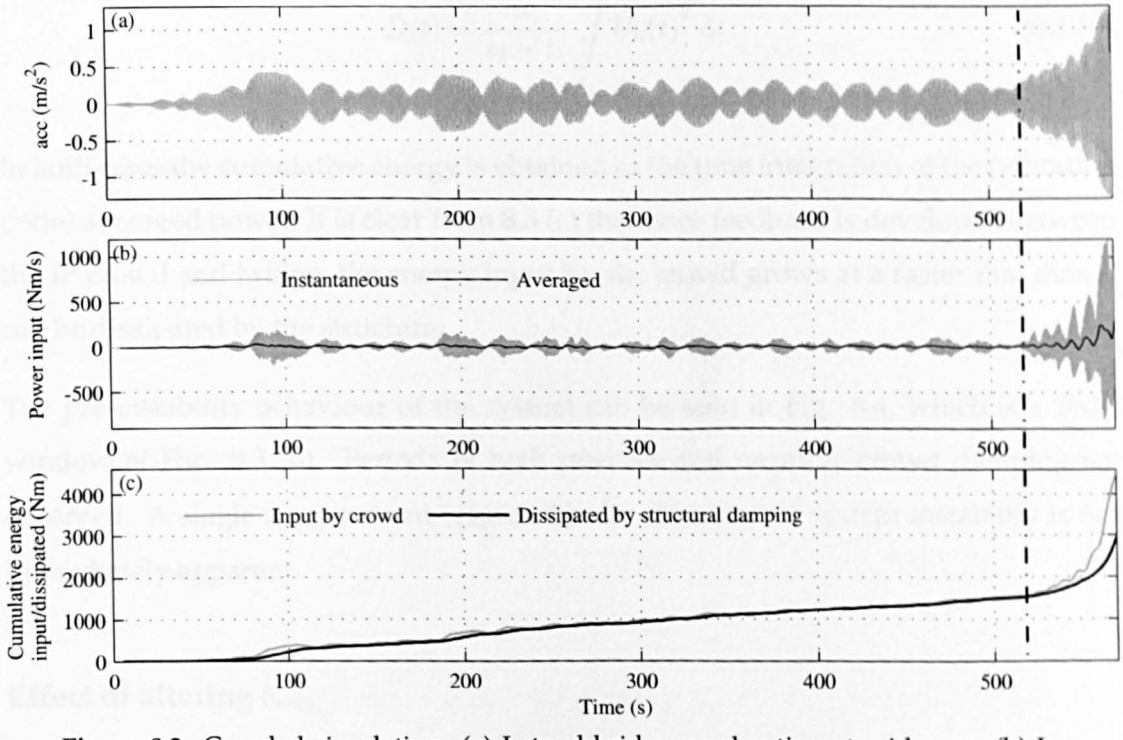

Figure 8.3: Coupled simulation: (a) Lateral bridge acceleration at mid-span, (b) Instantaneous and averaged crowd-induced power input, (c) Cumulative energy input by the crowd and dissipated by the structure.

It should be remembered that step synchronisation has not occurred. IP stepping fre-

quencies remain unaffected by bridge response. Figure 8.3 (b) shows both the instantaneous, $P(t)$, and averaged (over each bridge vibration cycle), $\bar{P}(T)$ power input by the IP crowd, obtained respectively as

$$P(t) = \sum_{p=1}^{N} H_p \, \dot{U}_n \, \phi(x_p) \tag{8.1.8}$$

$$\bar{P}(t) = \frac{1}{t_2 - t_1} \int_{t_1}^{t_2} P(t) \, \mathrm{d}t \tag{8.1.9}$$

where t_1 and t_2 denote the beginning and end of a bridge vibration cycle. Prior to the development of instability, the crowd-induced power varies from positive to negative, however as the bridge response increases the power input magnitude grows and on average remains positive. The effect is clearly seen, Fig. 8.3 (c), when comparing the cumulative energy input by the crowd against the energy dissipated by the structure's (viscous) damping, $\bar{D}$, where,

$$\bar{D}(t) = \frac{c_n}{t_2 - t_1} \int_{t_1}^{t_2} \dot{U}_n(t)^2 \, \mathrm{d}t \tag{8.1.10}$$

In both cases the cumulative energy is obtained as the time integration of the (vibration cycle) averaged power. It is clear from 8.3 (c) that once feedback is developed between the IP crowd and bridge, the energy input by the crowd grows at a faster rate than it can be dissipated by the structure.

The pre-instability behaviour of the system can be seen in Fig. 8.4, which is a 100 s window of Fig. 8.3 (b). Periods of both positive and negative crowd damping are observed. A single trigger event responsible for the onset of system instability is not immediately apparent.

Effect of altering b_{min}

In subsection 7.3 of the previous chapter, it was found that the IP model (and balance law), typically underestimates gait width for subjects walking on an oscillating structure. This effect was quantified with the ratio b_{fac}, in Eq. (7.3.1), repeated below,

$$b_{fac} = \frac{b_{dyn}}{b_{min}}$$

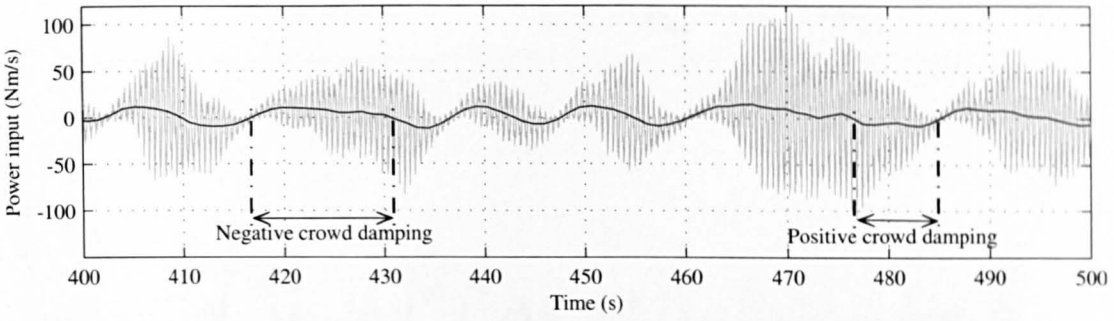

Figure 8.4: Coupled simulation, $t = 400s$ to $t = 500s$: Instantaneous and averaged crowd-induced power input.

When the test population averages are considered, the largest b_{fac} values do not exceed 1.36 and the average of all b_{fac} values is 1.17. In order to investigate the influence of an increase in stability margin, the previous simulation was repeated with the same initial conditions but with a range of increased stability margins applied uniformly across the crowd, Fig. 8.5. It is clear that simulations in which b_{min} was increased exhibit larger mean bridge response levels, due to the increased GRF magnitudes. However there is negligible influence on the initiation of lateral instability. This is in line with previous observations by Bocian et al. [15]. Based on this and considering the approximation associated with the estimation of b_{min} values is this study, it is considered prudent to maintain a value of $b_{min} = 0.0157$ m in the simulations that follow.

Crowd decoupled from the bridge

To further investigate the effect of coupling between the IP crowd and the bridge system, the previous simulation was repeated (with $b_{min} = 0.0157$ m for all IPs). However the IPs were decoupled from the bridge such that the bridge response had no influence on IP motion. However the crowd-induced force was still imposed on the bridge. This is achieved by setting $\phi_n(x_p)$ equal zero in Eq. (8.1.5) but leaving it unaltered in Eq. (8.1.6).

The system behaviour observed is considerably different, Fig. 8.6 (a)-(c). The peak bridge acceleration amplitudes are approximately three times smaller than those developed in the coupled simulation. Similarly, the RMS acceleration for the coupled system between $t = 0s$ and $t = 520s$ is 0.16 m/s^2, compared with 0.04 m/s^2 for the full duration of the decoupled simulation. Most significantly the large amplitude responses

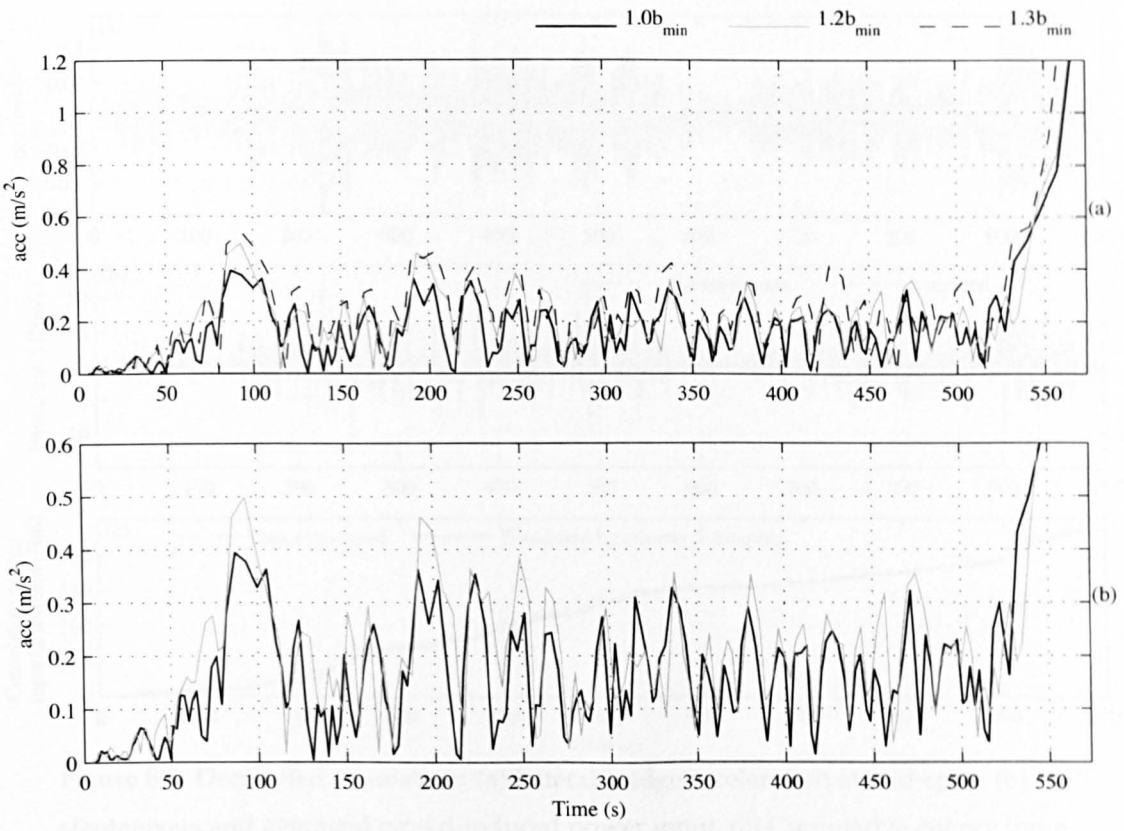

Figure 8.5: Peak lateral acceleration envelope for the static crowd simulation, with varying minimum stability margins applied uniformly across the crowd. Plot (b) shows a comparison between the original simulation and one in which a 20% increase in b_{min} is applied uniformly across the crowd.

observed in the coupled simulation are not developed, i.e. the rate of power input by the pedestrian crowd does not exceed the rate of dissipation by the structure for a significant period of time. The larger amplitude bridge response and instability observed previously clearly results from the coupling between the IP crowd and bridge.

The influence of bridge motion on the behaviour of a typical IP located 60m along the bridge can be seen in Fig. 8.7 (a). When the IP is coupled to the bridge, the balance law dictating the lateral position of foot placement, Eq. (2.3.18), causes the simulated gait width of the IP to narrow and widen in response to the inertia force imposed by the structural response. This results in AM of the lateral force imposed on the structure. The degree or depth of AM is a function of the degree to which IP stability is influenced by bridge motion. This is qualitatively consistent with the behaviour observed in test subjects, discussed previously. Figure 8.7 (b) shows the lateral force imparted on the structure by the same IP when decoupled from the bridge.

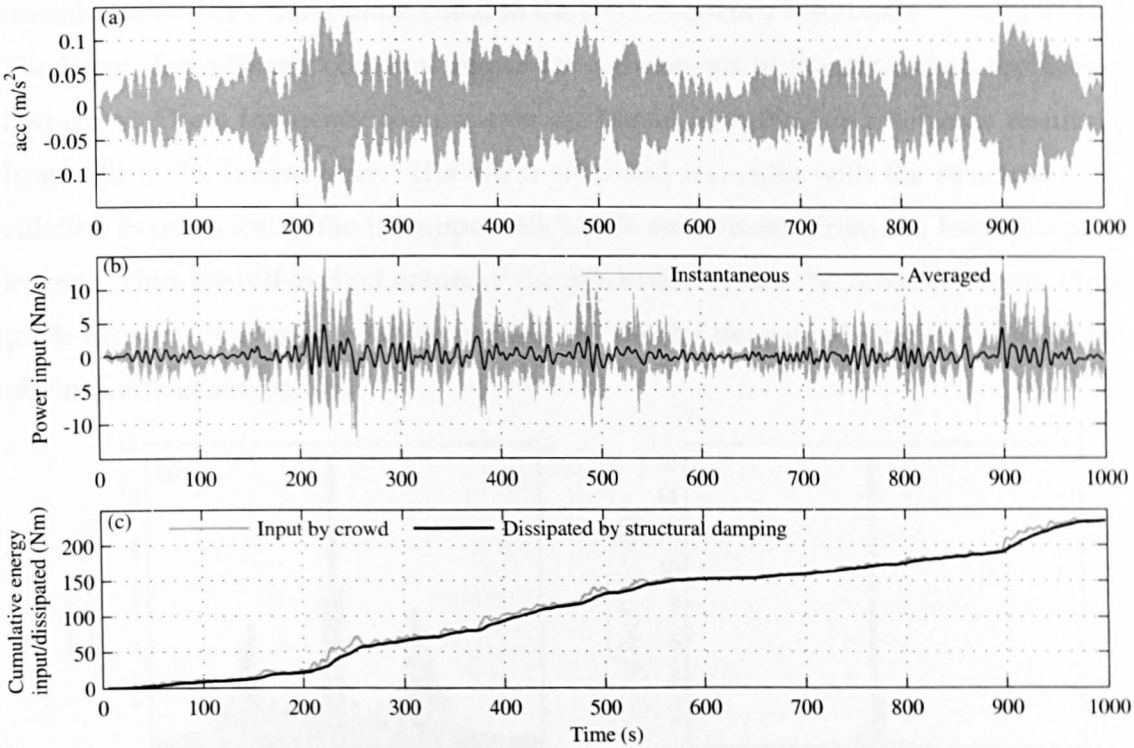

Figure 8.6: Decoupled simulation: (a) Lateral bridge acceleration at mid-span, (b) Instantaneous and averaged crowd-induced power input, (c) Cumulative energy input by the crowd and dissipated by the structure.

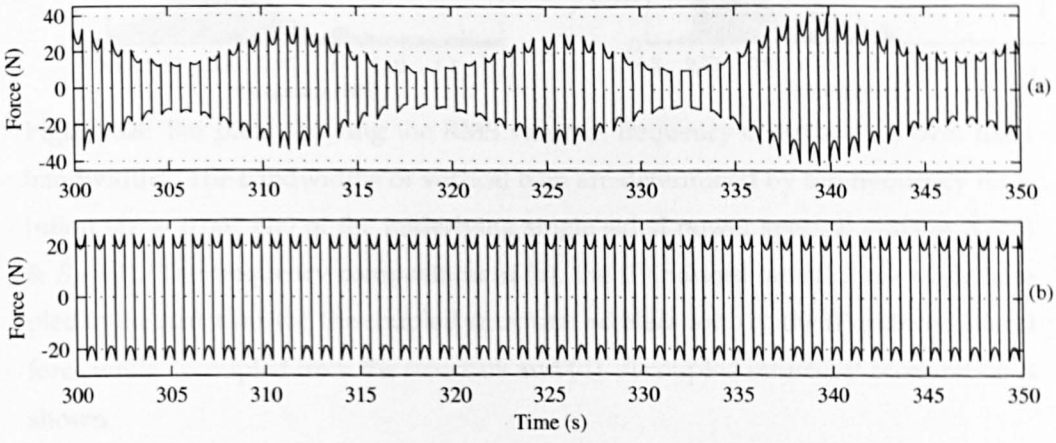

Figure 8.7: Lateral GRF for IP (a) coupled to structure, (b) decoupled from structure.

The results of this force AM when summed across the full IP crowd can be seen in Fig. 8.8. Plots (a) & (b) show the frequency composition of the lateral footfall force imposed by the aforementioned IP model and the frequency composition of the lateral bridge acceleration. Each plot is derived from the single sided power spectral density (PSD) of the underlying signal. The vertical bar heights indicate the RMS value of frequency

contributions over a bandwidth equal to the PSD frequency resolution, $\delta_f = 0.007$ Hz. The lateral force clearly contains frequency components at the structure's oscillation frequency. These frequency components are herein identified as sidebands resulting from AM of the lateral force. The lower sideband coincides with the structure's oscillation frequencies, while the upper sidebands are detuned from the frequencies of interest. Thus the self-excited nature of the dynamical system becomes apparent. Plots (c) & (d) show the same analysis carried out for the decoupled simulation with the obvious lack of sidebands.

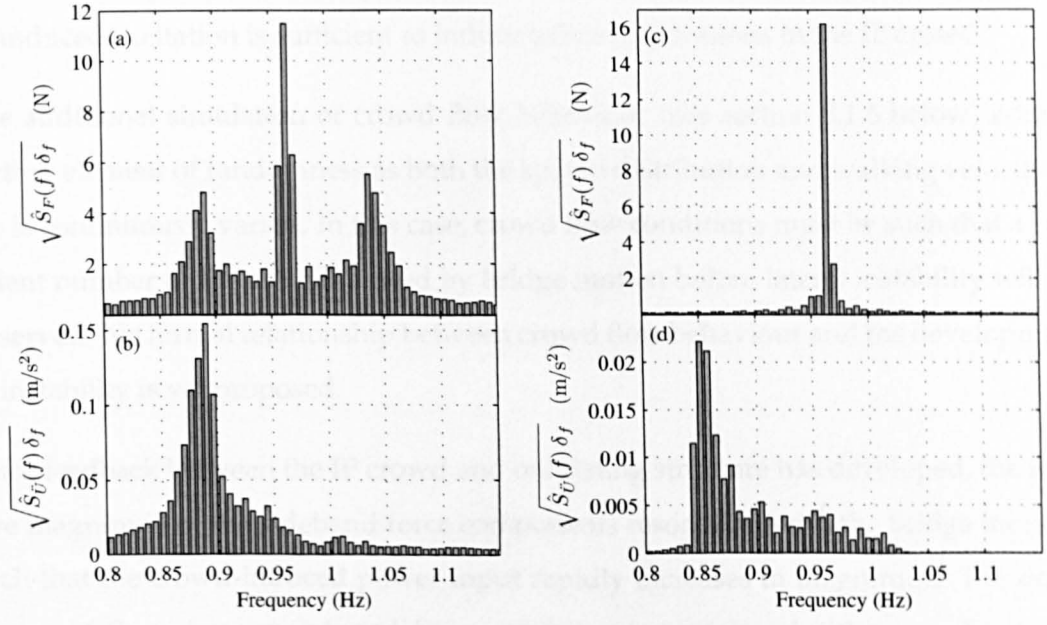

Figure 8.8: Bar plots showing the RMS value of frequency contributions over fixed bandwidths. The bandwidths of vertical bars are determined by the frequency resolution ($\delta_f = 0.007$ Hz) of the underlying single sided power spectral density, $\hat{S}_F(f)$ & $\hat{S}_{\ddot{U}_n}(f)$. The frequency composition of (a), the IP-induced lateral force while coupled to the structure, (b), the coupled structural acceleration, (c), the IP-induced lateral force while decoupled from the structure and (d), decoupled structural acceleration is shown.

The time at which instability occurs is essentially a random variable. For a given set of structural characteristics, it is related to the distribution of IP stepping frequencies and the proximity of these frequencies to the modal frequency of interest. When random IP excitation develops to the point that structural response induces gait width alterations among the IP crowd, self-excited force components are generated in the IP GRFs.

Whether or not the self-excited forces serves to increase or reduce the energy level of the bridge mode depend on the frequency relationship between the lateral forcing and bridge oscillation frequencies, as demonstrated in [37] for a single IP.

Thus if a sufficient number of IPs are influenced by base motion and possess lateral forcing frequencies resulting in energy addition for the modal frequency considered, the feedback between structural motion and crowd excitation is established from which large amplitude lateral oscillations are likely to develop. Therefore the initiation of lateral instability within this model can be traced back to the point at which random IP-induced excitation is sufficient to induce balance alterations in the IP crowd.

The additional simulation of crowd flow behaviour (see section 8.1.6 below) adds a further element of randomness as both the spatial distribution and walking velocity of IPs is continuously varied. In this case, crowd flow conditions must be such that a sufficient number of IPs are influenced by bridge motion before lateral instability will be observed. No formal relationship between crowd flow behaviour and the development of instability is yet proposed.

Once feedback between the IP crowd and oscillating structure has developed, the relative magnitude of the sideband force components resonating with the bridge increase such that the crowd-induced power input rapidly increases in magnitude. The dominance of these frequency-tuned force components explain why the crowd-induced power remains positive after system instability is observed.

In summary, the feedback demonstrated in this model it is not directly linked to the structure's natural frequency. That is to say that regardless of the natural frequency of a particular mode, if random pedestrian excitation is significant enough to excite that mode to the point that it sufficiently alters pedestrian gait width, AM based feedback may occur. This may in turn result in lateral instability, identified as the development of uncharacteristically large lateral vibration amplitudes. This can potentially explain crowd-induced instability of lateral modes outside the traditionally recognised problem range of 0.8 Hz – 1.1 Hz.

8.1.4 Coupling between crowd model and dynamical system

The influence of crowd behaviour is now introduced by coupling the discrete element crowd model discussed in chapter 5 with the dynamical system discussed above. The complete model is implemented and solved in a time-stepping loop. The time-step required for the crowd model was found to be 0.01 s (see subsection 5.2.4). A time-step of 0.001s was selected for the IP-bridge dynamical system, discussed above. Further reduction of either time-step results in negligible variation in model output. For every iteration of the crowd model in which pedestrian locations are advanced, there are 10 iterations in the numerical solution of the IP-bridge dynamical system. Thus the crowd and dynamic systems are never more than $1/100^{th}$ of a second out of synchronisation.

The pedestrian location along the bridge at the time of foot placement is passed from the crowd model into the dynamical system in order to determine $\phi_n(x_p)$ and thus provide a realistic and evolving pedestrian distribution across the bridge. In the event that a pedestrian is not on the bridge (after walking off or before walking on), $\phi_n(x_p)$ for the corresponding IP is set to zero in equations (8.1.5) and (8.1.6), thereby decoupling that IP from the bridge system.

At the time of foot placement, pedestrian walking velocity magnitude, $|\mathbf{V}_p|$ is also sampled from the crowd model. The velocity magnitude is converted into a pacing frequency, f_v, in the same manner described in section 5.2.2, using the empirical relationship (5.2.9) reported in [49] and repeated below. From Eq. (5.2.9), the time spent on one foot, T is calculated (8.1.11) thus identifying the time at which the pedestrian must take their next step and the corresponding IP must switch supporting legs.

$$f_v = 0.35|\mathbf{V}_p|^3 - 1.59|\mathbf{V}_p|^2 + 2.93|\mathbf{V}_p|$$

$$T = 1/f_v \tag{8.1.11}$$

In this way the variation in pedestrian walking speeds (and therefore lateral forcing frequencies) due to traffic or other obstacles is simulated.

Occasional pedestrian avoidance behaviours result in deviations in travel velocities. In reality such behaviour results in the application of short duration forces that may be approximated as impulses. These impulse forces are not considered in this model for two reasons. Firstly, simulation of the biomechanical behaviour (and resulting forces)

associated with changes in walking velocity (and in particular, direction) is outside the scope of the 2D planar IP model. Secondly, the resulting impulse forces have little dynamic effect against a dominant background of periodic lateral GRFs.

8.1.5 Biomechanical simulation of variable walking speed

A limitation of the passive IP model becomes apparent when a reduction in walking speed is simulated. The corresponding reduction in pacing frequency, (5.2.9), results in an increase in the ground contact time for the supporting leg, Eq. (8.1.11). This results in the IP mass 'falling' further in the medial direction, developing a larger velocity before the support position is altered resulting in a wider foot placement for subsequent steps. This increases both oscillation and lateral force magnitude, Fig. 8.9.

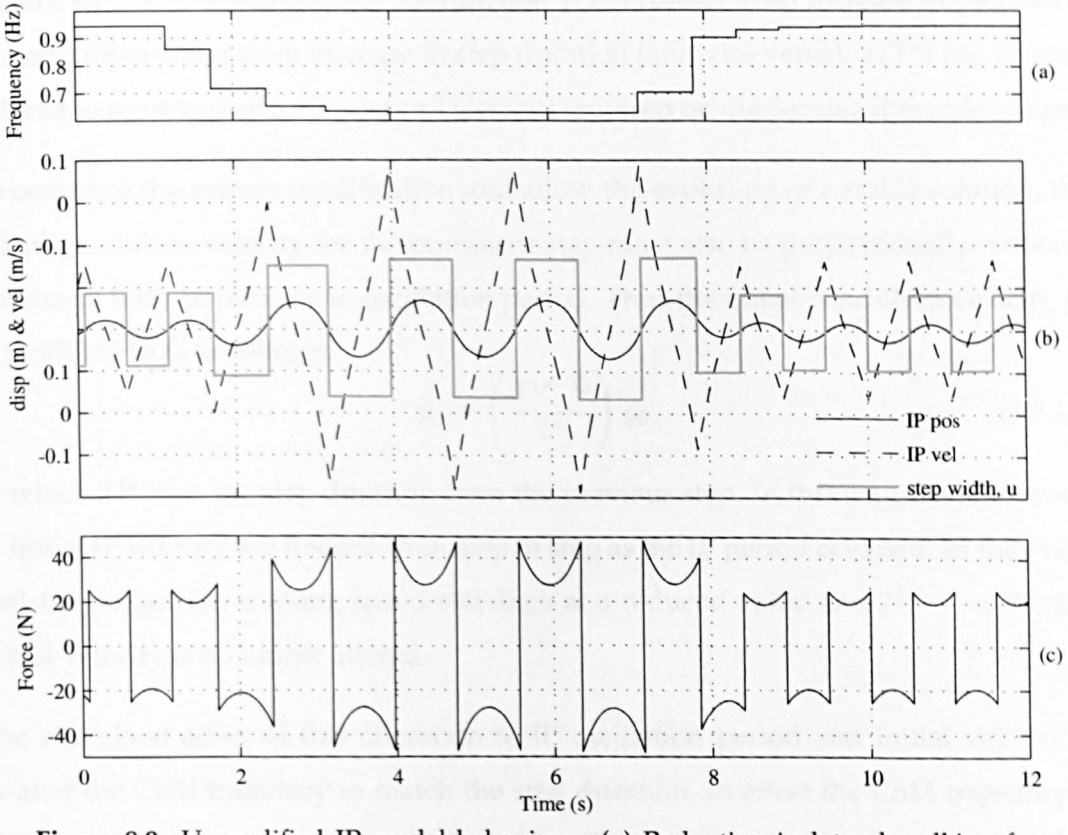

Figure 8.9: Unmodified IP model behaviour: (a) Reduction in lateral walking frequency due to a reduction in walking speed (b) IP mass position, velocity and lateral support position, u, (c) lateral IP-induced force imposed on base structure.

However, lateral footfall force magnitude is known to be independent of pacing frequency [7, 9]. Furthermore, an alteration in walking speed should not result in any

change in step width. Displacement and force magnitude should remain constant with only stepping frequency being altered.

To allow variation in CoM oscillation period, without generating biomechanically unrealistic CoM behaviour and GRFs, Eq. (8.1.5) describing IP acceleration is modified with an additional function, $f(T^s)$,

$$\ddot{y}_p = -\ddot{U}_n \, \phi_n(x_p) - [\omega_p + f(T^s)]^2 \, (u_p - y_p) \tag{8.1.12}$$

in which,

$$f(T^s) = \omega_p \left(\frac{T_d}{T^s} - 1 \right) \tag{8.1.13}$$

where T_d is the step duration corresponding to the pedestrian's desired velocity (specified at the beginning of the simulation) and T^s is the actual step duration for the imminent step, s. The inclusion of the function $f(T^s)$ results in an increase in oscillation period proportional to an increase in step duration (and vice versa). $f(T^s)$ can be considered to represent an active control element imposed on the passive dynamic system.

To complete the system modification and allow the evolution of a stable solution, the initial pendulum velocity for the imminent step must also be proportionally reduced, consistent with an increase in oscillation period. Thus the initial pendulum velocity, $\dot{y}_0$ is modified to $\bar{\dot{y}}_0$ as follows,

$$\bar{\dot{y}}_0 = \left(\frac{T^{(s-1)}}{T^s} \right) \dot{y}_0 \tag{8.1.14}$$

in which $T^{(s-1)}$ is the step duration from the previous step. In this way, the alterations to initial IP velocity are tracked from step to step as the IP period is varied. In the event that the pedestrian walking speed stabilises at a reduced value and $T^{(s-1)} = T^s$, the initial velocity is no longer altered.

The combined effect of this alteration to IP oscillation period and initial velocity is to alter the CoM trajectory to match the step duration, in effect the CoM trajectory is 'stretched' to simulate a more realistic CoM oscillation. The behaviour of the modified dynamical system evolves through the coupled solution of Eqs. (8.1.6) and (8.1.12).

It can be seen in Fig. 8.10, that step width, force amplitude and maximum pendulum displacement now remain constant, despite changes in walking velocity. This allows variable walking velocities dictated by the crowd model to be accommodated by the

coupled dynamical system. Thus any change in step width is due to base oscillations alone and not the result of variations in step duration arising from changes in walking velocity.

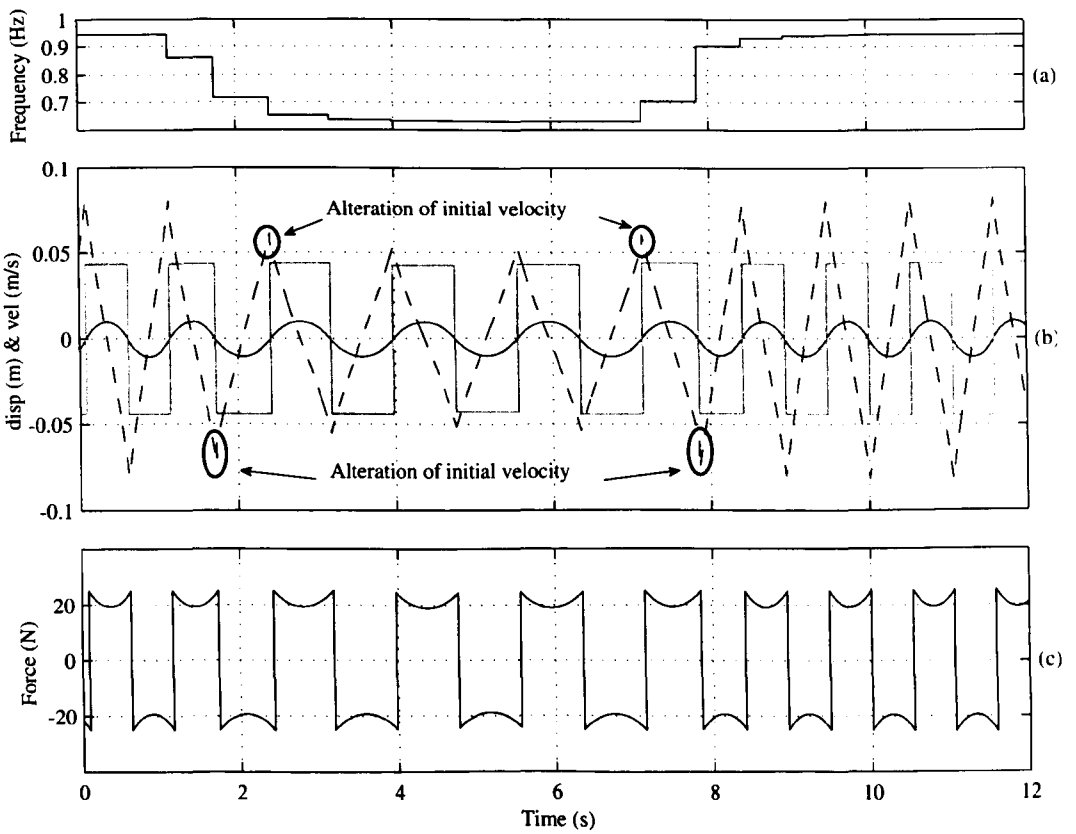

Figure 8.10: Modified IP model behaviour: (a) Reduction in lateral forcing frequency, (b) IP mass position, velocity and lateral support position, u, (c) lateral IP-induced force imposed on base structure.

From a mechanical viewpoint, an impulse is required to achieve a step-like change in pendulum velocity. However, no such impulse is considered in this analysis as it has no biomechanical relevance. Simulation of the effects of such an impulse, while being mechanically rigorous, would not improve the accuracy of the simulated behaviour. In terms of the simulated velocity, the modified IP model is thus a piecewise continuous model. The proportional modification of IP period and initial velocity have no biomechanical foundation. Rather, they are a simplified method of improving the simulation of what is, in reality, a much more complicated biomechanical and control system.

8.1.6 Coupled crowd-structure-biomechanical simulation

Simulation data from the complete model is now discussed, thus crowd behaviour and its influence on the dynamic response of the bridge is considered. A typical data set presented below. Simulation parameters are summarised in Table 8.2, randomly distributed initial conditions for IP position, velocity and support position were chosen from the distributions previously described.

Table 8.2: Full model simulation parameters.

Parameter	Value	Reference
Δt_{crowd}	0.01 s	
k_1	2000 N	[75]
k_2	0.08 m	[75]
k_p	6 m^{-1}	*empirical*
r_{psy}	0.35 m	[74]
t_r	0.5 s	[75]
$\|\mathbf{V}_d\|_{mean}$	1.5 m/s	[63]
$\|\mathbf{V}_d\|_{st.dev}$	0.125 m/s	[63]
N	*varies*	
Δt_{dyn}	0.001 s	
L	100 m	
B	4 m	
m_n	70×10^3 kg	
k_n	1.996×10^6 N/m	
c_n	3.738×10^3 Ns/m	
ζ	0.5 %	
f_n	0.85 Hz	
m_p	70 kg	[37]
L_p	1.2 m	[37]
b_{min}	0.0157 m	[37]

The mean desired walking velocity among the crowd was selected as 1.5 m/s. The simulation of traffic conditions within the crowd model results in realised walking velocities lower than desired velocities. Therefore the mean lateral forcing frequency among

the crowd was ≈ 0.94 Hz after traffic effects are simulated, which is in line with the static crowd simulation discussed above.

The lateral bridge acceleration along with the number of pedestrians present on the bridge is shown in Fig. 8.11 (a). The number of pedestrians exciting the bridge between $t = 10s$ and $t = 500s$ fluctuates about a mean of 247 (max = 274, min = 220). This fluctuation occurs due to non-coincident pedestrian entries and exits, a feature introduced by the inclusion of the discrete element crowd model. Lateral instability, indicated by the vertical dashed line is again developed. Fig. 8.11 (b) & (c) show the corresponding power and energy analysis for the simulation which are qualitatively similar to the previous static crowd simulation. It is interesting to note the system

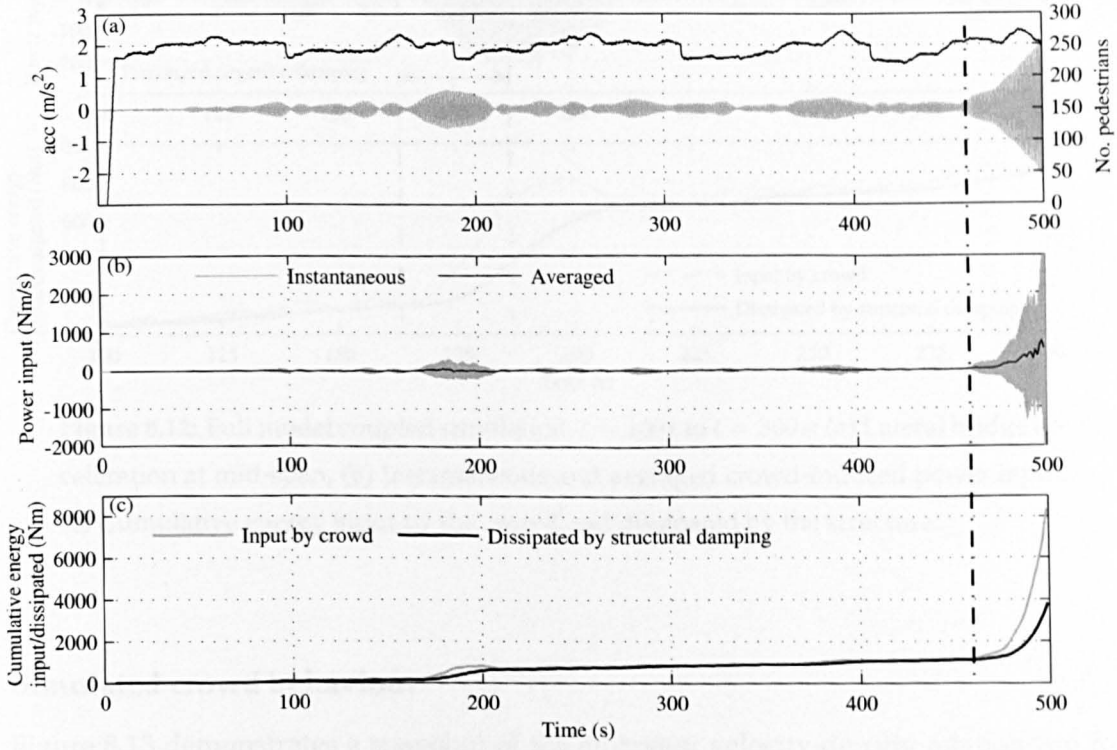

Figure 8.11: Full model coupled simulation: (a) Lateral bridge acceleration at mid-span, (b) Instantaneous and averaged crowd-induced power input, (c) Cumulative energy input by the crowd and dissipated by the structure.

behaviour between $t = 100s$ and $t = 300s$, shown in greater detail in Fig. 8.12. A prolonged period of positive power input by the crowd, Fig. 8.12 (b), appears to mark the initiation of unstable behaviour. The cumulative energy input increases at a higher rate than it is dissipated by the bridge, Fig. 8.12 (c). However, the development of instability is suddenly halted as the crowd-induced power input reduces. This reduc-

tion correlates well with the sudden departure of 27 pedestrians from the bridge. The feedback between the IP crowd and bridge response renders the behaviour of the dynamical system non-linear. Therefore this modest but swift reduction in coupled IPs may have been sufficient to stem the growth in response.

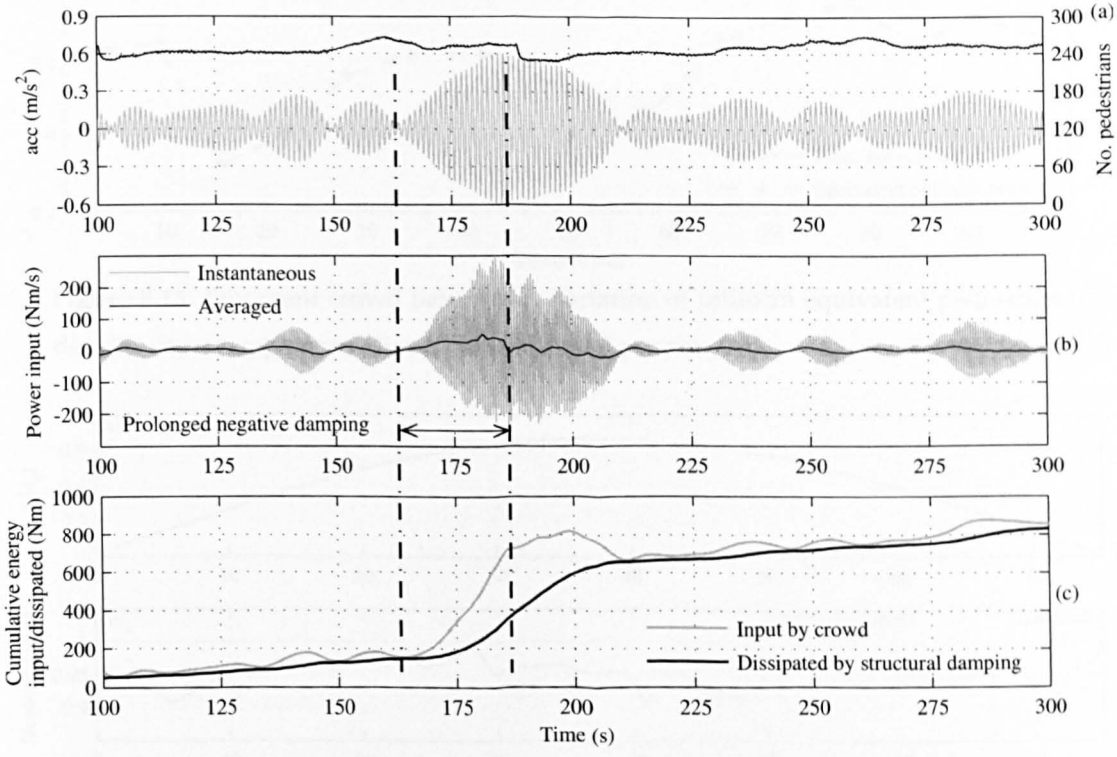

Figure 8.12: Full model coupled simulation, $t = 100s$ to $t = 300s$: (a) Lateral bridge acceleration at mid-span, (b) Instantaneous and averaged crowd-induced power input, (c) Cumulative energy input by the crowd and dissipated by the structure.

Simulated crowd behaviour

Figure 8.13 demonstrates a snapshot of the emergent velocity-density relationship for the crowd and is analogous to Fig. 5.26 previously discussed. The overall reduction in walking speed due to the presence of traffic is again demonstrated, with zones of particularly high density exhibiting correspondingly low average velocities and vice versa. It is worth repeating that the distribution of walking speeds among the crowd has a direct influence on the frequency of lateral force input. As such its realistic simulation is important for a complete description of the coupled crowd-bridge system.

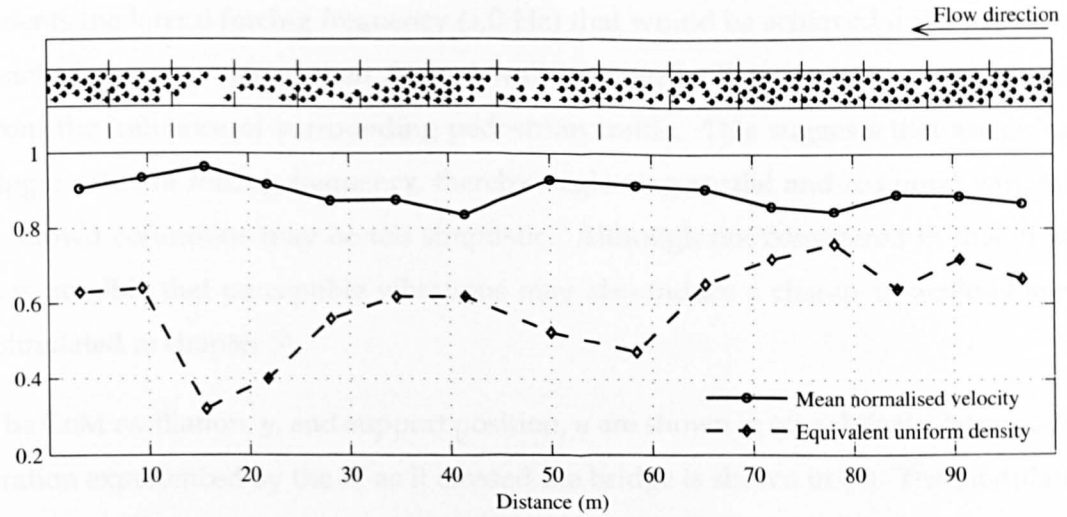

Figure 8.13: Emergent crowd behaviour: variation of uniform equivalent pedestrian density and average normalised walking speed per zone.

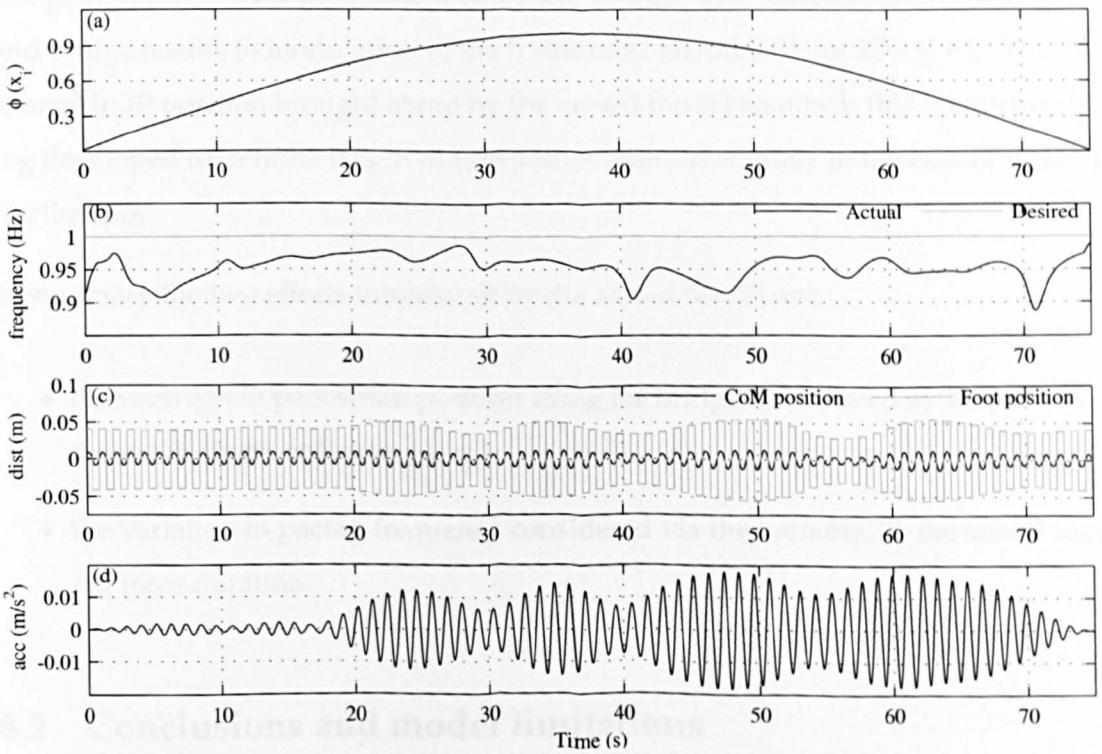

Figure 8.14: (a) $\phi_n(x_p)$ indicating longitudinal IP position as a function of time, (b) variation in lateral forcing frequency as IP crosses the bridge, (c) lateral CoM position and variation in support position u, (d) Acceleration at the IP's location (Acceleration experienced by the IP during the bridge crossing).

Figure 8.14 displays the variation in a single pedestrian's behaviour. Plot (a) shows the mode shape ordinate as a function of time for a pedestrian (among the crowd) crossing the bridge. The variation in forcing frequency is shown in plot (b). The dashed line rep-

resents the lateral forcing frequency (1.0 Hz) that would be achieved if the pedestrian reached and maintained their desired walking speed. This variation results directly from the influence of surrounding pedestrian traffic. This suggests that assigning a single value of forcing frequency, thereby neglecting spatial and temporal variations in crowd conditions may be too simplistic. Although not considered in this model, it is possible that perceptible vibrations may also induce a change in walking speed (simulated in chapter 5).

The CoM oscillation, y, and support position, u are shown in (c), while the lateral acceleration experienced by the IP as it crossed the bridge is shown in (d). The modulation of gait width brought about by bridge motion is clearly seen. For 0 s $\leq t \leq$ 20 s and $t >$ 70 s stride width is relatively unaffected, however as the IP advances across the bridge it becomes strongly influenced by the bridge. This interaction between the IP and bridge results in modulation of the IP-induced lateral GRF for 20 s $\leq t \leq$ 70 s. The change in IP position brought about by the crowd model results in this interaction being developed for a finite length of time rather than indefinitely in the case of walking 'on the spot'.

In summary the two effects introduced by the crowd model are;

- the variation in pedestrian position along the bridge, considered in the model via the mode shape ordinate, $\phi_n(x_p)$.
- the variation in pacing frequency considered via the variable, T, the lateral footfall force duration.

8.2 Conclusions and model limitations

In this chapter a model has been presented that attempts to capture the duel effects of HSI and wider evolving crowd behaviour. The central theme of this thesis is that consideration of both is a prerequisite for a full description of crowd-induced bridge vibration. The concept of using discrete element modelling to characterise the pedestrian crowd has been expanded from chapter 5 to include a biomechanical crowd coupled to the bridge structure. In so doing, two-way HSI is simulated.

It has been demonstrated that the cumulative effect of this interaction, when considered over many IPs, can lead to large amplitude bridge oscillations being developed, referred to as lateral dynamic instability. This results from a feedback mechanism in which random pedestrian excitation is sufficient to generate a deck response that influences IP gait width. As discussed previously, this leads to sideband force harmonics in the GRF that resonate with the bridge response, thereby increasing its magnitude. This in turn causes gait width to be further influenced, increasing the relative magnitude of the self-excited forces, and so the cycle continues. This is demonstrated by comparing coupled and decoupled crowd simulations in 8.1.3.

Perhaps the most significant feature of the behaviour demonstrated in this chapter is the lack of step frequency tuning. Thus an interaction mechanism has been demonstrated that may explain the experimental observations of Brownjohn et al. [6] and Macdonald [24] discussed in chapter 2. A subtle consequence of this is that the development of instability is not directly related to modal frequency, i.e. large amplitude response can develop in any mode, provided random crowd excitation of that mode is sufficient to influence gait widths in the crowd.

In the following chapter, the validity of this model will be assessed through comparison with the documented crowd-induced instability of the Clifton Suspension Bridge [24].

CHAPTER 9

Model validation

Chapter Summary

In this penultimate chapter, the validity of the model developed and discussed in the previous chapter is considered. For the purposes of this validation, a well documented crowd loading event is considered as a benchmark case study. The model is used to simulate pedestrian traffic traversing the Clifton Suspension Bridge (CSB) in Bristol, UK.

In section 9.1 the structure and dynamic characteristics of the CSB are described. The details of the recorded loading event are then presented in section 9.2. In order to simulate interaction between a pedestrian crowd and multiple modes of vibration simultaneously, several modifications are made to the model previously discussed in chapter 8. These are explained in section 9.3. Simulation results and discussion are presented in 9.4 before conclusions regarding model validity are drawn in section 9.5.

9.1 Clifton Suspension Bridge case study

On the night of Thursday the 7th of August 2003, between 10:00pm and midnight, the CSB experienced unusually dense crowd loading due to the Bristol International Balloon Fiesta. During this period, the second and third lateral vibration modes were excited to amplitudes approximately 10 times greater than the characteristic maximum under normal loading conditions. This is one of the most comprehensively documented crowd loading events during which sudden onset lateral instability was observed [24]. It is therefore an excellent candidate against which to test the proposed model. Information regarding the bridge construction, dynamic characteristics and crowd conditions have been obtained from [24] unless stated otherwise.

The CSB, Fig. 9.1, completed in 1864 [23], was designed by I.K. Brunel and spans the Avon Gorge west of Bristol city centre. The suspended deck spans approximately 194 m between abutments. The deck is constructed of timber (topped with modern paving), spanning longitudinally between transverse lattice girders. Longitudinal stiffening girders span between vertical suspension rods and frame the central roadway, approximately 6.1 m wide. Pedestrian walkways on either side of the roadway bring the total deck width to approximately 9.46 m. The total mass of the deck and supporting chains between both piers is estimated to be 1150 t.

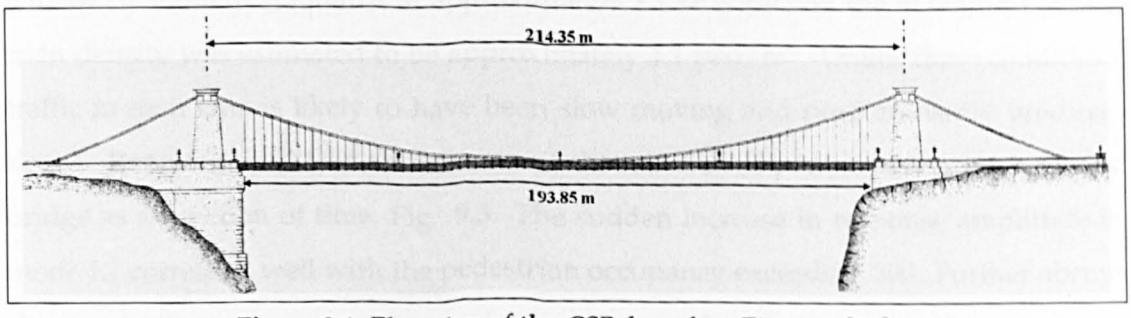

Figure 9.1: Elevation of the CSB, based on Fig. 1 in [23].

The bridge possesses twelve vertical modes, four lateral modes and eleven torsional modes in the bandwidth between 0.2 Hz and 3.0 Hz. Of these, only the second and third lateral modes are of interest. The relevant mode shapes have been estimated from [24], Fig. 9.2, yielding the approximate estimates of modal mass in Table 9.1.

Table 9.1: Lateral modal characteristics.

n	f_n	ζ_n	m_n
L2	$0.524Hz$	0.58%	554,000 kg
L3	$0.746Hz$	0.68%	561,000 kg

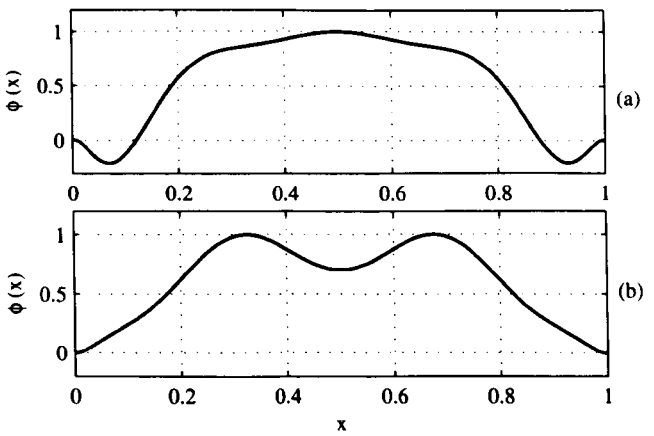

Figure 9.2: (a) second and (b) third lateral mode shapes, estimates from [24].

9.2 Loading event description

For the 2 hour duration of the loading event under consideration, pedestrian traffic was restricted to the walkways on either side of the carriageway. The walkways are quite narrow by modern standards at approximately 1.1 m wide and the maximum pedestrian density was estimated to be approximately 1.1 ped/m^2. Under these conditions traffic in each lane is likely to have been slow moving and predominantly unidirectional. Reported in [24] is an estimate of the number of pedestrians present on the bridge as a function of time, Fig. 9.3. The sudden increase in response amplitude in mode L2 correlates well with the pedestrian occupancy exceeding 200. Further abrupt changes in the response envelopes also correlate well with changes in the occupancy level.

After a large response was developed in mode L2, unusually large response levels built up in mode L3, Fig. 9.3. Simultaneous large amplitude responses in two lateral modes are not compatible with the theory that the pedestrian crowd were step synchronising with the bridge oscillation. For a pedestrian to step synchronise with an oscillation at one frequency would seem unlikely when already experiencing large amplitude oscil-

lations at another. A lack of peaks in the vertical response spectrum at twice the lateral modal frequencies further undermined the step-synchronisation mechanism, an observation also made by Browdjohn et al. [6] in relation to the Changi airport bridge. Thus an alternative mechanism is required to explain the vibration amplitudes observed.

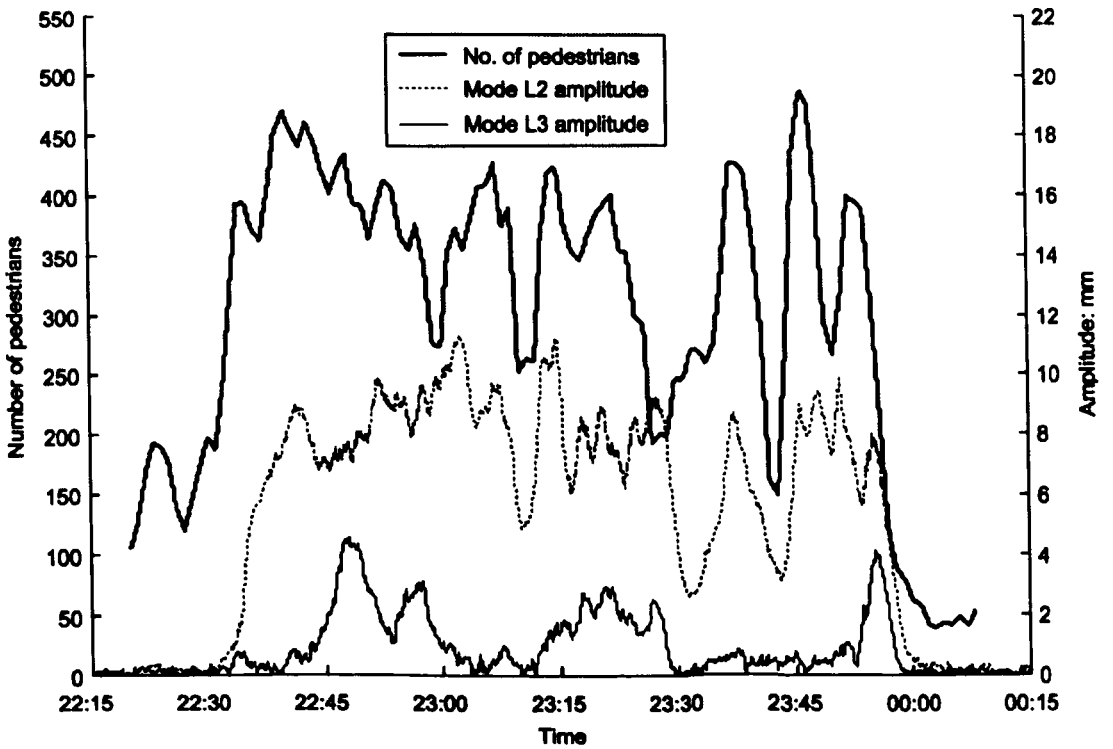

Figure 9.3: Peaks of filtered lateral displacement of mode L2 (0.45-0.65 Hz) and mode L3 (0.65-0.80 Hz) and a corresponding estimate of bridge occupancy, figure obtained from [24].

9.3 Model modification

To facilitate the following analysis, and in line with [24], it is assumed that the suspension chains moved with the deck, and that the combined mass per unit length of both remains constant. It is further assumed that there is no coupling between modes and orthogonality conditions are satisfied. Thus modal superposition is used to determine the multi-mode response experienced by pedestrians.

In order to model the IP response to multi-mode vibration the governing differential

equations for the dynamical system are modified from (8.1.6) and (8.1.12) to the following:

$$\ddot{y}_p = -\left[\ddot{U}_2\,\phi_2(x_p) + \ddot{U}_3\,\phi_3(x_p)\right] - [\omega_p + f(T)]^2(u_p - y_p) \tag{9.3.1}$$

for $p = 1$ to N pedestrians, and,

$$\ddot{U}_2 = \frac{1}{m_2}\left[\left(\sum_{p=1}^{N} m_{p,p}\,\omega_p^2\,(u_p - y_p)\,\phi_2(x_p)\right) - c_2\,\dot{U}_2 - k_2\,U_2\right] \tag{9.3.2}$$

$$\ddot{U}_3 = \frac{1}{m_3}\left[\left(\sum_{p=1}^{N} m_{p,p}\,\omega_p^2\,(u_p - y_p)\,\phi_3(x_p)\right) - c_3\,\dot{U}_3 - k_3\,U_3\right] \tag{9.3.3}$$

Thus there is no direct coupling between both vibration modes, rather, the modes are indirectly coupled via there influence on the behaviour of the IP crowd. In other words, a significant response in one mode will influence the dynamic behaviour of the crowd, which will in turn influence the dynamic behaviour of the second mode.

The structural model proposed is somewhat simplistic when compared against what is in reality a complex structure. However, the focus of this case study is to examine the validity of the proposed model, primarily by demonstrating its ability to simulate simultaneous multi-mode lateral instability.

The simulated pedestrian environment consists of two individual walkways each 1.1 m wide and 194 m long, matching the free suspended span of the deck. Unidirectional crowd flow is simulated from right to left.

9.4 Simulation results

The modal parameters are summarised in Table 9.1. The remaining simulation parameters can be obtained from Table 8.2 with the exception of $|\mathbf{V}_d|_{mean} = 0.7m/s$ (discussed below). Initial positions for the pedestrian crowd were drawn from a uniform distribution across an area to the right of the simulated bridge deck. Random pedestrian start times were assigned as described above, making pedestrian arrival times a uniformly distributed random variable.

Figure 9.4 (a) is a typical observation of the combined lateral displacement and corresponding number of pedestrians present. Plots (b) and (c) are the responses of modes

L2 and L3 respectively. For the first 400 s pedestrians populate the bridge after which the occupancy fluctuates around 250 as pedestrians both vacate and enter the bridge. At $t = 940$ s, a sustained increase in the response of mode L2 is observed, followed by similar behaviour of mode L3 at $t = 1300$ s. Response in both modes is recognisable as lateral dynamic instability defined and demonstrated in section 8.1.3. This is in agreement with observations of the CSB, Fig. 9.3, in which instability in mode L3 was triggered while large amplitude oscillations of mode L2 were experienced. From the point of view of model validation, it can be stated that the proposed model is capable of simulating simultaneous multi-mode lateral instability.

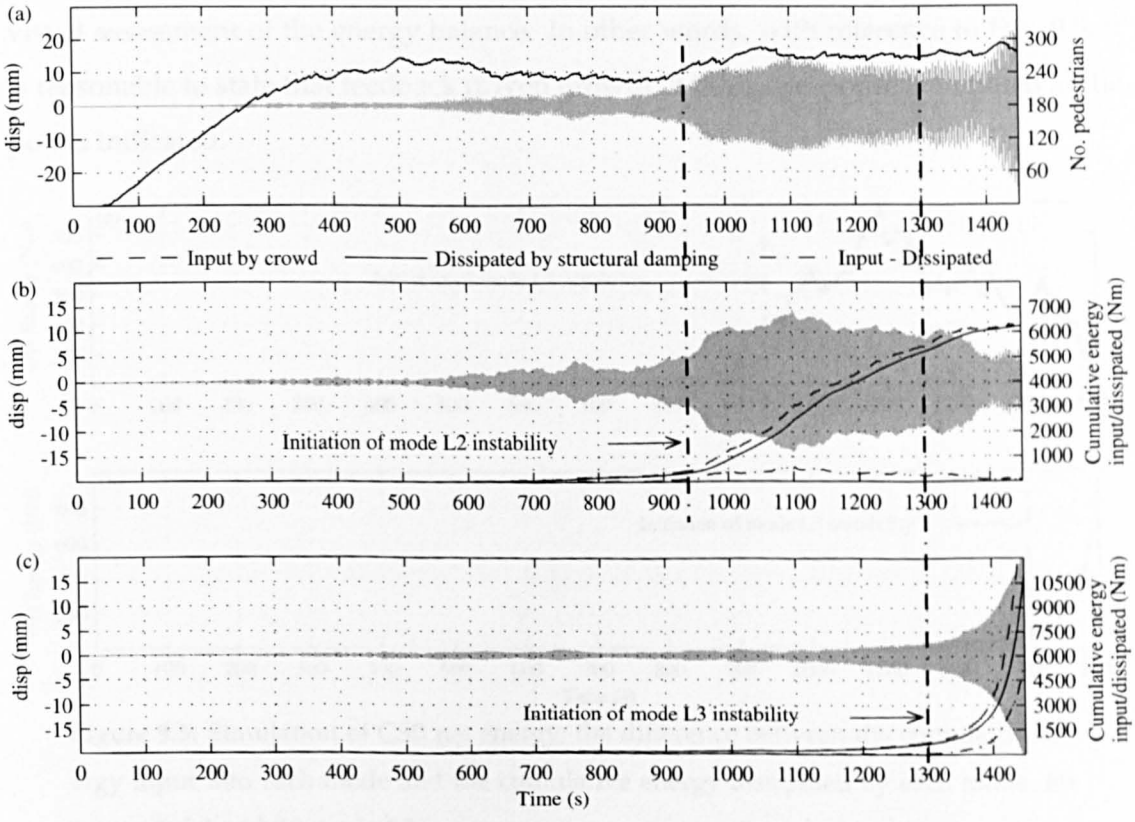

Figure 9.4: Simulation of CSB response: (a) Combined lateral mid-span displacement of modes L2 and L3 (left scale) and number of pedestrians present on the bridge (right scale), (b) Lateral displacement of mode L2 (left scale) and cumulative energy (right scale), (c) Lateral displacement of mode L3 (left scale) and cumulative energy (right scale).

Figure 9.4 (b) and (c) also show the cumulative energy input by the crowd and dissipated by the structure, calculated individually for each mode. The net cumulative energy, calculated as the difference between the input and output is also plotted. The

development of instability in each mode is more clearly seen in Figure 9.5 (a) and (b), which is a larger scale representation of the net cumulative energy. It can be seen that after instability has developed in mode L2, the net energy in mode L2 peaks at $t = 1100$ s, and begins to decline thereafter. This indicates the start of the system's return to characteristic behaviour for that mode. However, while mode L2 is still at a relatively high energy level, instability develops in mode L3 at $t = 1300$ s, indicated by the relatively sharp increase in net energy for the mode.

It should be stated that identification of the point at which instability is initiated (indicated by the vertical dashed lines in Figs. 9.4 and 9.5) is defined based on a qualitative visual assessment of the energy balance. In other words, with reference to Fig. 9.5, it is reasonable to state that feedback driven growth in bridge response is initiated at the points indicated.

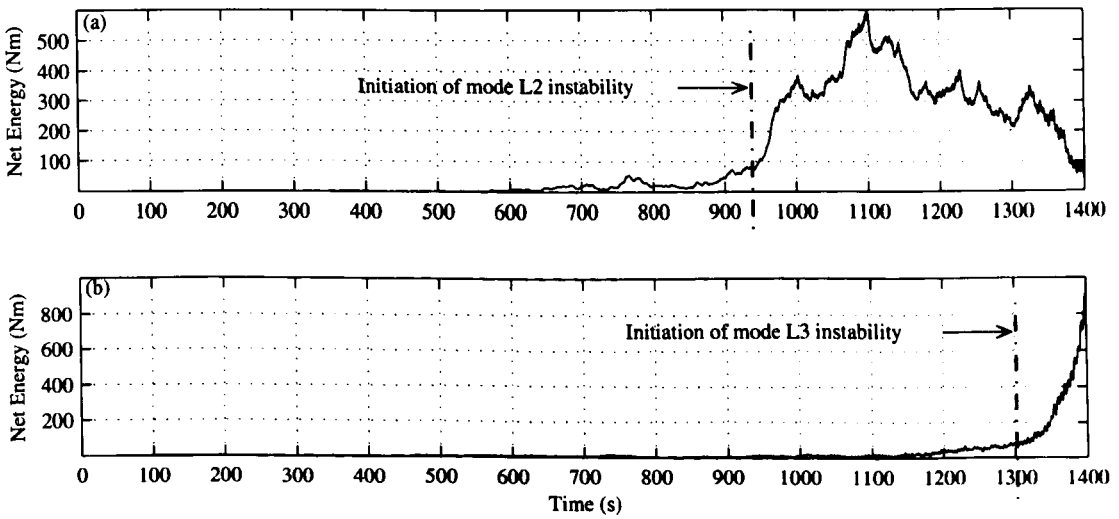

Figure 9.5: Simulation of CSB net energy; the difference between the cumulative energy input into each mode and the cumulative energy dissipated by each mode, for (a) mode L2 and (b) mode L3.

The peak displacement in mode L2 on the CSB was approximately 11 mm. This compares with a peak simulated displacement of 14 mm. For mode L3 the largest observed displacement was approximately 5 mm. However in the case of the simulation, the response of mode L3 continues to grow rapidly after instability is developed. This is because the self-limiting nature of the HSI phenomenon has not been coded into the model, i.e. there is no retardation or stop threshold imposed on the IP's behaviour. The reason for this (they are used as a means of demonstrating the capability of the mod-

elling technique in chapter 5) is that at present there is significant uncertainty regarding the values of such thresholds.

On the CSB the rapid growth in the response of mode L3 is initiated (judging from Fig. 9.3) approximately 10 minutes after the initiation of similar behaviour in mode L2. For the simulated response the delay between mode L2 and L3 instability is 6 minutes. Despite the obvious visual differences between observed (Fig. 9.3) and simulated (Fig. 9.4) response time histories, these quantitative measures indicate reasonably good agreement in the underlying dynamic behaviour.

The frequency composition of the combined (mode L2 + L3) lateral displacement and corresponding crowd-induced loading are shown in Fig. 9.6 (a) & (b) for $t = 0s$ to $t = 940s$, prior to any instability. As expected there is a broad range of excitation frequencies representing the pedestrian crowd, plot (b). Peaks are visible at the base oscillation frequencies, however their relative magnitudes are not excessively large in comparison to the other harmonic components.

The same analysis can be seen in Fig. 9.6 (c) & (d) for $t = 940s$ to $t = 1300s$, after L2 instability has developed but prior to instability in L3. The strong interaction between the IP crowd and mode L2 results in sideband harmonics within the GRF spectrum of each pedestrian. The summation of these force harmonics (at the oscillation frequency of mode L2) significantly outweighs the force harmonics distributed at the individual pedestrian lateral forcing frequencies plot (d). As such, the response of mode L2 is significantly greater than mode L3, plot (c).

Fig. 9.6 (e) & (f), show the frequency composition between $t = 1300s$ and $t = 1450$, after L3 instability has developed. The response in mode L3 has increased significantly while the response of mode L2 has diminished. The crowd-induced force during this period is dominated by self-excited harmonics at the oscillation frequency of L3. The crowd, initially influenced by mode L2, are now more strongly influenced by the increasing response of mode L3.

Multiple simulations with varying mean desired walking velocity revealed that in order for lateral instability to develop in both modes, the mean desired walking speed for the pedestrian crowd must be approximately 0.7 m/s. This results in a mean lateral forcing frequency of 0.63 Hz after crowd effects have been simulated. Thus the mean

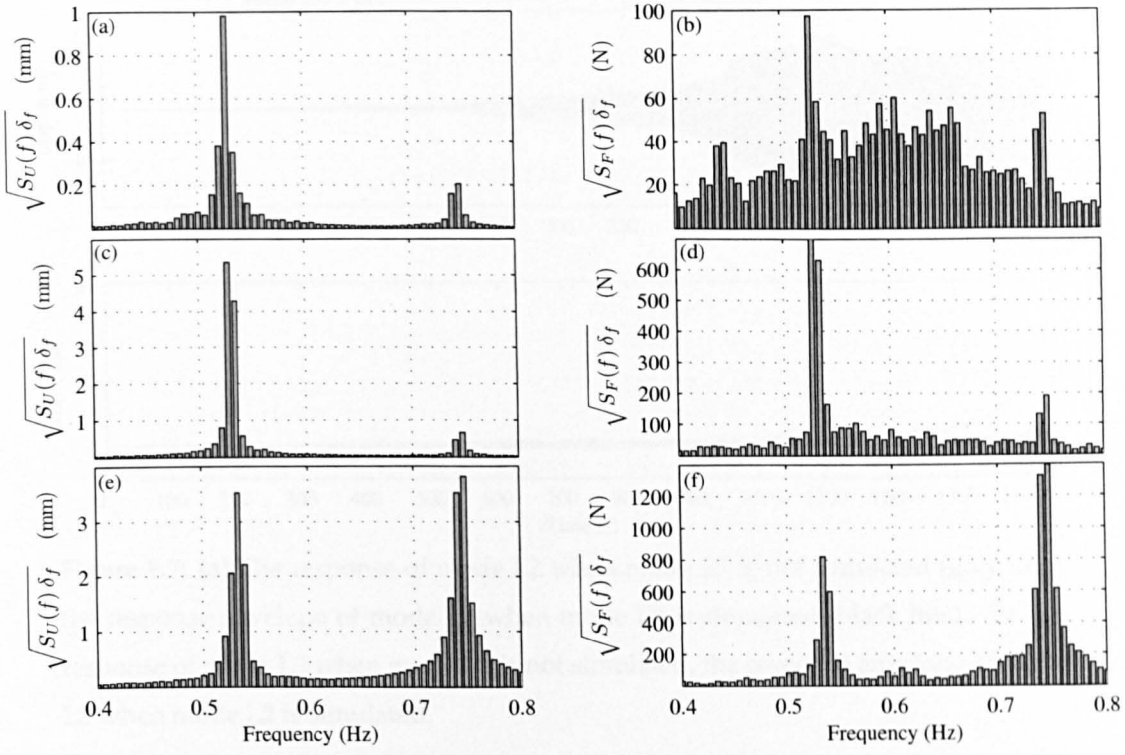

Figure 9.6: Coupled simulation of CSB response: The frequency composition (note different vertical scales) of (a) combined lateral bridge response from $t = 0s$ to $t = 940s$, (b) crowd-induced lateral loading from $t = 0s$ to $t = 940s$, (c) combined lateral bridge response from $t = 940s$ to $t = 1300s$, (d) crowd-induced lateral loading from $t = 940s$ to $t = 1300s$, (e) combined lateral bridge response from $t = 1300s$ to $t = 1450s$, (f) crowd-induced lateral loading from $t = 1300s$ to $t = 1450s$. Bar heights indicate the RMS value of frequency contributions over fixed bandwidths. The bandwidths of vertical bars are determined by the frequency resolution ($\delta_f = 0.007$ Hz) of the underlying single sided power spectral density, $\hat{S}_F(f)$ & $\hat{S}_U(f)$.

forcing frequency lies in the middle of the two modal frequencies. The lower sideband harmonics associated with mode L2 initially lead to development of instability in that mode, however, due to the symmetrical (about the lateral forcing frequency) nature of the sideband force harmonics, the upper sidebands simultaneously resonate with the higher modal frequency at 0.75 Hz leading to instability in that mode soon after.

To investigate the dependence of mode L3 instability on mode L2 (within this simulation), the simulation was repeated. However, in one case only the response of mode L2 was simulated, thus the influence of mode L3 on the IP models was eliminated. In another case, the response of mode L3 alone was simulated. The modal responses can be seen in Fig. 9.7 (a) and (b). In the first case, it can be seen that instability in mode L2

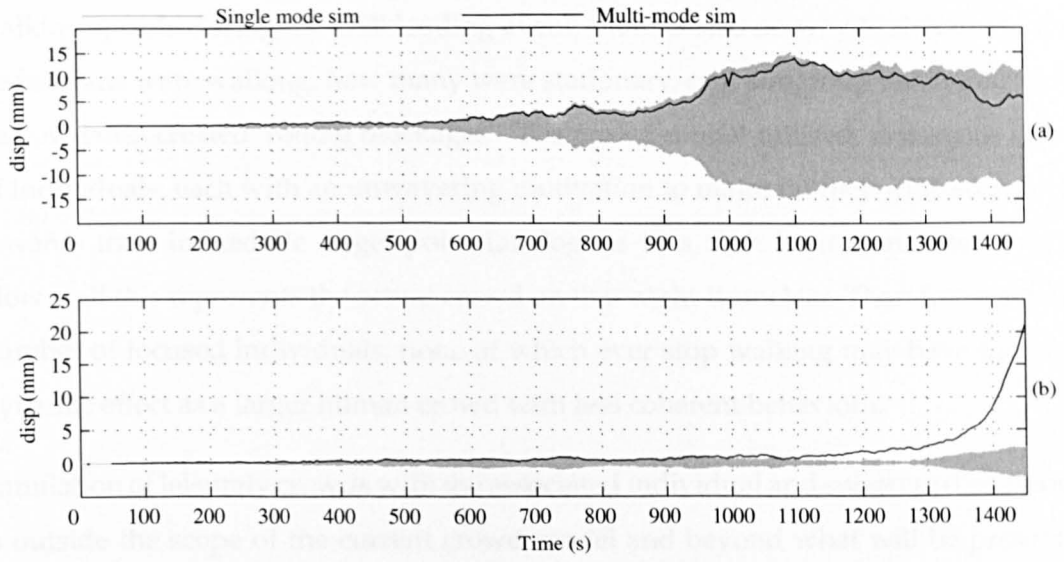

Figure 9.7: (a) The response of mode L2 when mode L3 is not simulated (grey line), the response envelope of mode L2 when mode L3 is simulated (black line). (b) The response of mode L3 when mode L2 is not simulated, the response envelope of mode L3 when mode L2 is simulated.

develops independently of mode L3, Fig. 9.7 (a). The response observed is similar to that in the original multi-mode simulation. However it appears that the reduction in response of L2 at the end of the multi-mode simulation is related to the development of L3 instability, as without the influence of L3's response, large response would have persisted in mode L2.

Most significantly, Fig. 9.7 (b) demonstrates that without the effect of mode L2 on the IP crowd, instability in mode L3 is not developed during the period of observation. This supports the assertion that self-excited (upper sideband) force harmonics developed during interaction between the crowd and mode L2, were responsible for initiating instability in mode L3. This observation may explain why instability was triggered in mode L3 while relatively large amplitude oscillations were being experienced in mode L2 on the real structure.

9.5 Discussion and conclusions

The mean desired walking speed (0.7 m/s) in this simulation is not unrealistic but is considerably lower than one would expect [63]. There is no data relating to the crowd

walking speeds during the CSB loading event, there is also no way to determine if all pedestrians were walking, how many were stationary, or if subgroup behaviour in the narrow lanes created 'rolling blockages'. The crowd model utilised, assumes a crowd of individuals, each with an unwavering motivation to maintain their desired velocity towards their immediate target point (analogous to a rush hour commuter crowd). How well this represents the actual crowd on that night is unclear. Therefore a smaller number of focused individuals, none of which ever stop walking may have the same dynamic effect as a larger human crowd with less coherent behaviour.

Simulation of leisurely crowds with the associated individual and subgroup behaviours is outside the scope of the current crowd model and beyond what will be presented in this thesis. Nevertheless, if the aim of an analysis is to determine dynamic behaviour compatible with evolving traffic conditions, then realistic simulation of crowd behaviour should be the objective.

The number of pedestrians on the bridge when instability is initiated (in the model) is 240 and 250 for modes L2 and L3 respectively. It was estimated that the number of pedestrians present on the CSB when instability was triggered was 200 and 470 for modes L2 and L3 respectively. This model suggests that instability can be triggered with fewer pedestrians, under the right conditions. However, it is equally possible that discrepancies between simulated data and field observations are due to modelling inaccuracies. It should be noted that the estimate of pedestrians on the bridge in [24] was obtained by monitoring CCTV footage of pedestrians entering the bridge only. No record was made of the corresponding number of pedestrian exiting the bridge. Therefore there is scope for inaccuracy in both the model and validation data.

Model predictions show reasonably good agreement with data recorded on the CSB. Significantly from a model validation point of view, multi-mode instability of the structure has successfully been predicted. This in itself provides a degree of validity to the proposed model, independently of the qualitative agreement discussed above. Furthermore it has been demonstrated within the model, that instability of mode L3 was initiated as a result of the interaction that took place between the IP crowd and mode L2. The upper side-band components of the self-excited force generated during interaction between the crowd and mode L2, resonated with mode L3, leading to instability

in that mode. This may explain the development of multi-mode instability observed on the real structure.

In the following chapter, final conclusions for the complete body of work are drawn. The limitations of this work are highlighted and areas requiring further research identified.

CHAPTER 10

Conclusions and further research

Chapter Summary

In this chapter the project conclusions are stated and the success with which the project aims have been satisfied is assessed. Conclusions regarding the biomechanics of HSI are put forward in section 10.1. This is followed in section 10.2 by conclusions regarding the crowd-structure interaction model development. In section 10.3, the contribution made to the field of crowd-induced bridge vibration is summarised and the limitations of the work are acknowledged. In section 10.4 areas requiring further research are highlighted.

10.1 Conclusions - The biomechanics of HSI

In chapter 4, a simple question was posed; *how does pedestrian balance behaviour in response to base motion lead to the generation of self-excited harmonics within the GRF spectrum?* Previous researchers have identified the existence of such harmonics but the mechanism responsible for their generation had not been experimentally identified. Based on the analysis in chapter 6, it is concluded that periodic gait width modulation, resulting in AM of the GRF is the mechanism responsible for generation of self-excited GRFs. Harmonics within the GRF spectrum occurring at the base oscillation frequency are identified as frequency sidebands.

Test subject's balance response to deck oscillation is dominated by changes to lateral foot placement position. The frequency of gait width modulation was identified as the modulus of the difference between the lateral forcing and deck oscillation frequencies. This is consistent with the identification of self-excited force harmonics as frequency sidebands. The sinusoidally varying inertia force experienced by the subject is the underlying reason for this frequency relationship. Thus the link between frontal plane balance behaviour and the generation of the self-excited component of the lateral GRF has been established.

In addition to this conclusion the successful reproduction of lateral GRFs from visual marker data was also demonstrated in chapter 6. To the author's knowledge, this is the first application of this inverse dynamics technique for the reproduction of lateral GRFs. The success demonstrated in this project may encourage other researchers to adopt similar minimally intrusive optically based data acquisition methods. Particularly for the investigation of HSI.

In chapter 4 it was hypothesised that active balance control in response to lateral base motion plays a significant role in determining frontal plane CoM motion. Therefore, the passive IP alone cannot adequately simulate pedestrian CoM motion during the single stance gait phase. In chapter 7 this hypothesis was disproven. It was demonstrated that the single stance oscillatory behaviour of subjects walking on a laterally oscillating deck is well described by a passive IP model. This was confirmed for oscillation amplitudes ≤ 20 mm and frequencies ≤ 1.1 Hz.

Direct comparison between simulated and observed GRFs in chapter 7 revealed that the magnitude of the GRF is underestimated due to the CoP typically not being placed at a sufficient lateral distance to the CoM. This inaccuracy can be reduced by increasing the minimum stability margin, however it was demonstrated in chapter 8 that correcting for this inaccuracy by simulating larger IP gait widths has a negligible influence on the development of lateral instability. Furthermore, it was demonstrated that the interaction behaviour exhibited by the IP model, stabilised by Hof et al's balance law [43], is a qualitatively sound representation of the experimentally observed interaction mechanism. Its use as a biomechanical model in chapter 8 was therefore justified.

10.2 Conclusions - Modelling crowd-induced bridge vibration

The task set out in chapter 4 was to model a virtual crowd in which each pedestrian is individually 'aware' of both their spatial environment and their dynamic relationship with the flexible bridge on which they walk. Based on this awareness, each pedestrian should behave accordingly.

Central to achieving this was the implementation of a discrete element crowd model which could address the limitations of the hydrodynamic crowd modelling approach. In chapter 5, this discrete modelling technique was successfully implemented demonstrating the viability of the concept. Low density traffic and discontinuous pedestrians distributions were simulated without the need to assume an equivalent continuous distribution of pedestrians spread over the deck. ISV was simulated and shown to have an significant influence on the behaviour of the coupled crowd-bridge system. The emergence of an 'organic' velocity-density relationship was also demonstrated. Furthermore, it was found that by tuning the variability in desired walking velocities, the emergent velocity-density relationship exhibited by the model was a good approximation to that obtained in the field by Fruin [67].

In chapter 8, the discrete element crowd model from chapter 5 and the validated IP biomechanical model from chapter 7 were combined to form the complete interaction model. Thus a crowd 'aware' of both their spatial environment and their dynamic relationship with the flexible bridge was simulated.

This model allows the cumulative effect of the experimentally identified HSI mechanism to be simulated. It has been shown that this interaction mechanism can lead to large amplitude bridge oscillations being developed, consistent with field observations of lateral dynamic instability. This results from a feedback mechanism in which random crowd excitation is sufficient to generate a deck response that influences IP gait width. This in turn induces self-excited GRF harmonics further increasing bridge response. Critically, this interaction and the development of large amplitude response occurs without step frequency tuning.

In chapter 9 the complete interaction model is used (with minor modification) to simulate the documented crowd loading of Bristol's CSB. Perhaps the most significant feature of this loading event is the development of simultaneous multi-mode instability. This was successfully reproduced and demonstrated in chapter 9. It should be noted that the mean desired walking speed among the simulated crowd was 0.7 m/s when multi-mode instability was developed. This results in a mean lateral forcing frequency of 0.63 Hz, in between the two modal frequencies of interest. This is likely to have been critical to the development of simultaneous multi-mode instability as the lower and upper sideband harmonics of the GRFs resonated with mode L2 and L3 simultaneously. Interestingly, simulation results also suggest that instability of the higher frequency mode, L3, resulted due to interaction between the crowd and mode L2.

10.3 The contribution and limitations of this thesis

The discussion in chapters 6 and 7 provides a clearer understanding of HSI, establishing the link between balance behaviour and the generation of self-excited GRFs; thus fulfilling the first aim set out in chapter 4. On the basis of the simulation data presented on chapters 5, 7 and 8 and the validation exercise in chapter 9, it is reasonable to conclude that the second aim has been satisfied.

As far as the author is aware, this is the first implementation of a discrete element crowd model as a means of simulating the evolving spatial distribution and frequency of dynamic loads on a structure. Although applied to a footbridge in this work, there is significant potential for this technique to be expanded to the simulation of occupant-

induced vibration of any structure. This technique, coupled with the probabilistic post-processing demonstrated in subsection 5.2.6 may offer a useful alternative to current 'worst case' design scenarios.

Despite the fulfilment of both project aims, there are limitations in the work presented in this thesis. Some are the result of time constraints; with an infinite amount of time, anything is possible, alas, that is not the case here. Other limitations result from budget restrictions, while some are simply due to a lack of foresight on the author's part.

A parametric study further exploring the behaviour of the proposed model would be a worthwhile exercise and is identified as a follow up activity to the work presented herein. Furthermore, the acquisition of experimental data obtained specifically to underpin the model validation presented in chapter 9 is also identified as a priority.

There are several limitations in the experimental campaign; identified in section 6.6, they are repeated here. The influence of visual stimulus on subject's behaviour was not adequately accounted for. Visual stimulus should be monitored and if possible controlled during testing. Subjects were also required to walk with the treadmill belt speed fixed for the duration of the test. Feedback between treadmill belt speed and subject walking speed would allow one to investigate a subject's tendency to step synchronise with the oscillating deck. The constraint on subject's walking speed biases any step synchronisation behaviour in this study.

In spite of the above drawbacks and limitations, the work presented in this thesis represents a worthwhile contribution to the study of crowd-induced lateral bridge vibration.

10.4 Further research

In order to address the some of the limitations in this work, a parametric study of the proposed virtual crowd-structure interaction model should be carried out. The aims of this work should be (i) to explore the system stability boundaries to allow better understanding of the transition to instability and (ii) to provide practical design guidance, possibly in the form of parameterised design charts. Further case study validation exercises should also be carried out to increase confidence in model output, the most

obvious candidate being the London Millennium Bridge.

In addition to the outstanding tasks identified above, there are many potential avenues for further research signposted by the work presented herein. The current lack of knowledge regarding the existence of vibration amplitude thresholds and the potential variability among the population represents a significant knowledge gap. If this gap is addressed, the discrete element modelling technique could be further exploited by seeding the crowd with threshold values as demonstrated in chapter 5. An experimental campaign to address this issue should endeavour to investigate pedestrian behavioural response on full scale footbridges, as the bias induced by the laboratory environment is likely to be significant.

As stated previously, the expansion of the discrete element modelling techniques presented herein, to the simulation of occupant-induced vertical vibration of other 'lively' structures is an area meriting further attention. An exploratory study to investigate the potential economies that may be achieved by implementation this simulation methodology over existing code based analysis approaches is merited.

The biomechanical model employed throughout this project has been confirmed as fit for purpose. However, further biomechanical model development may lead to more accurate estimates of GRFs in all three orthogonal directions, better capturing the 3-dimensional nature of human locomotion. This is likely to improve the accuracy of crowd-induced vibration simulation by (i) providing greater accuracy in the simulation of individual GRFs and (ii) providing greater insight into the sources of both inter and intra-subject variability.

The influence of visual stimulus on HSI represents one of the biggest outstanding questions. Related to this is the question of inter-pedestrian synchronisation; how likely are pedestrian to step synchronise with each other based on visual cues and how might this behaviour be related to crowd density? The investigation of inter-pedestrian synchronisation is potentially more demanding than the study of HSI, requiring interdisciplinary collaboration with researchers in branches of psychology, not traditionally within the comfort zone of the civil engineer. Greater collaboration between civil engineering dynamics, biomechanics and psychology is likely to hold the key to the big outstanding questions in the field of crowd-induced vibration. The work presented in

the preceding chapters represents a solid foundation from which to investigate these outstanding questions.

References

[1] http://commons.wikimedia.org.

[2] P. Dallard, A.J. Fitzpatrick, A. Flint, S. Le Bourva, A. Low, R.M. Ridsdill Smith, and M. Willford. The london millennium footbridge. *The Structural Engineer*, 79: 17–33, 2001.

[3] E.T. Ingolfsson, C.T. Georgakis, and J. Jonsson. Pedestrian-induced lateral vibrations of footbridges: A literature review. *Engineering Structures*, 45:21–52, 2012.

[4] S. Nakamura. Field measurements of lateral vibration on a pedestrian suspension bridge. *The Structural Engineer*, 81:22–6, 2003.

[5] S. Nakamura and T. Kawasaki. Lateral vibration of footbridges by synchronous walking. *Journal of Constructional Steel Research*, 62:1148–1160, 2006.

[6] J.M.W. Brownjohn, P. Fok, M. Roche, and P. Omenzetter. Long span steel pedestrian bridge at singapore changi airport - part 2: Crowd loading tests and vibration mitigation measures. *The Structural Engineer*, 82:28–34, 2004.

[7] A. Ronnquist. *Pedestrian induced lateral vibrations of slender footbridges*. PhD thesis, Norwegian University of Science and Technology, 2005.

[8] A. McRobie, G. Morgenthal, J. Lasenby, and M. Ringer. Section model tests on human-structure lock-in. *Bridge Engineering*, 156:71–79, 2003.

[9] C.H. Butz, C.H. Heinemeyer, A. Goldack, A. Keil, M. Lukic, E. Caetano, and A. Cunha. Advanced load models for synchronous pedestrian excitation and optimised design guidelines for steel footbridges. Technical report, Office for Official Publications of the European Communities, 2008.

[10] E.T. Ingolfsson, C.T. Georgakis, F. Ricciardelli, and L. Proncino. Lateral human-structure interaction on footbridges. In *Recent Advances in Structural Dynamics*, Southampton, 2010.

[11] E.T. Ingolfsson, C.T. Georgakis, F. Ricciardelli, and J. Jonsson. Experimental identification of pedestrian-induced lateral forces on footbridges. *Journal of Sound and Vibration*, 330:1265–1284, 2011.

[12] V. Racic, J.M.W. Brownjohn, and A. Pavic. Reproduction and application of human bouncing and jumping forces from visual marker data. *Journal of Sound and Vibration*, 329:3397 – 3416, 2010.

[13] A.L. Hof, R.M. van Bockel, T. Schoppen, and K. Postema. Control of lateral balance in walking: Experimental findings in normal subjects and above-knee amputees. *Gait & Posture*, 25:250–258, 2007.

[14] A.L. Hof, S. Vermerris, and W. Gjaltema. Balance response to lateral perturbations in human treadmill walking. *The Journal of Experimental Biology*, 213:2655–2664, 2010.

[15] M. Bocian, J.H.G. Macdonald, and J.F. Burn. Biomechanically inspired modelling of pedestrian-induced forces on laterally oscillating structures. *Journal of Sound and Vibration*, 331:3914–3929, 2012.

[16] Y.P. Ivanenko, R.E. Poppele, and F. Lacquaniti. Motor control programs and walking. *The Neuroscientist*, 12:339–348, 2006.

[17] E. Otten. Balancing on a narrow ridge: biomechanics and control. *Philosophical Transactions of the Royal Society B: Biological Sciences*, 354:869–875, 1999.

[18] M.W. Whittle. *Gait Analysis: An Introduction*. Butterworth Heinemann, Edinburgh, 2004.

[19] V.T. Inman, H.J. Ralston, and F. Todd. *Human Walking*. Williams and Wilkins, Baltimore, 1981.

[20] J. Hammil and K.M. Knutzen. *Biomechanical basis for human movement, 3rd Edn.* Lippincott Williams and Wilkins, 2009.

[21] C.L. Vaughan, B.L. Davis, and J.C. O' Conner. *Dynamics of Human Gait*. Kiboho Publishers, Cape Town, South Africa, 1999.

[22] J. E. A. Bertram and A. Ruina. Multiple walking speed-frequency relations are predicted by constrained optimization. *Journal of Theoretical Biology*, 209:445–453, 2001.

[23] W.H. Barlow. Description of the clifton suspension bridge. *Minutes of the Proceedings of the Institution of Civil Engineers*, 26:243–257, 1867.

[24] J.H.G. Macdonald. Pedestrian-induced vibrations of the clifton suspension bridge, uk. *Proceedings of the ICE - Bridge Engineering*, 161:69–77, 2008.

[25] P. de Leva. Adjustment to zatsiorsky-seluyanov's segment inertia parameters. *Journal of Biomechanics*, 29:1223–1230, 1996.

[26] P. Dziuba, G. Grillaud, O. Flamand, S. Sanquier, and Y. Tétard. La passerelle solférino comportement dynamique (dynamic behaviour of the solférino bridge). *Bulletin Ouvrages Métalliques*, 1:34–57, 2001.

[27] Setra. Assessment of vibrational behaviour of footbridges under pedestrian loading. French national guideline published by Setra, The Technical Department for Transport, Roads and Bridges Engineering and Road Safety, October 2006.

[28] P. Dallard, A.J. Fitzpatrick, A. Flint, A. Low, R.M. Ridsdill Smith, M. Willford, and M Roche. London millenium bridge: Pedestrian-induced lateral vibration. *Journal of Bridge Engineering*, 6:412–417, 2001.

[29] Y. Fujino, B.M. Pacheo, S. Nakamura, and P. Warnitchai. Synchronisation of human walking observed during lateral vibration of a congested pedestrian bridge. *Earthquake Engineering and Structural Dynamics*, 22:741–758, 1993.

[30] J.M.W. Brownjohn, P. Fok, M. Roche, and P. Moyo. Long span steel pedestrian bridge at singapore changi airport - part 1: Prediction of vibration serviceability. *The Structural Engineer*, 82:21–27, 2004.

[31] P. Charles and V. Bui. Transversal dynamic actions of pedestrians & synchronisation. In *Proceedings of Footbridge 2005, second international conference*, Venice, 2005.

[32] A. Low. *Footbridge Vibration Design*, chapter Design for dynamic effects in long span footbridges, pages 37–52. CRC Press, 2009.

[33] W. Hoorpah, O. Flamand, and X. Cespedes. *Footbridge Vibration Design*, chapter The Simone-de-Beauvoir Footbridge between Bercy Quay and Tolbiac Quay in Paris: Study and measurement of the dynamic behaviour of the structure under pedestrian loads and discussion of corrective measures, pages 101–114. CRC Press, 2009.

[34] A. Pizzimenti. *Analisi sperimentale dei meccanismi di eccitazione laterale delle passerelle ad opera dei pedoni (experimental analysis of the lateral pedestrian-induced mechanism of excitation of footbridges)*. PhD thesis, Department of Civil and Environmental Engineering, University of Catania, 2003.

[35] S. Nakamura, T. Kawasaki, H. Katsuura, and K. Yokoyama. Experimental studies on lateral forces induced by pedestrians. *Journal of Constructional Steel Research*, 64: 247–252, 2008.

[36] H. Bachmann and B. Weber. Tuned vibration absorbers for 'lively' structures. *Structural Engineering International*, pages 31–36, 1995.

[37] J.H.G. Macdonald. Lateral excitation of bridges by balancing pedestrians. *Proceedings of the Royal Society a-Mathematical Physical and Engineering Sciences*, 465: 1055–1073, 2009.

[38] G. Piccardo and F. Tubino. Parametric resonance of flexible footbridges under crowd-induced lateral excitation. *Journal of Sound and Vibration*, 311:353–371, 2008.

[39] A. Blekherman. Swaying of pedestrian bridges. *Journal of Bridge Engineering*, 10: 142–150, 2005.

[40] A. Blekherman. Autoparametric resonace in a pedestrian steel arch bridge. *Journal of Bridge Engineering*, 12:669–676, 2007.

[41] S. Nakamura and T. Kawasaki. A method for predicting the lateral girder response of footbridges induced by pedestrians. *Journal of Constructional Steel Research*, 65: 1705–1711, 2009.

[42] C.D. MacKinnon and D.A. Winter. Control of whole body balance in the frontal plane during human walking. *Journal of Biomechanics*, 26:633–644, 1993.

[43] A.L. Hof, M.G.J. Gazendam, and W.E. Sinke. The condition for dynamic stability. *Journal of Biomechanics*, 38:1–8, 2005.

[44] C Barker. Some observations on the nature of the mechanism that drives the self-excited lateral response of footbridges. In *Proceedings of the 1st International conference; design and dynamic behaviour of footbridges*, Paris, 2002.

[45] S.P. Carroll, J.S. Owen, and M.F.M. Hussein. Crowd-bridge interaction by combining biomechanical and discrete element models. In *Proceedings of the 8th international conference on structural dynamics*, Leuven, 2011.

[46] F. Venuti, L. Bruno, and N. Bellomo. Crowd dynamics on a moving platform: Mathematical modelling and application to lively footbridges. *Mathematical and Computer Modelling*, 45:252–269, 2007.

[47] F. Venuti and L. Bruno. An interpretative model of the pedestrian fundamental relation. *Comptes Rendus Mecanique*, 335:194–200, 2007.

[48] F. Venuti, L. Bruno, and P. Napoli. Pedestrian lateral action on lively footbridges: A new load model. *Structural Engineering International*, 17:236–241, 2007.

[49] F. Bruno, L.and Venuti. Crowd-structure interaction in footbridges: Modelling, application to a real case-study and sensitivity analyses. *Journal of Sound and Vibration*, 323:475–493, 2009.

[50] F. Venuti and L. Bruno. Crowd-structure interaction in lively footbridges under synchronous lateral excitation: A literature review. *Physics of Life Reviews*, 6:176–206, 2009.

[51] J. Bodgi, S. Erlicher, and P. Argoul. Lateral vibration of footbridges under crowd-loading: Continuous crowd modelling approach. *Key Engineering Materials*, 347: 685–690, 2007.

[52] S.P. Carroll, J.S. Owen, and M.F.M. Hussein. Reproduction of lateral ground reaction forces from visual marker data and analysis of balance response while walking on a laterally oscillating deck. *Engineering Structures*, 49:1034–1047, 2013.

[53] S.P. Carroll, J.S. Owen, and M.F.M. Hussein. A coupled biomechanical/discrete element crowd model of crowd-bridge dynamic interaction & application to the clifton suspension bridge. *Engineering Structures*, 49:58–75, 2013.

[54] R.K. Andersen. Pedestrian-induced vibrations: human-human interaction. Master's thesis, Department of Civil Engineering, Technical University of Denmark, 2009.

[55] U. Weidmann. Transporttechnik der fussganger. *ETH Zurich*, Ivt Report no. 90, 1993.

[56] J. Nielsen. How we walk: Central control of muscle activity during human walking. *Neuroscientist*, 9:195–204, 2003.

[57] A.E. Patla. Some characteristics of emg patterns during locomotion: implications for the locomotor control process. *Journal of Motor Behaviour*, 17:443–461, 1985.

[58] Y.P. Ivanenko, R.E. Poppele, and F. Lacquaniti. Five basic muscle actications patterns account for muscle activicty during human locomotion. *Journal of Physiology*, 556:267–282, 2004.

[59] J.B. Nielsen and T. Sinkjaer. Afferent feedback in the control of human gait. *Journal of Electromyography and Kinesiology*, 12:213–217, 2002.

[60] C. E. Bauby and A. D. Kuo. Active control of lateral balance in human walking. *Journal of Biomechanics*, 33:1433–1440, 2000.

[61] Y. Matsumoto, H. Nishioka, H. Shiojiri, and K. Matsuzaki. Dynamic design of footbridges. IABSE Proceedings, 1978.

[62] Y. Matsumoto. A study of dynamic design of pedestrian over-bridges. *Transaction of JSCE 4*, pages 50–51, 1972.

[63] A. Pachi and T. Ji. Frequency and velocity of people walking. *The Structural Engineer*, 83:36–40, 2005.

[64] N.H. Molen, R.H. Rozendal, and W. Boon. Graphic representation of the relationship between oxygen-consumption and the characteristics of normal gait of the human male. *Proceedings of the Koninklijke Nederlandse Akademie van Wetenschappen*, C-75:305–314, 1972.

[65] M. Townsend. Biped gait stabilization via foot placement. *Journal of Biomechanics*, 18:21–38, 1985.

[66] S. Zivanovic, A. Pavic, and E.T. Ingolfsson. Modeling spatially unrestricted pedestrian traffic on footbridges. *Journal of Structural Engineering*, 136:1296–1308, 2010.

[67] J.J. Fruin. *Pedestrian planning and design*. Metropolitan Association of Urban Designers and Environmental Planners, 1971.

[68] A.S. AlGadhi and K.G. Still. *Jamarat Bridge; Mathematical models, computer simulation and Hajjis safety analysis*. Ministry of Public Works and Housing, Saudi Arabia, 2003.

[69] R Challenger, C.W. Clegg, and M.A. Robinson. Understanding crowd dynamics: Simulation tools. The Cabinet Office, 2009.

[70] S. Sharma. A static-dynamic netweok model for crowd flow simulation. In *Proceedings, 6th International Space Syntax Symposium, Istanbul*, Istanbul, 2007.

[71] E. Morrow. Innovative approaches to pedestrian planning at toronto's union station. *Arup Research Review*, pages 29–31, 2008.

[72] N.P. Waterson and E. Pellissier. The steps pedestrian microsimulation tool - a technical summary. Technical report, Mott MacDonald Limited, 2010.

[73] D. Helbing and P. Molnar. Social force model for pedestrian dynamics. *Physical Review E*, 51:4282, 1995.

[74] P.A. Langston, R. Masling, and B.N. Asmar. Crowd dynamics discrete element multi-circle model. *Safety Science*, 44:395–417, 2006.

[75] D. Helbing, Farkas. I, and T. Vicsek. Simulating dynamical features of escape panic. *Nature*, 407:487–490, 2000.

[76] R.W. Clough and J. Penzien. *Dynamics of Structures*. McGraw-Hill, Singapore, 1993.

[77] S. Zivanovic. *Probability-Based Estimation of Vibration for Pedestrian Structures due to Walking*. PhD thesis, University of Sheffield, 2006.

[78] D.E. Newland. *An Introduction to Random Vibrations, Spectral & Wavelet Analysis.* Longman Group Ltd., Harlow, 1993.

[79] S. Coles. *An Introduction to Statistical Modeling of Extreme Values.* Springer, London, 2001.

[80] D.C. Montgomery and G.C. Runger. *Applied Statistics and Probability for Engineers.* John Wiley & Sons, Inc, 2007.

[81] V. Racic, A. Pavic, and J.M.W. Brownjohn. Experimental identification and analytical modelling of human walking forces: Literature review. *Journal of Sound and Vibration*, 326:1–49, 2009.

[82] *Coda mpx30 User Guide, Charnwood Dynamics Ltd, Leicestershire, UK.* Charnwood Dynamics Ltd., Leicestershire, UK.

[83] I. Newton. *Philosophiae Naturalis Principia Mathematica (Mathematical Principles of Natural Philosophy).* E. Halley, London, 1687.

[84] V. M. Zatsiorsky, V. N. Seluyanov, and L. G. Chugunova. *Contemporary Problems of Biomechanics*, chapter Methods of determining mass-inertial characteristics of human-body segments, pages 272–291. CRC Press, Massachusetts, 1990.

[85] D.A. Winter. Human balance and posture control during standing and walking. *Gait and Posture*, 3:193–214, 1995.

[86] F Ricciardelli and A Pizzimenti. Lateral walking-induced forces on footbridges. *Journal of Bridge Engineering*, 6:677–688, 2007.

[87] A. Godse and U. Bakshi. *Communication Engineering.* Technical Publications, 2009.

APPENDIX A

Amplitude modulation

Amplitude modulation is the process whereby the amplitude of a carrier wave, $F(t)$ is modulated by a second waveform known as the modulating wave, $M(t)$. In the context of communication theory, the carrier represents the medium of transmission while the modulating wave represents the information to be transmitted. The carrier wave is usually of a higher frequency than the modulating wave. To illustrate the process, let a carrier and modulating wave be represented by the following signals:

$$F(t) = F_l \, sin(\omega_l \, t) \tag{A.0.1}$$

$$M(t) = A_m \, cos(\omega_m \, t) \tag{A.0.2}$$

in which F_l and ω_l represent the amplitude and angular frequency of the carrier wave and A_m and ω_m represent the amplitude and angular frequency of the modulating wave. A_m corresponds to the modulation depth, MD, discussed in section 6.5. The modulated waveform, $F_m(t)$ is obtained as:

$$F_m(t) = [1 + M(t)] \, F(t) = F_l[1 + A_m \, cos(\omega_m \, t)]sin(\omega_l \, t) \tag{A.0.3}$$

Noting the trigonometric identity,

$$sin(A) \, cos(B) = \frac{1}{2}\Big[sin(A + B) \; + \; sin(A - B)\Big] \tag{A.0.4}$$

and rearranging, the modulated waveform can be represented by,

$$F_m(t) = F_l \, sin(\omega_l \, t) \; + \; \frac{F_l \, A_m}{2}[S_l \; + \; S_u] \tag{A.0.5}$$

where S_l and S_u are the lower and upper frequency sidebands given by,

$$S_l = sin[(\omega_l - \omega_m)\, t] \tag{A.0.6}$$

$$S_u = sin[(\omega_l - \omega_m)\, t] \tag{A.0.7}$$

When extended to consider a modulating signal consisting of N frequencies, the modulating signal takes the form,

$$M(t) = \sum_{i=1}^{N} A_{m,i}\, cos(\omega_{m,i}\, t + \phi_{m,i}) \tag{A.0.8}$$

resulting in a modulated signal, $F_m(t)$, containing all frequency components of $M(t)$,

$$F_m(t) = F_l\, sin(\omega_l\, t) \; + \; \frac{F_l}{2} \sum_{i=1}^{N} A_{m,i} \Big[S_{l,i} \; + \; S_{u,i} \Big] \tag{A.0.9}$$

where the upper and lower sidebands are given by,

$$S_{l,i} = sin[(\omega_l - \omega_{m,i})\, t - \phi_{m,i}] \tag{A.0.10}$$

$$S_{u,i} = sin[(\omega_l + \omega_{m,i})\, t + \phi_{m,i}] \tag{A.0.11}$$